SEARCH FOR LIGHTLY IONIZING PARTICLES USING CDMS-II DATA AND FABRICATION OF CDMS DETECTORS WITH IMPROVED HOMOGENEITY IN PROPERTIES

A Dissertation

by

KUNJ BIHARI PRASAD

Submitted to the Office of Graduate and Professional Studies of
Texas A&M University
in partial fulfillment of the requirements for the degree of

DOCTOR OF PHILOSOPHY

Chair of Committee,	Rupak Mahapatra
Co-Chair of Committee,	Rusty Harris
Committee Members,	Bhaskar Dutta
	David Toback
Head of Department,	George Welch

December 2013

Major Subject: Physics

ABSTRACT

Fundamental particles are always observed to carry charges which are integral multiples of one-third charge of electron, $e/3$. While this is a well established experimental fact, the theoretical understanding for the charge quantization phenomenon is lacking. On the other hand, there exist numerous theoretical models that naturally allow for existence of particles with fractional electromagnetic charge. These particles, if existing, hint towards existence of physics beyond the standard model. Multiple high energy, optical, cosmological and astrophysical considerations restrict the allowable mass-charge parameter space for these fractional charges. Still, a huge unexplored region remains.

The Cryogenic Dark Matter Search (CDMS-II), located at Soudan mines in northern Minnesota, employs germanium and silicon crystals to perform direct searches for a leading candidate to dark matter called Weakly Interacting Massive Particles (WIMPs). Alternately, the low detection threshold allows search for fractional electromagnetic-charged particles, or Lightly Ionizing Particles (LIPs), moving at relativistic speed. Background rejection is obtained by requiring that the magnitude and location of energy deposited in each detector be consistent with corresponding "signatures" resulting from the passage of a fractionally charged particle. In this dissertation, the CDMS-II data is analyzed to search for LIPs, with an expected background of 0.078 ± 0.078 events. No candidate events are observed, allowing exclusion of new parameter space for charges between $e/6$ and $e/200$.

With primary aim to increase sensitivity to detect WIMPs, it is necessary to expand the detector count and mass by more than two orders of magnitude over CDMS-II. This also increases sensitivity to detect LIPs. It becomes imperative

to obtain repeatability in the detection sensor quality over multiple detectors. In this dissertation, we also describe the improvements and process flow optimizations implemented to obtain higher yield in fabrication of useful detectors with homogeneous sensor properties within each detector and among different batches. It also allows for reduction in fabrication time, cost and removal of avoidable cost-intensive steps like ion-implantation. Most important is the control in obtaining tungsten thin film with desired superconducting transition temperature and improvements in photolithographic steps for sensor fabrication.

DEDICATION

I dedicate this dissertation to the "spirit of curiosity" which is the sole reason behind the research being performed and the dissertation getting written, and although it gets mostly criticized in recent times as being being out of reality and somewhat non-productive, it is possibly the single, most-important factor that makes humans... humans!

ACKNOWLEDGEMENTS

I would like to acknowledge the help, motivation and support of various people who have been an integral part of my life throughout the days in graduate school and without whom the research experience described in this dissertation, and the dissertation itself, would be absent. They are my family, my friends, my academic advisors and collaborators. I strive to thank them for their help and support, but my few words expressed below do not even marginally justify my deep, heartfelt gratitude towards them.

I would like to start by expressing my gratitude towards my academic advisor, Rupak Mahapatra, for providing me an opportunity to work in his research group and be part of the Cryogenic Dark Matter Search (CDMS) collaboration. One of the two topics discussed in this dissertation focuses on analysis of existing dark matter search data to instead search for events induced by Lightly Ionizing Particles (LIPs), and was primarily Rupak's idea. It is his ability to identify different aspects of a problem, one at a time, while simultaneously keeping the "big picture" in perspective that has been pivotal in defining multiple topics discussed in the dissertation. The other part of the dissertation focuses on development of phonon sensors employed by CDMS detectors. Although this topic was existent within the collaboration, it is the expert guidance of my co-advisor, Rusty Harris, that allowed our group to identify and optimize out multiple problems existing within the current detector fabrication procedure, and achieve feats otherwise thought "impossible". I would also like to thank Rusty for his guidance and support towards the development of my "professional mannerism".

In addition to my advisors, I would like to thank the members of our research

group comprising of Joel Sander (then postdoctoral member at our group and now a faculty at University of South Dakota, Vermillion), Mark Platt (group engineer) and James Phillips (technician). It is Joel's deep knowledge of various physical processes, a strong resolution towards carrying topics to a proper completion and a caring nature that has allowed not just me, but the entire group in having a steep learning curve and also helped in understanding and completing various tasks which otherwise seemed improbable to proceed with. Mark is the "soul" of the entire detector fabrication labs associated with our group and is the primary expert responsible for setting and maintaining the lab, training the new graduate students (including me) to use the machines and still being able to make time to kindly assist in required research efforts when requested. James is a recent addition in our group and assists in the all aspects of detector development efforts.

In addition to the group members, I would like to thank the excellent scientists and engineers who make the CDMS experiment possible. Without their help and their much-needed feedback over multiple topics discussed in the dissertation, it would have been difficult to see them to completion and I am truly fortunate to have had the opportunity to work closely and learn from them. CDMS group members Richard Schnee, Steven Yellin, Elias Lopez Asamar, Raymond Bunker, David Cerdeño, Daniel Brandt and Wolfgang Rau have provided an insightful guidance in construction of analysis techniques presented in the dissertation allowing an interpretation of an event as being caused by LIPs. Group members Betty Young, Paul Brink, Astrid Tomada and Matt Cherry helped the group by providing necessary measurements and insightful guidance in understanding and developing the fabrication procedure. I would also like to thank Jim Beaty for providing constant guidance and advice during my shifts at Soudan Underground Labs (SUL).

I would also like to thank the faculties and staff of the department for supporting

my stay and academically preparing me for the work presented in the dissertation. Additionally, I want to specially thank my Ph.D. committee members, Bhaskar Dutta and David Toback, for their constant guidance and encouragement along my graduate study.

Apart from the academic sphere, I would like to convey my thanks to my family, my parents, brother and sister-in-law, who have always emotionally, and financially when needed, supported my scientific inclinations and corresponding decisions leading up to this moment where I now write a scientific dissertation. Along with my family, I would like to thank my friends without whom the graduate life would have otherwise become "all work and no play, making Jack a dull boy" and I am extremely grateful to be the recipient of this pure and ever-lasting emotional support. I would like to thank my friends Siddhesh Kamat, Sean Downes, Sridhar Radhakrishnan, Saurabh Lele, Ishan Desai, Aaditya Bhat, Swapnil Chaudhary, Amruta Deshpande, Swapnil Ghodge, Angad Mehta, Andrew Jastram (group member), Tathagata Ghosh, Mehmet Ozkan, Jorge Mendoza. I would like to convey a special thanks to my friends Arun Aryasomayajula, Peter Zhokhov, Heshani Jayatissa for providing support during the last and most crucial years of my graduate life. Lastly, I would like to thank Sriteja Upadhyayula for providing additional support over multiple important and non-academic aspects of my graduate life, including motivating me to care for my health, being my driving teacher and helping me plan my final defense.

Finally, I would like to extend my deepest gratitude to my girlfriend, Mavreen Rose Tuvilla. It is my opinion that the entire research work is much like a "fun and play" in comparison to writing a dissertation hundreds of pages long. I am deeply thankful to her for supporting me through this extremely long and "excruciating" moment. Without the support, this dissertation would not have materialized.

NOMENCLATURE

e	Charge of an electron
QED	Quantum Electro Dynamics
FCP / fcp	Fractionally Charged Particle
SM	Standard model of elementary particle physics
BBN	Big Bang Nucleosynthesis
CMB	Cosmic Microwave Background
LIP(s)	Lightly Ionizing Particle(s)
CDMS	Cryogenic Dark Matter Search
WIMP	Weakly Interacting Massive Particle
DM	Dark Matter
$\hbar$	Planck's constant
ehp	Electron hole pair
ZIP	Z-sensitive Ionization and Phonon (detectors)
(J)FET	(Junction) Field Effect Transistor
TES	Transition Edge Sensors
SUL	Soudan Underground Labs
SQUID	Superconducting Quantum Interface Device
T_c	Superconducting transition temperature
aSi	Amorphous silicon
f	Ratio of charge of LIP to charge of electron

TABLE OF CONTENTS

LIST OF FIGURES

FIGURE Page

LIST OF TABLES

TABLE Page

1. INTRODUCTION

It is an experimentally known fact that all elementary particles discovered so far have electric charges in multiples of $e/3$, where e is the electron charge. For example, the upper limit on the electron-proton charge difference is $\lesssim 10^{-21}e$ [46]. Despite the obviousness, there is an absence of a theoretical motivation behind this apparent quantization of electric charges. On the other hand, it is theoretically consistent for a free, unbound particles with electric charge ϵe, where ϵ is any real number, to fit nicely within the framework of Quantum Electro Dynamics (QED). Since the Abelian theory of QED has no nontrivial commutation relations between its generators, there is no algebraic quantization of the charge eigenvalues [73]. In a seminal work by Dirac, it is described that the existence of magnetic monopoles would imply the observed charge quantization [3]. However, with the continuing absence of experimental evidence for monopoles, there is presently no explanation for charge quantization in the quantum theory of electrodynamics. This opens the possibility of encountering exotic particle species with fractional electromagnetic charge, or detecting existent particles, like neutrons, or neutrinos to have such a low value of electric change that it was, up to present, assumed to be neutral. We refer these particles as the Fractionally Charged Particles (FCPs).

FCPs can be introduced into the standard model of elementary particle physics (SM) in a variety of ways (for a review on SM, readers may refer [33]). It was shown by Foot *et al.* that charge quantization is not inherent without the additional constraint of equity of lepton quantum numbers among different flavors (family) of leptons [5]. Charge non-quantization (resulting from non-equality of lepton quantum number among different flavors) can show up as small charge difference between two of three

charged leptons, and a finite charge on two out of three neutrinos (which is currently assumed to be neutral). To be in agreement with experimental evidence sensitive to neutrino charge, these deviations must be of order $10^{-9}e$ or smaller. There are other experiments which seek to obtain limits on "charge quantization hypothesis by constraining charge difference between proton and electron and charge of a neutron.

One method to obtain FCP is to add an $SU(3)_C$ X $SU(2)_L$ singlet Dirac fermion with hypercharge $Y = 2\epsilon$. This is not simple if the hypercharge $U(1)_Y$ is embedded in a grand unified gauge group [4,17]. Another mechanism for introducing FCPs, but without compromising quantization of SM symmetries is described by Holdom [6]. It is done by introducing a separate U(1) interaction, mediated by a separate vector boson called "paraphoton, and allowing a dynamical mixing of paraphoton and photon. Any particle charged under paraphoton (thus, having a "paracharge) accumulates fractional electric charge due to this mixing. The novelty of this mechanism is that it allows for existence of exotic FCPs without inherently violating the electromagnetic charge quantization. Thus, allowing for existene of FCPs, without disregarding the results obtained from neutrinos and charge-neutrality experiments. A related, important point to note is that the presence of extra U(1) sector(s) is inescapable in string-theory landscape [56–63]. Thus, a search for FCP helps to validate string theory. An indirect search for paraphoton (by searching for FCPs) helps in identifying new mechanism by which particles interact with one another (beyond the currently known methods of gravitational, weak, electromagnetic and strong interaction).

Multiple experiments have been performed to restrict the allowable "mass-charge" parameter space of FCPs; using high energy and high-precision optical experiments, and from cosmological and astronomical observations. Since these results do not directly relate to the one presented in this dissertation, they are mentioned separately in Appendix F for completeness of discussion. Readers may refer [15, 17, 88] for re-

view on these experiments. Exclusions based on high energy experiments employ results from accelerator-based experiments, Lamb-shift experiments and observing decay of ortho-positronium into invisible products. They conclude an absence of FCP in certain parameter-space by negation (i.e., had those particles been present, the observed result would be different than experimental result obtained). Exclusions from precision experiments are based on results from spectroscopic experiments measuring vacuum birefringence and dichroism, and Cavendish like experiments and experiments based on creating FCPs through Schwinger mechanism in regions with high electric field. Cosmology based exclusions are done based on constraints arising out of framework of Big Bang Nucleosynthesis (BBN), modeling of observed Cosmic Microwave Background (CMB) considerations. It is also required that the contribution of mass density from FCPs to be sufficiently low to not overclose the universe. Exclusions based on astrophysical arguments are based on studying the alteration in stellar evolution (of sun, red giants, white dwarfs, supernova) caused by the presence of FCPs. Fig. 1.1 below shows all the constraints in a single plot.

If isolatable FCPs exist, there should be some relic abundance left over from the early Universe, located on Earth or outer space. Since the accelerator and colliders searches are not able to observe them, it implies that the FCPs are likely to be heavy. Therefore, it is likely that the geochemical and geophysical processes occurring during Earth's early history may have sunk them deep. Thus, model independent searched are done using the carbonaceous chondritic meteorites [7, 209], which are some of the most primordial and unprocessed sources of materials inside the solar system. At over 4.5 Gyrs old, these meteorites are some of the oldest dated objects in the solar system. It is also believed that they have undergone very little processing since formation [7]. Thus, if FCPs exist, these objects are likely to contain them at roughly the same abundance. Fractional charges are detected using an experimental set-up

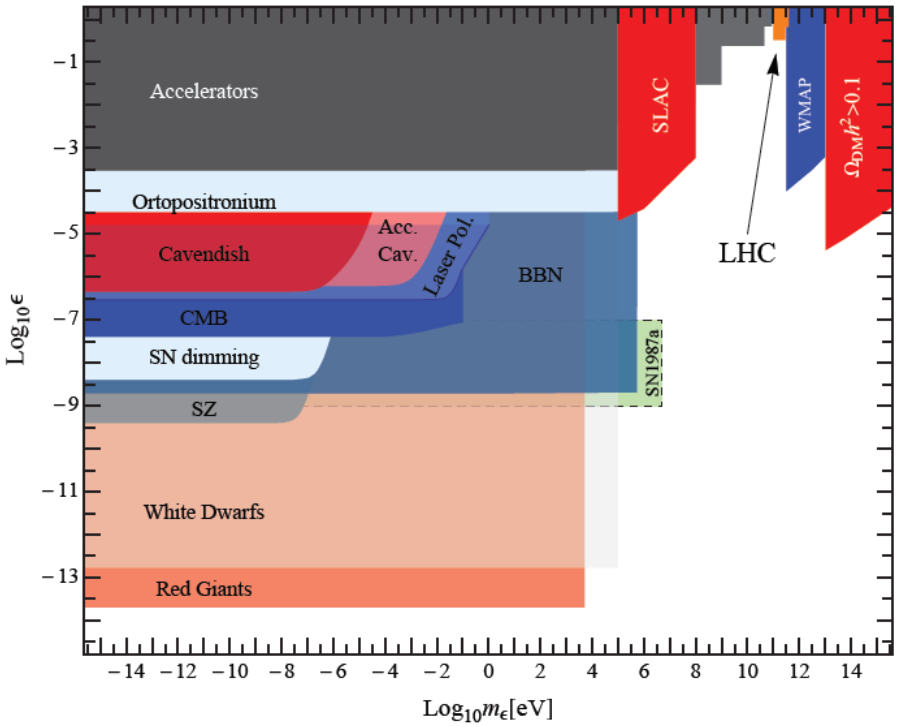

Figure 1.1: Constraints on "mass-charge" parameter space for FCPs from various high-energy experiments, precision optical experiments, cosmological and astrophysical considerations [15, 17, 88].

similar to Millikan oil drop method. Since these results too don't directly relate to the one presented in this dissertation, it is discussed separately in Appendix C.

The nature of experiment and result described in the dissertation relates to search for FCPs produced by interaction of cosmic rays and earth's atmosphere. Suitable constraints can be placed by searching for interactions between cosmogenically produced FCP with detectors placed either on earth's surface or underground. The main philosophy behind such experiments is to search for particles traveling in straight line, but depositing energies much less than that expected for a particle with charge e (like, cosmic muon). This is because the fractional charge of the particles reduce their electromagnetic interaction probability with the detector. Since these parti-

cles deposit less energy, they are also called Lightly Ionizing Particles (LIPs). Such an attempt was done using Liquid Scintillation Detector (LSD) at Mount Blanc laboratory [8], Kamiokande-II detector [9], and by the Monopole Astrophysics and Cosmic Ray Observatory (MACRO) [10]. Results from these experiments are shown in Fig. 1.2. The advantage of this process is that extremely high energy cosmic rays can create massive FCPs which cannot be created through by current particle accelerators. Details of theoretical and experimental motivation to search for LIPs is discussed in Section 2.

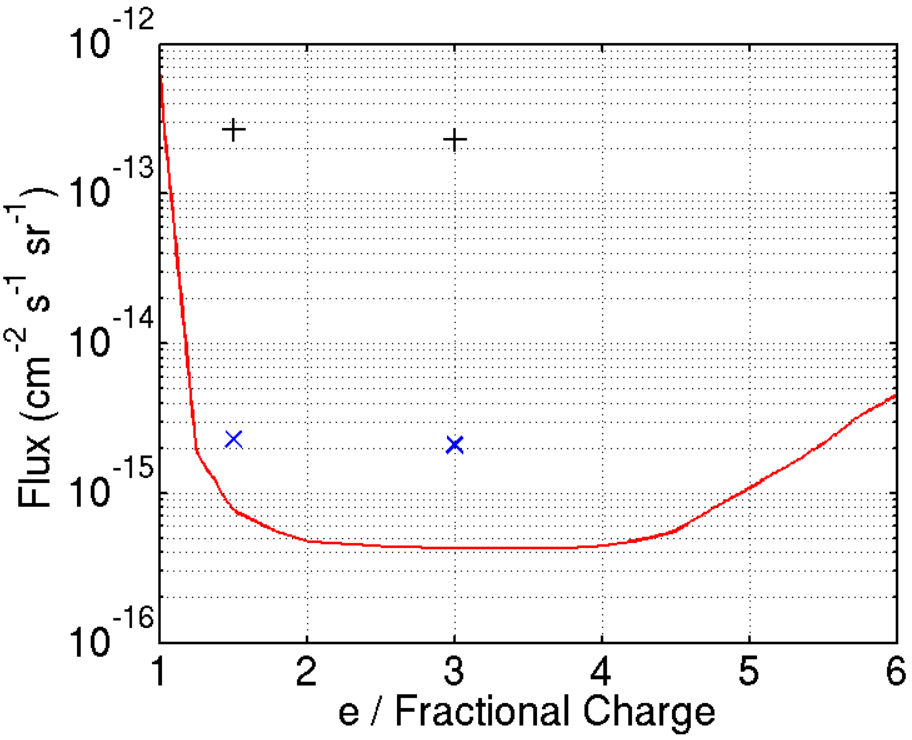

Figure 1.2: The 90% Confidence Level MACRO flux exclusion limits for FCPs (red) compared with previous limits from Kamiokande (blue X) and LSD (black +) [10].

The dissertation performs a search for FCP using data obtained from Cryogenic

Dark Matter Search experiment (CDMS) [11–13]. In performing this search, it is assumed that the FCP only interacts electromagnetically with CDMS detectors. We also assume that the particles are massive and relativistic (they are at minimum ionizing point on the Bethe-Bloch curve [14] and that their incident flux on CDMS detectors is sufficiently low that no more than a single FCP interacts with the detectors at a given time. It is also suggested that these particles are of cosmogenic origins (therefore, being able to move relativistically despite being massive).

The CDMS detectors are installed at the Soudan Underground Lab in northern Minnesota at a depth of 2090 meters water equivalent (mwe). As mentioned, the main aim of detectors is to search for Weakly Interacting Massive Particles (WIMPs) [1, 2, 14], which are a leading candidate to DM. WIMP induced interaction occur with an extremely low expected interaction probability of $<$ 1event/(kg day), with typical deposited energies of 10-100 keV. Thus, it is necessary to use highly sensitive detectors for WIMP detection. CDMS detectors use charge and phonon sensors which measure the electron-hole pair and phonons generated inside detector as a particle interacts with it. The sensitivity of detectors allows us to search for LIPs with very low fractional charges (LIPs interaction probability decreases with reduction of fractional charge). CDMS detectors are Germanium, or Silicon crystals with electrodes instrumented on one side (to collect holes created when external particle interacts with detectors). The other side of crystal is instrumented with sensors to collect phonons. The entire set-up is cryogenically cooled to 50mK. Low temperature enables the electron-hole pairs created during particle interaction to not get trapped within the crystal before they are collected by the electrode and also increases the responsivity to phonon detection.

Dark matter searches are performed deep underground to prevent getting fake signals from cosmogenic neutrons, or from neutrons formed due to interaction of

high energy cosmic muons with surrounding rocks. These depths are sufficient to reduce surface-level muon flux by a factor of ∼50,000 near the detectors. One may ask whether any underground experiment (like, CDMS) is bound to not observe any LIPs? To answer, it is observed that despite the reduction in muon flux, cosmic muons are still observed by CDMS detectors. Since LIPs interact progressively less (due to their reduced charge), we expect more of them to reach our detectors. Thus, the underground location of detectors do not pre-empt particle observation, if they exist.

The CDMS detectors are arranged in 5 towers, with each tower containing vertical stack of 6 detectors. Fake LIPs signals are tremendously reduced by requiring all 6 detectors in a tower show energy deposition signal from LIP interaction. It is also required that the energy deposited in each detector be sufficiently far from inherent noise levels in all detectors. A "Tracking criterion is applied requiring that interaction-location in each detector follows a straight line (as expected for a relativistic, massive particle moving in a straight line and not deviating as it interacts with detectors). An "Energy similarity criterion is applied requiring energy deposited in each detector follow a statistical distribution as expected from a LIP signal corresponding to certain fractional charge. Monte-Carlo studies estimate the total background for LIPs analysis to be 0.074 ± 0.053 events. With such a low background, the analysis is almost background free (observing a single candidate event would signal detection of LIPs). After analyzing the data, we obtain 0 candidates. The analysis concludes by asking the question "What is the flux of LIPs on our detectors (which we can state with 90% confidence), given the probability to observe LIPs in our detector and observing no events when detectors are run for certain days? A "Limit-curve addressing the above question is developed, and is presented in the dissertation.

Details of CDMS experimental setup is discussed in Section 3. Details of CDMS data analysis to search for LIPs is presented in Section 4. Section 4 also provides a description of future efforts towards obtaining improvement in future analyses to search for LIPs. These are not meant to be an exhaustive set of guidelines for improvement (discouraging alternate explorations and improvements), but simply as an initial guidance. As example, future analyzers may relax the criteria for a valid LIP to be an event which interacts with all 6 detectors of a tower. Since CDMS holds data from runs carried out at Stanford Underground Facility (SUF) which has a modest overburden of $\sim$17m.w.e., a future LIP analysis using the corresponding data may be more likely to detect candidates (since they experience much less overburden as compared to detectors at Soudan mine).

In addition to analyzing CDMS data to search for LIPs, the dissertation also suggests improvement in various aspects of detector fabrication procedure. Existent CDMS detectors' phonon sensors show a response that varies with location. The sensor response also changes among different detectors. These variations reduce the sensitivity of detectors towards WIMP detection. The variation in response of phonon sensors is primarily linked to variation in the superconducting critical transition temperature (T_c) of deposited tungsten thin-film (a tungsten strip performs the task of measuring phonon signals and converting it to measurable electrical signals), and so, multiple steps are taken to reduce the variation in T_c of fabricated sensors. Although effective, these efforts are extremely costly and time consuming, and negatively affect the feasibility for an experiment employing multiple detectors. With CDMS moving into a next SuperCDMS phase (using $\gtrsim$140 detectors to detect WIMP), and with the eventual aim of advancing to an experiment employing $\sim$1ton detector mass, it becomes imperative to advance the fabrication procedure and bring down the cost and time required to produce multiple detectors.

Another major problem relates to the fact that in the current detector fabrication scheme, only ∼30% of all detectors made are deemed as "nice detectors. The rejection of ∼70% of fabricated detectors may be due to presence of undesirable charge and/or phonon collection characteristics which only get apparent after a detector is fabricated and sent through cryogenic testing and again hurts the feasibility for a 1ton experiment. The dissertation describes various efforts undertaken in the CDMS detector fabrication lab at TAMU towards obtaining the goal of faster and cheaper production of detectors with homogeneous set of properties, both within a detector and among multiple detector.

The detector fabrication lab at TAMU uses Semiconductor Engineering Group Inc. (SEGI) sputter deposition system deposits the thin film in an extremely clean environment, monitored using an in-situ residual gas analyzer (RGA). This ensures that the quality of deposited film is uniform across the detector, and among different batches. Scanning electron microscopy is performed to optimize various steps, like ensuring that deposited film is of correct thickness, to optimize the etching time for certain thin films, etc. A simple 4-probe sheet-resistance measurement is found to correlate with the T_c of deposited tungsten film (this allows an easy identification of sample with poor film properties without performing cryogenic measurements).

With above mentioned improvements, the group was able to demonstrate a higher yield for production of sensors with better control on its properties and with uniform T_c. The achieved uniformity necessitates the incorporating an ion implantation step (ion implantation is used to homogenize the T_c variations in existent CDMS detectors). A description of future efforts towards improvement of fabrication process is also added at end. These are not meant to be an exhaustive set of guidelines for improvement (discouraging alternate explorations and improvements), but simply as an initial guidance.

Finally, a conclusion to the dissertation is put in Section 6.

The dissertation is prepared with topics to interest readers from different science background. To not overwhelm a reader by its length, only the details directly connected to the final results are described in the body of dissertation. However, to ensure that associated and essential details are not ignored, even if they do not directly relate to the final results, they are mentioned separately in appendices.

- The idea of existence of free, elementary FCPs is itself an interesting (and baffling) idea to pique the scientific interest of readers. This, combined with the description of various experiments used to search for existence of FCPs may form an interesting reading for a general audience (discussed in Section 2.5, Appendix C and F). It introduces readers to interesting physical phenomenon and how the results may be interpreted/analyzed with a totally new perspective to allow a search for FCPs.

- These readers may also find interest in statistical methods developed to perform analysis of CDMS data, and to allow interpretation of the results in context of LIPs search. This is one of the main topic of this dissertation.

- The theoretical motivation for the search may interest readers with interest/expertise in Quantum field theories (discussed in Section 2). Introduction to concept of magnetic monopole and its relation with electric charge quantization, conclusions put forth by Foot *et al.* [5] and Holdom [6] regarding possibilities of observing FCPs allow readers to appreciate the hidden richness inside the SM (and its extensions).

- The operating principle of CDMS experiment is also a fascinating scientific reading (discussed in Section 3, Appendix I, Appendix G and Appendix H).

- The detectors used by CDMS are fabricated on high purity germanium/silicon crystals and employ sensors obtained by patterning thin films. Currently, there exists variation variations in detector properties. Section 5 describes multiple efforts undertaken by our group to fabricate detectors with homogeneous properties and less variations. The section may be of interest to material scientists and readers with general interest in the field of semiconductor detector fabrication.

- For a CDMS member, the thesis is combination of all above, providing details on 3 important topics of detector development, interpreting WIMP search data analysis as caused by FCP, and discussions of relevant particle physics covered in sections detailing electromagnetic interaction of particles with detectors. It takes additional importance due to theoretical and experimental discussions suggesting FCPs as possible DM candidates [70, 177].

2. MOTIVATION FOR FRACTIONALLY CHARGED PARTICLES

There is huge empirical evidence that fundamental particles are quantized in units of $e/3$ (where e is the charge of an electron). Up to a long time, before discovery of quarks (which have charges of $e/3$ and $2e/3$), all elementary particles listed were either electromagnetically neutral, or had charges in multiple of e. Since quarks are never obtained as free particles in nature (they always combine with antiquarks to give mesons, or other quarks to give hadrons), all freely existing particles in nature still have charges in multiple of e. Although above is a well-known fact, there is a complete lack of theoretical formulation to support this quantization. It may be mathematically described by noting that the Abelian theory of QED has no nontrivial commutation relations between its generators allowing for algebraic dequantization of the charge eigenvalues. In other words, since electromagnetic force carrier (photon) does not exhibit self-interaction, the particles are theoretically allowed to have any electromagnetic charge. While charge quantization seems inexplicable, various phenomenological and sting theory motivated models naturally support the existence of FCPs. A successful FCP search experiment is physically important as it signals towards existence of new, undiscovered mechanism of interaction between particles which is beyond the scope SM.

To understand the theoretical and experimental motivation behind existence of FCPs, we start by Section 2.1 with a discussion on relating charge quantization to existence of magnetic monopoles. Section 2.2 suggests charge quantization feature due to compactness of electromagnetic group. However, there exists no proof that the minimum charge quantum should be $e/3$. Section 2.3 describes theoretical possibility of charge dequantization within SM. Section 2.4 describes a phenomenologi-

cal construction involving a new, undiscovered "hidden photon" which dynamically interacts with electromagnetic photon to naturally allow for existence of FCPs. Section 2.5 discusses the experimental results detecting presence of FCPs in cosmic rays. Possible future efforts are described in Section 2.6.

While this section introduce the theoretical motivation towards FCP search, the next major section (Section 3) describes the the general set up of CDMS experiment, proving an understanding of the detector working principle, installation and data processing which is necessary to design an analysis paradigm to allow interpretation of CDMS data as being caused by FCPs against backgrounds (the set of events measured by detector, but not induced by FCPs are called "Backgrounds").

2.1 Magnetic Monopoles and Charge Quantization

In 1864, while publishing the unified theory of electromagnetic force [19], Maxwell did not include isolated magnetic charges from his four equations because no isolated magnetic pole had ever been observed by the time. In reviewing the Maxwell's equations by Pierre Curie,no reasons were found as to why they should not exist [20]. Magnetic monopoles [21] would complete the symmetry between the electric and magnetic components of Maxwell's equations. Maxwells equations suggest that divergence of electric field related to electric charge, but magnetic fields are divergence-less (magnetic monopole/ charges have not been experimentally found during the time).

Dirac has shown that the existence of magnetic monopoles would impose a constraint on the possible values of electric and magnetic charge [3]:

$$eg = \frac{n\hbar c}{2} \tag{2.1}$$

where, e is electric charge, g is magnetic charge, n is an integer and c is the speed of light in vacuum. Thus, the existence of particles with nonzero 9 leads immediately

to quantization of both types of charge.

It was later discovered by Polyakov [22] and 't Hooft [23] that general ideas about the unification of the fundamental interactions naturally lead to existence of monopoles. They showed that any "unified theory" naturally contain monopoles. Since it is a deeply held belief that the observed strong, weak and electromagnetic gauge interactions having three apparently independent gauge coupling constants become unified at extremely high energies into a single gauge interaction with just one gauge coupling constant [24, 25], such a "unified gauge theory" would naturally contain magnetic monopoles. Thus, while Dirac had demonstrated the consistency of magnetic monopoles with quantum electrodynamics, 't Hooft and Polyakov demonstrated the necessity of monopoles in grand unified gauge theories. Today, magnetic-monopole solutions are found in many modern theories such as grand unified theories, string theory and M-theory.

While magnetic monopoles signal the presence of charge quantization, they may also acquire an electric charge in the presence of CP violations due to the Witten eect [31]. The Witten effect [30] refers to the shift of the allowed electric charges carried by magnetic monopoles. Since CP violation is a non-quantized parameter, the acquired electric charge may take any value.

The experimental search for magnetic monopoles is discussed in Appendix A.

2.2 "Compactness" Restrictions on Allowable Fractional Charges

It is already described that since electromagnetic force carrier (photon) does not exhibit self-interaction, the particles are theoretically allowed to have any electromagnetic charge. However, restrictions on allowable fractional charges are placed following the logical relationship between the quantization of the electric charge and the mathematical concept of the compactness of the electromagnetic gauge group [32]

(For Lie groups, compactness has a determining influence on the nature of the representations of the group).

Consider a space-time-independent gauge transformation on charged fields ψ_j, of charge e_j

$$\psi_j \rightarrow \psi_j' = \psi_j exp(ie_j\alpha) \tag{2.2}$$

For finite values of α, if the different es $(= e_1, e_2, ...)$ of different fields (different fields correspond to different representations of electromagnetic group) are not commensurate with each other, the transformation Eq. (2.2) is different for all real values of α, and the gauge group must be defined so as to include all real values of . Hence, the group is not compact [32].

On the other hand, if and only if all different e's are integral multiples of a universal unit of charge, then for two values of α different by an integral multiple of $2\pi/e$, the transformations Eq. (2.2) for any fields ψ_j are the same. Hence the gauge group as defined by Eq. (2.2) is compact. Thus, the requirement of compact electromagnetic gauge forces quantization of electric charge, but it does not prove that $e/3$ is the fundamental unit.

2.3 Charge Dequantization Within the Standard Model

The following section is based on the review by Foot et al. [5] (also described in [16]) which asks whether or not the SM criteria are sufficient to naturally produce charge quantization. Alternate models are also studied (by adding new particles to know SM particles) to explore different criteria which may/ may not produce charge quantization.

The standard model of particle physics [33] is a Yang-Mills theory that appears to successfully describe three non-gravitational forces (the strong, weak and electromagnetic forces) under the gauge group $[SU(3)_C$ X $SU(2)_L$ X $U(1)_Y]$. Under this

gauge group, the quarks and leptons of each generation transform as

$$\begin{aligned} Q_L &\sim (3, 2, \frac{1}{3}) & u_R &\sim (3, 1, \frac{4}{3}) & d_R &\sim (3, 1, -\frac{2}{3}) \\ f_L &\sim (1, 2, -1) & e_R &\sim (1, 1, -2) \end{aligned} \tag{2.3}$$

where, the Q_L denotes left handed quark-doublet, u_R, d_R denote right handed up and down quark, f_L denote left handed lepton-doublet and e_R denote right handed electron. The first two numbers in bracket denote the multiplet of particles under the $SU(3)_C$ and $SU(2)_L$ symmetry. The third number denotes the hypercharge associated with the particles under $U(1)_Y$ symmetry.

There is also a Higgs doublet ϕ which can be defined through the Yukawa interaction Lagrangian (L_{Yuk}),

$$L_{Yuk} = \lambda_1 \bar{f}_L \phi e_R + \lambda_2 \bar{Q}_L \phi d_R + \lambda_3 \bar{Q}_L \phi^c u_R + other - terms \tag{2.4}$$

where, $\lambda_1, \lambda_2, \lambda_3$ are corresponding interaction strength. ϕ transforms under SM as $\phi \sim (1, 2, 1)$.

The authors consider different examples to conclude that "If a Lagrangian contains global symmetries which are anomaly free (and hence gaugeable) and independent of the standard hypercharge Y, then that Lagrangian does not yield electric-charge quantization". The examples considered [5] study the single generation SM and three generation SM. These are described below (Section 2.3.1 and Section 2.3.2). The three generation SM seem to favor charge dequantization which may manifest in various ways. Based on their conclusion, the authors describe alternate models where charge quantization may/ may-not occur. It is discussed in Section 2.3.3 Various experimental results constrain the limits of charge dequantization observed in

SM particles. As mentioned in Section 1, the experimental limits on SM particle charge dequantization does not directly relate to the result presented in dissertation. However, for completeness it is mentioned in Appendix B.

2.3.1 Single Generation Standard Model

Consider a toy model asserting that only the first generation SM particles exist (only one generation of quarks and leptons). If we leave the 5 possible hypercharge values in Eq. (2.3) (left handed quark and lepton doublet, right handed up quark, right handed down quark and right handed electron. Higgs boson hypercharge is set to +1) undetermined, then there are two possible categories of constraints that may be applied.

$$\begin{array}{lll} Q_L{\sim}(3,2,y_1) & u_R{\sim}(3,1,y_2) & d_R{\sim}(3,1,y_3) \\ f_L{\sim}(1,2,y_4) & e_R{\sim}(1,1,y_5) & \end{array} \tag{2.5}$$

Three constraints on hypercharge values apply by requiring that the classical structure of the part of Lagrangian describing the Yukawa interactions between SM particles and Higgs boson (L_{Yuk}), described in Eq. (2.4), be symmetric under action of $U(1)_Y$.

$$y_1 = y_3 + 1 \qquad y_1 = y_2 - 1 \qquad y_4 = y_5 + 1 \tag{2.6}$$

Two extra constraints follow by requiring cancellation of the gauge anomalies (which is necessary to ensure the renormalizability of the theory) [34–36]. Rise of gauge anomalies may be understood by studying fermionic triangle Feynman diagram

with gauge bosons on the external lines. Their amplitudes are proportional to

$$Trace(T^a\{T^b, T^c\}) = Ad^{abc} \tag{2.7}$$

where A is a representation-dependent anomaly coefficient, and d^{abc} is a set of numbers characteristic of the group. In this equation, T^a, T^b and T^c denote the generators in the appropriate representations of the Lie algebra of the gauge group. Theories are anomalous if the anomaly coefficient does not vanish when it is summed over the chiral fermions of the theory (the left- and right-handed fermions enter with a relative minus sign).

There are two anomaly equations in the SM which are independent of the classical constraints, Eq. (2.6). The first of these arises when two of the external lines in the triangle graph are from $SU(2)_L$ gauge bosons with the third being $U(1)_Y$ (The anomaly cancellation equations are the same whether or not spontaneous gauge symmetry breaking occurs. So, we may work in the weak eigenstate basis). The second triangle anomaly arises when all three external lines are $U(1)_Y$ gauge bosons. Evaluating these anomalies by using eqs. (2.4) to (2.6) leads to the equations

$$y_1 = -\frac{1}{4}y_4 \qquad\qquad y_4 = -1 \tag{2.8}$$

from $[SU(2)_L]^2U(1)_Y$ and $[U(1)_Y]^3$ anomaly cancellation, respectively.

For 5 unknown hypercharge values, we get 5 constraints eqs. (2.6) and (2.8). Thus for the toy-model case of SM restricted to only one generation we see that the consistency conditions of gauge invariance and anomaly cancellation of the Yukawa Lagrangian assign correct hypercharge to elementary SM particles. After the electroweak symmetry breaking, the electric charge associated with a particle (Q) depends

on its hypercharge (Y) and $SU(2)_L$ isospin (I_3).

$$Q = I_3 + \frac{Y}{2} \tag{2.9}$$

Since the hypercharge and isospin is fixed, the electric charges of the particles have their standard, quantized values in the one-generation SM.

2.3.2 Three Generation Standard Model

In the three-generation SM the picture is a bit more complicated. Since there is no a priori reason to assume that the generations are perfect copies of one another, the hypercharge values can differ between generations. Therefore, both hypercharge and electric charges (through Eq. (2.9)) may depend on a free continuous parameter, ϵ.

To analyze charge quantization in this model, all anomaly-free global U(1) symmetries need to be found. The SM Lagrangian with three generations has four global U(1) symmetries: electron-lepton number (L_e), muon-lepton number (L_μ), tau-lepton number (L_τ) and baryon number (B). The most general linear combination of U(1) conserved charges (L') may be constructed where

$$L' = \alpha L_e + \beta L_\mu + \gamma L_\tau + \delta B \tag{2.10}$$

Two independent anomaly cancellation constraints may be placed on L':

$$[U(1)_{L'}]^3 \Rightarrow \alpha^3 + \beta^3 + \gamma^3 = 0 [SU(2)_L]^2 U(1)_{L'} \Rightarrow 3\delta + \alpha + \beta + \gamma = 0 \tag{2.11}$$

All other gauge anomaly equations are not independent of above constraints.

Despite above constraints, there are still 2 free parameters through which an infi-

nite number of gaugeable, anomaly free global U(1) symmetries may be constructed. It can be parametrized as

$$L' = \alpha L_e + \beta L_\mu + (-\alpha^3 - \beta^3)^{1/3} L_\tau + \frac{1}{3}[-\alpha - \beta - (-\alpha^3 - \beta^3)^{1/3}]B \tag{2.12}$$

This leads to hypercharge (and hence electric-charge) dequantization (where L' depends on two continuous free parameters)

$$Y = Y_{SM} + L' \Rightarrow Q = Q_{SM} + \frac{L'}{2} \tag{2.13}$$

With faith in quantum gravity, one may insist on a further restriction: the cancellation of the mixed gauge-gravitational anomaly [37–39]. This requirement is equivalent to

$$Trace(L') = 0 \tag{2.14}$$

which gives the constraint

$$\alpha + \beta + \gamma = 0 \tag{2.15}$$

Along with the gauge anomaly cancellation criteria, Eq. (2.15) reduces the possibilities for L' to three discrete sets:

$$\begin{aligned} L' &= L_e - L_\mu \qquad \gamma = 0 \\ &= L_e - L_\tau \qquad \beta = 0 \\ &= L_\mu - L_\tau \qquad \alpha = 0 \end{aligned} \tag{2.16}$$

This is clearly insufficient to uniquely determine the hypercharge, and the electric charge. Therefore, it follows that the three-generation SM does not enforce charge

quantization.

2.3.3 Some Simple Extensions of the SM

By applying the result obtained from above discussions, that "If a Lagrangian contains global symmetries which are anomaly free (and hence gaugeable) and independent of the standard hypercharge Y, then that Lagrangian does not yield electric-charge quantization" to some simple SM extensions, the following conclusion can be made regarding charge quantization [5, 16]:

- In the SM with only one generation, plus a massless right-handed neutrino, charge is not quantized. It is because the difference between baryon and lepton number, or (B L) is anomaly free.

- In the SM with only one generation, plus a right-handed Majorana neutrino, charge is quantized. It is because the Majorana mass term breaks the (B - L) symmetry.

- In the three-generation SM with Dirac neutrinos, charge is not quantized. It is because (B L) is anomaly free.

- In the three-generation SM with three right-handed Majorana neutrinos, charge is quantized. It is because no global U(1) symmetries other than $U(1)_Y$ are unbroken.

- In the three-generation SM with exactly one right-handed neutrino (with or without Majorana mass), charge is quantized. It is because no anomaly free global U(1) symmetries other than $U(1)_Y$ are unbroken.

- In the three-generation SM with an extra Higgs doublet, charge is quantized. It is because no anomaly-free global U(1) symmetries other than $U(1)_Y$ are

unbroken.

There are many other extensions of the lepton and neutrino sector, in particular, which lead to electric-charge quantization [40].

2.4 Multiple U(1)s and Charge Dequantization

Previous subsection concludes that if there are unbroken, anomaly free U(1) symmetries besides the $U(1)_Y$ symmetry in the SM, then it is possible to have charge dequantization. On similar lines, there exists phenomenological possibility of obtaining FCPs if multiple, conserved U(1) fields exists (other than photon), and can dynamically interact with photon [6, 16]. Such a model remains in concordance with SM charge quantization constraints obtained through multiple experiments (described in Appendix B) by introducing new, exotic particles carrying fractional charges.

The phenomenological construction starts with the assumption that at low energy scales, the description of complete set of interactions between particles in the universe contains, but is not limited to, two (or more) U(1) gauge groups ($U(1)_A$ X $U(1)_B$). Each group has its own photon and its own electric charge. In the most general case, the part of Lagrangian describing the evolution of two gauge fields will contain terms [6]

$$-L^{kin}_{U(1)} = \frac{1}{4}F^{\mu\nu}_A F_{A\mu\nu} + \frac{1}{4}F^{\mu\nu}_B F_{B\mu\nu} + \frac{\chi}{4}F^{\mu\nu}_A F_{B\mu\nu} \tag{2.17}$$

where the first two terms represent kinetic energy of the two U(1) gauge fields, and the last term represents mixing between two types of photons, χ is a free parameter representing the mixing strength. At tree level, such mixing between two groups is disallowed within the framework of a GUT. It is because each is a free field in itself. However, an effective mixing of the form can be induced by radiative corrections corresponding to higher order terms in perturbative expansion of Lagrangian.

One of the physical manifestations of such mixing is a nonzero coupling between

the fermions charged under $U(1)_B$ and the photon of $U(1)_A$, amounting to an apparent electric charge of type A for the B-type fermions. If type A bosons are the photons corresponding to electromagnetic charge, then the fermions charged under type B bosons develop fractional electromagnetic charge.

A suggested model for observing dynamical mixing of multiple U(1) gauge bosons is described below in Section 2.4.1. Following it, a discussion on various phenomenological constructions that can be made to implement dynamical mixing is provided in Section 2.4.2. Few of the experimental constraints on "mass-charge" parameter space for FCPs may change depending on whether or not the particles get their fractional charge due to coupling with hidden photon sector. Since these observations do not directly relate to the result presented in the dissertation, they are described separately in Appendix F.

2.4.1 Implementing Dynamical Mixing of U(1) Gauge Bosons

Holdom describes a means of obtaining above mentioned kinetic mixing at loop level [6].

Consider a toy model with four fermions f_l, f_2, f_{12}, f'_{12} having charges (e_1,0), (0,e_2), (e_1,e_2), (e_1,$-e_2$) under a vector gauge symmetry [$U(1)_A$ X $U(1)_B$], with corresponding gauge fields $A_{A\mu}$ and $A_{B\mu}$. Assume that the mass of fermions order with respect to each other as $m'_{12} > m_{12} > m_1 \sim m_2$. The mass splitting (inequality on mass assignment) and the charge assignments contribute to a nonzero dynamical mixing between the gauge bosons corresponding to $U(1)_A$ and $U(1)_B$, as shown in Fig. 2.1. For a most general form of Lagrangian describing the evolution of the gauge field kinetic terms, Eq. (2.17), the dynamical mixing coefficient χ depends on mass of fermions that simultaneously charged under both $U(1)_A$ and $U(1)_B$ gauge groups,

and is given by:

$$\chi = \left(\frac{e_1 e_2}{6\pi^2}\right) ln \left(\frac{m'_{12}}{m_{12}}\right) \tag{2.18}$$

χ can be of order 10^{-7}, for natural values of $\frac{e_1 e_2}{4\pi} \sim \alpha$ (with $\alpha = \frac{e^2}{4\pi}$ being the electromagnetic fine-structure constant), and nearly degenerate masses, $\frac{m'}{m} \sim 1.0002$ [56]

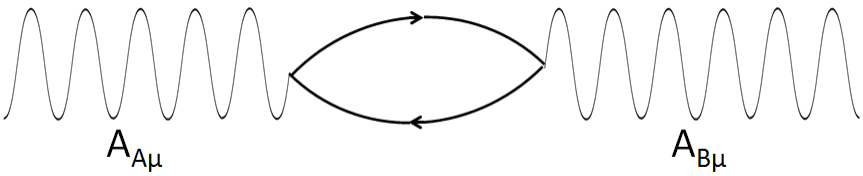

Figure 2.1: Dynamical mixing of fields belonging to two *U(1)* groups mediated by virtual fermions charged under both fields [6]

In order to regain diagonal kinetic terms with conventional normalization, new gauge fields $A'_{A\mu}$ and $A'_{B\mu}$ may be defined, which respectively do and do not interact with the fermion f_1. Defining f_1 as the electromagnetically charged fermion which experiences no charge and does not interact with any other "hidden boson" field, the $A'_{A\mu}$ would correspond to the electromagnetic field. The orthonormal partner to the photon, the paraphoton would, by definition, not couple to known fermions. In order to obtain above redefinition of $A'_{B\mu}$ (as the field which does not interact with fermion f_1), the effect of interaction between $A_{A\mu}$ and $A_{B\mu}$ bosons needs to be absorbed within the definition of newly constructed $A'_{A\mu}$ field. This allows $A'_{A\mu}$ field to interact with fermions which did couple to the paraphoton and impart it a fractional electromagnetic charge (like, for fermion f_2), or have their original photon couplings altered (like, for fermion f_{12} and f'_{12}). Thus ratio of coupling by $A'_{A\mu}$ to f_2

and f_1 is in ratio

$$\epsilon = -\frac{e'_B \chi}{e'_A} \tag{2.19}$$

where, e'_B is the charge of f_2 under $A'_{B\mu}$ and e'_A is the charge of f_1 under $A'_{A\mu}$ fields.

Note that the appearance of fractional charge is due to field redefinition and does not violate the principle of charge quantization. Therefore, the construction does not violate the charge quantization criteria put by Dirac (discussed in Section 2.1), or the existence of a charge quantum by requiring compactness of $U(1)_Q$ group (discussed in Section 2.2).

2.4.2 Phenomenological Constructions

Based on above discussion, there are different possibilities for the generation of ϵ charge shifts [6]. As mentioned, such a model remains in concordance with SM charge quantization constraints obtained through multiple experiments (discussed in Section 2.3 and Appendix B) by introducing new, exotic particles carrying fractional charges.

A least exotic possibility is to consider new families of fermions with SM quantum numbers alongwith a new vectorial paraphoton charge. A simple way to cancel anomalies is to have two such families with paraphoton charge +1 and -1 respectively. Mass splittings among the parafermions can yield a mixing between the photon and the paraphoton. The parafermions would then experience e charge shifts with respect to the standard photon.

One may consider $U(1)_Y$ hypercharge becoming mixed with a second U(1) (as described in Section 2.3). The fermions responsible for the mixing would have to couple to both U(1)'s and according to the above example they must be massive and not break the U(1) gauge symmetries (the necessity for unbroken symmetry is discussed later in this section). As example, there may be fermions with a gauged (B

L) symmetry but are singlet under $SU(2)_L$. This situation would lead to hypercharge shifts for those fermions coupling to the second U(1). When $[SU(2)_L \text{ X } U(1)_Y]$ breaks to electromagnetism, the low energy fermions would be left with electromagnetic charge shifts. A fractional charge of $\epsilon \sim 10^{-8} - 10^{-2}$ can be generated via these mechanisms [65].

There exists possibilities for mixing of U(1)'s without involving massive fermions. Consider a gauge group $[G_1 \text{ X } G_2 \text{ X } G_3]$ where the G_i's are simple nonabelian groups. Due to formation of condensate, or otherwise, the group can break down to $[H \text{ X } U(1)_A \text{ X } U(1)_B]$. Here H has no abelian factors and the U(1) fields can be written in terms of G_i fields.

Many SM extensions coming from string theory predict additional hidden U(1) factors which can give rise to the kinetic-mixing phenomenon ($\chi \neq 0$) [56–63]. The string scale$\simeq 10^{11}$ GeV predicts the existence of particles with $\epsilon \geq 10^{-9}e$, thus making the region $\epsilon \simeq 10^{-9} - 10^{-5}e$ of great interest for searching for FCPs. The required FCPs obtained from String theory are a generic (not being model-specific) and testable prediction of a large class of string theory models [56, 64].

In adding to possible mechanism for obtaining photon mixing, it is possible to obtain a "magnetic mixing" in settings where the hidden sector at low energies contains a U(1) gauge factor with magnetic monopoles, for instance 't Hooft-Polyakov monopoles of an underlying non-abelian gauge group [69]. In the presence of CP violation these monopoles may generally acquire small electric charges under the visible electromagnetic gauge group due to "magnetic mixing" (in addition to acquiring an electric charge in the hidden sector due to the Witten eect [30]). This "magnetic mixing" is shown to often arises as a natural partner of kinetic mixing. Both kinetic and magnetic mixing are naturally induced radiatively even if the multiple low-energy U(1) gauge groups arise from a single non-abelian gauge group below a

symmetry-breaking energy scale.

A related phenomenological question is whether the paraphoton can gain a large mass and still leave the "parafermions" obtain fractional electromagnetic charge [6] The answer is no. The operator whose vacuum expectation value breaks the symmetry obviously has the charge of the broken U(1) and no charge under the unbroken U(1). Orthonormal gauge fields are then chosen with respectively do and do not couple to this charge. The unbroken U(1) is analogous to the $A'_{B\mu}$ field which did not couple to the fermion f_1. Thus the unbroken U(1), as for $A'_{B\mu}$, does not end up with ϵ charge shifts. Although the fractional charge is "undone" by an on-shell massless photon, this is not the case for off shell or for massive photons (as, for instance, in a plasma) [66]. Despite the model's inability to create fractional charges, hidden sector heavy photons are experimentally interesting pursuit. One of the major motivation for the heavy bosons is their ability to describe dark matter annihilation results observed by ground, space and satellite borne detectors [70]

Similarly, consider models containing more than one paraphoton with at least one paraphoton being exactly massless and one light, $keV \gg m_{\gamma'} \neq 0$, and the fermion transforming in the bifundamental representation of these two U(1) factors [67]. In vacuum, the fermion acquires an electric charge ϵ due to a kinetic-mixing between the photon and the two paraphotons. However, this electric charge is reduced in the stellar plasma by a multiplicative factor $\left(\frac{m_{\gamma'}}{\omega_p}\right)^2$, where ω_p ~few keV is the plasma frequency. This charge screening mechanism is caused by a partial cancellation between two paraphotons interacting with the bifundamental fermion [56, 67]. Kinetic-mixing could be avoided in theories with dynamical mixing of multiple U(1) gauge field bosons if the particle spectrum has some particular properties, as discussed in [56, 68].

2.5 Experimental Limits from Cosmic Ray Based Searches

Cosmic Rays are relativistic particles have been observed with energies ranging over more than 12 orders of magnitude, extending to tens of joules per particle [224]. These particles are continuously incident on the Earths atmosphere. The high energy cosmic rays are capable of creating massive FCPs through interaction with Earth's atmosphere, if they exist. The particles created are themselves extremely energetic. Thus, they pass through a sequence of detectors along their path of travel. However, due to their fractional electromagnetic charge, they interact very less with the detectors and deposit very low energies. Additionally, it may be required that the particle track follows a straight line due to its high energy. For cosmogenic FCP searches, the conditions for productions of the fractionally charged particles may vary. This implies that the range of mass of particle in unknown. Therefore, the search sensitivity is usually given in terms of the limit on incoming flux of FCPs detected (with units of $cm^{-2}sr^{-1}s^{-1}$) [209].

"This mode of cosmogenic FCP search is discussed because it directly relates to the form of result presented in this dissertation".

Search for cosmogenic FCPs was done by Liquid Scintillation Detector at Mont-Blanc (LSD) [8], Kamiokande detector [9] and at Monopole and Cosmic Ray Observatory (MACRO) [10]. These experiments conclude by setting a "limit curve" on the flux of FCPs. It implies the following "In running the detector for a certain period of time and their being a calculated probability to observe FCP events; Observance of N events in teh detector imply that the flux of FCPs cannot be higher than a certain value, else more events would have been observed". Thus, the flux of FCPs above a certain value (shown in the "limit curve") is experimentally excluded. Owing to non-observance of events, limiting flux rates for the fractionally charged particles

may be deduced, which is shown in Fig. 2.2 below.

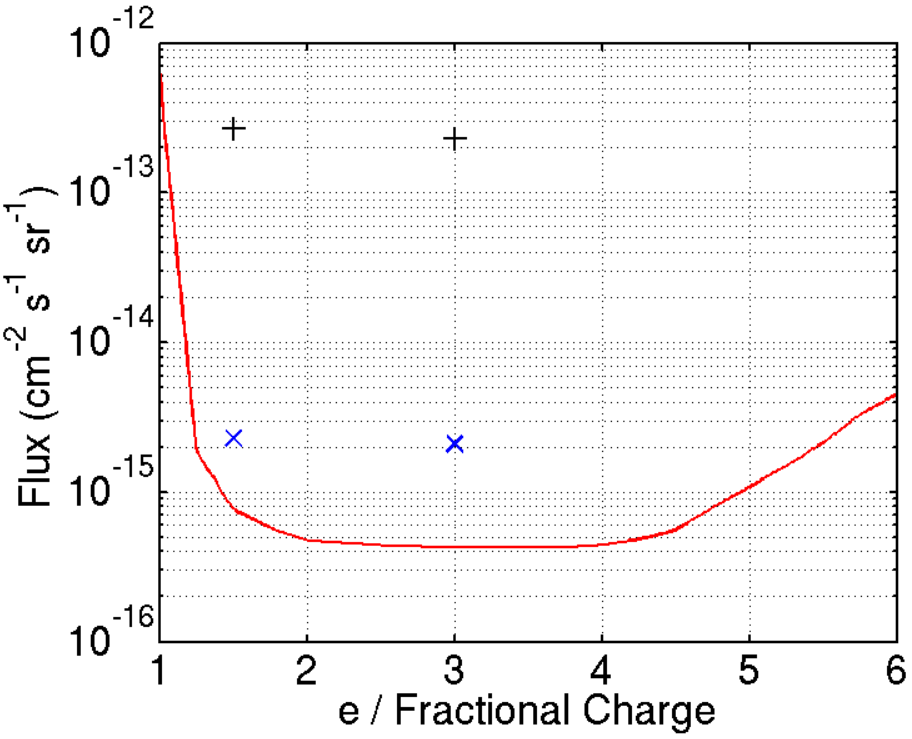

Figure 2.2: The 90% Confidence Level MACRO flux upper limits for FCPs (red) compared with previous limits from LSD (black +) and Kamiokande (blue X) [10].

FCPs, due to their fractional charge, interact less with any medium and create less ionization as it passes through it. If is for this reason, they are also called Lightly Ionizing Particles (LIPs), as mentioned in [10]. Since the results presented in this dissertation is similar to the result from MACRO [10], we use similar terminology and hereby refer FCPs as LIPs.

Cosmic rays can also interact with bulk materials on Earth and create FCPs trapped inside them. Alternately, one can also study for presence of FCPs in ancient meteoritic materials where any relic density of FCP would get trapped and remain

preserved. Since these experiments do not directly relate to the result presented in the dissertation, it is discussed in Appendix C. Additionally, there exists a vast set of experiments where the rate/cross-section for FCP production and/or detection is theoretically calculated. An analysis of the result yield constraint on the "mass-charge" parameter space for FCPs. These experiments also don't directly relate to the one described in the dissertation. However, to provide a complete picture of FCP search efforts, they are described in Appendix F.

2.6 Future Efforts

Most of the results presented in Appendix F are dependent on the value of Hubble constant. Recent results from Planck collaboration show a change in estimated value of Hubble constant [99], which appear to be slightly different from the values determined through studies of supernova. Possible future studies may try to update the results, based on newly obtained value of Hubble constant.

3. THE CRYOGENIC DARK MATTER SEARCH (CDMS) EXPERIMENT

As discussed in the introduction (Section 1), to search for FCPs, the dissertation analyzes data obtained by the Cryogenic Dark Matter Search (CDMS) detectors which are installed at the Soudan Underground Labs (SUL) in northern Minnesota. The main aim of CDMS detectors is to search for WIMPs with an extremely low expected interaction probability of $<$ 1event/(kg day), with typical deposited energies of 10-100 keV. To be sensitivity to these rare occurrences, the CDMS collaboration uses Z-sensitive Ionization and Phonon (ZIP) detectors.

The ZIP detectors are fabricated on germanium (Ge) or silicon (Si) substrate and cryogenically operated at 40 mK. The substrates are 3inch diameter and 1cm thick, high purity crystals. The ZIP detectors have the capability to measure the ionization (electron-hole pairs) and the athermal phonons created as a particle interacts with the germanium/ silicon substrate. One (plane) side of the cylindrical crystal is instrumented with electrodes to collect the holes generated as a particle interacts within substrate. The other side is instrumented with sensors to detect athermal phonons, also generated due to interaction. A schematic along with pictures of fabricated charge and phonon sensor is shown in Fig. 3.1.

The interactions between the crystal substrate and the incoming particle can be of two type, where an incoming particle interacts electromagnetically with the charged electron sea, or be typical of an uncharged particle (e.g., neutron) interacting with the substrate nuclei (LIPs are electromagnetically charged particles. They interact with the electron sea inside the crystal. Nuclear recoils are more relevant to WIMP detection. They will be marginally discussed, simply for completeness purposes).

The high sensitivity of these detectors allow them to be used for searching parti-

Figure 3.1: Left to right: Schematic of ZIP detector, with phonon sensors (4 independent phonon measurement channels arranged in quadrants) and charge sensors (2 concentric aluminum electrodes); A picture of fabricated charge electrodes (taken from [239]); A picture of fabricated phonon sensors (taken from [231]). The sections below discuss relevant details on corresponding signal generation and measurement.

cles with low fractional charges. Following the theoretical motivation for FCP search as discussed in previous section, it is desired to perform such a search using these sensitive ZIP detectors. An understanding of the detector working principle, installation and data processing is necessary to design an analysis paradigm to allow interpretation of CDMS data as being caused by FCPs against backgrounds (the set of events measured by detector, but not induced by FCPs are called "Backgrounds").

Before proceeding with further details, it is desired to reiterate the statement made in Section 2.5 that a FCP, due to its fractional charge, interacts less with any medium and create less ionization as it passes through it. If is for this reason that it is also called a Lightly Ionizing Particles (LIPs), as mentioned in [10]. Since the results presented in this dissertation is similar to the result from MACRO [10], we use similar terminology and hereby refer FCPs as LIPs.

The sections below describes the basic principles guiding ionization (Section 3.1) and phonon collection (Section 3.2) in ZIP detectors. A related idea of detector ionization yield is described in Section 3.3. Lastly, the detector installation at Soudan Underground Labs (SUL) is described in Section 3.4, along with the details of sub-

strates on which the ZIP detectors were fabricated (discussed in Section 3.5),. This is done because the unique configuration of detector arrangement is one of the factors which allows for LIPs search using CDMS data. Detailed descriptions of the CDMS-II detectors and experimental installation at the SUL can also be found in [227–231], and also discussed in relevant appendices (mentioned appropriately in the details below).

While this section introduces the basics of detector operation and installation, the next major section (Section 4) outlines the usage of these details to construct an analysis framework allowing an interpretation of CDMS data as being caused by LIPs.

3.1 Ionization Signal

This section describes the basic principle behind generation of ionization signal in the ZIP detector substrate (germanium, or silicon crystal) due to interaction with a penetrating particle. However a complete discussion warrants additional details on the transport, readout electronics, noise characteristics, processing and calibration of obtained signal, etc. Since these are important details, but do not directly relate to the results discussed in the dissertation, they are mentioned separately in Appendix G.

3.1.1 Generation of Ionization

Electrons and holes, free to correspondingly move in the conduction and valence bands, contribute to conduction of electrical current inside semiconducting materials. Conduction electrons can be generated by exciting electrons from the valence band into the conduction band. An equal number of holes are created in the valence band from this process. Electron excitation can be accomplished through thermal agitation or through electromagnetic excitation (optical excitation and excitation by

interaction with penetrating particles [253]). At low temperatures, the thermal energy is insufficient to excite the electrons over the bandgap into the conduction band. By further ensuring that the substrate is kept away from high energy optical radiations, the only possibility to obtain electron-hole pairs (ehp) is from an interaction with a energetic penetrating particle.

Energy lost by an incoming electromagnetically charged particle is directly imparted to electrons, exciting it to levels much higher than conduction band minimum. Interactions with uncharged particles, like neutrons, cause energy to be imparted to substrate nucleus, which is then transferred to electrons and in creating high frequency athermal phonons. The excited "hot" electron, formed in both scenarios, relaxes by exciting additional electrons (Additional additional high frequency athermal phonons are also created, discussed in Section 3.2. A Monte Carlo of such relaxation in silicon is discussed in [244]. Similar calculations for nuclear recoil type events are discussed in [236]). Thus, a track of ehp are formed in the vicinity of particle track. Shedding of original energy in creating phonons causes an increase in the total energy required to produce a single ehp in germanium (silicon) to 3eV (3.83eV), even though the corresponding bandgap (i.e., minimum energy needed to excite an electron to conduction band and create an ehp) is 0.7437eV (1.170eV) [252].

3.1.2 Ionization Collection and Shockley Ramo Theorem

An external electric field is applied to prevent the ehp from recombining with each other before they are measured. A bias of -3V (-4V) is applied to charge measurement electrodes fabricated on one of the faces of cylindrical germanium (silicon) crystals, while keeping the other surface grounded (The reason for different bias values is discussed in Section 3.2.1). As discussed in Appendix G.3, it is preferred to measure holes because the movement of electrons inside the substrate is anisotropic.

For this reason, a negative bias is applied. Additionally, the charge electrode is not made as a single unit over one of the crystal surface, but consists of two concentric electrodes, with the inner electrode occupying ∼85% of total surface. this is primarily done for the purpose of obtaining background reduction in WIMP analysis. Cryogenic operation of detector also allows for a negligible probability of ionization signal annihilation by recombining with thermally excited charges, and, the "detector leakage current" due to drifting thermal charges is also low.

3.1.2.1 Shockley Ramo Theorem

However, it is a false understanding that ionization sensing works as: the biased electrodes attract charge to the electrode, the charge enters the metal, and a current is produced. In reality, the electrode senses the electric current induced by a charge moving near an electrode formed due to the instantaneous change in the number of electric field lines terminating on the electrode. This instantaneous current I is given by

$$I \propto e(\overrightarrow{E}_{electrode} \cdot \overrightarrow{v}) \tag{3.1}$$

where, A is the area of electrode, $\overrightarrow{v}$ is the electron velocity and $\overrightarrow{E}_{electrode}$ is the electric field at the location of the charge only due to the sensing electrode and assuming all other conductors are grounded (this is not the drift field), also called "weighing field" or "Ramo field".

Since CDMS experiment reads out the electrode current on large timescales, the effect of the total current induced by the entire drift process of both electrons and holes which is measured. For a ehp created at same point a, with electron drifting from point a to point b, and hole drifting from point a to point c, the integral version

of the Shockley Ramo theorem becomes

$$\begin{aligned}\int I &\propto (-e)\left\{V_{ramo}(a) - V_{ramo}(b)\right\} + (+e)\left\{V_{ramo}(a) - V_{ramo}(c)\right\} \\ &\propto (e)\left\{V_{ramo}(b) - V_{ramo}(c)\right\} \end{aligned} \tag{3.2}$$

The final charge signal, then, is seen to be simply proportional to the number of charge carriers created, and the Ramo voltage successfully crossed without trapping. If the charge signal is not trapped, then the ionization signal approximately independent of the depth from crystal surface where it is created.

3.2 Phonon Signal

The phonon physics of ZIP detectors is much more involved than ionization signal. The phonons measured by the ZIP detectors are generated through several distinct processes, with each having very different energy spectrum and transport properties. They are measured at small time scale (on the order of 1-100μs), before they equilibrate and cause a rise in crystal temperature (This occurs on the order of milli-seconds). For this reason, these are called "athermal phonons". Since phonon is technical term for vibrations/sound inside the crystal, the set of phonon detectors employed by ZIP detectors effectively act as microphones. By comparing the amount and delay in arrival of phonons at different detectors, the location of event occurrence inside a detector can be triangulated. This additional information is otherwise lost if one opts to detect thermal phonon. This section discusses these different processes for phonon generation and how they relate to the actual recoil energy (i.e., the energy lost by the penetrating particle). It also introduces various physical quantities of interest which may be inferred from the phonon pulse. The section also describes the physics employed by the ZIP detector's phonon read out technology,

called Quasiparticle trap assisted Electrothermal feedback Transition edge sensors (or simply QETs).

In addition to the bare details mentioned in this section, a complete discussion warrants additional details on the transport, readout electronics, noise characteristics, processing and calibration of obtained signal, etc. Since these are important details, but do not directly relate to the results discussed in the dissertation, they are mentioned separately in Appendix H. Since phonon interaction in the ZIP detectors is an interesting, but involved topic interested readers may also refer to [235] and CDMS theses on Detector Monte Carlo efforts [236, 237], presenting an extensive study of phonon physics.

3.2.1 Phonon Generation

The phonons generated by a particle interaction originate from three distinct mechanisms: primary phonons, recombination phonons and Luke phonons.

3.2.1.1 Primary Phonons

A penetrating particle interacts with the crystal either electromagnetically or through nuclear recoils. The energy lost by the incoming particle is correspondingly gained by the recoiling electron or nucleus inside the substrate. In relaxing back to equilibrium, this initially displaced electron or nucleus deposits part of its kinetic energy as phonons [227, 240, 241, 258]. By subtracting the energy used to create an ionization signal (in exciting N_Q electron across the bandgap), one may estimate the the amount of recoil energy deposited as primary phonons.

$$E_{Primary} = E_{Recoil} - N_Q E_g \tag{3.3}$$

where E_g is the energy band gap of the crystal.

3.2.1.2 Recombination Phonons

Once the charged particles(ehp) are generated, they may recombine if there is not enough external electric field to drift them apart. In doing so, they release the corresponding ionization energy back to the phonon system. Even when the carriers do not recombine inside the crystal and are effectively mobilized towards their respective electrodes, the corresponding ionization energy still appears in the phonon system. This occurs because the electrons and holes recombine with free charges at their respective electrodes, and each created pair releases the bandgap energy in phonons [232]. This fails if charges are trapped on ionized impurities and are prevented from recombining. Thus, the recombination phonons have a total energy

$$E_{Recomb} = N_Q E_g \tag{3.4}$$

3.2.1.3 Luke Phonons

Luke phonons (also commonly referred to as Neganov-Trofimov-Luke phonons) are emitted analogous to Cerenkov radiation, but instead when the charge carriers travel at the speed of sound in the crystal. This mechanism for energy dissipation inside the crystal via phonon radiation was proposed by Neganov, Trofimov and Luke [260,261]. The radiation of Luke phonons contributes towards additional energy deposited in the crystal (not part of energy lost by incident particle), and is equal to the work done on each charge by external electric field:

$$E_{Luke} = \sum_{i}^{2N_Q} q_i \int_{path} \overrightarrow{E}.\overrightarrow{dx} \tag{3.5}$$

where, the sum is over each charge i (there are N_Q electrons and N_Q holes, so a total of $2N_Q$ charged particles), and $q_i \int_{path} \overrightarrow{E}.\overrightarrow{dx}$ denotes the work done by the applied

electric field over the charged species i. If the electric field is uniform and the charge carrier has elementary charge e (the charge of an electron), Eq. (3.5) becomes:

$$E_{Luke} = eV_b \sum_i \frac{d_i}{a} \tag{3.6}$$

where V_b is the applied bias voltage, a is the thickness of the crystal and d_i is the distance traveled by charge carrier i. If the detector always has complete charge collection, one obtains:

$$E_{Luke} = eV_b N_Q \tag{3.7}$$

This is because the work done is independent of the position of the creation of the charge pairs, which in turn is because the sum of the path lengths of the two charges of a pair is always the thickness of the crystal (in the absence of trapping).

As discussed in Section 3.1, it takes an energy E_{ehp} of 3eV (3.83eV) to produce a single ehp in germanium (silicon) crystal. The measured ionization energy in the ZIP detector is then given by $E_Q = N_Q E_{ehp}$. The Luke contribution to the phonon signal becomes

$$E_{Luke} = \frac{eV_b}{E_{ehp}} E_Q \tag{3.8}$$

Thus, for case of complete ionization collection, if the ZIP detectors are biased at -3V (-4V) for germanium (silicon), then the Luke phonon contribution is same as ionization energy. The operation of detector at the specific bias has one more important consequence. Although a relatively modest electric field of ∼200mV/cm is sufficient to achieve nearly full charge collection [238], the production of Luke phonons allow increased sensitivity to measurement of events with low recoil energy. Additional phonon energy makes it easier to detect these events over the phonon noise. However, an extremely large electric field will cause the recoil phonon contribution

to total phonon measurement to be undermined by the presence of Luke phonons. This hampers the original motivation of ZIP detectors to detect WIMP, as the ratio of Ionization to Recoil energy is a useful measure in distinguishing nuclear recoil (characteristic of WIMP signal), against possible electromagnetic backgrounds. It is further discussed in Section 3.3.

Eq. (3.8) is initially obtained assuming complete charge collection. However, this formula also remains true for case involving incomplete collection of charges during to trapping of ehp. This is because when some charges get trapped in the crystal, the loss in the ionization signal is in the same proportion as the loss to Luke phonons. In case when total ionization signal is collected and the detectors are operated under a bias of 3V (4V) for germanium (silicon) crystals, the total phonon energy is given by:

$$\begin{aligned} E_{Total} &= E_{Primary} + E_{Recombination} + E_{Luke} \\ &= E_{Recoil} + E_Q \end{aligned} \tag{3.9}$$

Since the ZIP detectors measure the total phonon energy (and not the recoil and Luke phonons separately), it is necessary to use both ionization and total phonon energy measurements to estimate the recoil energy, using Eq. (3.9). However, such an estimation is more noisy than the charge and total phonon estimation alone.

3.2.2 Phonon Detection

As described in Appendix H.1, the phonons generated from particle interaction inside the crystal quickly downconvert to $\lesssim$1THz ballistic phonons, of wavelength comparable to crystal thickness. These ballistic phonons are collected in "Quasiparticle trap assisted Electrothermal feedback Transition edge sensors" (QETs) patterned

on the detector surface. The QET comprises of the main sensing element which is a ∼250μm long, 1μm wide, 40nm thick tungsten (W) transition edge sensor (TES) with superconducting transition temperature $T_c \sim 80mK$; fed by a set of 10 aluminum (Al) phonon collector fins, each ∼350μm long, 50μm wide and 300nm thick. The entirety of aluminum fins cover ∼15% of detector face. The TES serves as a sensitive thermometer and the fins act as a reservoir, concentrating phonon energy from a wide area onto the tiny TES. Detailed descriptions of the CDMs-II QETs can be found in a number of papers and CDMS theses [241, 243, 257–259].

3.2.2.1 Phonon Transfer to TES

At the 40mK operating temperature of ZIP detectors, the aluminum fins are superconducting (T_c ≡1.2K), and contain pair of electrons bound into "Cooper-pairs". Phonons with at least twice the superconducting gap energy (2Δ=0.36meV or 87GHz) they can excite a Cooper pair to generate quasiparticles. This minimum energy is much greater than the typical energy ∼3.4μeV of thermal phonons at 40mK. Therefore, only energetic, athermal phonons can create quasiparticles. Since the ballistic phonons have frequency $\lesssim$1THz, they create quasiparticles well above the superconducting bandgap. These energetic quasiparticles relax by emitting additional pair-breaking phonons and creating a cascade in which ∼60% of the initial phonon energy is converted into quasiparticles at the gap energy, while the remaining energy is lost as sub-gap phonons [250].

These quasiparticles can then diffuse into tungsten transition edge sensors (TESs) connected to the end of the fin. Since the tungsten transition temperature is much lower than aluminum, it has a lower value of bandgap ∼25μeV. Thus, the phonons again relax by rapidly emitting phonons and fall below the gap of the aluminum, thereby getting trapped in tungsten TES [251]. This allows phonon energy incident

on a large fraction of the detector surface area to be concentrated in small volume TESs. As the quasiparticles diffuse in tungsten TES, they transfer their energy to the electron system in tungsten film. The CDMS-II ZIP detector QET design was the result of a quasiparticle collection optimization [241], yielding a quasiparticle-collection efficiency of nearly 25%. A schematic representation of the phonon trapping process is shown in Fig. 3.2.

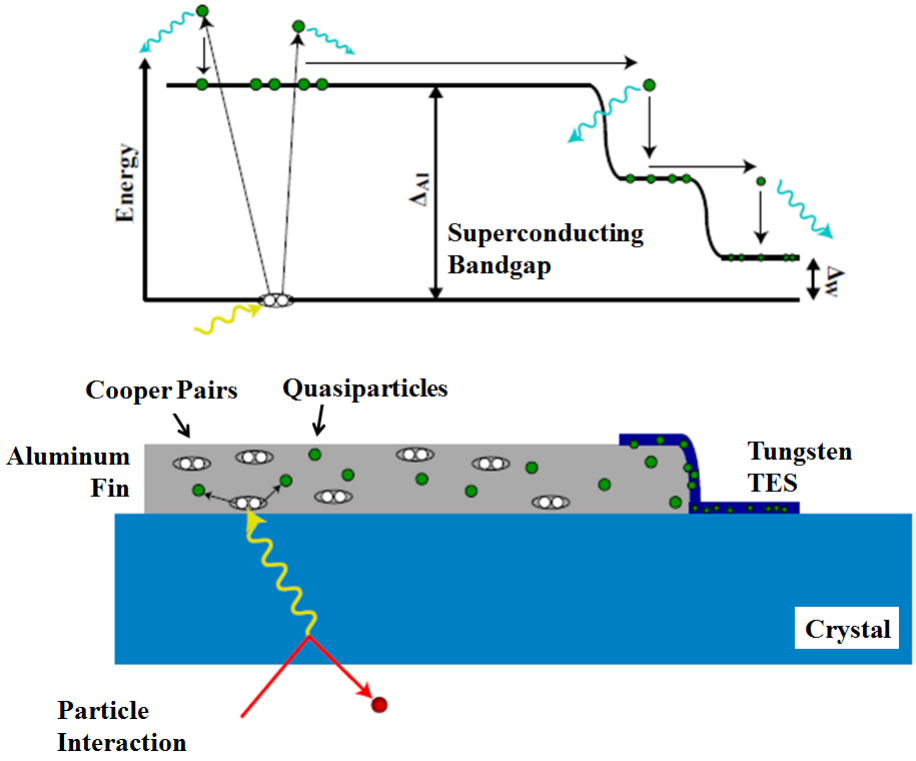

Figure 3.2: A Schematic of athermal phonon collection and quasiparticle diffusion in a QET. ∼1THz ballistic phonons arriving at aluminum fins excite the cooper pair beyond superconducting bandgap (∼90THz) to create quasiparticles. These quasiparticles diffuse into the tungsten TES (dark blue) and get trapped. The upper part of the figure shows the downconversion process, where energetic quasiparticles quickly downconvert to the gap edge by emitting phonons and creating additional quasiparticles. Note that the bandgap in the Al/W interface region is suppressed (compared to Al bandgap) due to the proximity effect (by presence of low bandgap material, tungsten). Figure from [239].

3.2.2.2 Phonon Measurement by TES

The TES are kept in a negative electrothermal feedback (ETF) loop to allow for stable operation. In a negative ETF, the TES is voltage biased, just sufficiently that the current flowing through it heats it via Joule heating ($P = I^2R$). The circuit providing the voltage bias is described in Appendix H.2. Due to the deposition of energy by quasiparticles, the sensor temperature and hence, its resistance increases. However, since the sensor is biased at a fixed voltage, an increase in its resistance causes a reduction in Joule heating ($P = \frac{V^2}{R}$), allowing the sensor to cool back to its equilibrium point. The change in current through TES, as its resistance changes, is measured to generate the measured phonon signal, as described in Appendix H.3. The operation of TES, as described above, also requires that it is kept at cryogenic temperatures. At low temperatures, the coupling of the electron and phonon systems is small (with thermal conductance $G \propto T^5$). This provides a weak thermal link between the electron system in the TES and the bath, allowing the TES to self-heat into its transition, even though the substrate is maintained at 50mK. To be able to use TES (when the substrate is at 50mk), it is fabricated using tungsten thin films with a superconducting transition temperature (T_c) ∼80mK. Operation at low temperatures also allow for an extremely low sensor heat capacity. This helps in obtaining larger temperature excursions for a given amount of energy deposited by quasiparticles. Additional details on rather extensive topic of TES dynamics can be found in [226, 235].

To measure phonons generated anywhere inside the substrate, one of the faces of silicon or germanium crystal (with the other face containing the ionization electrodes) is instrumented with multiple phonon sensors. There are 4 such "channels" for phonon measurement arranged in a quadrant, which collect the signal from 1036

TES to create a corresponding electrical trace. To allow each TES in a channel to operate independently from other sensors, and to be kept in a negative ETF configuration, they are wired parallel to each other. The arrangement of phonon measurement channels and TES is shown in Fig. 3.3. The intrinsically high resistance of tungsten film ensures that the overall resistance of the channel remains sufficiently high, despite the TES being operated in parallel to each other. A low channel resistance affects the electrical readout scheme and associated noise bandwidth, correspondingly discussed in Appendix H.3 and Appendix H.4.

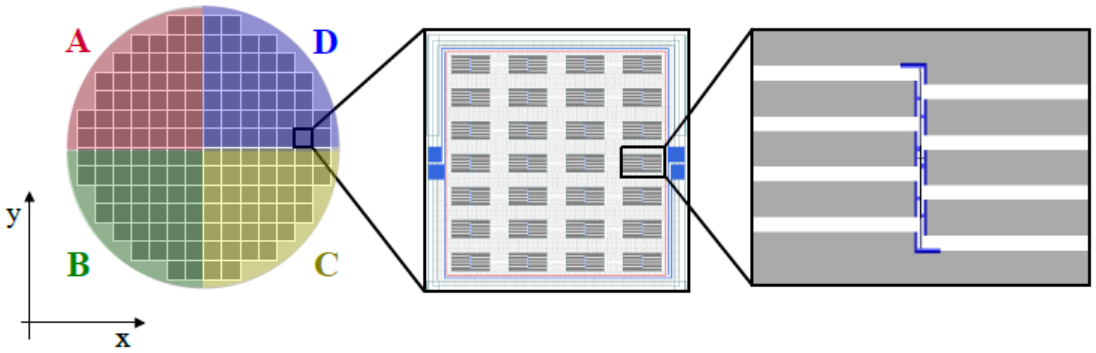

Figure 3.3: Physical layout of phonon sensors in ZIP detectors. One of the detector is patterned with athermal phonon sensors divided into 4 quadrants labeled (A, B, C, D). Each quadrant consists of 37 identical tiles consisting of 28 TESs each, giving at total of 1036 TESs per quadrant, wired in parallel. The zoomed regions show the Al absorbing fins(gray), 8 of which are connected to each TES (blue). Figure from [239].

During operation, the TES is biased along its superconducting transition where the slope (dR/dT) is sharpest, as shown in Fig. 3.4. This allows for maximal sensitivity as any small temperature excursions about this point produces the largest change in sensor resistance and electrical signal. For the TES in CDMS-II, the ETF provides a characteristic recovery time of $\lesssim 40\mu$s, while phonon-mediated events

have a longer fall time $\sim 250\mu$s.

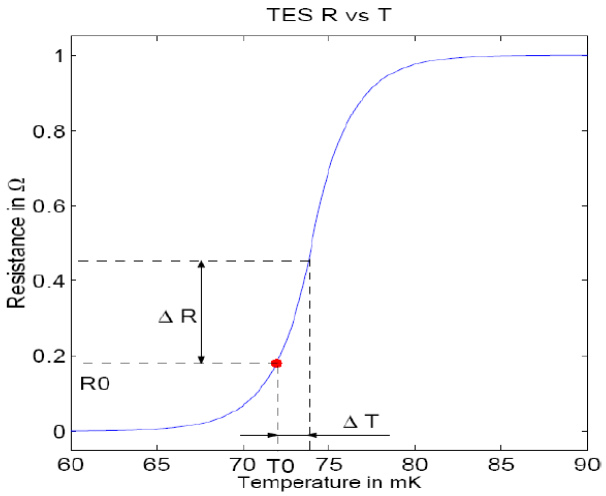

Figure 3.4: Resistance (R) of TES, as function of the temperature (T). To be kept active and maximally sensitive, the TES is kept at the superconducting transition edge, biased along the R(T) curve where the slope is largest. The value of Tc and the transition width are characteristics of the tungsten films used for the ZIPs. Figure from [231].

The above discussions make an implicit assumption about the phonon signal not being large. When an event deposits large phonon energy, then the TES may be driven outside the superconducting transition edge and become normal. In normal state, the change in sensor resistance due to temperature excursions is greatly reduced, which in turn reduces TES responsiveness to phonon signal. An extreme example of such a situation is shown in Fig. 3.5 where an entire phonon channel is driven to saturation. This is countered by applying additional corrections to quantities obtained after processing of phonon pulse, described in Appendix H.7.

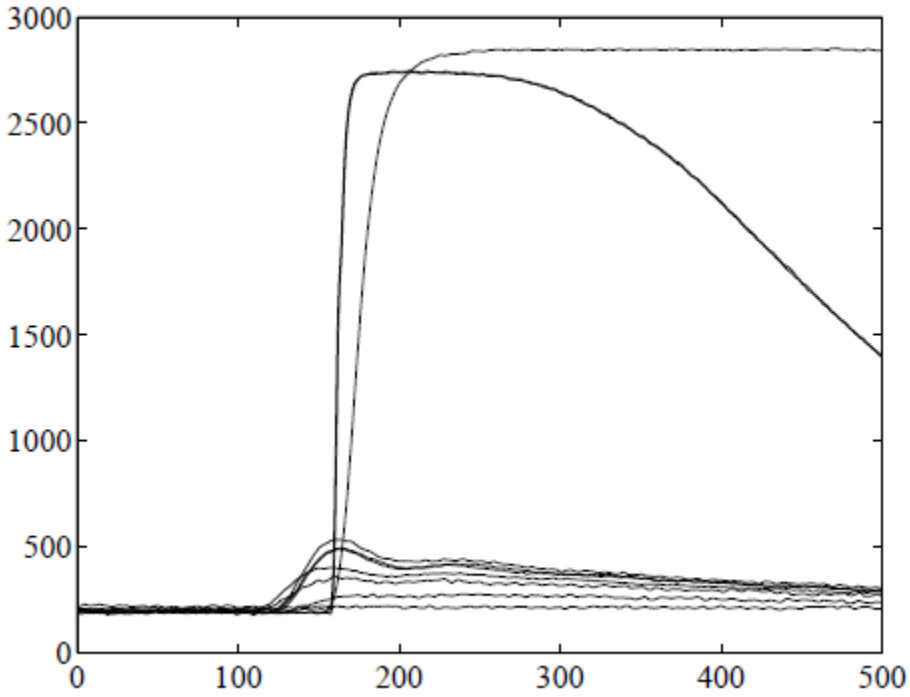

Figure 3.5: Example of pulses which saturates a phonon sensor by driving the tungsten completely normal. Figure from [243].

3.2.3 Information from Phonon Signal

As mentioned above, phonon sensors are fabricated on one of the faces of silicon or germanium crystal (with the other face containing the ionization electrodes). There are 4 such "channels" for phonon measurement arranged in a quadrant, with each phonon measurement channel comprises of 1036 tungsten QETs wired in parallel to each other (to keep them in a negative ETF configuration). This section looks at typical phonon pulse (obtained from phonon readout electronics) and introduces readers to various physically relevant feature on the pulse. A typical example of phonon pulse, observed by ZIP detectors is shown in Fig. 3.6. The features to note are:

- The temporal separation between the charge pulse and the phonon pulses. There is also a separation between the start-time of pulses corresponding to different phonon channels.

- The difference in height (amplitude) of different phonon pulses.

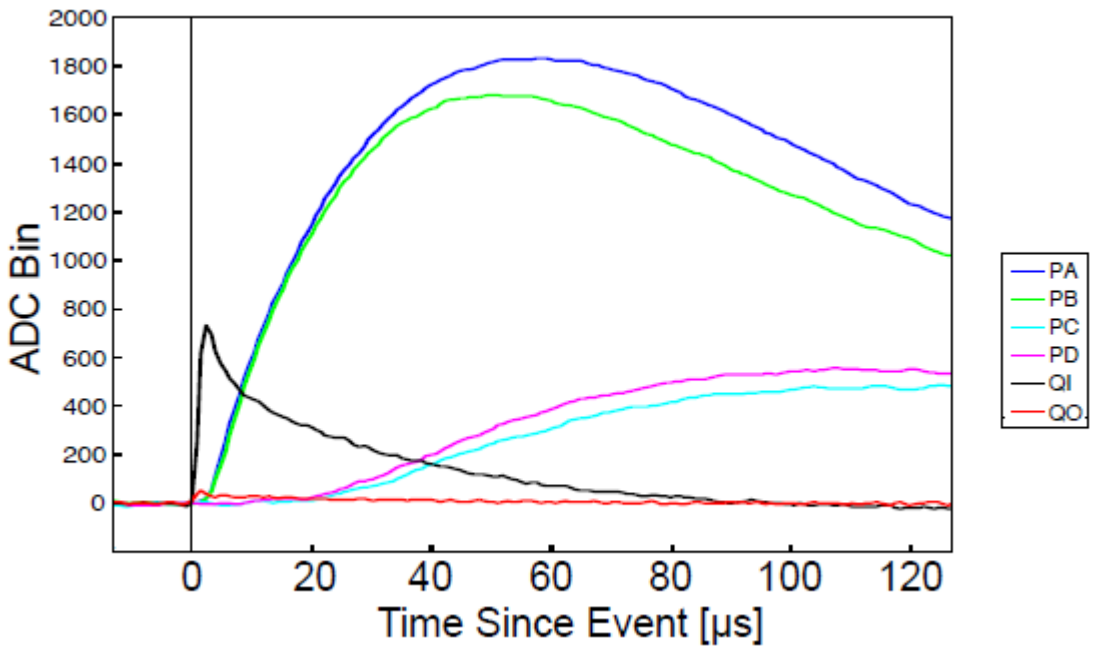

Figure 3.6: A typical CDMS-II event. The charge signals, being fast, are used to tag the start of an event. "QI, QO" represents the charge signal traces in inner and outer electrode. "PA, PB, PC, PD" represents phonon signal traces in the 4 phonon channels. Depending on event location inside the detector, the amplitude of phonon pulse (and their time-delay from charge pulse) is different. Figure from [236].

3.2.3.1 Basic Features in Phonon Pulse and its Physical Significance

Depending on proximity of different phonon measurement channels to the location of event occurrence within the crystal (the event is the interaction of a penetrating

particle with the crystal), they receive a larger flux of phonons if the channels are located closer to the event occurrence location. Similarly, phonons arrive sooner to a phonon measurement channel located closer to the event occurrence location. This accounts for the observed behavior among phonon signals. Thus, the difference between phonon amplitude and arrival time at different channels can be used as a measure of the lateral location of event occurrence.

Another feature which is noticed is that the charge pulses arrive before the phonon pulse. This is because the phonon propagation speed ($\sim$5mm/μs in germanium and $\sim$8mm/μs in silicon [231])is much slower than the drift speed of charge carriers (ehp). It is for this reason that the charge pulse is used to denote the moment of event occurrence within the crystal. It is also known that the temporal delay of a fastest phonon pulse in comparison to the charge pulse would relate to the depth of event occurrence inside the crystal. While irrelevant to LIPs analysis, this information is used to distinguish valid WIMP scatter events from possible electromagnetic backgrounds occurring close to the flat surface of the crystal [228–231]. Due to the detector's ability to provide an estimate for the depth of event occurrence, they are termed as being sensitive along "Z-direction", giving them the name of "Z-sensitive Ionization and Phonon" detectors, or ZIP detectors.

While multiple measurements can be made out of the phonon pulses, two measurements of primary importance to LIPs analysis are described below. These are "Amplitude Based Position" and "Phonon Delay Based Position" estimation.

3.2.3.2 Amplitude Based Position Reconstruction

As mentioned above, the relative phonon amplitude in each channel can be used to construct a quantity which relates to the lateral position of event occurrence within

the detector. These quantities, labeled (xppart,yppart), are defined as

$$xppart = \frac{pc + pd - pa - pb}{pt}$$
$$yppart = \frac{pa + pd - pc - pb}{pt} \tag{3.10}$$

where pa, pb, pc, pd are the phonon energies deposited in 4 phonon channels, usually labelled as phonon channel A, B, C and D; pt = pa + pb + pc + pd, is the sum of the four phonon energy from the four channels, and is the total phonon energy deposited (The procedure to obtain phonon energy, or amplitude estimation is described in Appendix H.5.1). Fig. 3.3 shows the convention for choosing (x,y) direction in relation to four phonon sensors. The corresponding combination of positive/negative sign with phonon channels are used to obtain the definition of (xppart,yppart).

Fig. 3.7 shows a typical example of distribution of (xppart,yppart). It has a characteristic square shape and is traditionally referred as a "box plot". The box like shape is because of fact that as the lateral location of event occurrence inside the detector moves away from the boundary between two phonon measurement channels, a majority of phonon energy from the event gets absorbed in the single, closest phonon channel. Thus, even if the events are widely distributed within the lateral region spanned by a single phonon channel, they all tend to deposit a large portion of total phonon energy in the corresponding phonon channel and get reconstructed to almost similar values of (xppart,yppart).

3.2.3.3 Delay Based Position Reconstruction

Similar to the amplitude based position estimation, it is possible to estimate the lateral position of event by measuring the relative delay in arrival of phonon pulses at different channels. The phonon-delay based position estimation quantities, labeled

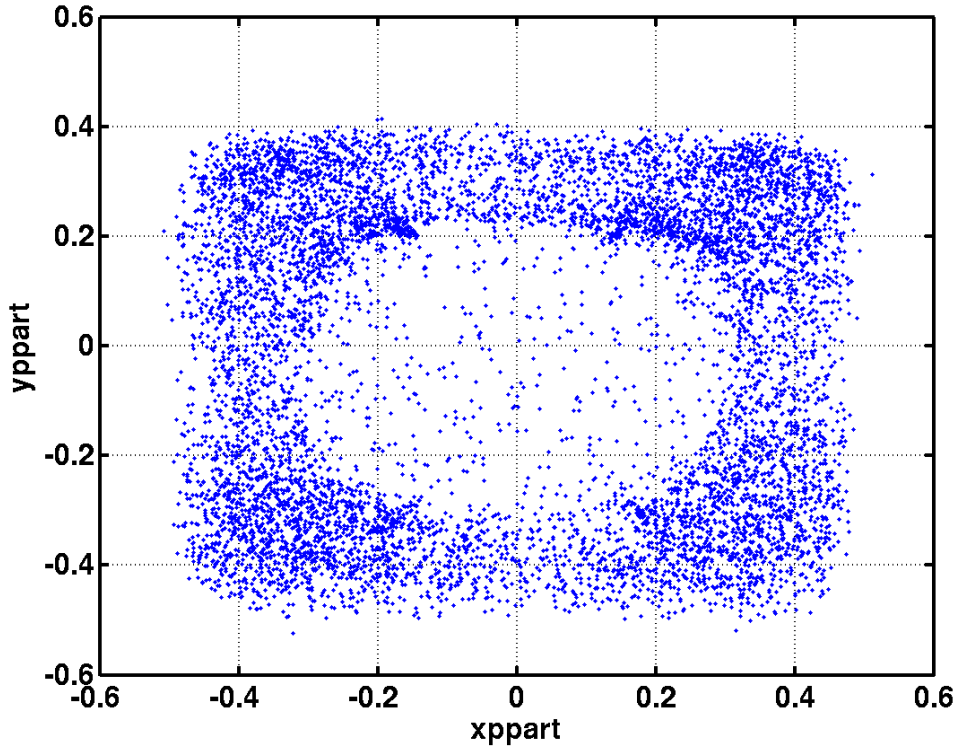

Figure 3.7: A typical "box plot". The (xppart,yppart) are quantities constructed using phonon amplitude, defined in Eq. (3.10). They relate to the location of event occurrence inside the detector.

(xdel,ydel), are defined as

$$
\begin{aligned}
xdel &= \begin{cases} PAr20 - PDr20 & Interaction\ in\ Channel\ A\ or\ D \\ PBr20 - PCr20 & Interaction\ in\ Channel\ B\ or\ C \end{cases} \\
ydel &= \begin{cases} PBr20 - PAr20 & Interaction\ in\ Channel\ A\ or\ B \\ PCr20 - PDr20 & Interaction\ in\ Channel\ D\ or\ C \end{cases}
\end{aligned}
\tag{3.11}
$$

where, $r20$ represent the time required by phonon pulse in correponding channel to rise to 20% of its maximum amplitude from a common reference (Obtained using

a "Walk" algorithm, described in Appendix H.5.2). The procedure is used to determine $PAr20$, $PBr20$, $PCr20$ *and* $PDr20$ for phonon channels A, B, C and D correspondingly. As shown in Fig. 3.3, the definition for (xdel,ydel) follows from the arrangement of phonon measurement channel on the crystal surface.

Fig. 3.8 shows the distribution of (xdel,ydel). It is traditionally termed as "delay plot". Unlike phonon amplitudes, the phonon delay varies smoothly for events distributed within the lateral region spanned by a single phonon channel. Thus, the delay-plots do not show the box-like form exhibited by box-plots, constructed using (xppart,yppart). The smallness of values spanned by the silicon detector's delay-plot is because the phonons cover similar detector size with a faster speed (Phonon speed for silicon is $\sim$8mm/μs, and germanium $\sim$5mm/μs).

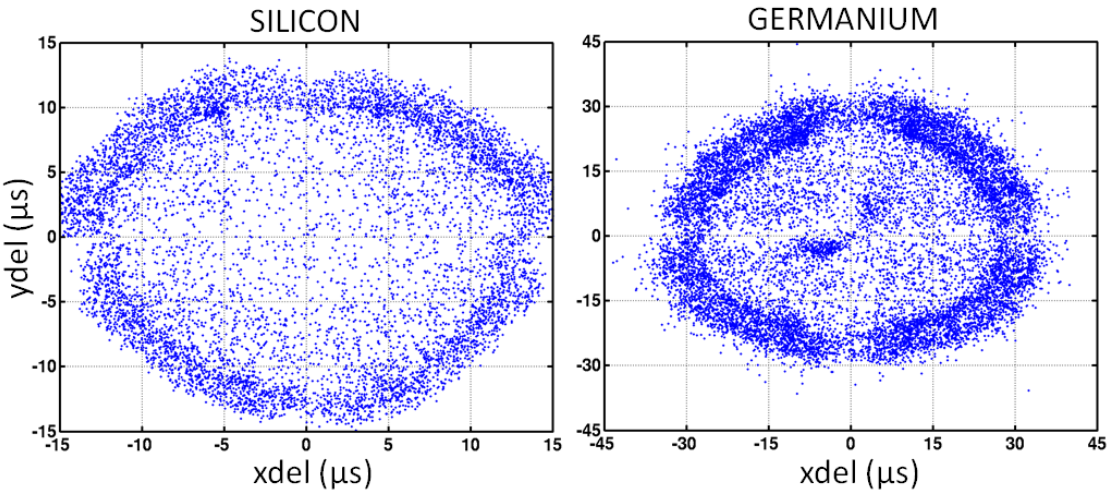

Figure 3.8: A typical "delay plot". The (xdel,ydel) are quantities constructed using phonon delay relative to charge signal, defined in Eq. (3.11). They relate to the location of event occurrence inside the detector. The smallness of values spanned by the silicon detector's delay-plot is because the phonons cover similar detector size with a faster speed.

3.2.3.4 Foldback

After being created at the site of interaction, the phonons quickly downconvert into low energy, large wavelength ballistic phonons. As the ballistic phonons propagate, they reflect from crystal surface till they are absorbed by the phonon sensors. This phonon reflection creates a "Foldback" feature in the delay and amplitude based position estimation. Phonons from the events occurring close to the curved cylindrical surface of the crystal, reflect from the curved surface and get distributed among the 4 phonon measurement channels in such a manner that an estimation of amplitude based position (xppart,yppart) places such events as occurring in the bulk of crystal (closer to the cylindrical axis). This feature, where the events occurring at large radii get estimated as occurring close to the cylindrical axis of detector, is called "Foldback". Presence of foldback, both in amplitude and delay based position estimation, is shown in Fig. 3.9. Due to foldback, the delay/amplitude based position estimation and the physical location of event occurrence do not relate through a functional dependence.

3.3 Yield of Ionization versus Phonon Signal

For the set of interactions between a substrate and uncharged particle occurs via a nuclear recoil type event and the energy lost by incident particle is lost to the substrate nuclei. Such a recoil creates low ionization signal, and proportionately higher phonon signal (This is not relate to nucleus being lattice bound [236]). The "quenching" of ionization signal as compared to phonon signal for nuclear recoils is energy dependent and different for silicon and germanium targets, as explained in the papers by Lindhard [254, 255]. Conversely, an electromagnetic recoil type event deposits energy in the electron sea of the substrate. Since electrons are light and not bound inside the crystal, they can move a longer distance and create more ehp. A

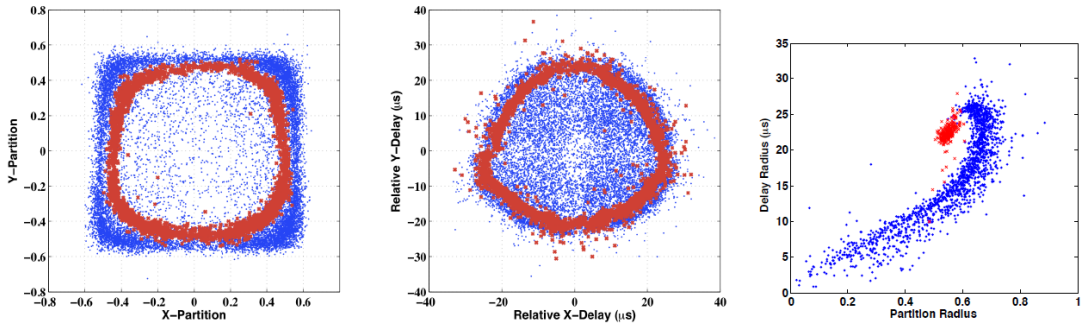

Figure 3.9: Left to right: Exhibiting "Foldback" in distribution of (xppart, yppart), (xdel,ydel) and for a small subset of events, the distribution of (rdel,rppart) is shown. (xppart,yppart) is defined in Eq. (3.10). (xdel,ydel) is defined in Eq. (3.11). Two new quantities are defined, $rppart = \sqrt{xppart^2 + yppart^2}$ and $rdel = \sqrt{xdel^2 + ydel^2}$. The events in red occur at high radius, close to circular boundary of detector, and are selected by requiring large ionization signal in outer charge electrode. The events in blue are required to have large ionization signal in inner charge electrode. Figure taken from [236]

quantity, "Yield" (Y), or ionization yield, can be defined as the ratio of ionization to recoil phonon energy.

$$Y = E_Q / E_{Recoil} \tag{3.12}$$

3.3.1 Distinction by Yield

An example of the ionization yield measured for nuclear recoils from the ^{252}Cf neutron source and electron recoils from the ^{133}Ba gamma source is shown in Fig. 3.10. The yield for electromagnetic recoil type events is 1, and the yield for nuclear recoil type events is $\sim$1/3. Thus, the ionization yield can distinguish between nuclear and electromagnetic recoil type events. Above $\sim$5keV, there is a clear separation between the bulk of the nuclear and electromagnetic recoil distributions. However, at low energies the populations begin to merge because the ionization signal starts to become comparable to noise. The increased fluctuation in ionization signal (E_Q) and in estimation of recoil phonon (Noise in charge signal affects estimation of re-

coil phonon because latter is obtained by subtracting ionization from total phonon energy) causes a widening and merging of the two yield bands.

Although an electromagnetic event has a yield of unity, it is possible to obtain similar type events which have lower yield. These are events where the ionization signal is incompletely measured.

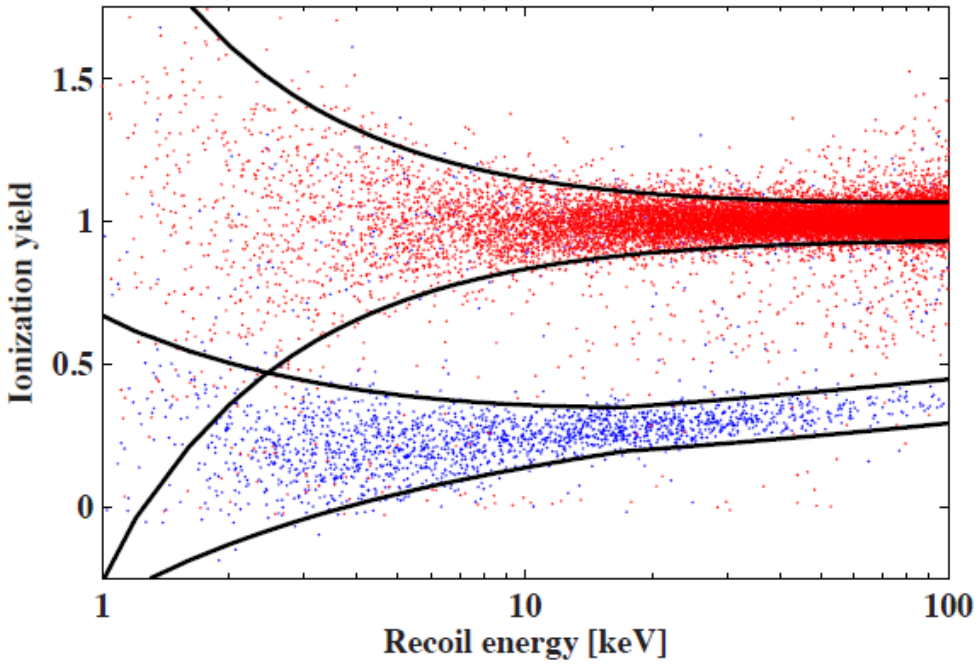

Figure 3.10: Ionization yield versus recoil energy for ^{133}Ba calibration data (red), which primarily consists of electromagnetic recoil events from Compton scattering of γs; and ^{252}Cf calibration data (blue), which primarily produces neutron-induced nuclear recoils. The black lines indicate the $\pm 2\sigma$ confidence yield bands for the corresponding type of recoils. Figure taken from [239].

3.3.2 Charge Trapping

There are 2 main processes causing charge trapping. "Sidewall Trapping", discussed below, can cause valid electromagnetic recoil type events to have incomplete

charge collection and have yield as low as 0.1.

- **Trapping on Charged Impuritities:** Charged impurities in the crystal bulk can trap ehp formed from particle interaction. These are discussed in detail in Appendix G.1. However, they do not affect the data because their effects are "neutralized" before detector starts taking data, and it remains maintains for$\sim$8 hours more. Detector neutralization is discussed in Appendix G.2.

- **Sidewall Trapping:** An additional trapping is due to "Sidewall trapping". At the bare cylindrical surfaces of the crystal, the periodicity in atomic arrangement in lost and the energy levels become much harder to predict. The irregularity in spatial topology and presence of dangling bonds at the sidewall create a highly irregular band structure in which drifting charges get trapped. The loss in ionization collection can cause yield to go as low as 0.1 or lower.

3.3.3 Surface Events

These low-yield events are due to interactions occurring very near the surface of the detector, where the ionization can be incompletely collected. When an event occurs near the surface of the detector, the charges produced are hot (energy much higher than band minimum) and they may diffuse into the wrong electrode before the drift field has a significant effect on their motion. As an example, for an event occurring near the negatively biased electrode, the electrons formed may be energetic enough to diffuse into the negatively biased electrode, rather than drifting towards the detector face which is grounded. The charge cloud produced by a recoiling particle may also shield itself because the separating charges have dipole fields that counter the drift field [232]. The region with incomplete ionization collection is termed as "dead layer", and exists within 10-20μm of the detector surface [238].

The effect of the incomplete ionization collection (from events occurring close to detector surface) is clearly seen in a plot of the ionization yield for calibrations using a collimated ^{109}Cd source, shown in Fig. 3.11. This source has x-ray and γ lines at 22keV and 88keV, as well as mono-energetic electrons at 63, 85 and 88 keV due to internal conversion of the γ. The 88 keV γ and 22 keV x-rays primarily interact in the bulk of the detector and lie around an ionization yield of 1. In contrast, the range of mono-energetic electrons, also shown in Fig. 3.11, does not allow them to go past the dead layer. These electrons interact within the dead layer and have suppressed ionization yield. In addition to the fully collected events, a broad energy distribution of low-yield events is seen due to back-scatter of electrons that do not deposit their full energy in a single detector.

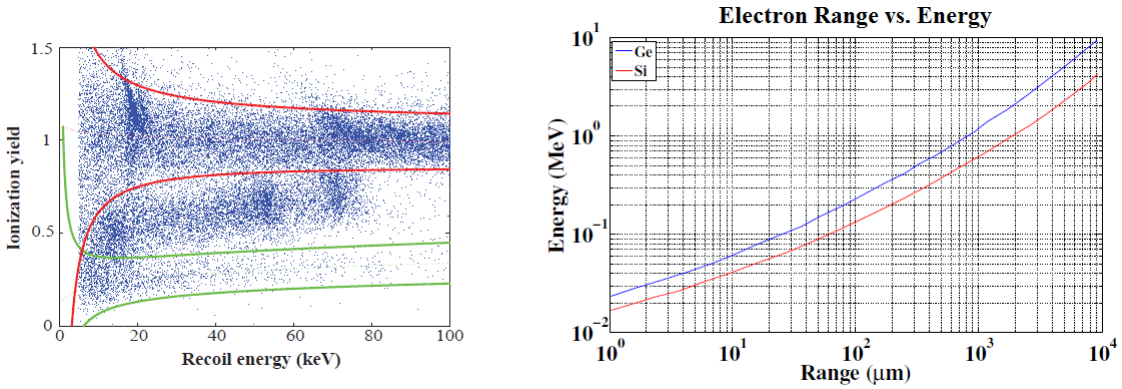

Figure 3.11: Left: Data for a collimated ^{109}Cd source. Fully collected bulk electromagnetic recoils appear in the corresponding 2σ band (red), including γ and x-ray lines at 88 and 22keV. Surface events, primarily due to the internally converted electron from the source have reduced ionization collection and can leak into the band (green) corresponding to 2σ nuclear recoil type events. Figure taken from [239]. Right: Electron range inside silicon and germanium. Figure taken from [237].

3.4 Installation

This section describes the installation of ZIP detectors, fabricated on germanium and silicon crystals, in Soudan Underground Labs in Northern Minnesota. In particular the section describes the key features of detector installation which allows the possibility to analyze the data for LIPs, even though the data was obtained with an original motivation to search for WIMPs. A detailed discussion on detector installation is provided in Appendix I

The CDMS collaboration fabricated 30 of these detectors among which 19 of them were made of Ge and 11 were made of Si. These detectors are installed in Soudan Underground Labs (SUL), situated in northern Minnesota. The lab is on the 27th level of a decommissioned iron mine, at a depth of 714 m below the surface. The rock overburden at the SUL provides a cosmic ray flux that is equivalent to 2090 meters of water overburden, reducing the muon flux by a factor of $5{\cdot}10^4$ relative to the flux at the surface (the remaining muon flux is <1 per minute). The reduction in muon flux is imperative to obtain a reduction in cosmogenic neutron (produced interaction of high energy, cosmic muons with materials surrounding the detectors, through muon-induced nuclear disintegration or various secondary processes within muon-induced hadronic and electromagnetic showers), which is a major background for WIMP analysis. Since LIPs are fractionally charged, their flux will not be as much reduced as muon flux. This allows a possibility to detect LIPs despite the detectors being installed underground.

Since the mine rocks contain trace amount of radioactive elements, additional concentric layers of shielding are installed covering the entire detector. On the outermost is a 5cm thick layer of plastic scintillator panels allowing a minimum ionizing muon to deposit sufficient energy to be detected. These cosmic muons can interact

with other materials around the detectors and create cosmogenic neutrons. Going from outside to inside, after the scintillator layer, there are layers of 40cm thick outer polyethylene layer, 18cm thick outer Lead layer, an inner 4.5cm thick layer of "ancient lead" with low radioactivity levels (lower ^{210}Pb) and a 10cm thick innermost layer of polyethylene. The layers serve to reduce backgrounds from energetic x-rays, γ-rays and radiogenic neutrons. Immediately inside the innermost polyethylene layer is a 2mm thick mu-metal shield to prevent the inside region from external magnetic field. This is necessary because QET signals are read out using SQUIDs, which would respond to external magnetic field and its variations. Inside the mu-metal shield are set of concentric copper cans called "Icebox", and the detectors are kept inside the innermost can. The region between the mu-metal and outermost can is purged with nitrogen (from boiling-off liquid nitrogen) to prevent radioactive radon gas from entering the region. A ^{3}He-^{4}He dilution refrigerator from Oxford Instruments is thermally connected to various layers of the icebox, and used to cool the detectors to $\sim$40mK (The detectors are kept separate from the fridge to prevent the exposure of former from radioactive contaminants in latter). The setup of different layers of shielding around detectors provide a low background environment suitable for detection of particles with small interactions cross-section. Traditionally, it is employed for WIMP analysis, but is used for LIPs analysis presented in this dissertation.

The CDMS-II experiment employs 30 ZIP detectors made using silicon or germanium substrate, and stacked inside the innermost can in 5 vertical towers, each containing 6 detectors, as shown in Fig. 3.12. The ZIP detectors in a tower are arranged adjacent to other detectors and are vacuum separated by $\sim$2.2mm. The vertical arrangement of multiple detectors within a tower allows discrimination of relativistic LIP signal by requiring them to interact with all detectors in a tower

along a straight path.

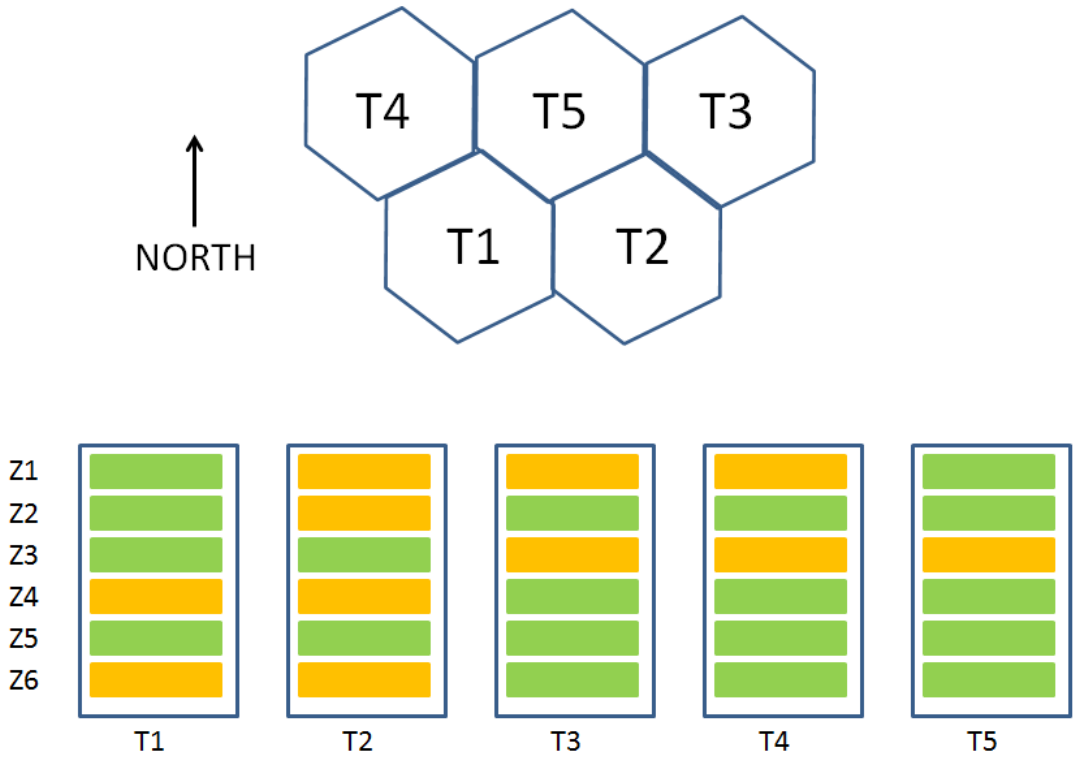

Figure 3.12: Arrangement of 30 ZIP detectors in 5 vertical towers (T), each containing 6 ZIP detectors (Z). The detectors are fabricated on either silicon (orange) or germanium (green) substrate. Adapted from [231].

3.5 ZIP Detector Substrate

ZIP detectors are fabricated on cylindrical crystal of high purity germanium or silicon. The substrate is either made of p-type or n-type semiconductor crystal. It is 1 cm thick and 3 inches in diameter. The outer edge of the crystal has five flats, as shown in Fig. 3.13, in order to facilitate alignment and handling. There are two major flats at the north and south positions, separated by 7.22 cm; two minor flats

at east and west, separated by 7.55 cm; and a small fifth flat at the northwest, with a distance of 3.77 cm to the center. The exact position of the fifth flat indicates the orientation of the crystal axis, [242]. The cylinder axis of each detector is either oriented along a $\langle 100 \rangle$ crystal axis (centered at 45°) or $\langle 111 \rangle$ [228, 231] (centered at 30°).

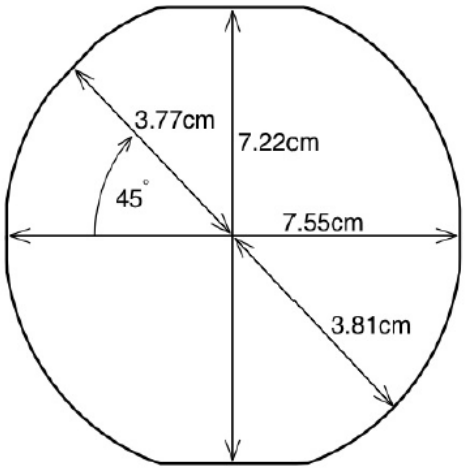

Figure 3.13: Geometry of a ZIP detector substrate as seen from the top, showing all flats. The major flats are at top and bottom, and the minor flats are at right and left. The small fifth flat is at 45° in top left position, indicating a $\langle 100 \rangle$ crystal axis. Figure from [231, 242].

The substrate material used to make the ZIP detectors are prepared with low impurity and dislocation concentrations ($\sim 10^{11}$impurities/cm^3 and less than 5000 dislocations/cm^2 for Ge) to ensure that the electron hole pairs created due to interaction of a particle within the substrate gets collected at the electrode and does not get trapped within these defects. A detailed information on material property used to fabricate the 30 ZIP detectors is listed in Table 3.1.

Table 3.1: List of CDMS-II detectors names, material used as substrates, thicknesses and masses. The difference between boules A, B and C are the doping type and the impurity concentrations. Boule A has an impurity concentration of $9.5{\cdot}10^{10} - 10^{11} cm^{-3}$, Boule B has $2.7 \cdot 10^{11} - 4.7 \cdot 10^{11} cm^{-3}$), and Boule C has $8.5 \cdot 10^{10} - 1.9 \cdot 10^{11} cm^{-3}$ [231]. The CDMS-II experiment employs 30 ZIP detectors stacked in 5 vertical towers, each containing 6 detectors. The name "T1Z1" refers to the substrate corresponding to Detector-1 in Tower-1.

Detector Name	Material	Thickness (cm)	Mass (g)
T1Z1	Ge (n-type boule A)	9.65±0.05	230.5
T1Z2	Ge (n-type boule A)	9.53±0.23	227.6
T1Z3	Ge (n-type boule A)	9.18±0.05	219.3
T1Z4	Si (n-type boule A)	10.00±0.05	104.6
T1Z5	Ge (n-type boule A)	9.18±0.05	219.3
T1Z6	Si (n-type boule A)	10.00±0.05	104.6
T2Z1	Si (n-type boule A)	9.70±0.05	101.4
T2Z2	Si (n-type boule B)	10.00±0.05	140.6
T2Z3	Ge (n-type boule A)	9.18±0.05	219.3
T2Z4	Si (n-type boule B)	10.00±0.05	104.6
T2Z5	Ge (n-type boule B)	10.00±0.05	238.9
T2Z6	Si (n-type boule B)	10.00±0.05	104.6
T3Z1	Si (n-type boule B)	10.00±0.05	104.6
T3Z2	Ge (n-type boule B)	9.68±0.05	231.2
T3Z3	Si (n-type boule A)	10.00±0.05	104.6
T3Z4	Ge (p-type boule C)	10.00±0.05	238.9
T3Z5	Ge (p-type boule C)	10.00±0.05	238.9
T3Z6	Ge (n-type boule B)	9.70±0.05	231.7
T4Z1	Si (p-type boule A)	9.70±0.05	101.4
T4Z2	Ge (n-type boule A)	10.00±0.05	238.9
T4Z3	Si (n-type boule A)	9.70±0.05	101.4
T4Z4	Ge (p-type boule C)	9.82±0.23	234.6
T4Z5	Ge (p-type boule C)	9.71±0.05	231.9
T4Z6	Ge (p-type boule C)	10.00±0.05	238.9
T5Z1	Ge (n-type boule A)	9.40±0.23	224.5
T5Z2	Ge (p-type boule C)	9.61±0.23	229.5
T5Z3	Si (n-type boule B)	9.70±0.05	101.4
T5Z4	Ge (n-type boule B)	9.40±0.05	224.5
T5Z5	Ge (p-type boule C)	9.83±0.05	234.8
T5Z6	Ge (n-type boule B)	9.36±0.05	223.6

4. ANALYSIS

This section describes the analysis of data obtained by CDMS detectors, to search for lightly ionizing particles (LIPs).

Section 4.1 describes the mathematical calculation underlying the LIPs analysis and the corresponding physical quantity of interest reported by the analysis. Performing the analysis requires modeling the interaction of LIPs with CDMS detectors, and is described in Section 4.2. Additionally, an understanding of the detector working principle, installation and data processing (provided in previous chapter, Section 3), is necessary to design an analysis paradigm to allow interpretation of CDMS data towards a LIPs search. It is described in Section 4.4. Section 4.5 applies this knowledge on the physical data, performs an analysis to search for LIPs and presents the corresponding result. Since this is a first effort towards performing a LIPs search on CDMS data, few aspects of the analysis still have scope for improvement, and is described in Section 4.6.

4.1 Mathematical Framework

The science question asked by LIPs analysis is as follows, "Given that the detector are operated for a certain number of time, and have a certain efficiency (probablity) towards observation of LIPs incident at any angle (from the vertical); If a certain number of valid signals N are observed, then it implies that the total flux of incident LIPs passing through detectors would be less than or equal to a certain amount. Stated with 90% confidence, what is that flux value? The remainder of the section elaborates this question, introducing and mathematically defining related terms.

4.1.1 LIP Detector

The detection-unit used in LIPs analysis is not just one ZIP detector, which is the unit used in WIMP analysis [11], but a vertical stack of 6 ZIP detectors arranged in a tower (as shown in Fig. 3.12, and described in Appendix I.4). It is required that only an "event" where simultaneous non-zero signal is generated in all 6 ZIP detectors of a tower is considered as being caused by a LIP. The detailed reasoning behind employing such a criteria is described in Section 4.5.6.

4.1.2 Flux

It is the primary quantity of interest sought in the LIPs analysis, and is labeled as I_v^{90} (the superscript *90* denotes that the reported flux value can be stated with 90% statistical confidence). It denotes the effective flux of LIPs passing through the "LIP detector" (vertical stack of 6 ZIP detectors in a tower), and includes contribution both from vertically incident LIPs and from those which strike the detectors at a certain angle from vertical (polar angle). However, the contributions from the latter are weighted by a $cos(\theta)$ factor, where θ is the polar angle, as shown in Eq. (4.1). This weighting is done because the LIP detector is only sensitive to vertically incident LIPs; horizontally incident LIPs strike only 1 detector (out of a stack of 6 ZIP detectors) and are inherently rejected based on the requirement for a valid LIPs signal to interact with all 6 vertically stacked ZIP detectors. It if for same reason that the subscript$v$ is used in the label I_v^{90}.

$$I_v^{90} = \int_{\theta=0}^{\pi/2} \int_{\phi=0}^{2\pi} I_v^{90}(\theta,\phi) cos(\theta) \cdot sin(\theta) d(\theta) \cdot d(\phi) \tag{4.1}$$

where, θ is the polar angle, ϕ is the azimuthal angle. $I_v^{90}(\theta,\phi)$ is the corresponding angle dependent LIP flux interacting with the LIP-detector. However, its exact

nature is not of interest. The θ integral is stopped at $\pi/2$ by asserting that only downward going LIPs exist, i.e. no LIPs are coming out from Earth (as described in Section 4.3)

By basic definition of flux, it can be written that:

$$I_v^{90} = \left(\frac{N^{90}}{\tau \cdot \sigma}\right) \tag{4.2}$$

where, τ is time for which the detectors are kept running. N^{90} is the 90% confidence estimate on the number of events observed within the CDMS data due to possible LIP interaction with the LIP-detector. The estimate for N^{90} depends on the number of events observed in the data and the total background estimate for the analysis (backgrounds are detected events which aren't caused by LIP, but still leave a deposition signal in detector similar to a LIP). Consider an example: the total background level is much less than a single event, and $\equiv$0. Thus, the total events observed is only due to LIPs. Also consider that after the analysis, 0 events are found. However, one may say that the process of observing LIP induced event is probabilistic in nature, and it is just by chance that 0 events were seen. Assuming Poisson distribution (since the probability of observing LIPs is very small, and only 0 events were obtained), one may assert that even if the actual number of events observed were 2.3, there is a 90% probability to observe only 0 events, as was reported by the analysis. Thus, with 90% confidence, one may say that the observance of 0 events is due to statistical fluctuation where the actual number of events should have been $\leq$2.3. In this example, N^{90}=2.3, not 0. σ is the cross-section for the same (LIP interaction with the LIP-detector). The cross-section (σ) changes for particles with different electromagnetic charges *fe*, where e is the charge of electron and f is the ratio of charge of LIP to the charge of electron. To show this dependence explicitly,

the cross-section is henceforth written as $\sigma(f)$ to denote the same. In general, the same is also true for N^{90} (if the criteria used to select possible LIP event is dependent upon its fractional charge). Thus, the dependence also shows up in the value of flux inferred from the analysis.

$$I_v^{90}(f) = \left(\frac{N^{90}(f)}{\tau \cdot \sigma(f)} \right) \tag{4.3}$$

4.1.3 LIP Interaction Cross-section

Stated simply, the cross-section ($\sigma(f)$) for interaction between LIP and LIP-detector is the product of cross-sectional area of the LIP-detector, A, (same as cross-sectional area of 3-inch diameter ZIP detector), and the charge dependent probability for LIP interaction with LIP-detector, *P(f)*. Thus, one may rearrange Eq. (4.3) to obtain

$$N^{90}(f) = I_v^{90}(f) \cdot \tau \cdot A \cdot P(f) \tag{4.4}$$

and interpret it as, "The LIP-induced events observed in LIP-detector depends on the time for which the detector is operated and the rate of incidence of LIPs over the detector of area A, scaled by the probability that a LIP also interacts with the LIP-detector after being incident on it". Without loss of generality, one may assert that the probability for LIP interaction (with LIP-detector) is also dependent upon the polar (θ) angle of the incident LIP (since the detector is cylindrically symmetric, there is no intrinsic dependence on the azimuthal angle, ϕ).

$$\begin{aligned} P(f) &= \int_{\theta=0}^{\pi/2} \int_{\phi=0}^{2\pi} P(\theta, \phi; f) \cdot sin(\theta) d(\theta) \cdot d(\phi) \\ &= 2\pi \left[\int_{\theta=0}^{\pi/2} P(\theta; f) \cdot sin(\theta) d(\theta) \right] \end{aligned} \tag{4.5}$$

The θ integral is stopped at $\pi/2$ for similar reason applied in Eq. (4.1), i.e., by asserting that only downward going LIPs exist and no LIPs are coming out from Earth (as described in Section 4.3).

4.1.4 Interaction Probability

There are 3 main considerations which guide the structure of interaction probability ($P(\theta; f)$), described below.

The LIP flux incident on LIP-detector with non-zero polar angle is scaled by a $cos(\theta)$ factor, as shown in Eq. (4.1). Similar considerations require that a $cos(\theta)$ factor be included in the definition of $P(\theta; f)$.

While defining a LIP-detector, it is mentioned that for an events to considered as being caused by a LIP, simultaneous non-zero signal must be observed in all 6 ZIP detectors of a tower (a detailed reasoning behind employing such a criteria is described in Section 4.5.6). However, LIPs incident with non-zero polar angle won't simultaneously pass through the vertically arranged stack of ZIP detector, as shown in Fig. 4.1. A suitable factor, $F(\theta)$ is introduced to account for this effect, defined in Eq. (4.6). It being a geometric factor, is not dependent on the charge of LIP, or *fe*.

$$\begin{aligned} F(\theta) &= 2\left[R^2 \cdot \alpha - \frac{R \cdot H \cdot sin(\alpha) \cdot tan(\theta)}{2}\right] / \pi R^2 \qquad \theta \leq tan^{-1}\left(\frac{2R}{H}\right) \\ &= 0 \qquad \theta > tan^{-1}\left(\frac{2R}{H}\right) \end{aligned} \tag{4.6}$$

where, R is the radius of each ZIP detector, H is the height of tower (i.e. height of 6 ZIP detectors and the sum of gap between 5 detectors), θ is the polar angle in radians and α is defined such that $\alpha = cos^{-1}\left(\frac{Htan(\theta)}{2R}\right)$.

Excluding above factors, the requirement for a valid LIP signal to interact with each LIP detector itself occurs with a probability. Since a LIP-detector is made of 6

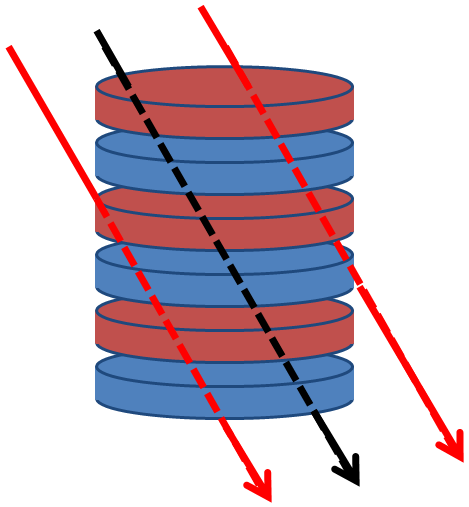

Figure 4.1: For non-vertically incident LIPs (at angle θ), not all particles incident at top surface of uppermost detector also exit through the bottom surface of lowermost detector of the tower. This introduces a *theta*-dependent geometric efficiency in detection of LIPs by the stack of 6 ZIP detectors, also called "LIP-detector". Valid LIP signal are shown in black and those rejected are shown in red. The path of LIPs within the LIP-detector is dashed.

stacked ZIP detectors, the LIP interaction probability for all 6 ZIP detector need to be multiplied with each other.

$$P(\theta; f) \propto \Pi_{i=1}^{6} P_{ZIP_i}(\theta; f) \tag{4.7}$$

Calculation of LIP interaction probability for each ZIP detector involves multiple factors, described below:

- There is a certain probability for LIPs to deposit energy inside the detector, $P_{Det}\left(E_{Dep}, f, \theta\right)$. However, the probability distribution gets smeared due to finite energy resolution of the detector, $Reso_{Det}(E_{Mes})$. In the following analysis, it is empirically obtained by analyzing the data collected by detector itself, as described in Section 4.2.4. So, it depends on the energy measured by

the detector. But, to a first approximation, $Reso_{Det}(E_{Mes}) \equiv Reso_{Det}(E_{Dep})$. By performing the resolution smearing, one obtains the probability distribution corresponding to energy measured by detector as it interacts with LIP, $P_{Det}\,(E_{Mes}, f, \theta)$.

$$P_{Det}\,(E_{Mes}, f, \theta) = P_{Det}\,(E_{Dep}, f, \theta) * Reso_{Det}(E_{Mes}) \tag{4.8}$$

where '$*$' denotes the convolution operation. Additionally, it needs to be noted that the probability for deposition for certain energy inside detector depends on the material used to construct the detector (germanium/silicon substrate) and on the number of interactions a LIP undergoes inside the detector (discussed in Section 4.2). The latter depends on detector thickness and the quantity $f^2/cos(\theta)$ instead of independent dependence on f and θ. For different detectors made of same material (Si/Ge) and same thickness (1cm), the probability distribution for measured energy is $P_{Det}\,(E_{Mes}, f^2/cos(\theta))$

- It is also required that the detector be able to measure the deposited energy, which may not always occur. This introduces a detection efficiency factor, $Eff_{Det}(E_{Mes})$. Primarily, it is not due to the inability of the detector to measure the deposited energy, but due to the variations in associated physical properties of the event making it resemble closer to a background than to a LIP signal. The variations may occur due to detector resolution. A calculation of this efficiency factor is done using data collected by detector itself. So, it depends on the energy measured by the detector.

- Even if an there is a non-zero probability of energy deposition by LIPs as it interacts with detectors, and also that the detector is able to measure it; such

a capability won't be of any use if the energy range is outside the analysis region, bounded by some upper and lower energy threshold for LIPs analysis ($E_{th,high}$ and $E_{th,low}$). The thresholds may themselves be set separately for each detector.

Using above considerations, the probability for LIP interaction within a single ZIP detector is:

$$P_{ZIP_i}(\theta; f) = \int_{E_{th,low;i}}^{E_{th,high;i}} P_{Det_i}\left(E_{Mes}, f^2/cos(\theta)\right) \cdot Eff_{Det_i}(E_{Mes}) \cdot d(E_{Mes}) \quad (4.9)$$

Combining all the above consideration, Eq. (4.6 - 4.9), one obtains:

$$P(\theta; f) = \left[\Pi_{i=1}^{6} P_{ZIP_i}(\theta; f)\right] \cdot F(\theta) \cdot cos(\theta) \quad (4.10)$$

4.1.5 Extra LIP-detector Efficiencies

The above calculation assumes that if a LIP event is detected by each ZIP detector (making up the LIP-detector), then the event is automatically selected as a valid LIP event. There exist additional analysis criteria which prevent it from always happening. As an example, one may require that the energy deposition in all 6 detectors occur with a distribution as expected for an event caused by LIP of certain fractional charge. If the criteria is not met, then the event is labeled as being caused by a background and not by a LIP. Thus, even though every detector comprising the LIP-detector signaled the occurrence of an interaction within it, the event may still get discarded. More of such criteria are qualitatively described in Section 4.4. It is possible that the statistical criteria mistakes an actual LIP induced event as occurring due to background. This introduces a corresponding efficiency factor (efficiency of the statistical criteria to identify an event as being caused by LIP), and is labeled

as $Eff_{LIP-Det}$. In the current analysis, the construction of such criteria is done in a manner that the corresponding efficiencies are at most dependent upon the fractional charge of the LIP (described in Section 4.5).

4.1.6 Equation of Interest

Combining Eq. (4.3 - 4.5) and Eq. (4.10), and the $Eff_{LIP-Det}$ factor, one gets:

$$I_v^{90}(f) = \left(\frac{N^{90}(f)}{\tau \cdot 2\pi A \cdot Eff_{LIP-Det} \cdot \left[\int_{\theta=0}^{\pi/2} \{\Pi_{i=1}^{6} P_{ZIP_i}(\theta; f)\} \cdot F(\theta) \cdot cos(\theta) \cdot sin(\theta) d(\theta) \right]} \right) \tag{4.11}$$

The θ integral is stopped at $\pi/2$ for similar reason applied in Eq. (4.1), (4.5), i.e., by asserting that only downward going LIPs exist and no LIPs are coming out from Earth (as described in Section 4.3).

4.2 Modeling LIPs Interaction with Detectors

The term "Modeling LIPs Interactions" imply obtaining an understanding of energy loss process as a LIP interacts with the 1cm thick crystal substrate. The interaction of LIP within the substrate is a statistical process with inherent fluctuation in the distance between two consecutive collisions and the energy deposited in each collision. It is due to these fluctuations that the existent details/estimates on average stopping power (average energy lost by an incident particle as it travels through the substrate), described by "Bethe Equation" [14,278], may not be used for this analysis. Average stopping power estimate inherently assumes that the detector is of very long length and has no minimum or maximum threshold (i.e. all energies deposited in the detector are finally measured). However, the CDMS detector substrates are of

finite thickness and the number of interactions occurring inside them will statistically fluctuate, specially for very low fractional charges where $\leq$1 interaction may occur on average inside the substrate. In each interaction, the physical value of energy lost by the LIP can vary. Lastly, there may exist lower and upper threshold to the event energy, i.e. events with energy deposition in a detector being outside the range bound by the lower and upper threshold are not used in LIPs analysis (described in Section 4.5.4). To account for these effects towards calculation of LIPs flux incident on detector (the final science goal of the analysis), $I_v^{90}(f)$, it is necessary to model the energy loss and associated fluctuations as LIPs interact within a detector.

4.2.1 Collision Cross-section

As the LIP interacts and passes through a detector, the energy lost is imparted to electrons, either creating an excitation of bound and unbound atomic states or as Rutherford-like scatters imparting large energy to them. The excited "hot" electron then relaxes by exciting additional electrons and/or phonons. A Monte Carlo of such relaxation in silicon is discussed in [244]. In this section, it is the former process which is of interest, i.e. understanding the process by which LIPs lose energy in the detector, and not the processes guiding the redistribution of the deposited energy (via creation of multiple electron-hole pairs (ehp) in the vicinity of particle track, and in creation of phonons, measured by the detector). This also allows an understanding of the probability distribution for LIPs to deposit a given energy in a single collision with the electrons of the detector substrate.

Assuming that the electrons are freely existing, its interaction with a heavy LIPs (more massive than electrons) of charge *fe* is described by the Rutherford differential cross-section (dependent upon the energy transferred E in a single collision and the

ratio of speed of incident heavy particle to speed of light in vacuum β) [11, 271]

$$\left(\frac{d\sigma_R(E;\beta,f)}{dE}\right) = \frac{2\pi r_e^2 m_e c^2 f^2}{\beta^2}\frac{(1-\beta^2 E/E_{max})}{E^2} \tag{4.12}$$

where, r_e, m_e is the classical radius and mass of electron, c is the speed of light in vacuum, and $E_{max} \sim 2m_e\beta^2c^2\gamma^2$ is the maximum energy transfer possible in a single collision, $\gamma = \frac{1}{\sqrt{1-\beta^2}}$. The differential cross-section changes insignificantly with $\beta\gamma$ in the relativistic region ($\beta\gamma \gtrsim 4$) [272]. Within a single collision, these kind of "hard interactions" are the primary reasons for transfer of high energy to the electron, but they occur with a very small probability.

However, the electrons in a real detector are bound inside the atom and the atoms are bound inside crystal. In interacting with atoms, the incident particle undergoes additional "soft interaction" in which the atom as a whole absorbs a virtual photon, in addition to Rutherford scattering (In quantum field theory, the electromagnetic interaction between charged particles are postulated to occur via exchange of virtual electromagnetic photons, or simply, "virtual photons"). The energies involved in such collisions are characterized by the atomic structure of the material and the collision cross-section sharply increases in the region of the photo absorption edges, i.e. when the energy of virtual photon is sufficient to ionize the electrons from an atomic orbital [272]. Since the electromagnetic field of a moving charged particle can be described as expanding in the transverse dimension as its velocity approaches the phase velocity of light in the medium, the energy loss cross-section grows logarithmically with the $\beta\gamma$ of the particle. In a medium of finite density, the dielectric properties modify this electromagnetic field, limiting its expansion, and stopping the logarithmic growth in the cross-section [272]. These effects (in addition to the Rutherford cross-section) are accounted in the final collision cross-section by introducing an energy dependent

"inelastic form factor",

$$\left(\frac{d\sigma_C(E;\beta,f)}{dE}\right) = IFF(E)\cdot\left(\frac{d\sigma_R(E;\beta,f)}{dE}\right) \tag{4.13}$$

A detailed understanding of the "inelastic form factor" is one of the continuing studies in high energy physics, extending over the entire last century, starting with studies on classical stopping of a fast heavy charged particle by an electron bound in a harmonic potential [273, 274], derivation of an expression for a cross-section (doubly differential in energy loss E and momentum transfer K) using the first Born approximation for inelastic scattering on free atoms [275] and extension of the same for solids [276]. Additional details may be obtained in [14, 278]. In the dissertation, an approximate method, known as Photo Absorption Ionization, or, PAI model [272] (also called Fermi Virtual Photon method, FVP, or Weizsäcker Williams approximation) is used to obtain the inelastic form factor, as described in Section 4.2.2.

4.2.2 Photo Approximation Ionization Model (PAI)

The details of the Photo Approximation Ionization Model (PAI) is discussed in [272]. Utilizing concepts from the semiclassical radiation theory, it obtains the energy loss as the the work done against the incident LIP by an electric field generated inside the substrate with given dielectric constant (assumed to be isotropic), as the particle passes through it. The energy loss is dictated by the imaginary part of complex dielectric constant of the substrate $\epsilon_2(E,P)$, which depends on both the energy, E, and momentum, P, transferred to the substrate as the particle interacts with it via virtual photons. The particular feature of the PAI model is that it approximates $\epsilon_2(E,P)$ as shown in Eq. (4.14). The first terms corresponds to the case when the momentum transferred by the virtual photon is much less than the energy, creating a dipole-like excitation of the atom. [272] refers it as the "resonance

region". The second case is for the case of large momentum transfer and allows the approximated form of complex dielectric constant to match the "Bethe sum rule" [275]. [272] refers it as the "quasi-free region".

$$\epsilon_2(E,P) = \frac{Nc}{EZ}\left[\sigma_\gamma(E)\cdot H\left(E-\frac{P^2}{2m}\right) - \int_0^E \sigma_\gamma(\acute{E})\cdot\delta\left(E-\frac{P^2}{2m}\right)\cdot d\acute{E}\right] \quad (4.14)$$

where N is the number of electrons per unit volume of the material comprising the detector substrate, Z is its substrate's atomic number, m is the mass of electron, c is the speed of light in vacuum, and $\sigma_\gamma(E)$ is the photoattenuation cross-section and $\sigma_\gamma(E) = \frac{EZ}{Nc}\left(\frac{\epsilon_2(E)}{\sqrt{\epsilon_1(E)}}\right)$, $\epsilon_1(E)$ and $\epsilon_2(E)$ are the real and imaginary part of dielectric constant as experienced by a photon inside the detector substrate (It should be noted that [272] describes $\sigma_\gamma(E)$ as the photoabsorption cross-section. However, coherent scattering inside a silicon/germanium substrate can be measured as phonons. Thus, for the purpose of this dissertation, the photoattenuation cross-section is used). Fig. 4.2 provides an example showing the difference between the approximation and estimates based on rigorous calculations.

As referred from [272], the above approximation is used to construct the differential cross-section for energy lost by a LIP (of charge fe) to a single electron inside the substrate $d\sigma(E;f)/dE$, and is given by

$$\begin{aligned}\frac{d\sigma(E)}{dE} =& \frac{\alpha}{\beta^2\pi}\frac{\sigma_\gamma(E)}{EZ} ln\left[\left(1-\beta^2\epsilon_1\right)^2+\beta^4\epsilon_2^2\right]^{-1/2} + \frac{\alpha}{\beta^2\pi}\frac{1}{N\hbar c}\left(\beta^2-\frac{\epsilon_1}{|\epsilon|^2}\right)\Theta \\ &+ \frac{\alpha}{\beta^2\pi}\frac{\sigma_\gamma(E)}{EZ} ln\left(\frac{2mc^2\beta^2}{E}\right) + \frac{\alpha}{\beta^2\pi}\frac{1}{E^2}\int_0^E \frac{\sigma_\gamma(\acute{E})}{Z} d\acute{E} \\ \frac{d\sigma(E;f)}{dE} =& f^2\left(\frac{d\sigma(E)}{dE}\right)\end{aligned} \quad (4.15)$$

where the definitions from Eq. (4.14) follow, along with α is the fine structure con-

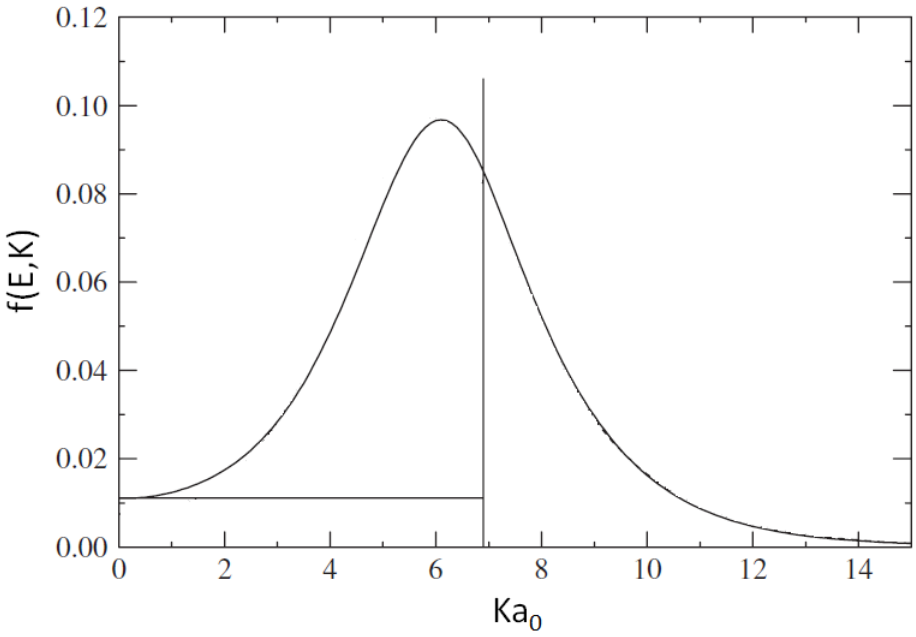

Figure 4.2: Generalized oscillator strength ($f(E,K)$) for Silicon for an energy transfer E of 652.8eV to the 2p-shell electrons, calculated with HermanSkilman potential [277]. The horizontal and vertical line define the PAI approximation. Along with the definitions from Eq. (4.14), P is the momentum transferred by incident particle, $K = P/\hbar$, a_0 is the Bohr radius, $f(E,K) = \frac{me}{2\pi^2 Ne^2}\epsilon_2(E,K)$. Figure taken from [279].

stant, β is the ratio of speed of particle to speed of light in vacuum (the following calculations assume $\beta = 0.95$. A reason is mentioned in Section 4.3), $\Theta = arg\,(1 - \epsilon_1\beta^2 + i\epsilon_2\beta^2)$, and $\frac{d\sigma(E)}{dE}$ is the differential cross-section for energy lost by a incident heavy particle of charge e to an electron inside the substrate, via electromagnetic interactions. The ratio of the differential cross-section with the integrated interaction cross-section gives the probability for corresponding energy deposition within a single collision.

The interpretation of various terms in Eq. (4.15) follows from [272]. The first two terms are referred to as the transverse cross-section. They come from the magnetic vector potential term (in the Coulomb gauge) for which the electric field is transverse

to the direction of virtual photon momentum. For $\epsilon_2(E) = 0$, the $\ln\left(\frac{1}{1-\beta^2\epsilon_1}\right)$ factor is responsible for the logarithmic rise in the cross-section for energy loss, as described in Section 4.2.1. In the similar limit, the second term describes the emission of Cerenkov radiation. The third and fourth terms are known as the longitudinal cross-section. They come from the electrostatic term (in the Coulomb gauge), which has the electric field parallel to the direction of virtual photon momentum. In a nonrelativistic theory, these are the only appearing terms. Since, their dependence on velocity is solely through the $1/\beta^2$ factor, they become effectively constant in the relativistic region. The third term comes from the resonance region while the fourth represents Rutherford scattering from those electrons that are quasi-free for an energy transfer E. For a low density medium the longitudinal cross-section does not depend on either ϵ_1 or density. Although the PAI model is not as accurate as other existent theoretical treatments, its resourcefulness lies in its ease of application for various materials. Fig. 4.3 shows the ratio of energy dependent collision cross-section to Rutherford cross-section, obtained by the PAI model and by a more accurate Betha-Fano theory [277].

The ease of using PAI model can be seen from Eq. (4.15), where only the complex dielectric constant of the medium is needed to obtain the distribution. For the model applied in this dissertation, the data for dielectric constant are obtained from:

- For silicon and germanium, in 0-10eV range, the only available data from [282] is used. However, it is assumed that no energy deposition occurs less than the material bandgap (E_g). $E_g = 1.17eV$ for siliocon, and $E_g = 0.74eV$ for germanium [290].

- For silicon, in 10-30eV, the data from [285] is preferred against [282] because it is more recent, and against [283] as the latter gives negative refractive index

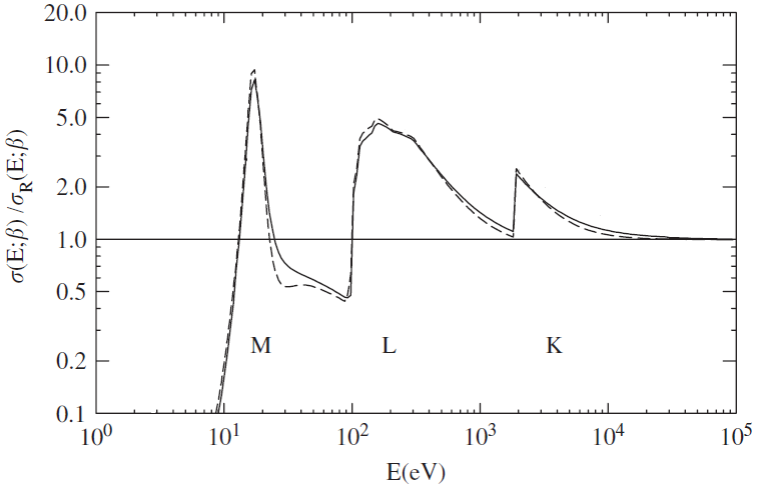

Figure 4.3: The aim of figure is to illustrate the closeness of cross-section estimation obtained from PAI model with those obtained from more rigorous calculations. It shows the ratio of differential collision cross-sections $\frac{d\sigma(E)}{dE}$ to the Rutherford cross-section for single collisions in silicon by particles with $\beta \cdot \gamma = 4$. The solid line is obtained with the a more accurate "BetheFano theory" [277]. The cross-section calculated with PAI model is shown by the dashed line. The different peak correspond to resonant excitation of K, L, M shell electrons. Figure taken from [279].

when applied using Kramers-Kronig relationship [282, 287]. For germanium, in 10-30eV, the more recent data from [285] is preferred against [282].

- For silicon and germanium, in 30-1000eV, the data from [286] is preferred against [283] because the latter produces a result where ratio of differential collision cross-section to Rutherford cross-section does not asymptote to 1 (large energy transfer occur through Rutherford type colllisions, as mentioned in Section 4.2.1).

- For silicon and germanium, above 1keV, the data from [282] is preferred against [283] because the former is more recent and finely binned. The data from [286] is not used because the definition of Eq. (4.14) is as a photoattenuation cross-section, not photoabsorption cross-section.

Fig. 4.4 below shows the energy dependent variation in ratio of differential cross-section to Rutherford cross-section for silicon, obtained from data/methodology employed in this dissertation against a published result [279]. Similar result for germanium is also shown, although no published result to perform a cross-check was obtained.

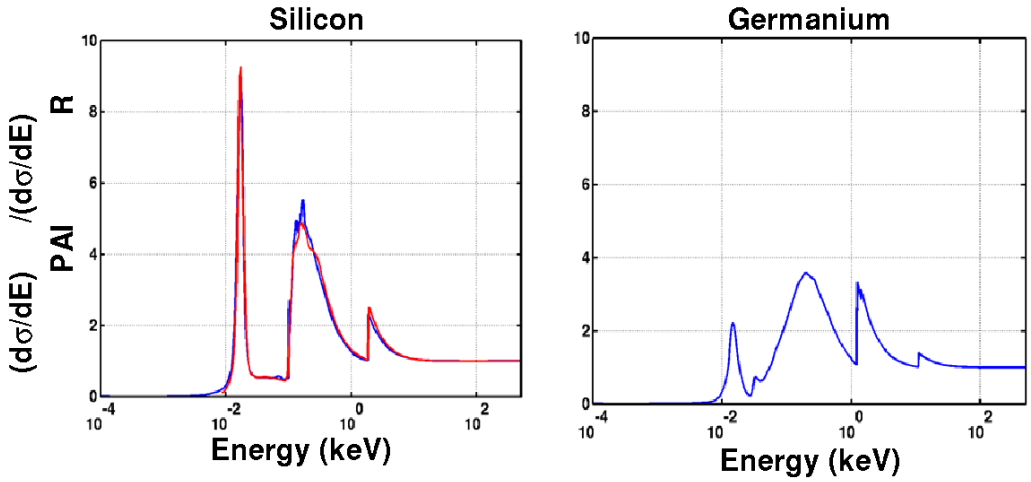

Figure 4.4: The energy dependent variation in ratio of differential cross-section to Rutherford cross-section for silicon obtained in this dissertation (Blue), and cross-checked against published result from [279] (Red). Similar result for germanium are also shown.

4.2.3 Fluctuation in Interactions

In addition to the energy deposition process being probabilistic in nature, the total number of interaction encountered by a LIP within the detector substrate also fluctuates. Hence, it is necessary to obtain the probability distribution for the number of interactions incurred as LIPs passes through a detector substrate. Additionally, it is also required to model the effect of these fluctuation on the total energy deposited by LIPs in the substrate.

Following [279], the probability for occurrence of N-interaction as a LIP passes through a substrate (vertically, or at a different angle, shown in Eq. (4.17)) is modeled as a Poisson distribution, with mean number of interactions dependent upon the fractional charge of LIP, the total collision cross-section for a LIP to experience an interaction and effective length traveled by LIP inside the substrate (depends on both the substrate thickness and the polar angle of incidence, shown in Eq. (4.16).

$$m_{intr}(f,x) = \left[\frac{N_A \cdot Z \cdot \rho}{m_{mol}} \int_0^{E_{max}} \left(\frac{d\sigma(E;f)}{dE}\right) dE\right] \cdot t/cos(\theta) \tag{4.16}$$

$$N(f,x) = \frac{m_{intr}^n}{n!} e^{-m_{intr}} \tag{4.17}$$

where definition of Eq. (4.12) follows, and N_A is the Avogadro number, m_{intr} is the mean number of interactions experienced by LIPs as it passes through a detector of thickness t-cm, atomic number Z (14 for silicon, 32 for germanium), density ρ-g/cm^3 (2.33g/cm^3 for silicon, 5.323g/cm^3 for germanium [291]), molar mass m_{mol}-g/moles (this is same as mass number, 28.0855g/mol for silicon, 72.64g/mol for germanium [292]), collision cross-section $\left(\frac{d\sigma(E;f)}{dE}\right)$ and at a polar angle θ-radians, traveling an effective length of $x = t/cos(\theta)$-cm inside the detector. The term in [] is the mean number of interaction within 1cm ($5.98 \cdot 10^6$ for silicon and $1.42 \cdot 10^7$ for germanium). The probability distribution for actual number of interactions experienced by LIPs is given by $N(f,x)$.

Following [279] again, the probability for a certain energy deposition after exact N-collisions, $P_{Det,N}(E)$, is simply the N-convolution of the probability spectrum for energy deposition in a single collision, $P_{Det,N=1}(E)$, and is shown in Eq. (4.18) (as mentioned in Section 4.2.2, the probability for certain energy deposition within a single collision, $P_{Det,N=1}(E)$, is given by the ratio of differential cross-section to the

integrated cross-section). Fig. 4.5 shows the variation of energy deposition probability as the LIP undergoes different number of interaction with the a detector substrate.

$$P_{Det,N}(E) = P_{Det,N=1}(E) * P_{Det,N=1}(E) * P_{Det,N=1}(E) \ldots \quad N - times \tag{4.18}$$

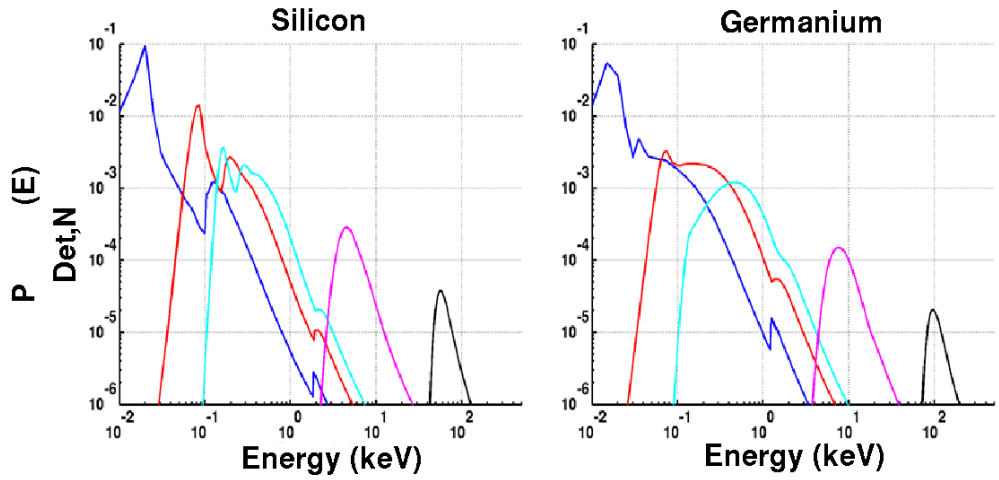

Figure 4.5: The variation of energy deposition probability by massive particle of charge e inside silicon and germanium substrate for various interactions: 1 (blue), 5 (red), 10 (cyan), 100 (magenta), 1000 (black).

By combining the definitions in Eq. (4.17, 4.18, 4.9), one obtains the total probability for certain energy deposition E, as a LIP of given fractional charge fe passes through a detector at a polar angle θ.

$$P_{Det}(E, f, \theta) = \sum_{N=0}^{\infty} N(f, x = t/cos(\theta)) \cdot P_{Det,N}(E) \tag{4.19}$$

Employing the results from PAI model and Eq. (4.19), one obtains the probability for LIPs to deposit energy in detectors. Result for specific examples are shown in Fig. 4.6.

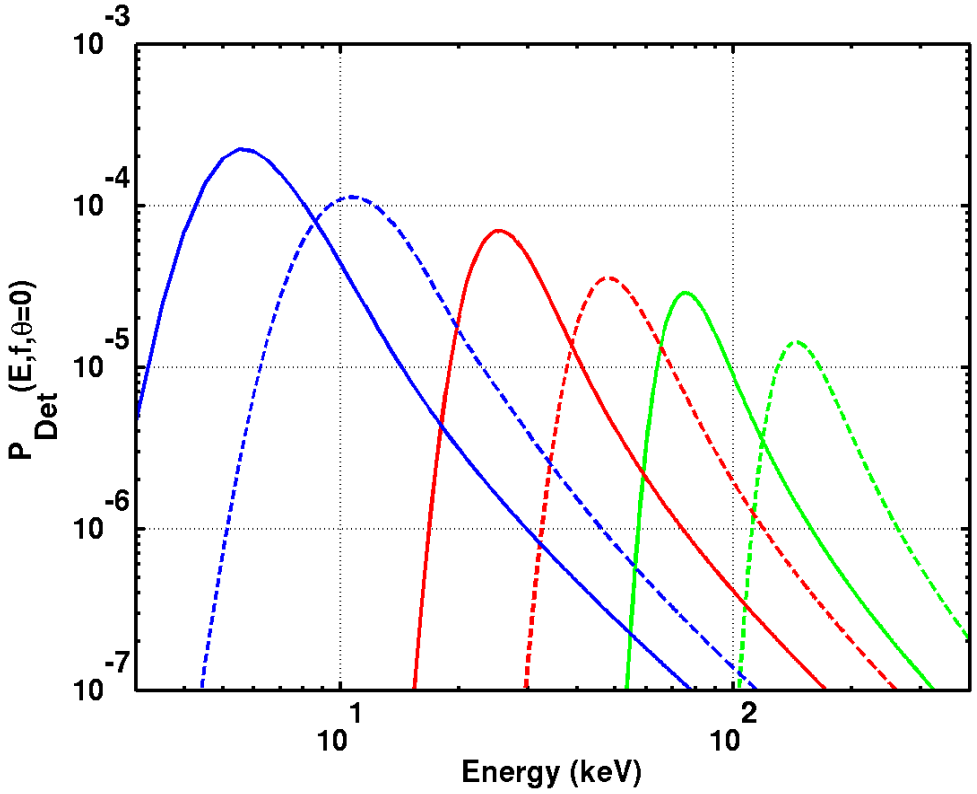

Figure 4.6: Energy deposition probability by LIP of fractional charge fe, for f=1/6 (green), f=1/10 (red), f=1/20 (blue) in silicon (solid) and germanium (dashed) detectors of 1cm thickness. The LIPs are vertically incident on the detectors, i.e.θ=0/

4.2.4 Detector Resolution and LIPs Energy Measurement Probability

As mentioned in Section 4.1.4, and described by Eq. (4.8), the energy deposition measured by detector is similar to the energy deposited by LIPs, up to the detector energy resolution. For LIPs analysis, the half of total phonon energy if used as

estimator of energy deposited in detectors (defined later, in Section 4.4.5 and Section 4.5.3). This energy dependence of CDMS detector resolution ($Reso_{Det}(E_{Mes})$, as defined in Eq. (4.8)) is characterized as [136]:

$$Reso_{Det}(E_{Mes}) = \sqrt{A_1 + A_2 \cdot E + A_3 \cdot E^2} \tag{4.20}$$

where A_i are free parameters, and E is the recoil phonon energy. The constant term corresponds to the detector noise resolution when no energy is deposited. The term $\propto \sqrt{E}$ is associated with (not-quite-Poisson) fluctuations in the number of phonons and charge carriers produced during an interaction of a given energy (the Fano factor [281]), and guides the resolution variation for energy deposition $\sim 10-100keV$. The third term $\propto E$ is the result of the fluctuation in phonon estimate from template-based pulse-fitting method.

A_1 is easily obtained by studying the energy distribution corresponding to noise pulses, shown in Fig. 4.7. The results for zero-energy detector resolution is given in Table 4.1. A_1 is simply the square of the noise-width values.

A_2 is obtained by studying the resolution of 10.36keV in various germanium detectors used in LIPs analysis, assuming $A_3 = 0$ (typically $A_3 \lesssim 0.03$ [136]) and subtracting the effect of A_1 (^{71}Ge is produced by thermal neutron capture during neutron calibrations and decays by electron capture to ^{71}Ga with a half-life of $\sim$11 days. Most of the time, this decay proceeds via capture of a K-shell electron, followed by emission of 10.36 keV of energy in x-rays and Auger electrons [239]). A_2 estimation for different germanium detectors used in LIPs analysis is presented in Table 4.2. For LIPs analysis, a conservative estimate (allowing largest resolution) of $A_2 = 0.05$keV is chosen, and the same number is also used for applied to silicon detectors (because there are no 10.36keV lines in silicon).

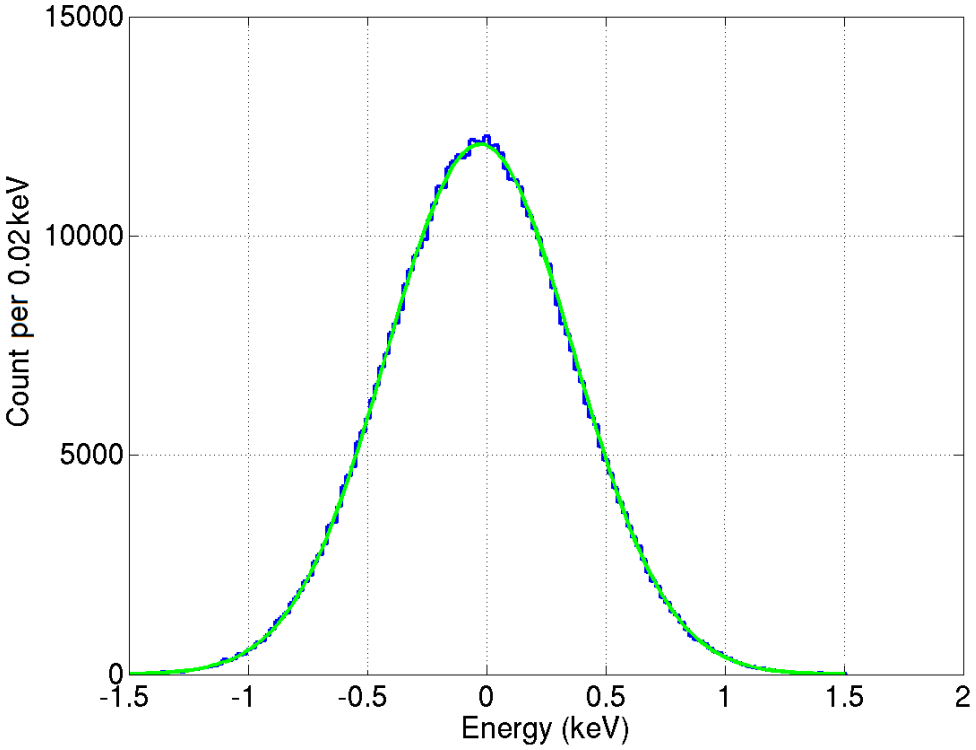

Figure 4.7: Obtaining detector noise by study of noise pulses. The figure shows results from one of the detectors used for LIPs analysis, T4Z1. The noise behavior is assumed to be same for a detector through different runs, but different from others for each detector. For this detector, the total phonon noise pulses correspond to an energy level of 0.03±0.55keV for 1σ width. However, LIPs analysis defines deposited energy as half of total phonon energy, and noise in corresponding measurement would be 0.01±0.28keV. Figure taken from [288].

A_3 estimation is done by asserting that the variation of electromagnetic recoil yield band at high energies is only due to resolution in phonon estimation:

$$\Delta E_{phonon} = E_{phonon} \cdot \Delta Y \tag{4.21}$$

Table 4.3 shows that almost every detector can be conservatively asserted to have a yield-based resolution of ∼15keV at 200keV(silicon)/400keV(germanium). This result provides an estimates of $A_3 = 0.0054$ for silicon detectors and $A_3 = 0.0013$

Table 4.1: Phonon noise in various detectors used for LIPs analysis, corresponding to zero energy deposition. Results taken from [288].

Detector Name	Noise (Mean$\pm 1\sigma$ width; keV)
T2Z1	0$\pm$0.09
T2Z2	0$\pm$0.06
T2Z3	0$\pm$0.26
T2Z4	0$\pm$0.07
T2Z5	0$\pm$0.15
T2Z6	0$\pm$0.07
T4Z1	0.01$\pm$0.28
T4Z2	0$\pm$0.34
T4Z3	0$\pm$0.06
T4Z4	0$\pm$0.28
T4Z5	0$\pm$0.26
T4Z6	0$\pm$0.41

Table 4.2: A_2 estimation for different germanium detectors used in LIPs analysis, using measured width of 10.36keV line, Eq. (4.20), results from Table 4.1. Results taken from [289].

Detector Name	Resolution (keV)	$A_2(keV)$
T2Z3	0.39	0.01
T2Z5	0.47	0.02
T4Z2	0.72	0.04
T4Z4	0.67	0.04
T4Z5	0.57	0.03
T4Z6	0.65	0.03

for germanium detectors. It should be noted that the ionization yield is dependent upon both charge and phonon measurements. Thus, by asserting that the variation in yield is only due to phonon resolution, one obtains a "larger than actual" resolution estimation. Also, this procedure cannot be used to determine resolution at low energies (i.e. in determination of A_1 and A_2). This is because at low energies the yield measurements ae extremely influenced by charge noise, and one gets unnaturally

high values of resolution.

Table 4.3: Yield based resolution for different detectors and runs used in LIPs analysis, reported at corresponding analysis threshold for the detector (200keV for silicon, 400keV for germanium, as discussed in Section 4.5.4). Results taken from [305]

Detector Name	R125	R126	R127
T2Z1	16.03keV	-	-
T2Z2	14.16keV	-	-
T2Z3	14.55keV	-	-
T2Z4	13.57keV	-	-
T2Z5	9.86keV	-	-
T2Z6	11.92keV	-	-
T4Z1	10.83keV	13.43keV	10.90keV
T4Z2	8.05keV	10.88keV	8.32keV
T4Z3	12.88keV	12.80keV	11.98keV
T4Z4	15.15keV	9.36keV	8.66keV
T4Z5	12.83keV	17.87keV	8.80keV
T4Z6	10.33keV	9.81keV	11.07keV

The detector resolution is convoluted with LIPs energy deposition probability to obtain the probability for energy measured by detector as LIPs of a certain fractional charge passes through it. An example illustrating the difference between the two (for a specific case) is shown in Fig. 4.8.

4.3 Defining Basic LIP Characteristics

This section describes the basic characteristics implied on to LIPs, either to facilitate the analysis, or simply by choosing to use the PAI model for describing the energy loss by LIPs.

To perform a search for LIPs using CDMS detectors, it is necessary that the particles have sufficient energy to reach the underground detectors. Thus, the LIPs are required to be:

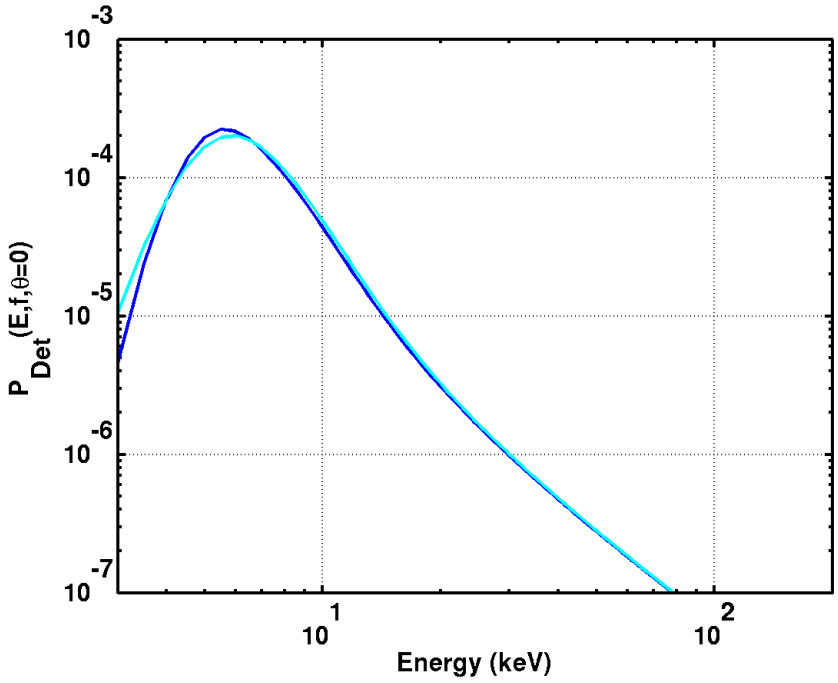

Figure 4.8: The change in LIPs energy deposition curve (blue) for f=1/20 passing through 1cm silicon detector at θ=0 after convolution it with energy dependent detector resolution (cyan), corresponding to ($\sqrt{A_1}$=0.41keV, A_2=0.05keV, and A_3=0.0054).

- Relativistic: Unless the LIPs have large energy, they would not be make it through the large rock overburden over the detectors. Additionally, slow LIPs will also have higher energy loss per unit length, as shown in Fig. 4.9. As a possible source for relativistic LIPs, it is suggested that they are cosmogenic and produced by interaction of cosmic rays in upper atmosphere. For similar reason, it is asserted that only downward gong LIPs are detected, i.e. there are no LIPs formed inside Earth and traveling upwards towards atmosphere.

- Massive: Despite being relativistic, the LIPs will be substantially deflected through successive collisions within the rock overburden, reducing the probability for them to arrive at the CDMS detectors. Since CDMS does observe

cosmic muons, it is asserted that the LIPs should be as massive or more massive than muons.

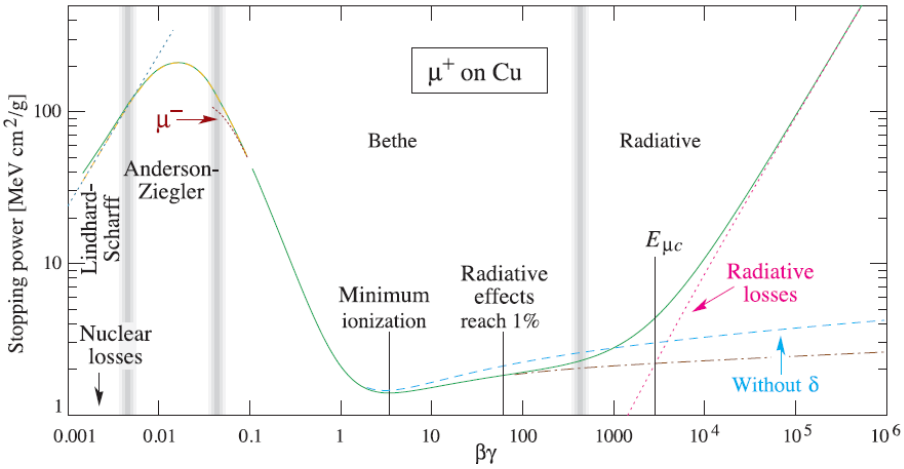

Figure 4.9: Stopping power (= $\langle dE/dx \rangle$) for positive muons in copper as a function of $\beta \cdot \gamma$ over nine orders of magnitude in momentum (12 orders of magnitude in kinetic energy). For the analysis purposes, LIPs are considered minimum ionizing. Figure taken from [14].

In choosing to employ the PAI model to describe the energy deposition probability as the LIP interacts with the substrate, the assumptions inherent in the PAI model are applied to the LIP. The assumptions are:

- The energy and momentum transferred to the electron (in the substrate) in a single collision is much less than the energy and momentum of the LIP.
- The speed of incident LIP is much larger than the orbital speed of electrons in the substrate. This assumption also unnecessitates the application of "Shell corrections", or "Barkas corrections" applied to the Bethe Equation [278].

- By choosing to use the PAI model to uniquely describe the interactions between the LIPs and the substrate, it is implicit that the LIPs only have electromagnetic charges and that their incident flux on detectors are so low that no more than one LIP strike the CDMS detectors at a time. This assumption may be questioned by realizing that the LIPs are cosmogenic in nature, and if two LIPs with small fractional charge are simultaneously produced, they may be capable to simultaneously arrive and strike multiple towers (the low fractional charges prevent their flux from diminishing off as they travel from surface to the CDMS detectors installed underground). Currently, the analysis assumes that this is not the case. Future studies may be performed to quantify the probability for such an occurrence (mentioned in Section 4.6).

The above two criteria are automatically satisfied by requiring LIPs to be relativistic, as mentioned earlier.

From Eq. (4.3), one notes that the reported LIP flux ($I_v^{90}(f)$) increases as the cross-section ($\sigma(f)$) decreases. It is desirable while performing the analysis that the most conservative flux value is reported which can be improved upon by future, more sensitive analysis. Under this ideology, one should choose the minimum possible cross-section for relativistic LIPs that occurs when the particles are minimum ionizining, as shown in Fig. 4.9. For the analysis presented in the dissertation, the LIPs are assumed to have $\beta = 0.95$, and $\beta \cdot \gamma = 3.04$.

Previous studies on LIPs flux, by MACRO collaboration [10] places strict constraints for LIPs of frctional charge $e/6 < fe < e$. Since the detector mass employed by CDMS is much less than that employed by MACRO, any study for $fe > e/6$ will be non-competitive with the limits set by MACRO. SO, the current dissertation performs a search for LIPs in range $e/200 < fe < e/6$.

4.4 CDMS Installation and LIPs Analysis

The possibility to use the data from CDMS-II experiment to serach for LIPs is mainly due to the setup of CDMS experiment, including, the arrangement of detectors in a vertical stack. This section lists various features of the CDMS-II experimental setup and their effects on corresponding aspects of LIP analysis. A detailed description of the CDMS-II experimental setup is provided in Appendix I.

4.4.1 Underground Operation

The CDMS-II experiment is located in the Soudan Underground Laboratory (SUL) in northern Minnesota. The lab is on the 27th level, at a depth of 714 m below the surface. The rock overburden at the SUL provides a reduction in cosmic ray flux that is equivalent to 2090 meters of water overburden, reducing the muon flux by a factor of $5{\cdot}10^4$ relative to the flux at the surface. Thus, the possibility to obtain an event due to interaction with cosmic muon, either directly or indirectly (cosmic muons interacting with the materials surrounding the detectors and creating energetic particles through muon-induced nuclear disintegration or muon-induced hadronic and electromagnetic showers) is extremely diminished. It is mentioned in Section 4.3 that the LIPs being search for in the analysis are cosmogenic in origin. However, unlike muons, their reduced electromagnetic charge allow for a higher probability for them to reach the detectors, and be detected. Thus, the underground operation of CDMS-II experiment does not precludes its ability to observe LIPs, if they exist. It also benefits the search effort by preventing unnecessary triggering of detectors by cosmic muons (if the muon flux would have been higher).

4.4.2 Active Shield (Veto)

The CDMS-detector are all-covered with layers to shielding to avoid unnecessary triggering of detectors from background radioactivity. The outermost layer of shielding in a scintillation panel connected to photomultiplier tubes, and creates a huge signal when a muon, or a particle of charge e passes through it (losing energy in the scintillation panels). Since LIPs are fractionally charged and have a charge between $e/200$ and $e/6$ (as mentioned in Section 4.3), they create a much weaker signal inside these panels. This criteria is used to an advantage in the LIPs analysis, by rejecting events where the scinitillator panels shown a high energy deposition which is extremely unlike of the LIPs being studied. This also removes unnecessary muon-induced events (like production of energetic neutrons, hadronic and electromagnetic showers).

It may be debated whether application of such a criteria may not be valid because both the LIPs and muons are cosmogenic in nature and are highly likely to be simultaneously produced. Hence, it is very likely that they may be simultaneously incident on the detector. In such a case, rejecting events with large veto signal (indicating presence of muons) will inadvertently remove all valid LIPs signal. This argument is refuted on the basis that the LIP flux incident on detector would not be as suppressed as muon flux, due to their reduced fractional charge. Hence, it is likely to observe LIP signal but not a simultaneous muon signal which got suppressed before reaching the detectors. Thus, using this criteria does not preclude the ability to observe LIP signals in the analysis.

Another interesting scenario is when the LIPs are themselves pair-produced from the cosmic-muons. In such a case, rejecting the incidence of muons will inherently remove the corresponding LIPs from being analyzed. Although, this is a possibility,

it is not the only possibility to obtain LIPs. The mechanism of pair-production (from high energy gammas formed in upper atmosphere) is another source to obtain LIPs which can be detected by CDMS detectors.

4.4.3 Passive Shield

The layers of polyethylene and lead suppress the radioactivity levels experienced by the detectors. This is useful to prevent triggering of detector by these unnecessary events which may other swamp a valid signal due to interaction of LIPs with the detectors. Additionally, the probability for a LIP to get stopped within the passive shielding is negligible. Thus, while preventing backgrounds, the passive shielding does not affect the occurrence rate for possible signals.

4.4.4 Cryogenic ZIP Detectors

The sensitivity and low noise of cryogenically operated ZIP detectors allow detection of small signals, i.e. interactions where very less energy is deposited in the detectors. This is one of the main factors which make it possible to search for LIPs using CDMS-II data even though the LIPs inherently deposit small energy in the detectors (due to their fractional charge).

4.4.5 Electromagnetic Recoil Type Events

LIPs interact electromagnetically with the silicon/germanium crystal (via their electronic charge). It is discussed in Section 3.3.1 that such events create a phonon signal as large as the ionization signal, excluding contributions from Luke phonons which are also of similar strength as the ionization signal. Hence, in performing a LIPs search, one may assert that the recoil phonon energy is simply the half of total phonon energy (which includes contributions from both recoil and Luke phonons). Such a definition unnecessitates the requirement of using both the ionization and

total phonon energy of an event to reconstruct the recoil phonon energy (as described in Eq. (3.9)), and is helpful to obtain a recoil energy estimate without it being influenced by charge noise (specially when a low energy is deposited in detector and the charge measurements from detector are extremely influenced by charge noise).

Surface events (Section 3.3.3) may be considered as an exception to above rule, where an event has an improper charge collection and the ionization yield for the event is not 1. This also reduces the contribution of Luke phonon to total phonon energy. In such a case, asserting that recoil phonon energy estimate is half of total phonon energy overestimates the Luke contribution and underestimates the actual recoil recoil phonon energy deposited by LIPs in the substrate. However, such events are confined to only $\sim$10-20μm from the substrate surface [239], and it is $\sim$98% probable that LIP interaction in each of the 6 ZIP detectors does not occur within the dead layer.

4.4.6 Detection Thresholds for ZIP detector

It is required that a valid LIP-induced event deposits sufficient energy in the detector to ensure that the event is not caused by noise-induced fluctuations. This is done by requiring a valid event to have an energy deposition above a certain lower limit, or lower analysis threshold. An upper threshold estimation is influenced by the fact that detector properties and calibration (Appendix H.6) should be properly known within the bounded energy interval used for the analysis. This guides the decision to set the upper threshold for detectors fabricated on germanium substrate, where the calibration up to $\sim$400keV exist (using decay lines from ^{133}Ba). Additional analytical considerations influencing the analysis thresholds are described in Section 4.5.4.

4.4.7 Arrangement of ZIP Detectors as Towers

The vertical stacking of ZIP detectors, as towers, is the most crucial feature of the CDMS experimental setup that allows construction of multiple discriminators to select valid LIP-induced signals from possible backgrounds. The construction of these discriminators also employ the assertion that the LIPs being searched for in the analysis are relativistic and massive, and have an incident energy much higher than energy deposited in each detector (as mentioned in Section 4.3). The following discriminators are constructed:

- Being massive, a LIP interacts with all detectors in the tower. Thus, if one or more detectors do not have sufficient energy deposition (over and above the detector noise), then the event is more likely to be caused by backgrounds. In the analysis, this is referred as "Multi-detector Hit" criteria.

- Since the LIP is relativistic, it traverses the stack of detector almost immediately. Thus, a valid LIP-induced event should be such that the event occurrence time in all detectors of the tower should occur close to each other. In the analysis, this is referred as "Start-time" criteria.

- The energy deposited by a LIP in each detector is much less than its incident energy. It may be approximately stated that their energy (and speed) does not change even when they interact with a detector. From Eq. (4.15) in Section 4.2.2, it is inferred that the energy deposition probability for a relativistic LIP depends on the its speed (other factors held constant). Since the speed of LIP does not change, it interacts with multiple detectors of a towers in an independent manner, i.e. the probability for LIP to deposit certain energy in a detector is independent of energy deposited by it in previous detector. Thus,

the distribution of physical energy deposited by LIP in different detectors of a tower should follow the probability distribution for LIP to deposit energy in a single detector. In the analysis, this is referred as "Energy Consistency" criteria.

- Since the energy lost in each detector is much less than energy of the LIP, it travels through the detectors in a straight line. Thus, if the locations corresponding to event occurrence in different detectors of a tower appear to not fall in a straight line, then the event is more likely to be caused by backgrounds. In the analysis, this is referred as "Track Linearity" criteria.

4.4.8 Electronic Glitches

"Electronics glitches" denote a broad class of events which are generated by the readout electronics rather than by particle interactions in the detectors. In seaching for low energy LIP recoils, the phonon glitches (i.e. non-zero phonon signal and a charge signal consistent with noise) form a major background to the analysis because they affect all the detectors simultaneously, causing them to report a non-zero, low-value phonon signal. However, it is observed that whenever these glitches affect all detectors of a tower, they are also severe enough to effect detectors in other towers. Employing an assumption that the flux of LIPs incident on the set of multiple towers is low enough that not more than 1 LIP strike it at one time, one may reject the glitch events by requiring that only the detectors in one tower (the one being analyzed for LIPs) show non-zero energy deposition and the others have signal consistent with noise. Such a criteria rejects occurrence of glitch events which tend to strike multiple towers simultaneously.

4.5 LIPs Search Analysis

This section describes the actual analysis done on the data recorded from July 2007 to September 2008 by CDMS collaboration [11], separated by full or partial warm-ups of the dilution refrigerator to address corresponding cryogenic issues. Each of the runs lasted from 2-6 months, and are denoted as cryogenic runs 125-127, or, R125-127. This sections introduces the detectors used in LIPs analysis and presents the statistical definitions corresponding to the various physicality arguments, mentioned above in Section 4.4, allowing a search for valid LIP induced events amongst other background-induced events. Some of the criteria select whether the characteristic of event observed in a single ZIP detector is consistent with that of LIP, while other determine whether the collective behavior of events observed in 6 ZIP detectors of a tower qualify it as occurring due to LIPs. Since there is a chance that these criteria mistakenly tag a valid LIP-induced event as a background, they are also attributed a corresponding "LIP detection efficiency". Finally, using the formulation developed in Section 4.1 and the results for energy deposition probability (using PAI model, described in Section 4.2.2), the corresponding result on LIPs flux, $I_v^{90}(f)$, is presented.

4.5.1 LIP-Detector Selection

It is mentioned above that data from cryogenic runs R125-127 are used in the current analysis. Even amongst these runs, it is not that the data from all the towers (vertical stack of 6 ZIP detectors) are employed for LIPs analysis. Only the towers where all 6 ZIP detectors are functioning normally and not known to have any issues with phonon and charge collection are used for the analysis [280] (the collection of these 6 ZIP detectors of a tower forms a LIP-detector). This is done because one of the requirements of a valid LIP signal is that it should interact and deposit energy in

all 6 detectors of a tower (described in Section 4.5.6). These are Tower 2 and Tower 4 for R125, and Tower 4 only for R126-R127. The 6 ZIP detector in Tower 2 are labeled from T2Z1 to T2Z6. The 6 ZIP detector in Tower 4 are labeled from T4Z1 to T4Z6. Details on their physical properties are mentioned in Section 3.5.

4.5.2 Bad Detector Time

Appendix G.2 mentions that as the detectors are operated, trapped charges start to form within it that reduces the ability of the detectors to properly measure an ionization signal. For this reason, the data collected by detectors within are single run exist as a collection of multiple time intervals after which the detector was neutralized. Each of these periods of contiguous of data collections within a single cryogenic run is called a "series". There are certain detector-specific data-series when the data collected from the corresponding "properly behaved" detector may instead be unsuitable for performing a LIPs analysis. The criteria defining these series with improper data-collection, or "bad-series", are collected to form a "cut" and "applied" on the entire dataset (comprising of all the series within a run). It prevents the events in the bad-series from being analyzed. The data used for performing the analysis belongs to the series which is simultaneously not part of bad-series for each of the 6 detectors, i.e. when none of 6 ZIP detectors of a tower are experiencing a poor data collection. A description of these criteria is referred from [228, 230, 231, 239], and mentioned below. After removing the period of bad detector operation, it is found that the active operational time for Tower2 is 59.52 days, and for Tower4 is 142.44 days.

4.5.2.1 Series-to-series Detector Stability

Using Kolmogorov-Smirnov tests, each data-series is tested with a sample of 30 "known, good" data-series, and is rejected if the corresponding deviations are

statistically significant.

4.5.2.2 Event Triggering

A LIP induced event should not be the one where it was the DAQ generating the trigger (done randomly to monitor detector noise). Such events are removed. Additionally, a handful of events for which the trigger history is incorrectly recorded by the DAQ, or, when the trigger was inadvertently disabled, or, when the trigger rate is >0.7Hz over 100 consecutive non-random events; such events are removed. Event triggering was also increased for events collected from December2007-January2008 for R125, and July-August2008 for Run 127 due to leakage of helium and formation of helium film over the detectors. These events are also rejected.

4.5.2.3 Stable Detector Biasing

Periods of data collection before the QET have been properly biased, or when the trigger thresholds are non-optimal are removed. Improper QET bias implies that the TES are being operated at a non-optimal point and the detector is not at its highest sensitivity. A "less than optimal" trigger threshold causes the detectors to be triggered by noise fluctuations. A "higher than optimal" trigger threshold causes the detectors to miss valid particle interactions depositing low energy in the detector. Additionally, periods with poor biasing of charge channels are also removed.

4.5.2.4 Poor Noise Performance

Isolated periods of time where the readout noise for the charge or phonon channels for a given detector is abnormally high are removed. It includes removal of the data series from each run where the amplitude or timing resolution for the phonon signal is >25% higher than the median resolution, or, the time periods within a single data-series where the ionization energy resolution is different from the mean resolution

by more than 4σ, or where a significant rate of charge-only electronics glitches are observed (As mentioned in Section 4.4.8, it is the phonon glitches which are a major background to LIPs analysis, not charge glitches. The latter are thus removed). Additionally, the data-series with phonon and charge noise different from detector noise (averaged over entire run) by more than 3 standard-deviation are removed.

4.5.2.5 Bad Detector Regions

Certain detectors had readout problems with a single phonon channel or portion of their ionization electrodes but still allowed events interacting far from the location of the malfunctioning sensors to be used. Thus, the events falling in the "bad detector regions" are removed.

4.5.3 Recoil Energy Estimation

Following the above discussion from Section 4.4.5, the quantity used to estimate the energy deposited by LIPs inside the detector is half of the total phonon energy. It is mentioned in Appendix H.7 that position and energy dependent variations in responsivity of the TES (used to measure phonons) needs to be normalized out to obtain the correct estimation corresponding to energy deposited in the detector. However, for energies $\lesssim$10keV, the correction routine no longer improves the resolution, and the analysis uses uncorrected phonon energy estimates (obtained directly from the detector).

4.5.4 Analysis Thresholds

In the LIPs analysis, only phonon energy (half of deposited total phonon energy) is used to estimate the energy deposited in a detector. To ensure that the event is not caused by noise-induced fluctuations, it is required that a valid LIP-induced event deposits sufficient "phonon" energy which cannot be attributed to noise-induced

fluctuation with a confidence of 6σ or more. This forms a lower threshold for the analysis. The maximum 1σ noise width in any detector used for LIPs analysis is 0.41keV (from Table 4.1). Thus, a lower threshold of 2.5keV is chosen for the analysis.

The LIPs analysis also employs an upper energy threshold, i.e. events with energy deposition above a certain limit are not considered for the analysis. The determination of this upper limit, or, upper threshold is guided by 2 main factors:

- Calibration of phonon signal (Appendix H.6)in detectors made on germanium substrate are done up to 380keV, using the events induced by corresponding line in ^{133}Ba-calibration dataset. Thus, it may be assumed that these detectors are calibrated up to 400keV, which is the upper analysis threshold for corresponding detectors. Average energy deposition in silicon crystals due to electromagnetic interactions tend to be half as much as energy deposited in germanium crystal [14]. Thus, an upper analysis threshold of 200keV is used for detectors fabricated on silicon substrate.

- From the results of PAI model, it is found that the probability for LIPs to deposit energy within the lower and upper analysis threshold (as described above) forms $\gtrsim$90% of the probability for LIPs to deposit energy above the lower analysis threshold. An example is shown in Fig. 4.10.

4.5.5 Trigger Efficiency

A detector may fail to register an event if the warm electronics does not consider the event to be "significant" enough to create a trigger (Appendix I.5). This happens if the detector trigger thresholds are set at a high limit, or simply due to noise induced variations causing an improper reconstruction of a low energy signal to even lesser energy. This introduces a probability, or efficiency for valid LIP-induced events to be measured by the detectors, and is called as "LIP trigger efficiency".

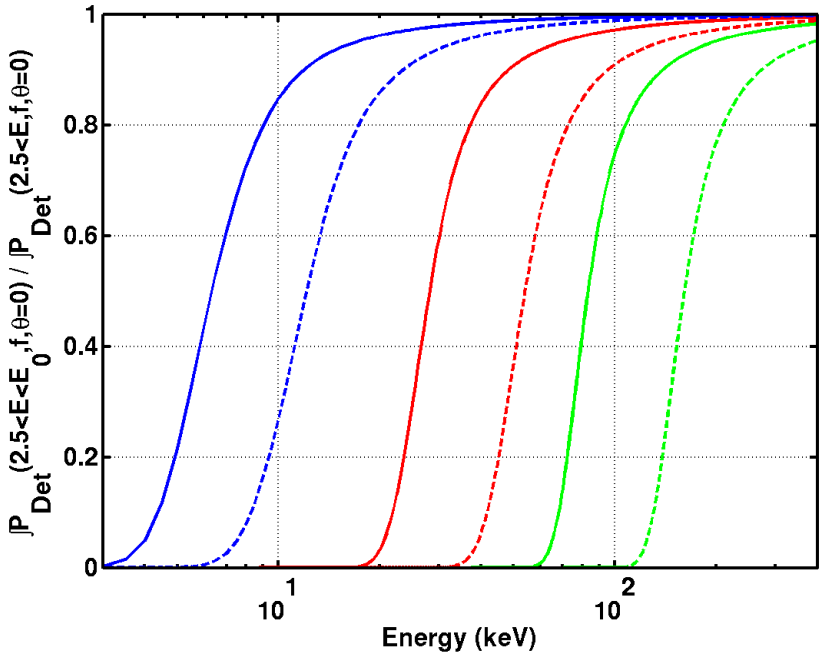

Figure 4.10: For both silicon (solid) and germanium (dashed) detectors of 1cm thickness and an incidence of LIPs of f=1/6 (green), f=1/10 (red), f=1/20 (blue) at θ=0, 90% or more or probability to deposit energy above the lower analysis threshold (2.5keV) occurs within 200keV (silicon), or 400keV (germanium).

Since a valid LIP event must interact with all 6 ZIP detectors of a tower (described next in Section 4.5.6), it is required for at least one detector to trigger to the energy deposited by the LIPs. Once a trigger is generated, the readings in each of installed ZIP detectors are automatically recorded. Thus, the LIP trigger efficiency is when none of the detectors create a trigger.

For CDMS detectors, it is known that the detector T2Z4 (in Tower 2) and T4Z3 (in Tower 4) have perfect triggering up to 2keV (for runs R125-R127) [298]. Therefore, imperfect triggering does not contribute to inefficiency in LIP detection, i.e. LIP trigger efficiency is 1.

4.5.6 Multi-detector Hit and Miss Criteria

The photons (γ-rays) from from nuclear decays occurring in the shielding and in the supporting structures contained within the shielding are the primary sources that induce events in the CDMS detectors. From a Monte Carlo study of CDMS detectors, it is found that the photons (from nuclear gamma decays) mostly strike one or two CDMS detectors only. However, there is a very small chance that either single high energy photon hits all ZIP detectors in one tower, or, two or more coincident photons hit different set of ZIP detectors comprising a tower; while the energy deposited in each detector is within the analysis thresholds. Due to a shear reduction in the possibility for observing simultaneous energy deposition in multiple detectors of a tower by γ-rays, and the criteria being easily satisfied by a relativistic LIP; it is used to identify valid LIP-induced events against possible backgrounds.

The analysis also assumes that the incident LIP flux is low enough that no more than 1 LIP strikes the CDMS experiment at a time. Thus, it is required that no other detectors (except the ones being used for LIPs analysis) show a substantial energy deposition beyond "noise induced fluctuations". This is defined by requiring that energy measured in "other" detectors be consistent with noise within 3σ, where σ is the variation in reconstructed energy associated with detector noise. However, it may be that simply due to noise-induced variations, one of the detectors (not analyzed for LIPs) show a high energy deposition and cause a rejection of an otherwise valid event. This introduced a LIPs-detection efficiency for each tower; an efficiency of 0.9838 ± 0.0003 for Tower 2 in R125, 0.9823 ± 0.0002 for Tower 4 in R125, 0.9815 ± 0.0004 for Tower 4 in R126, 0.9755 ± 0.0005 for Tower 4 in R127.

Fig. 4.11 shows the distribution in counts of γ-induced event with simultaneous energy depositions in one or multiple detectors of a tower, while requiring that other

detectors do not measure substantial energy deposition (above noise levels). Additionally, it is found that the rate of occurrence of simultaneous energy deposition in 6 ZIP detectors (of one tower) from interaction with two separate γ-rays is suppressed by a 6 order of magnitude in comparison to the same occurring due to interaction of all detectors with a single, high energy γ-ray. The energy distribution of γs simultaneously interacting with 6 ZIP detectors of Tower 2 and Tower 4 is shown in Fig. 4.12.

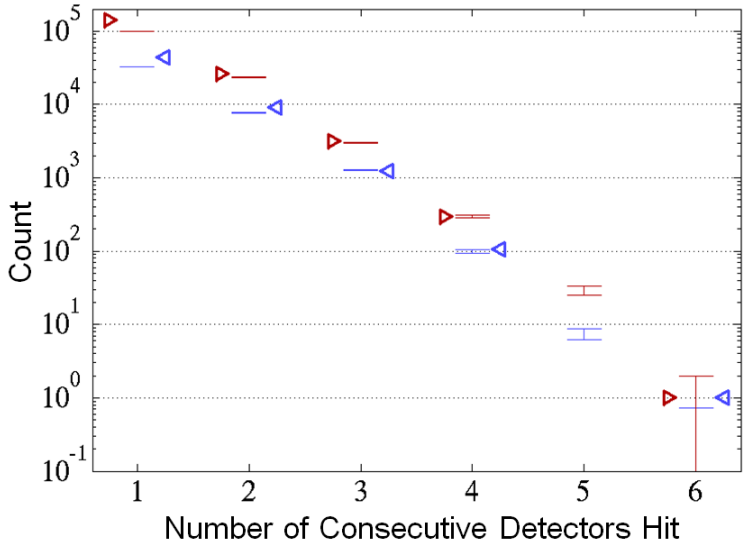

Figure 4.11: The simulated (lines, with error bar) and observed number of events (shifted, diamond) for multiple detector hit due to photon background, shown separately for Tower 2 (red) and Tower 4 (blue). The result for observing simultaneous hits in 5 consecutive detectors is not shown, and may be used for future analysis (Section 4.6). The result for 6 detector hit was obtained only after the entire analysis routine was developed. Figure taken from [293], based on results from [294].

4.5.7 Good Detected Events

While the previous section(Section 4.5.2) describes the period of bad detector operation, not all events within the period of good detector operation have the proper

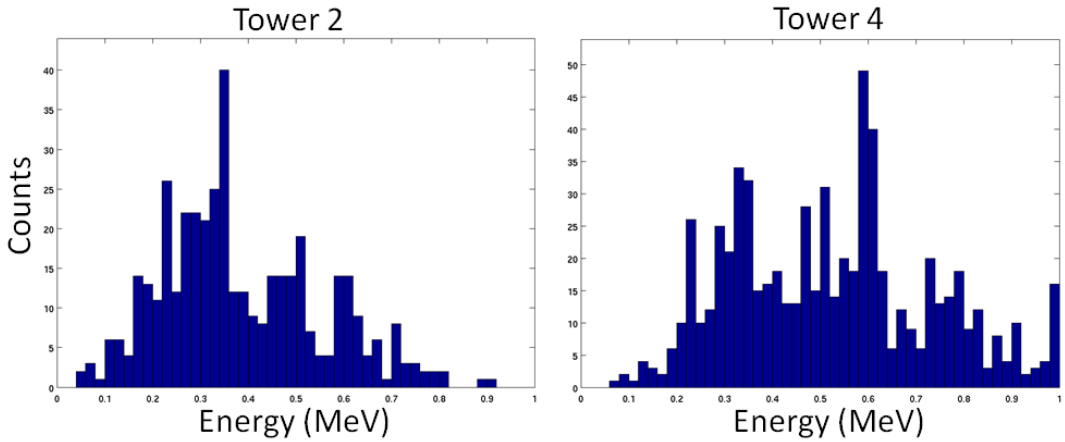

Figure 4.12: The energy distribution of γs simultaneously interacting with 5 or 6 ZIP detectors of Tower 2 and Tower 4. The case for 5 consecutive detector hit is considered because they have very high probability of also causing a 6 detector hit due to statistical fluctuations. Figure taken from [295].

set of characteristics to be used for further analysis, e.g. an improper reconstruction of otherwise valid event. Removal of these events from the analysis imparts an "efficiency", or a probability for the detector to observe valid LIP-induced events (the inefficiency being caused by the probability that valid events are inadvertently removed from the analysis). The following reasons may be attributed to the failure of an otherwise valid event from being considered in LIPs analysis:

- It is natural to expect that before an event is detected, the noise levels in the detector would not be different from an average behavior. Such a criteria may not be met due to occurrence of residual phonon tails from the preceding events, specially, if two events occur in close temporal proximity to each other. These events do not fit the usual phonon template used to determine the energy of the events, and are thereby discarded.

- The charge noise levels for a particular event can suddenly become high due to microphonic pickup from cryocooler mechanical vibrations [231]. Such events

are also discarded.

The efficiency of LIPs detection due to these considerations, for different detectors and runs (R125-R127) used in LIPs analysis is shown in Table. 4.4.

Table 4.4: The efficiency of "Good Events" criteria for different detectors and runs used in LIPs analysis. results taken from [304]

Detector Name	R125	R126	R127
T2Z1	0.8841±0.0005	-	-
T2Z2	0.9992±0.0001	-	-
T2Z3	0.8243±0.0006	-	-
T2Z4	0.9995±0.0001	-	-
T2Z5	0.9891±0.0002	-	-
T2Z6	0.9964±0.0001	-	-
T4Z1	0.9994±0.0001	0.9998±0.0001	0.9999±0.0001
T4Z2	0.9995±0.0001	0.9999±0.0001	0.8251±0.0008
T4Z3	0.9904±0.0002	0.9986±0.0001	0.9991±0.0001
T4Z4	0.9997±0.0001	0.9997±0.0001	0.9999±0.0001
T4Z5	0.9018±0.0005	0.9283±0.0006	0.9292±0.0005
T4Z6	0.9969±0.0001	0.9995±0.0001	0.9998±0.0001

It should be noted that a standard WIMP analysis [11] includes extra considerations which are irrelevant for LIPs analysis. These are described below:

- In a WIMP analysis, the quality ionization-pulse reconstruction by charge optimal filter is assessed by the use a χ^2, calculated on an event-by-event basis. All abnormal events above certain energy dependent value of χ^2 are rejected. This criteria is mainly used for rejecting "pile-up events", i.e. events occurring so close to each other that the charge pulse coincide and is extremely useful in selecting valid events inside ^{133}Ba-calibration data where the event rate is high. However, the event rate in dataset used for LIPs analysis is extremely

low and it is negligible to obtain "pile-up events". Thus, it is not necessary to use the criteria. As an additional benefit, this criteria also rejects otherwise valid low energy events that get rejected due to mismatch of template and the noise-distorted charge pulse.

- In a WIMP analysis, it is enforced that the start time of the "primary" phonon pulse (it is the largest among the traces obtained by 4 phonon channels) lies about the global trigger, within the interval of [-50,+10]μs for germanium and [-25,+10]μs for silicon. Such a criteria rejects low energy signals where the pulse start time is greatly affected by detector noise.

- As mentioned in Appendix G.4, a WIMP analysis requires an event to have substantial ionization collection within the inner charge electrode. This helps to distinguish it against electromagnetic events which produce a large signal in the outer charge electrode. However, by simply requiring that all 6 detectors be simultaneously hit, the low energy electromagnetic background is automatically reduced (discussed in Section 4.5.6). Thus, using this criteria is unnecessary in LIPs analysis.

4.5.8 Active Shield (Veto) Based Rejection

The scintillator "veto" panels surrounding the detectors (Appendix I.2.1) experience an energy deposition of $\sim$10MeV by cosmic muons. However, owing to its reduced fractional charge, a LIP with fractional charge of *e/6* or less will deposit an average of $\lesssim$300keV in the veto panels. Thus, the events with "muon-like" energy deposition in the veto panels are disregarded from LIPs analysis. This criteria has an efficiency of 0.9993 for each run.

4.5.9 Nonzero Charge and Yield Requirement

Although the charge signal from an event is not used in estimating its recoil energy, it is judicious to employ the data in a useful manner towards selecting valid LIP-induced events.

In usual WIMP analysis [11], it is asserted that the charge signal from a valid event in the inner electrode should be sufficiently high that there is $\sim$4-4.5σ confidence of it not occurring due to noise-induced variations. However, application of this criteria prevents observing events depositing low energy in the detector, which is typical of LIPs with small fractional charges (Table 4.5 lists the minimum charge signal measured by a detector for it to be asserted with 4σ confident that the event is not noise-induced. If the criteria is applied then the lower threshold will become as high as 5keV for Tower 4). Thus, the criteria is modified to require that a valid LIP-induced event should cause each of the 6 detectors of a tower (a LIP-detector) have a charge signal more than 1σ from average charge noise in the detector. It is referred as the "charge threshold" criteria. The associated confidence with non-occurrence of such an event due to detector noise is similar to the confidence imposed by the criteria used in WIMP searches. Another modification employed in LIPs analysis is that the charge measurements correspond to the summed ionization energy (obtained from inner and outer charge electrode), instead of simply using results from inner charge electrode, as done in a WIMP analysis.

Another criteria used in WIMP analysis requires a valid event to have an ionization yield corresponding to nuclear recoil type events, i.e. yield$\equiv$1/3 (Section 3.3.1). Similarly, it may be required that a valid LIP induced event have an ionization yield corresponding to electromagnetic recoil type events, i.e. yield$\equiv$1. However, due to fluctuation in measurement of charge and phonon signal, the yield values are dis-

Table 4.5: Minimum charge signal measured by a detector for it to be asserted with 4σ confident that the event is not noise-induced. Different limits exist, and are reported for different runs.

Detector Name	R125	R126	R127
T2Z1	3.17keV	-	-
T2Z2	2.74keV	-	-
T2Z3	3.19keV	-	-
T2Z4	2.29keV	-	-
T2Z5	2.56keV	-	-
T2Z6	2.70keV	-	-
T4Z1	2.24keV	2.29keV	2.23keV
T4Z2	1.77keV	2.09keV	3.18keV
T4Z3	4.91keV	3.05keV	2.94keV
T4Z4	1.58keV	1.66keV	1.61keV
T4Z5	2.04keV	2.13keV	2.00keV
T4Z6	2.35keV	2.22keV	2.22keV

tributed in a band about unity. The events with yield larger than unity by 5σ are not considered for LIPs analysis, where σ is the energy dependent variation in measured yield of valid electromagnetic recoil type events, an illustrated by Fig. 3.10. However, to not miss valid LIP-induced event where the yield may be artificially lowered (specially for low deposited energies, where the charge values are extremely influenced by noise in charge channel), the analysis does not disregard the low-yield events, except when the yield become ≤ 0.1. The latter are representative of background induced events occurring near the curved surface of substrate and not of LIP induced events primarily occurring in bulk of substrate.

The efficiency of LIPs detection due to the simultaneous application of these two considerations, obtained by their application on electromagnetic recoil type events obtained from ^{133}Ba-calibration dataset, is shown in Fig. 4.13. Separate efficiencies for different detector and runs are obtained.

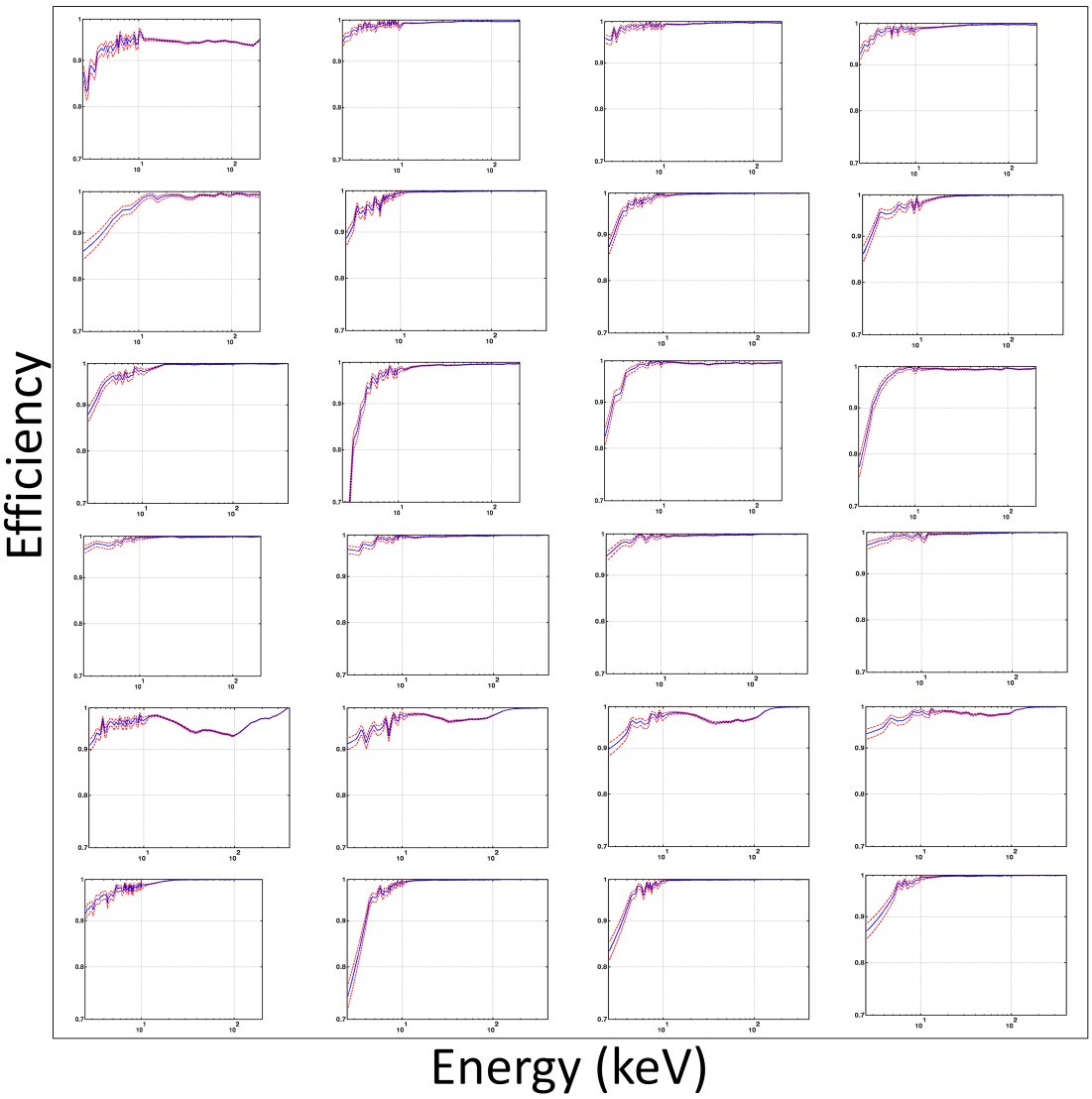

Figure 4.13: Efficiency of LIPs detection due to the simultaneous application of charge threshold and yield criteria. Going left to right, the columns represent Tower 2 (R125), and Tower 4 (R125, R126, R127). Each row represents the detector in the tower, with first detector placed at top, e.g. element in first row and first column represent result for T2Z1 for run R125. The horizontal axis corresponds to energy deposition in detector and spans from 2.5keV to 200keV (silicon), or 400keV (germanium), with vertical grids representing 10 and 100keV mark. The vertical axis span detection efficiency from 0.7 to 1, with horizontal grids representing 0.8 and 0.9 efficiency mark.

4.5.10 Simultaneous Start-time Requirement

The LIPs are asserted to be relativistic particles and will travel through the 6cm thick detector stack in ∼200ps. But, the charge and phonon collection by detectors occur over timescales of μs. Thus, it is expected that valid LIP-induced events should have charge and phonon pulses appear in all 6 detector within a small timespan. In reality though, a finite difference between the start time of charge and phonon pulse among different detectors can arise to variations in pulse fitting, etc.

To optimize this criteria, a study of the difference between maximum and minimum start time of phonon and charge pulses among 3 detector simultaneously hit by a single γ was performed, and the results are shown below in Fig. 4.14. When obtaining the start-time for charge pulse, it is required that the best fit between the signal and the template pulse occur as the latter is temporally shifted in a window around the global trigger, as mentioned in Appendix G.7. Events with charge start-time close to the boundary values for the fit-window are likely to be improperly fit and are not used when obtaining the results.

Using above results, it is defined that an event is background induced if the difference between arrival of phonon pulse in any 2 detector is $> 20\mu s$ AND the difference in arrival of charge pulse is also $> 20\mu s$ (for detectors where the charge pulse start-time is not close to the boundary values for the fit-window). Such a criteria also holds at different levels of energy deposited in detector.

A LIP detection efficiency of 0.9886 ± 0.0004 can be attributed to a more constrained requirement for LIP induced event to have a difference in phonon start-time of $< 20\mu s$. The analysis conservatively associated same efficiency to the actual start-time criteria used in the analysis (based on both charge and phonon start-time).

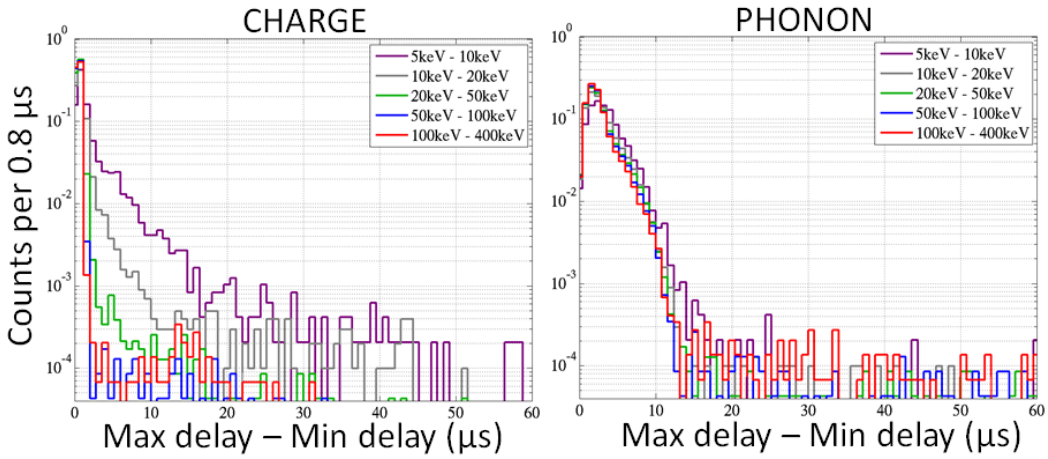

Figure 4.14: Difference between the maximum and minimum start time of charge and phonon pulse, separately, for event comprising of 3 consecutive detector hit simultaneously by a single γ. Figure taken from [296].

4.5.11 Energy Consistency Requirement

As a LIP crosses a tower, it deposits energy in all detectors in an independent manner. Had all detectors been made of similar material, the distribution of values corresponding to energy deposited by a LIP of charge *fe* in each of the detector would mirror the probability distribution for LIP to deposit energy in a single detector (as mentioned in Section 4.3, it is asserted in the analysis that the LIP flux is sufficiently low that only a single LIP passes through the tower at a time). This is the "Energy Consistency" criteria. In reality though, all detectors of a tower are not made of similar material (they are either silicon, or germanium), only the events with measured energies within the analysis threshold contribute to the analysis and the energy measured by detector is not the same as that deposited by LIPs (it gets randomly varied by the corresponding detector resolution). It becomes necessary to include the effect of these features before a check for "energy consistency" can be performed.

4.5.11.1 Energy Consistency for Ideal Scenario

This section describes the formulation to determine "Energy Consistency" for an ideal scenario where all detectors of a towers are made of similar material, the detector resolution is perfect and there is no upper or lower analysis threshold. The quantification of "statistical matching" (or, energy consistency test-statistic, E_c) is defined as:

$$F_i(E_i) = \left(\frac{\int_{E=0}^{E_i} P_{Det_i}(E, f, \theta)}{\int_{E=0}^{\infty} P_{Det_i}(E, f, \theta)} \right)$$
$$E_c = -2 \sum_{i=0}^{6} w_i \cdot ln \left(\frac{\Delta F_i}{w_i} \right) \tag{4.22}$$

where, $P_{Det_i}(E, f, \theta)$ is the energy deposition probability by LIP in i^{th} ZIP detector of the tower and follows from Eq. (4.19), $F_i(E_i)$, or simply F_i is the cumulative probability to obtain an energy deposition of E_i in same detector, ΔF_i are the difference between successive cumulative probabilities (a toy example illustrating it is shown in Fig. 4.15), and w_i are the mean values of ΔF_i. This definition is based on the observation that if the distribution of energies deposited in 6 ZIP detectors is indeed according to a postulated probability distribution, then the corresponding cumulative probabilities are uniformly distributed between 0 and 1. A schematic representation is shown in Fig. 4.15 *assuming* a gaussian distribution of energy deposition probability to simply highlight the rationale.

4.5.11.2 Imperfect Detector Resolution

Imperfect detector resolution implies that the energy measured by detector is different from the energy deposited in the detector; the difference guided by the detector resolution. To account for this effect, the energy consistency criteria is modified to

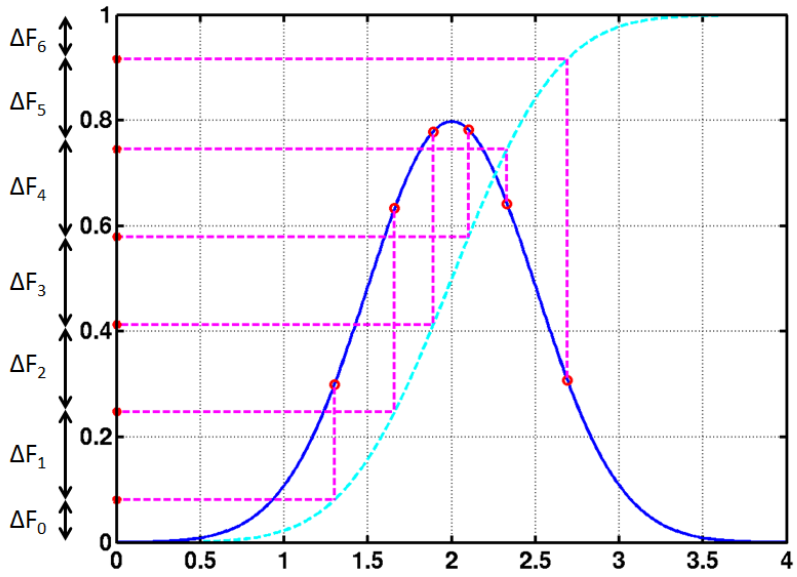

Figure 4.15: Rationale behind definition of energy consistency, exemplified using a gaussian distributed energy deposition probability spectrum. The circles (red o) correspond to actual energy depositions in conformation with the gaussian shaped probability distribution (blue). It is observed that the corresponding cumulative probabilities (red *) are uniformly distributed.

obtain the statistical match between the distribution of energies "measured" by 6 ZIP detectors with the LIPs energy measurement probability, as described in Section 4.2.4. Thus, one obtains the definition for the energy consistency test-statistic as:

$$F_{meas,i}(E_i) = \left(\frac{\int_{E=0}^{E_i} (P_{Det_i}(E,f,\theta) * Reso_{Det}(E))}{\int_{E=0}^{\infty} (P_{Det_i}(E,f,\theta) * Reso_{Det}(E))} \right)$$

$$E_c = -2 \sum_{i=0}^{6} w_i \cdot ln \left(\frac{\Delta F_{meas,i}}{w_i} \right) \tag{4.23}$$

where, definition from Eq. (4.8) follows.

4.5.11.3 Existence of Analysis Threshold

Existence of an analysis threshold implies that only the events with energy deposition within the analysis threshold are of interest. Thus, only a certain region of the entire LIP-induced energy deposition probability curve, bounded in energy by the upper and lower analysis threshold, is of interest while constructing the energy consistency criteria. This change is executed by instead measuring the similarity of the "scaled cumulative probabilities" ($F_{scale,i}$) with an uniformly distribution ranging between 0 and 1, where the"scaled cumulative probabilities" are defined as:

$$F_{scale,i} = \left(\frac{\int_{E=Low-Thresh}^{E_i} (P_{Det_i}(E, f, \theta) * Reso_{Det}(E))}{\int_{E=Low-Thresh}^{High-Thresh} (P_{Det_i}(E, f, \theta) * Reso_{Det}(E))} \right)$$
$$E_c = -2 \sum_{i=0}^{6} w_i \cdot ln \left(\frac{\Delta F_{scale,i}}{w_i} \right) \tag{4.24}$$

where, definitions from Eq. (4.22, 4.23) follows, and *Low-Thresh* and *High-Thresh* are the lower and upper analysis thresholds correspondingly.

4.5.11.4 Detector of Different Materials

To account for this effect, the cumulative probability used in definition of energy consistency criteria is obtained using the energy deposition probability curve corresponding to the material of that detector. It is shown in Eq. (4.22 - 4.24), but wasn't explicitly emphasized earlier.

4.5.11.5 Energy Consistency for Real Scenario

The above corrections to form of energy consistency test-statistic are simultaneously included to define the final form of criteria used in the LIPs analysis. This models the consistency of energy depositions observed in different detectors of a tower (made of different materials, having different thickness, different energy reso-

lution and different analysis threshold) to being caused by LIPs of given fractional charge passing through the tower at a certain azimuthal angle. Fig. 4.16 shows an example of distribution of energy consistency test-statistic for LIP-induced and background-induced events, obtained using Monte Carlo studies.

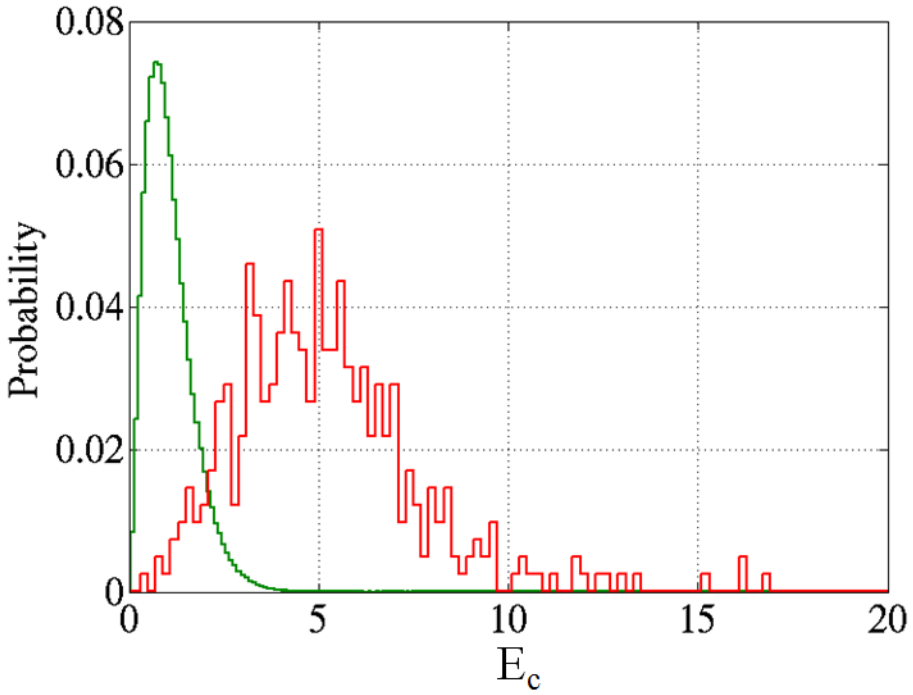

Figure 4.16: Distribution of energy consistency test statistic (E_c) for photon background induced events instead modeled as occurring due to LIP of fractional charge *e/15* incident at θ=0 (red). The E_c distribution for valid LIP-induced events (green), with similar charge and incident angle is also shown. Figure taken from [297].

4.5.11.6 Defining the Energy Consistency Criteria

The energy consistency test-statistic (E_c) defined in Eq. (4.24)compares the consistency of energy deposition pattern as occurring due to a LIP of fractional charge *fe*, and incident on the towers with an azimuthal angle θ. However, the azimuthal

angle of LIP incidence is not a physically measurable quantity. Thus, it is only justifiable to ask whether the observed energy distribution pattern is consistent as occurring due to LIP of a given fractional charge *fe*, incident at any azimuthal angle (but not with an extremely large angle precluding the possibility for LIP to simultaneously interact with all 6 ZIP detectors of a tower). To account for this change in the definition of energy consistency criteria, the test-statistic E_c is redefined as

$$E_c(f) = min\left(E_c(f,\theta); 0 < \theta < theta_{max}\right) \tag{4.25}$$

where, $E_c(f,\theta)$ is same as quantity E_c defined in Eq. (4.24), $min()$ denotes the minimization function selecting the minimum value among its arguments, θ_{max} is the maximum azimuthal angle of LIP incidence beyond which it cannot interact with all 6 ZIP detectors of a tower.

With the above definition for the energy consistency test-statistic, it is decided to require that a valid LIP induced event have $E_c < 2.37$, which is $\approx$99% efficient in selecting LIPs induced events, with a probability of leq10% for background (γ) induced events to be mistakenly accepted [297].

4.5.12 Track Linearity Criteria

As a LIP crosses the tower, it deposits very little energy in each detector as compared to its original kinetic energy. Thus, it is expected that the LIP will pass through all ZIP detectors of a tower in a straight path. This is the "track linearity" criteria and it quantifies whether the location of event occurrence in multiple detectors lie in a straight line, up to allowable variations in the ability of the analysis to correctly reconstruct the physical location of event occurrence in a detector, also called as "resolution of reconstructed location". This section describes the procedures used to reconstruct location of event occurrence in a detector, to obtain the

resolution of reconstructed location and application of these results to define a "track linearity" criteria.

4.5.12.1 (X,Y) Location Reconstruction Algorithm

Reconstruction of the lateral location of event occurrence inside the detectors (i.e., the (x,y) location of event occurrence) is done using the model developed in previous CDMS thesis [242]. A primary assumption employed in the model is that the distribution of lateral location of events depositing 40-400keV energy in a detector, when the detector is not exposed to any external radioactive sources (e.g., ^{133}Ba, or ^{252}Cf) is uniformly over its surface. This assumption is physically justified because in absence of external sources, the events observed by ZIP detectors are primarily induced by γs given off by trace radioactive contaminants existing on detector surface or in the copper housings containing the detectors. These impurities are uniformly distributed over detector surface, and it follows that the lateral location of events induced by them should also be uniformly distributed. Additionally, the high energy of γs allow them to penetrate and interact with the crystal substrate any possible location with an uniform probability. One more point to mention is that the employed model separately reconstructs the radial and angular location of event occurrence inside the detector. These values can eb used to obtain the reconstructed (x,y) location.

The reconstruction model asserts that best guess to angular location for event occurrence is functionally related to the quantity θ_{ppart}, defined as:

$$\theta_{ppart} = tan\left(\frac{yppart}{xppart}\right) \tag{4.26}$$

where, definitions from Eq. (3.10) follow. This, best guess angular location, or re-

constructed angular location (θ_{recons}) is defined as:

$$\theta_{recons} = \theta_{ppart} - A_1 \cdot sin\,(4theta_{ppart}) - A_2 \cdot sin\,(8theta_{ppart}) \tag{4.27}$$

where, $A_1,\ A_2$ are detector specific coefficients that render the distribution of 40-400keV γs uniform in reconstructed angular location (θ_{recons}). The parameters $A_1,\ A_2$ used in the current analysis for different detectors are described in Table 4.6 below.

Table 4.6: Value of coefficients $A_1,\ A_2$ used to reconstruct angular location of event occurrence inside a detector [301].

Detector Name	A_1	A_2
T2Z1	0.139	-0.00778
T2Z2	0.119	-0.0139
T2Z3	0.198	-0.0304
T2Z4	0.13	-0.0223
T2Z5	0.199	-0.025
T2Z6	0.143	-0.0196
T4Z1	0.218	-0.032
T4Z2	0.211	-0.0339
T4Z3	0.151	-0.0247
T4Z4	0.207	-0.0282
T4Z5	0.213	-0.0314
T4Z6	0.206	-0.0268

The reconstruction of radial location of event occurrence inside the detector is iteratively done such that at the end of this routine, a group of selected phonon amplitude and phonon timing based quantities show least departure from corresponding functional form relating them to the reconstructed radial location values. Thus, the reconstructed radial location (θ_{recons}) is obtained via a χ^2-minimization like routine,

and unlike a simple functional form used to obtain θ_{recons}. Due to the apparent disconnect between the detailed presentation of the radial reconstruction routine with the results presented in the dissertation, it won't be discussed in detail and [242] may be referred for an in-depth description. However, it is important to obtain the resolution of reconstructed radial and angular location, and it is discussed next.

4.5.12.2 Resolution of Reconstructed Radial Location

Since different ZIP detectors exhibit non-homogeneous set of characteristics, it is necessary to obtain the resolution separately for each detector. Additional, it is possible that the resolution itself has radial and energy dependence. The energy dependence may come because the signal to noise ratio increases for low energies, specially for the phonon timing based quantities used in radial reconstruction procedure. The following steps are used to obtain the resolution of reconstructed radial location of events occurring in a given detector, within a certain range of reconstructed radial location and depositing a given energy in the detector:

- For the event (satisfying above mentioned criteria), the "variation" in "input parameters" is obtained. "Input parameters" refer to the select group of phonon amplitude and phonon timing based quantities used in radial reconstruction model. The term "variation" refers to allowable deviation in the quantity that still renders the events to have similar reconstructed radial values.

- A Monte Carlo is done where each of the "input parameters" are allowed to independently vary according the values obtained in previous step. The new instances are again subjected to the radial reconstruction procedure and the deviation in reconstructed values of radial location corresponding to similar events are obtained. This provides an estimate of radial resolution.

For a given detector and for events occurring within a certain range of reconstructed radial location, the energy dependent variation of radial resolution (in mm) is fit to a function of form

$$\Delta r_{recons} = A_3 + A_4/E + A_5(E-100)^2 \cdot Heaviside(E-100) \tag{4.28}$$

where, the particular form is empirically obtained, $A_3,\ A_4,\ A_5$ are detector and radial dependent coefficients, E is the energy deposited in detector, in keV, $Heaviside()$ is the Heaviside, or step function, all length measurements ($r_{recons} and \Delta r_{recons}$) are in mm. It is also empirically observed that the error in obtaining the radial resolution also follows a similar form

$$\Delta\left(\Delta r_{recons}\right) = A_6 + A_7/E + A_8(E-100)^2 \cdot Heaviside(E-100) \tag{4.29}$$

where, definitions from Eq. (4.28) follow, and $A_6,\ A_7,\ A_8$ are detector and radial dependent coefficients, and $\Delta\left(\Delta r_{recons}\right)$ are in mm.

An important and relevant detail is that the resolution corresponding to radial locations less than 5mm is not obtained. It is assumed that the resolution of events with reconstructed radial location less than 5mm will be same as events occurring at 5mm radial location. This prevent dealing with the term "radial location" becoming undefined for negative values.

4.5.12.3 Correcting the Reconstructed Radial Resolution

The reconstructed radial resolution obtained in previous step may be an underestimation of true radial resolution values due to possible inaccuracies in the model used to obtain the reconstructed radial location. Additionally, they should be large enough to account for systematic/random inconsistencies between the physical and

reconstructed radial location of event occurrence inside detector. However, a major hurdle to performing such comparison is that the physical radial location is an unknown for each and every event; this is the primary reason to obtain reconstructed event location.

Although the physical radial location of event occurrence is an unknown, the corrections to resolutions can still be obtained using the set of low yield, surface events caused by energetic electrons (Section 3.3.3) which strike a pair of neighboring detectors at similar physical radial location. The reconstructed radial location for these events will differ from physical radial location by corresponding reconstructed radial resolution (This is the true estimate for reconstructed location resolution), making the events appear to be occurring at different reconstructed radial location in the neighboring detectors. Thus, the correct reconstructed radial resolution can be obtained by comparing the distribution of radial separation between reconstructed event location against the value obtained by adding the uncorrected resolution corresponding to the two detectors in quadrature.

The problem with above procedure is that there are very few surface events available to get an energy, reconstructed radial location and detector dependent radial resolution solely using these events. Thus, it is necessary to start by obtaining an initial form for the reconstructed radial resolution (as described above), and then correct it by comparing it against the distribution of separation between electron induced surface events. Due to the low availability of surface events, the correction is done employing an approximate, two-step procedure iteratively correcting the radial dependence and energy dependence in resolution. It is repeatedly done such that at the completion, at least 90% of electron induced surface events have a separation between them which is less than the value obtained by adding the corrected resolution corresponding to the two detectors (which are struck by electron induced event) in

quadrature.

- An energy and detector independent, but, reconstructed radial location dependent correction to radial resolution is performed (i.e., for a given radial location, the coefficient A_3 is increased by a constant multiplicative factor; the same factor being used to correct A_3 for all detectors) by requiring that 90% of all surface events occurring between any two consecutive detectors in Tower2 and Tower4 have smaller radial separation between them than the value obtained by adding the resolution corresponding to the two detectors in quadrature.

- An energy dependent, but detector and reconstructed radial location independent correction to radial resolution is performed (i.e., for a given energy value, the coefficient A_4 is increased by a constant multiplicative factor; the same factor being used to correct A_4 for all detectors) by requiring that 90% of all surface events occurring between any two consecutive detectors in Tower2 and Tower4 have smaller radial separation between them than the value obtained by adding the resolution corresponding to the two detectors in quadrature.

- Similar corrections are also applied to parameters $A_6,\ A_7$ describing the error in estimation of radial resolution.

The parameters $A_3\ -\ A_8$ used in the current analysis for different detectors and radial locations are described in Table (4.7, 4.8).

Table 4.7: Coefficients $A_3 - A_8$ describing the detector, energy and reconstructed radial dependent reconstructed radial resolution for Tower-2 detectors [302], and definitions from Eq. (4.28, 4.29) follow. A linear extrapolation is done to obtained the correction factor for radial locations $r > 43mm$, while simultaneously ensuring that the extrapolation does not cause the value to drop below that for $38 < r < 43mm$

Location		T2Z1	T2Z2	T2Z3	T2Z4	T2Z5	T2Z6
$5 < r < 10$	A_3	0.34	2.34	0.21	0.33	0.12	0.29
	A_4	23.22	52.47	28.91	12.37	17.82	13.74
	A_5	0	0.0003	0	0	0	0
	A_6	0.04	0.31	0.30	0.41	0.02	0.04
	A_7	1.46	5.30	3.32	1.0	1.89	0.31
	A_8	0	0	0	0	0	0
$10 < r < 15$	A_3	0.97	0.18	0.82	0.73	0.42	0.74
	A_4	29.58	76.72	21.78	17.51	25.74	20.24
	A_5	0	0.0002	0	0	0	0
	A_6	0.12	0.06	0.08	0.1	0.04	0.08
	A_7	1.59	4.15	1.01	0.49	1.10	0.49
	A_8	0	0	0	0	0	0
$15 < r < 20$	A_3	5.55	2.95	3.91	3.69	3.25	3.86
	A_4	8.71	67.31	32.41	36.91	33.33	27.19
	A_5	0.0001	0	0	0	0	0
	A_6	0.54	0.33	0.23	0.37	0.15	0.21
	A_7	2.26	11.33	1.50	1.45	1.41	2.02
	A_8	0	0	0	0	0	0

continued on next page

Table 4.7 Continued

Location		T2Z1	T2Z2	T2Z3	T2Z4	T2Z5	T2Z6
$20 < r < 25$	A_3	2.58	1.42	1.60	1.77	1.33	1.32
	A_4	8.10	46.78	22.87	30.43	22.87	9.19
	A_5	0.0001	0	0	0	0	0
	A_6	0.19	0.13	0.11	0.12	0.07	0.10
	A_7	0.61	2.85	3.12	0.56	4.48	0.84
	A_8	0	0	0	0	0	0
$25 < r < 30$	A_3	11.06	6.84	4.90	6.86	4.03	5.49
	A_4	27.59	50.81	30.91	32.03	29.96	16.36
	A_5	0	0.0001	0	0	0	0
	A_6	0.6	0.51	0.32	0.40	0.23	0.29
	A_7	2.04	3.61	2.68	1.43	1.63	0.51
	A_8	0	0	0	0	0	0
$30 < r < 35$	A_3	1.42	0.82	0.79	1.0	0.58	0.91
	A_4	46.19	17.13	33.98	10.64	51.94	25.73
	A_5	0	0	0	0	0	0
	A_6	0.10	0.08	0.04	0.08	0.03	0.05
	A_7	1.34	2.12	2.24	0.47	1.92	0.89
	A_8	0	0	0	0	0	0

continued on next page

Table 4.7 Continued

Location		T2Z1	T2Z2	T2Z3	T2Z4	T2Z5	T2Z6
$35 < r < 38$	A_3	1.09	0.83	0.79	1.6	0.69	0.78
	A_4	66.51	38.42	33.39	3.80	44.40	32.09
	A_5	0	0	0	0	0	0
	A_6	0.09	0.07	0.03	0.08	0.03	0.04
	A_7	4.75	2.05	1.01	0.67	1.55	1.85
	A_8	0	0	0	0	0	0
$38 < r < 43$	A_3	0.7842	3.93	0.53	0.25	0.23	0.98
	A_4	29.42	29.42	27.73	6.69	8.16	14.18
	A_5	0	0	0	0	0	0
	A_6	0.09	0.20	0.07	0.03	0.03	0.11
	A_7	5.24	5.24	3.59	0.69	1.36	2.04
	A_8	0	0	0	0	0	0

Table 4.8: Coefficients $A_3 - A_8$ describing the detector, energy and reconstructed radial dependent reconstructed radial resolution for Tower-4 detectors [302], and definitions from Eq. (4.28, 4.29) follow.

Location		T4Z1	T4Z2	T4Z3	T4Z4	T4Z5	T4Z6
$5 < r < 10$	A_3	1.57	1.07	2.34	1.50	1.70	1.59
	A_4	61.07	54.15	21.73	12.22	44.60	60.90
	A_5	0	0	0.0003	0	0	0
	A_6	0.22	0.19	0.31	0.18	0.16	0.15
	A_7	5.30	1.05	0.16	0	0	0
	A_8	0	0	0	0	0	0
$10 < r < 15$	A_3	3.05	1.47	2.88	1.67	1.93	3.0
	A_4	25.32	35.29	18.78	31.07	57.10	45.0
	A_5	0	0	0.0001	0	0	0
	A_6	0.32	0.13	0.25	0.11	0.11	0.09
	A_7	0	0.17	0	0.83	2.13	13.03
	A_8	0	0	0	0	0	0
$15 < r < 20$	A_3	7.48	6.79	8.46	7.52	13.05	13.05
	A_4	49.74	42.74	6.18	35.94	28.13	28.13
	A_5	0	0	0	0	0	0
	A_6	0.52	0.21	0.54	0.26	0.32	0.16
	A_7	0.14	3.0	0	4.46	2.83	5.17
	A_8	0	0	0	0	0	0

continued on next page

Table 4.8 Continued

Location		T4Z1	T4Z2	T4Z3	T4Z4	T4Z5	T4Z6
$20 < r < 25$	A_3	2.26	1.81	1.91	2.39	2.38	1.67
	A_4	53.38	36.65	34.36	27.81	52.03	59.96
	A_5	0.0001	0	0.0001	0	0	0
	A_6	0.21	0.10	0.17	0.12	0.03	0.06
	A_7	0	2.84	0	2.19	5.51	5.91
	A_8	0	0	0	0	0	0
$25 < r < 30$	A_3	11.01	7.24	8.42	9.94	7.70	7.22
	A_4	23.72	55.78	26.29	29.81	20.27	61.29
	A_5	0	0	0	0	0	0
	A_6	0.83	0.52	0.78	0.56	0.44	0.31
	A_7	0	1.04	0.46	2.05	1.11	1.94
	A_8	0	0	0	0	0	0
$30 < r < 35$	A_3	1.86	1.13	2.04	1.20	1.02	3.0
	A_4	57.81	66.05	26.40	49.69	59.78	45.0
	A_5	0	0	0.0001	0	0	0
	A_6	0.14	0.06	0.09	0.05	0.05	0.04
	A_7	0.74	2.58	0	2.20	1.46	4.76
	A_8	0	0	0	0	0	0

continued on next page

Table 4.8 Continued

Location		T4Z1	T4Z2	T4Z3	T4Z4	T4Z5	T4Z6
$35 < r < 38$	A_3	1.24	1.04	1.63	0.98	1.0	3.0
	A_4	64.83	63.07	14.61	67.72	67.52	45.0
	A_5	0	0	0.0001	0	0	0
	A_6	0.05	0.03	0.11	0.03	0.03	0.02
	A_7	4.75	7.29	1.5	2.14	0.87	9.60
	A_8	0	0	0	0	0	0
$38 < r < 43$	A_3	2.99	1.12	3.93	1.37	3.0	3.5
	A_4	29.42	19.50	6.68	46.06	21.23	8.16
	A_5	0	0	0	0	0	0
	A_6	0.12	0.11	0.20	0.10	0.08	0.06
	A_7	5.24	3.43	3.14	4.95	6.45	5.45
	A_8	0	0	0	0	0	0

4.5.12.4 Resolution of Reconstructed Angular Location

From the definition of reconstructed angular location, Eq. (4.27), it is apparent that the reconstructed angular resolution is dependent on the value of reconstructed angular location and on the resolution of θ_{ppart} (defined in Eq. 4.26). A conservative choice of largest angular resolution over entire reconstructed angular values is chosen in defining the detector, energy and reconstructed radial dependent reconstructed

angular resolution.

$$\Delta\theta_{recons} = (1 - 4A_1 cos(4\theta_{ppart}) - 8A_2 cos(8\theta_{ppart})) \cdot \Delta\theta_{ppart}(E)$$
$$\Delta\theta_{recons}|_{max} = (1 + 4A_1 - 8A_2) \cdot \Delta\theta_{ppart}(E)$$
$$\Delta\theta_{ppart}(E) \approx \left(\frac{1}{rppart}\right)\left(\frac{Reso_{Det}(E)}{E}\right) \tag{4.30}$$

where, definition of Eq. (4.8, 4.26, 4.27) follows. Ignoring the $\left(\frac{1}{rppart}\right)$ term, the energy and detector dependent resolution of reconstructed angular resolution is easily obtained using energy resolution of detectors, defined in Section 4.2.4.

An important and relevant detail is that the resolution corresponding to radial locations less than 5mm is not obtained. It is assumed that the resolution of events with reconstructed radial location less than 5mm will be same as events occurring at 5mm radial location. This prevent dealing with the term "angular location" becoming undefined for negative values of radial location. Also, unlike reconstructed radial resolution, the error in reconstructed angular resolution is not obtained, because the latter is calculated using energy resolution which is based on parameters estimated in a conservative manner (Section 4.2.4).

4.5.12.5 Correcting the Reconstructed Angular Resolution

The procedures developed to correct reconstructed radial location using electron induced surface events in neighboring detectors are again employed with similar rationale, but to instead correct for reconstructed radial and energy dependence in angular resolution.

Defining, $A_{1,E}$, $A_{2,E}$, $A_{3,E}$ as similar to parameters A_1, A_2, A_3 as used in Eq. (4.20) (the latter parameters are not used to prevent confusing it with parameter A_1, A_2 in Eq. (4.27) and A_3 in Eq. (4.28)), and corrected, reconstructed angular

resolution as

$$\Delta\theta_{recons} = (1 + 4A_1 - 8A_2) \cdot Fac(r_{recons}) \cdot \left(\frac{\sqrt{A_{1,E} + A_{2,E}E + A_{3,E}E^2}}{E} \right) \quad (4.31)$$

The parameters $A_{1,E}$, $A_{2,E}$, $A_{3,E}$ (to obtain reconstructed angular resolution) used in the current analysis for different detectors and radial locations is almost same as that mentioned in Section 4.2.4. $A_{1,E}$ is the square of phonon noise values shown in Table 4.1 and $A_{2,E}$=0.05. $A_{3,E}$ values are thrice as high as that mentioned previously (Section 4.2.4), i.e. values for $A_{3,E}$ of 0.0162 for silicon detector and 0.0039 for germanium detectors are used [303]. This difference is incorporated to account for energy correction of reconstructed angular resolution. $Fac(r_{recons})$ is a radial location dependent correction factor that includes correcting the angular resolution for $\left(\frac{1}{rppart}\right)$ factor otherwise missed in Eq. 4.31, and additional radial dependences. Table 4.9 provides the values for radial dependent correction factor.

Table 4.9: Value of radial dependent correction factor, $Fac(r_{recons})$, used to correct reconstructed angular resolution [303]. A linear extrapolation is done to obtained the correction factor for radial locations $r > 43mm$, while simultaneously ensuring that the extrapolation does not cause the value to drop below that for $38 < r < 43mm$.

Radial location (mm)	$Fac(r)$
$5 < r < 10$	3.15
$10 < r < 15$	1.85
$15 < r < 20$	1.00
$20 < r < 25$	1.00
$25 < r < 30$	1.00
$30 < r < 35$	1.05
$35 < r < 38$	1.50
$38 < r < 43$	1.50

4.5.12.6 Defining the Track Linearity Criteria

Reconstructed radial and angular location are used to obtain the reconstructed (x,y) location of event occurrence inside the detector. Similarly, the reconstructed radial and angular resolution is used to obtain the reconstructed (x,y) resolution. The "Track Linearity" criteria is defined using the following procedure:

- For a given fractional charge, a Monte Carlo of possible LIP tracks crossing through each of the ZIP detectors of a tower is obtained. The locations are smeared to obtain the distribution of reconstructed event occurrence location as a LIP would cross a tower. The "linearity" of these locations (up to the detector resolution corresponding to these reconstructed location) is obtained by calculating the χ^2 values characterizing the difference between the distribution of reconstructed locations in comparison to the best fit straight line connecting them, and dividing it by degree-of-freedom for the fitting routine (in fitting a 3-dimensional straight line through 6 detectors, there are 8 degree of freedom)

- In performing above calculation, it is also needed to assign a "z-location" of event occurrence within the detector, i.e. the depth from the surface at which the interaction occurs within the crystal. Additionally, an assignment of resolution for the corresponding quantity needs to be done. The "z-location" and "z-resolution" is defined using a function describing the probability for "energy

averaged z-location" to lie at certain depth from the surface, P(z).

$$
\begin{aligned}
P(z) &= Prob(\frac{\sum_{i=1}^{N} z_i \cdot E_i}{\sum_{i=1}^{N} E_i}; \sum_{i=1}^{N} E_i > Low - Thresh) \\
z_{mean} &= \int_{z=0}^{z=d} z \cdot P(z) \\
z_{reso} &= \sqrt{\left(\int_{z=0}^{z=d} z^2 \cdot P(z)\right) - z_{mean}^2}
\end{aligned}
\tag{4.32}
$$

where, the LIP undergoes N interactions within d units of detector thickness, depositing energy E_i in each interaction. P(z) is the probability distribution corresponding to the quantity in the bracket on the right side of equation, over all instances when the total energy deposited by LIP as it passes through the detector is more the the lower threshold of LIP-analysis, denoted by *Low-Thresh*.

- A "Background Monte Carlo" [294,295] studies events induced by γs that strike all 6 ZIP detectors of a tower (emulating a LIP induced event) and provides the physical location of background induced event occurrence inside the detector. The physical location is smeared to obtain the distribution of reconstructed event occurrence location which are then used to obtain the distribution of χ^2 per degree-of-freedom corresponding to background induced events.

- Defining *S(v), B(v)* as the cumulative probability for LIP induced, background induced event correspondingly to have a value of χ^2/degree-of-freedom less than a value v, and v_0 as the quantity at which the function $\left(\frac{S(v)^2}{S(v)+B(v)}\right)$ is maximized; Requiring that an observed event with energy deposition in all 6 ZIP detectors of a tower have corresponding χ^2/degree-of-freedom value less than v_0 simultaneously maximizes the probability that the observed event is

LIP induced and minimizes the probability for it being background induced. This requirement is used to define the track linearity criteria used in the current analysis. Fig. 4.17 shows the variation of value v_0 for different fractional charges applied on events occurring in Tower2 and Tower4. Since the values oscillate around 2.35 for Tower-2 and around 2.5 for Tower-4, the tracking cut selecting valid LIP induced events is defined as requiring the corresponding χ^2/degree-of-freedom value for the event be less than 2.35, if the event occurs in Tower-2, or less than 2.5, if it occurs in Tower-4.

4.5.12.7 "Old" Tracking Criteria

In an attempt to finish the LIPs analysis, an initial version of tracking criteria was developed which was later realized to be riddled with various systematics. The appeal of this construct was based on the fact that it used reconstructed locations $(x_{recon,old}, y_{recon,old})$ (in mm) obtained by scaling the phonon partition based quantities xppart, yppart (Eq. (3.10)) by a constant factor of 76.2. The rationale for this scaling is based on the empirical observation that the quantities xppart and yppart range from ≈-0.5 to +0.5 (shown in Fig. 3.7), and should correspond to event occurrence location spanning from -38mm to +38mm over the detector surface, the origin being at axial center of cylindrical crystal substrate.

$$\begin{aligned} x_{recon,old} &= xppart * 76.2 \\ y_{recon,old} &= yppart * 76.2 \end{aligned} \tag{4.33}$$

The detector and energy resolution of the reconstructed locations $(\Delta x_{recon,old}, \Delta y_{recon,old})$ is obtained by studying the variation in ratio of minimum phonon energy measured by any phonon detection channel to the combined phonon energy measured by 4 phonon

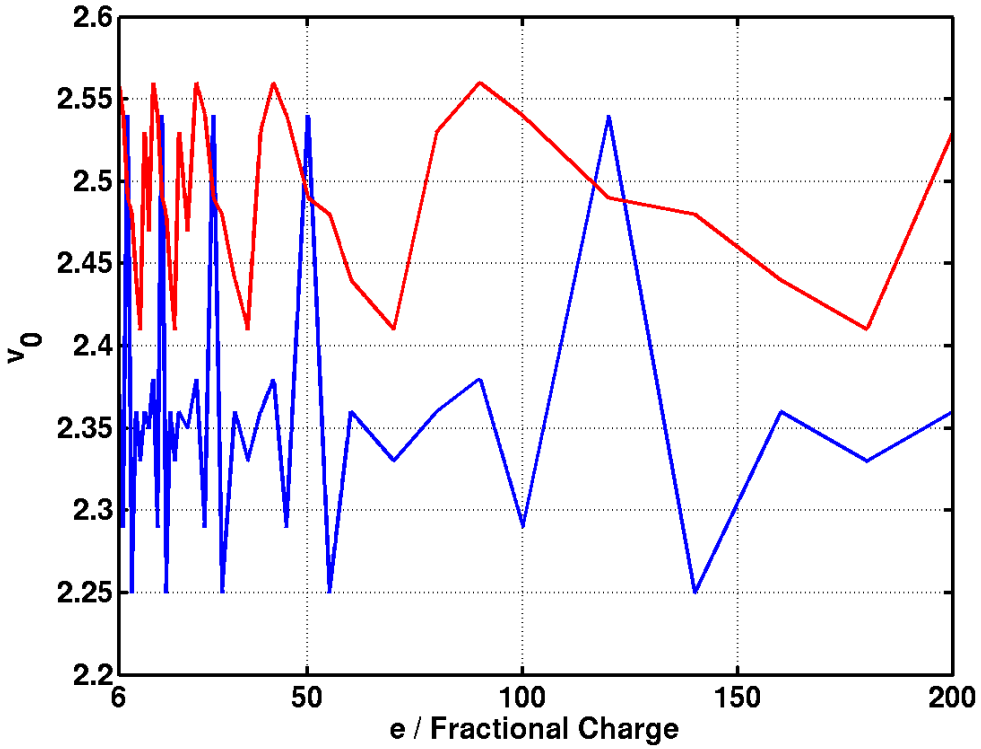

Figure 4.17: The variation of v_0 (the maximum value of χ^2/degree-of-freedom corresponding to simultaneous maximization for selection of LIP induced event and minimization in selection of background induced events) for different towers, Tower-2 (blue) and Tower-4 (red), and fractional charges. To use values that are "easier to work with", v_0 is instead chosen to be 2.35 for Tower-2 and 2.5 for Tower-4, for all fractional charges.

detection channels (Phonon detection channels are described in Section 3.2.2.2).

This construct suffers from two-fold grave systematics. It does not account for foldback in partition based quantities (i.e. xppart and yppart does not increase but instead decrease when the physical location of event occurrence is beyond a certain radial location from center of detector. The phenomenon is discussed in Section 3.2.3.4). Thus, the xppart and/or yppart value of 0.5 does not correspond to event occurrence at 38mm radial location. More importantly, the box-like shape of

xppart and yppart causes an event physically occurring at similar radial location (but different angular locations) into getting reconstructed at different radial locations. Consider the following example to illustrate the systematic. Events occurring near the outer periphery of the (xppart,yppart) distribution, at (xppart,yppart) = ($\pm$0.5,$\pm$0.5), (0,$\pm$0.5), etc. are assumed to be occurring at same physical radial location. However, using Eq. (4.33), the corresponding reconstructed locations would be $(x_{recon,old}, y_{recon,old})$ = ($\pm$38.1,$\pm$38.1)mm, (0,$\pm$38.1)mm, etc. which corresponds to a reconstructed radial location of $x_{recon,old} = \sqrt{x^2_{recon,old} + y^2_{recon,old}}$ = 53.9mm, 38.1mm, etc.

Due to this systematic in definition of the initial tracking cut, it was abandoned. However, quite unfortunately, before understanding the systematic and abandoning the criteria, an attempt to search for LIPs was already made using this criteria and corresponding data was unblinded. Thus, it becomes imperative to quote the results of LIPs analysis if this "old" tracking criteria is used for search efforts. Henceforth, this criteria is referred as "old" tracking criteria, and the one describe in sections above is referred as "new" tracking criteria.

4.5.13 Combined Track Linearity and Energy Consistency Criteria

Although the track linearity and energy consistency cuts are separately developed, they are applied in conjunction to each other. This is done to account for the existence of correlation/anti-correlation between the two criteria. It is expected that if the energy deposited in each detector is less than the energy of γ, then the γ is minimally deflected as it interacts with various detectors. However, the case with small energy deposition in each detector of a tower is more consistent with occurring due to a LIP with small fractional charge. Thus, if a background induced event satisfied tracking criteria, the pattern of energy deposition is more consistent as

occurring due to a LIP with small fractional charge. On the other hand, if an event fails the tracking criteria, then it is more likely that large energies are deposited in each detector and the pattern of energy deposition is more consistent as occurring due to a LIP with large fractional charge.

Fig. 4.18 shows the LIP acceptance efficiency for the combined track linearity and energy consistency criteria, applied to events occurring in Tower-2 and Tower-4, as a function of LIP fractional charge. Separate figures show the efficiency when old and the new tracking criteria is applied.

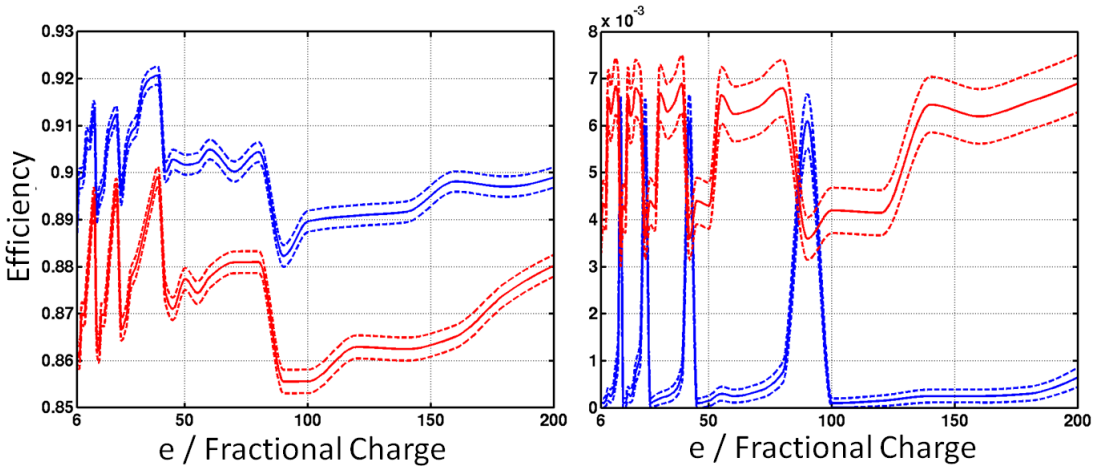

Figure 4.18: LIP acceptance efficiency for the combined track linearity and energy consistency criteria, for events occurring in Tower-2 (blue) and Tower-4 (red), as a function of LIP charge. LEFT: Calculated using the newly defined tracking cut. RIGHT: Calculated using "old" tracking cut.

4.5.14 Background Estimate

Background for LIPs analysis are events which are γ induced but still satisfy the above criteria developed to select LIP induced event against γ induced event. For LIPs analysis, the count of single γ induced events causing simultaneous energy

depositions in 6 ZIP detectors of a tower (while not causing energy depositions in remaining ZIP detectors) and also satisfying the energy consistency and tracking criteria forms the background of LIPs analysis. In a rigorous calculation, it is also necessary to further reduce the background estimate by the efficiency to observe these events (depending on the energy deposited by background events in ZIP detectors). Such a reduction is not done to prevent complication, and also to quote a larger and conservative value for background estimate.

Fig. 4.19 shows the background estimate for LIPs analysis at different fractional charges. Since the efficiency for "old" tracking is extremely low, the background estimate using the same is not shown. It will always be less than the true background estimate. The background for LIPs analysis is 0.078 ± 0.078 events. Thus, up to 90% confidence, the probability for a background-induced event to satisfy the criteria design for LIP selection is $\sim$0.18. The background increases for the values of *e/Fractional-Charge*$\approx$10-20 because the background induced events exhibit a larger "energy consistency" with the energy distribution corresponding to LIP-induced interactions.

4.5.15 Results from LIPs Analysis: Event Information

On applying the above criteria to the events recorded by Tower2 and Tower4 (with primary aim to serach for WIMP induced events), it is found that only no events satisfy all of the above criteria. There are 2 events (one in Tower-2, run R125, and other in Tower-4, run R126) which satisfy all criteria but either fail the energy consistency and/or tracking criteria. Fig. 4.20 shows the variation in difference of track χ^2/degree-of-freedom from the corresponding acceptance cutoff, and the variation in difference of E_c from the corresponding energy consistency cutoff for these events, corresponding to different fractional charges. Both the events fail tracking

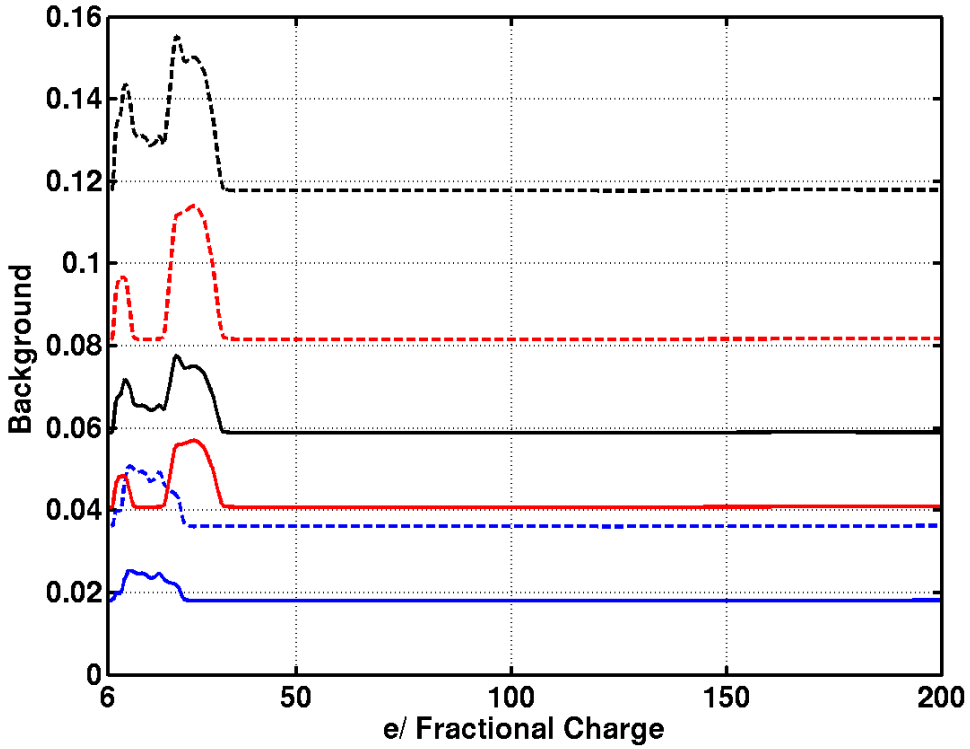

Figure 4.19: Background estimate for LIPs analysis at different fractional charges (black). Separate background estimates for Tower-2 (blue) and Tower-4 (red) alone are also shown.

and energy consistency criteria.

In addition to above, there are 3 other events which have energy deposition in one out of 6 ZIP detectors of a tower barely above the analysis threshold ($\lesssim 30keV$), and otherwise satisfy all criteria for selecting LIP induced events (before testing them on the tracking and energy consistency criteria). These are called "near miss" events, and it may be possible that the physical energy deposited in detector got increased by detector resolution, making the event get rejected from consideration for LIPs analysis. By assigning an energy 15keV below the maximum analysis threshold (15keV is the detector resolution at the maximum analysis threshold, as mentioned in

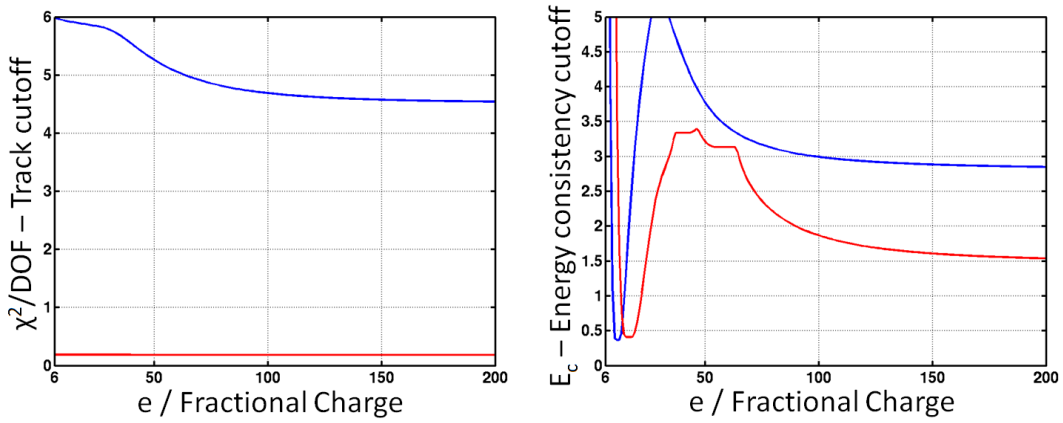

Figure 4.20: The variation in difference of track χ^2/degree-of-freedom (LEFT) and E_c (RIGHT) from corresponding cutoff for the two events satisfying all LIPs search criteria, except the combined tracking and energy consistency cut. One of the event occurs in Tower-2 (blue), and the other in Tower-4 (red). Values greater than zero indicate that the event is rejected by corresponding criteria. Thus, both the events are rejected as being LIP-induced for any fractional charge.

Section 4.2.4), the variation in difference of track χ^2/degree-of-freedom and E_c from corresponding cutoff for these events corresponding to different fractional charges are studied, and shown in Fig. 4.21.

4.5.16 Results from LIPs Analysis: Limit Curve

Using the mathematical framework developed in Section 4.1 and the result from LIPs analysis (i.e. observance of 0 candidate events), a 90% confident estimate on the lower bound to excluded LIP flux (incident on detectors) can be obtained, i.e. If the LIP flux were higher than the estimated value, then the analysis should have observed non-zero candidate events. A more rigorous and mathematical definition to LIP flux is defined through Eq. (4.1 - 4.11). Fig. 4.22 shows the 90% confident LIP flux estimate (defined as I_v^{90} in Eq. (4.1)). Fig. 4.6 provides an explanation for the saturation of the in the values *e/Fractional-Charge*≈6-30 because the total probability for interaction of LIPs remains almost same. For fractional charges smaller than

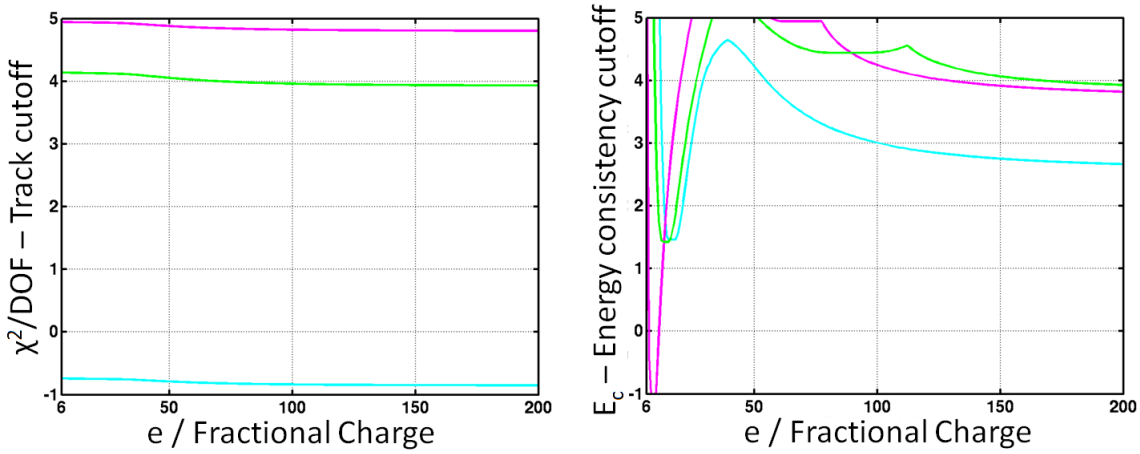

Figure 4.21: The variation in difference of track χ^2/degree-of-freedom (LEFT) and E_c (RIGHT) from corresponding cutoff for the three events satisfying all LIPs search criteria, except being slightly outside the analysis threshold and failing the combined tracking and energy consistency cut. All 3 events occur in Tower-4. Values greater than zero indicate that the event is rejected by corresponding criteria. Thus, even if the upper analysis threshold is increased to make these events valid, they are rejected as being LIP-induced for any fractional charge.

e/30, there is an increase in the probability that LIP interaction causes a low energy deposition in detector, and is read out by detector as a deposition of energy less than the minimum analysis threshold (2.5keV) in each detector. Thus, the sensitivity towards LIP detection decreases for low fractional charges restricting the result towards rejection of larger flux values.

Fig. 4.22 above also shows the 1σ error in estimation of LIPs flux. However, the error region is unfortunately encompassed by the thickness of the limit curve plot. Fig. 4.23 below shows the percentage error in estimation of LIPs limit flux for different fractional charges. It includes contribution from error in efficiency estimation of different criteria described above, error in estimation of detector thickness (affecting the total probability for LIPs to interact within the detector) and energy calibration error (i.e. in mentioning that the LIPs analysis extends over an interval of

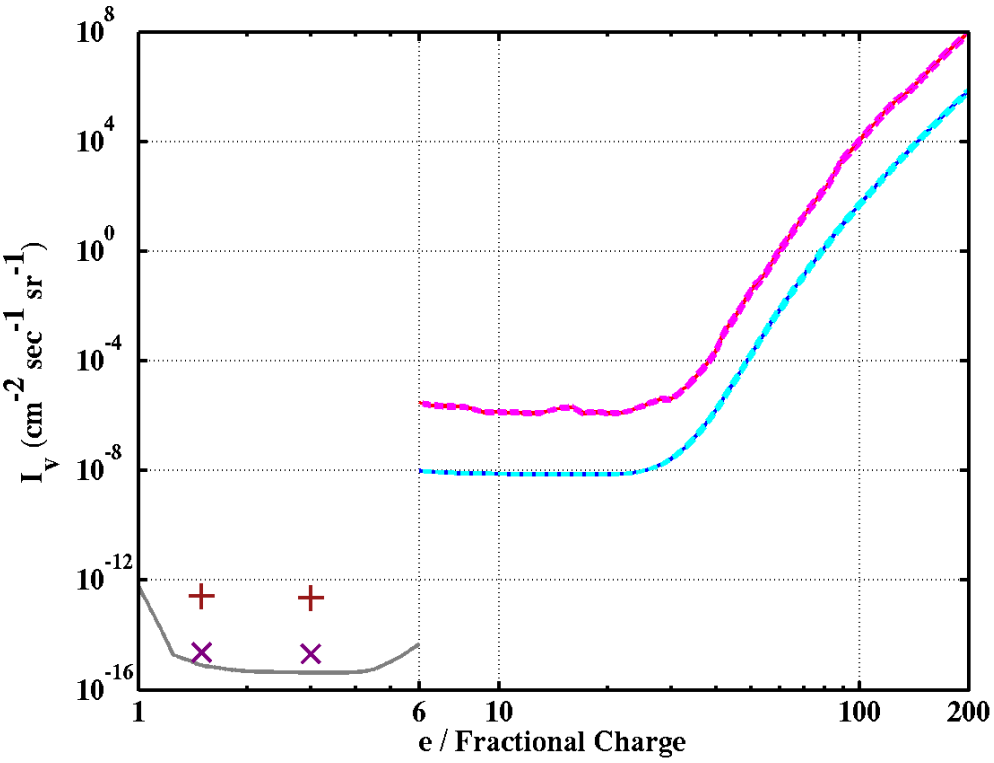

Figure 4.22: The 90% confident exclusion plot for LIP flux (lower bound to excluded LIP flux) corresponding to different fractional charges, incident on Tower-2 and Tower-4, based on the LIPs analysis. The two set of results correspond to analysis performed using "old" tracking criteria (red, with 1σ error in broken, magenta lines) and the new tracking criteria (blue, with 1σ error in broken, cyan lines). 1σ error bars, in broken lines, are also shown, but they get hidden due to the enormity of ordinate scales. The 90% Confidence Level limits for LIP flux from MACRO (grey), LSD (maroon +) and Kamiokande (purple X) are also shown (based on data from [10]).

2.5-200keV of energy measured by detector, the actual energy range of events studied by the analysis may be different if the detector isn't been properly calibrated). For germanium detectors, a calibration error of 0.1keV exists at low analysis threshold of 2.5keV (causing 1.29keV line from decay of ^{71}Ge into ^{71}Ga through L-shell electron capture, to be reconstructed at 1.35keV) [300]. For silicon detectors, a cali-

bration error of 0.15keV exists at low threshold of 2.5keV (causing ≈45keV line from radioactive decay of ^{210}Pb to be reconstructed at ≈43.5keV) [299].

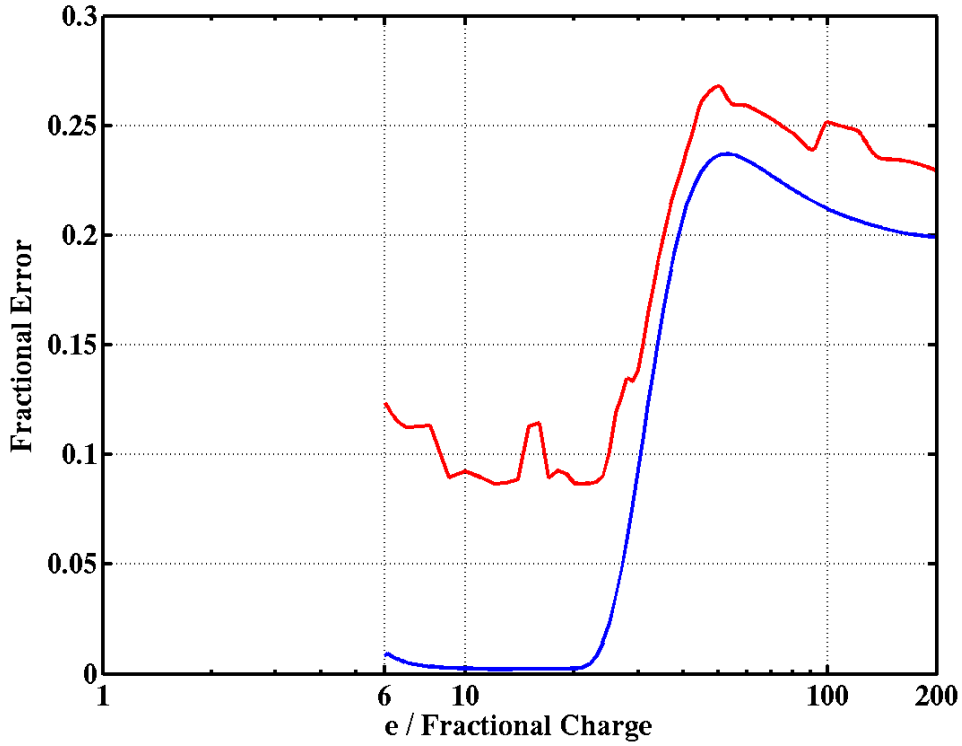

Figure 4.23: Fractional error corresponding to 1σ variation in estimation of 90% confident excluded LIPs flux, calculated using "old" tracking criteria (red) and new tracking criteria (blue).

4.6 Future Efforts

The section lists some of the possible future efforts and studies which can be done to improve the existent analysis routine or extend the scope of its applicability.

- As mentioned in Section 4.3, it is assumed that no more than 1 LIP strikes the CDMS towers. The application of this criteria may be questioned by realizing

that the LIPs are cosmogenic in nature, and if two LIPs with small fractional charge are simultaneously produced, they may be capable to simultaneously arrive and strike multiple towers (the low fractional charges prevent their flux from diminishing off as they travel from surface to the CDMS detectors installed underground). The current analysis assumes that this is not the case. Future studies may be performed to quantify the probability for such an occurrence.

- A WIMP search analysis removes events during periods when the rate of detector triggering becomes abnormally high, considering them to be related of sudden jump in detector noise levels. However, the cosmic activity is different among various days, and future studies may be done to verify that period of high cosmic activity aren't accidentally being removed by the analysis.

- As described in Section 4.4.8, the requirement that energy depositions in different towers (except the one being analyzed) be consistent with detector noise allows rejection of glitch induced events. Future studies may aim towards finding additional new/existent parameters that are able to classify glitch events with higher fidelity. Such studies are currently ongoing within the CDMS collaboration, as described in [235]. Additional efforts may aim to study the distribution of energy and event occurrence location corresponding to glitch induced events.

- The current LIP analysis requires sufficiently large energy to be deposited in each of the 6 ZIP detectors of a tower (i.e., energy deposition in each of the 6 ZIP detectors should be above low analysis threshold) before it is considered to be a valid LIP induced event. Future efforts may be relax the criteria and perform LIPs analysis requiring significant energy depositions in 5, or 4 consecutive and/or non-consecutive detectors of a tower. This would also

change the corresponding background estimates.

- Future studies may aim to improve the model used to reconstruct the location of event occurrence inside the detector (the reconstruction model used in current analysis is described in [242]). The current model obtains necessary coefficients to reconstruct the radial position by studying electromagnetic recoils with ionization yield≈1. Similar model is then used to reconstruct event occurrence location for surface events (with low yield). Surface events are known to have different phonon properties than events occurring due to interactions in the bulk of crystal (as described in various CDMS thesis [228–231]), and it may be expected that a correct reconstruction procedure should use different set of coefficients for the former. An improved model may help in more accurate estimate of reconstructed location for surface events, which in turns improves the correction procedure employed to obtain reconstructed location resolution (described in Section 4.5.12.3 and similar sections). Additionally, the procedure employed to perform the correction to resolutions using the distribution of distance between surface event occurrence location in neighboring detectors may itself be improved.

- The definitions for the energy consistency test-statistic, Eq. (4.24, 4.25) may be developed in future analysis. One of the possibility is to combine the energy consistency and tracking criteria into a single criteria wherein energy consistency test statistic is only calculated over the likely estimates for polar angle of LIP incidence obtained from linear tracking fitting routine.

- Above mentioned improvements may be coupled with an extended LIPs study based on increased upper thresholds to re-analyze the events (described in Section 4.5.15) and either accept them as being indicator for LIPs, or to reject

them with greater confidence. The 511keV line from annihilation of positively charged beta emission with electron may be used to calibrate detectors upto ≈550keV.

- Future studies may aim to obtain a predicted value of LIP flux incident on underground detector. This may be done by employing a certain mechanism for cosmogenic LIP creation and a second model describing energy loss by LIPs as it travels from its point of creation to underground detectors. The predicted LIP flux can be compared against the obtained limiting flux value to reject physical parameter space for existence of LIPs of a given fractional charge.

5. FABRICATION EFFORTS AT TAMU

The previous section (Section 3 and Section 4) of this dissertation describe the setup of CDMS experiment which is primarily designed for WIMP search, but is alternately used for detection of LIPs. With a further emphasis on WIMP detection and achieving higher sensitivity, as shown in Fig. 5.1, it is ultimately required to use detectors with ∼1ton or larger target mass (This also allows an increase in sensitivity towards LIPs search). Feasibility of such a large experiment requires a significant decrease in the cost of fabricating individual detector elements. However, detector production step alone costs ∼350k per kilogram of detector [306], making it unfeasible to simply scale the usual fabrication efforts to achieve ∼1ton detector mass. Thus, it is required to reanalyze the existent fabrication steps and introduce necessary improvements allowing for a reduction in fabrication cost. Appendix K describes the set of steps used by CDMS collaboration to fabricate a ZIP detector, starting with a cylindrical germanium/silicon crystal.

In addition to cost considerations, it is known from Appendix H.7 that the properties of phonon sensor (TES) changes with position. For signals depositing low energies, this variation cannot be normalized out using the "position correction" procedure. Thus, a homogeneity in detector properties allow the WIMP analysis to be pushed down to lower energies, and with greater confidence.

Section 5.1 below describes a few of the existent problems corresponding to certain detector fabrication steps, and Section 5.2 describes the efforts undertaken to address them. Additional fabrication related efforts are described in Section 5.3. Possible future efforts are described in Section 5.4.

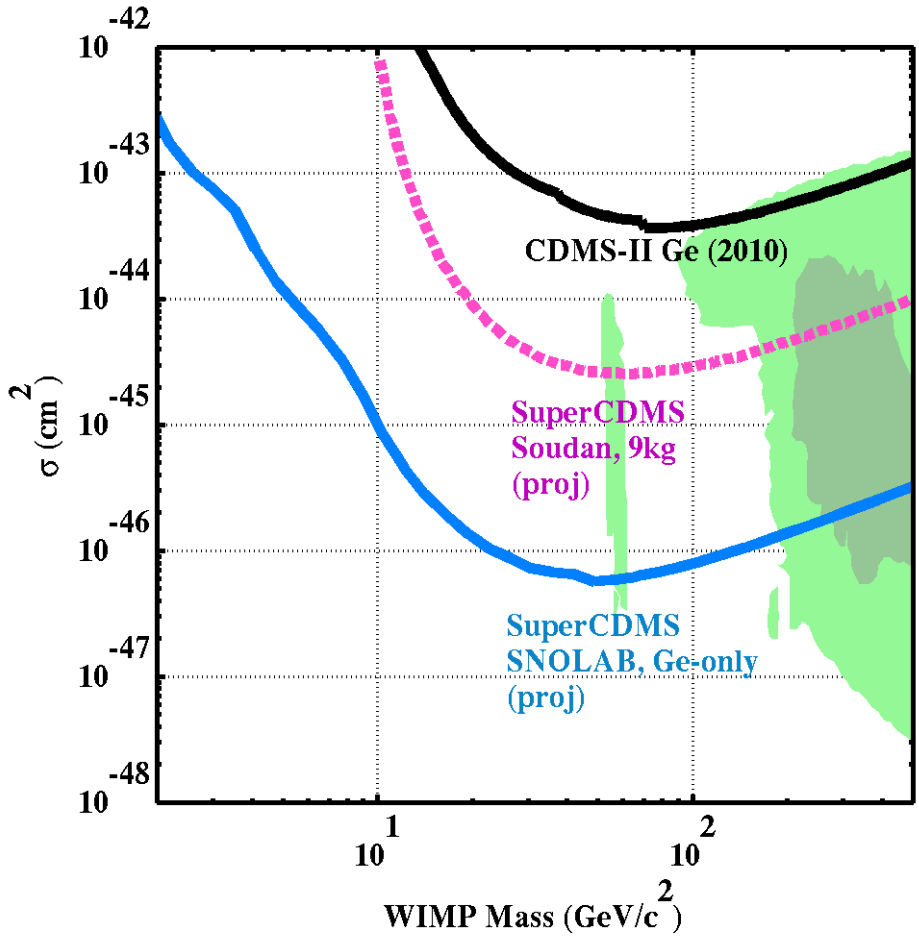

Figure 5.1: The green shaded regions represent 68% (light green) and 95 % (dark green) confidence interval on phenomenologically favored parameter space for WIMP existence relating the cross-section for its scalar interaction with nucleus and WIMP mass. The favored regions are determined from profile likelihood fits including LHC and direct detection constraints [343]. The solid and dashed curves indicate the current and future sensitivity for CDMS, assuming ≈0 background operation can be maintained. Plot taken from [344]

5.1 Existent Barriers to Scaling Detector Fabrication

Feasibility of a ∼1ton scale experiment requires a significant decrease in the cost of involved with individual detector. However, for the CDMS-II detector production, the dominant cost per detector (∼85% of total cost) was due to detector fabrication

and testing, rather than raw materials [239]. The detector production step alone costs ∼350k per kilogram of detector [306], making it unfeasible to simply scale the usual fabrication efforts to achieve ∼1ton detector mass. In addition to the associated cost with fabricating one detectors, the associated fabrication time also hurts the feasibility of proposed scaling. As describes below, the time to obtain a batch of detector can be as large as ∼1month, with only about 30% of total detectors fabricated in a batch deemed suitable for underground installation in the CDMS experiment [306].

The sections below describe two major hurdles (bottleneck in crystal polishing rate and variation in TES properties) which increase the cost and detector fabrication time, hurting the feasibility of a 1ton experiment.

5.1.1 Bottleneck in Crystal Polishing Rate

ZIP detectors employ 40-300nm thick sensors pholithographically fabricated on metallic films. To obtain films with uniform thickness and for a successful lithography step, it is necessary that any surface irregularities (like scratches, dents, chips, shown in Fig. 5.2) on the crystal be removed, it is polished to a surface roughness much less than the minimum thickness of any metallic film deposited on it (∼1nm), and the maximum topographical variation in surface height should be of the same size (or less) as the smallest pattern/feature on the sensor circuit ($\sim 2\mu m$). The former describes the limit on crystal smoothness, and the latter describes the limit on crystal flatness, to be obtained through polishing and before the crystal is sent through other fabrication steps. It is necessary to polish crystal when obtained for the very first time and after each attempt where the fabricated sensors on the crystal substrate do not match the desired characteristics and need to be removed before a second attempt at sensor fabrication on same crystal can be made.

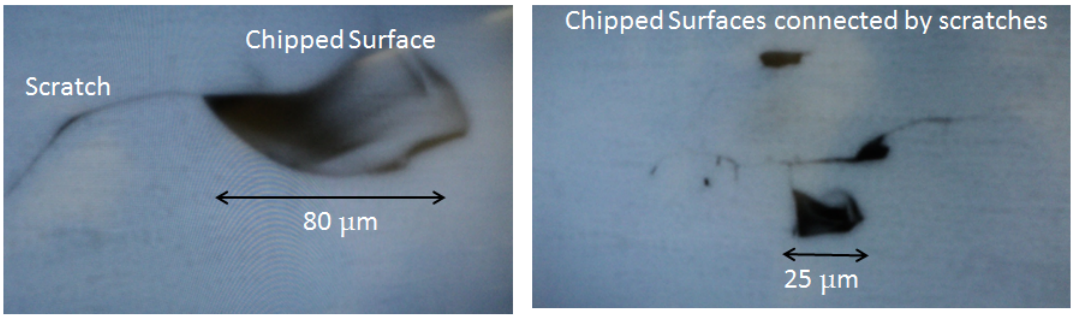

Figure 5.2: Examples of defects on crystal surface (scratches and surface chips) are shown.

Although it is not a technically challenging step (as described in Appendix K.2), it is still an extremely time consuming step requiring as much as ∼7-10days to polish both surfaces of the crystal. Additionally, it is not guaranteed that a polished crystal will definitely be available after the elapsed time, as the presence of even a single scratch one of the two surface may force the crystal to be sent back to the polishing step. Currently, crystal polishing is done by external service providers. It is an uncertainty in the throughput rate of polished crystals (obtained back from the external service providers) which may act as bottleneck in the overall detector fabrication required to make a ∼1ton detector mass experiment feasible.

5.1.2 Variation in Quasiparticle Trap Properties

Before CDMS-II, the ZIP detectors had nearly all the phonon side covered by aluminum collector fins. Such a configuration is non-optimal because the average distance a quasiparticle has to diffuse before being able to diffuse to a TES is ∼3.5 times larger than the quasiparticle diffusion length ($\sim 180\mu m$) [136, 231]. Due to recombination of quasiparticles back into the Cooper pairs, the design suffered from a quasiparticle collection inefficiency of ∼95%. It has a limited sensitivity to the small energy depositions expected from WIMP-nucleus interactions because the signal-to-

noise ratio (S/N) in the phonon channel is critically dependent on the number of collected quasiparticles per keV of deposited energy.

The CDMS-II ZIP detector QET design was reoptimized, but still providing an efficiency of ∼25% [231,235,241]. The result is based on a special test device, designed and ran to measure the diffusion characteristics of aluminum films [235]. It was also inferred that :

- The quasipaticle diffusion length (or, the length travelled by quasiparticles before they recombine, l_{trap}) inside the aluminum film is $\sim 180 \pm 10\mu m$ [235]. However, this result cannot be applied to CDMS-II aluminum films, because their thickness was increased to 300nm, as compared to 150nm aluminum film thickness used in the abovementioned device. Thus, if the quasiparticle diffusion in the test-device was limited by the film thickness, then increasing it by a factor of 2 would increase l_{trap} by $\sqrt{2}$. By contrast, if the diffusion constant for the film was already intrinsically limited, then l_{trap} is more likely to be invariant. Additionally, it is known from residual resistivity ratio (RRR) measurements, obtained by comparing resistivity of aluminum film at room and 4K temperatures, that quality of aluminum films are of widely variable quality (Smallness in RRR relates to largeness in presence of impurities inside a thin film [345]).

- The quasiparticle transmission probability across the aluminum/tungsten boundary is 0.0025 ± 0.0005, which can cause a qualiparticle collection loss by ∼30% [235].

5.1.3 Variation in TES Properties

A significant driver of the detector fabrication cost and time is the variation in the superconducting transition temperature (T_c) of the tungsten thin film (which

forms the TES) and the efforts undertaken to nullify the effect of those variations. As described in Section 3.2.2.2, the ZIP detectors employ 4 phonon measurement channels arranged in a quadrant and collect the electrical signals from 1036 parallel wired TES to create an electrical trace of corresponding phonon measurement. A position-dependent variation in sensor T_c and superconducting transition width produces a position dependent TES response to similar signal occurring at different location inside the crystal. The variation in phonon response also occurs depending on the depth of event occurrence, and is used to distinguish WIMP signal against possible background. However, this rejection capability suffers due to the mixing of depth dependent variations in phonon signal with the effects caused by T_c variations.

The tungsten films is deposited using DC sputtering (Sputtering a process of depositing thin films. It is discussed in Appendix J.1), and can be deposited as one of the two crystalline phases: α ($T_c \sim 15mk$, resistivity $\rho \sim 5.3\mu\Omega cm$ having bcc crystal structure) phase similar to that found in bulk tungsten, and β ($T_c \sim 1-4K, \rho \sim 150-350\mu\Omega cm$ having A15 cubic structure) phase [308, 310, 316], or a mixture of two crystalline phases [309] with the resultant phase having strong dependence on film thickness, oxygen partial pressure in the chamber, substrate bias, temperature, and deposition power [310, 311]. It is also reported that beyond an empirical critical thickness ~50nm, the film transforms from the beta to the alpha phase and further deposition occurs only in this phase [309,312]. It is reported that the as-deposited films are mostly beta phase and undergo transformation to the alpha phase at room temperature in tens of hours to several days. However, the occurrence of this transformation is dependent upon the substrate used to deposit the film [316]. In addition to above, the properties of tungsten film depend strongly on the film purity. The films exhibit an incremental increase in resistivity due to incorporation of impurities, by 1.1-4.2nΩcm/ppm-wt, where ppm-wt is the impurity

level by weight [313–315]. Focusing on the transition temperature of tungsten thin film (which relates to its applicability in TES), it is found to relate with film stress and the substrate on which the film is deposited [316].

For use in CDMS experiment, a tungsten thin film TES with a controlled mixture of the two phases (predominantly α phase) is needed, exhibiting $T_c \sim 100mK$. A fabrication recipe to achieve this goal was developed at Stanford [320,321]. Although the fabricated films are predominantly composed of α phase, the T_c values vary for phonon channels corresponding to different batches of detector, shown in Fig. 5.3.

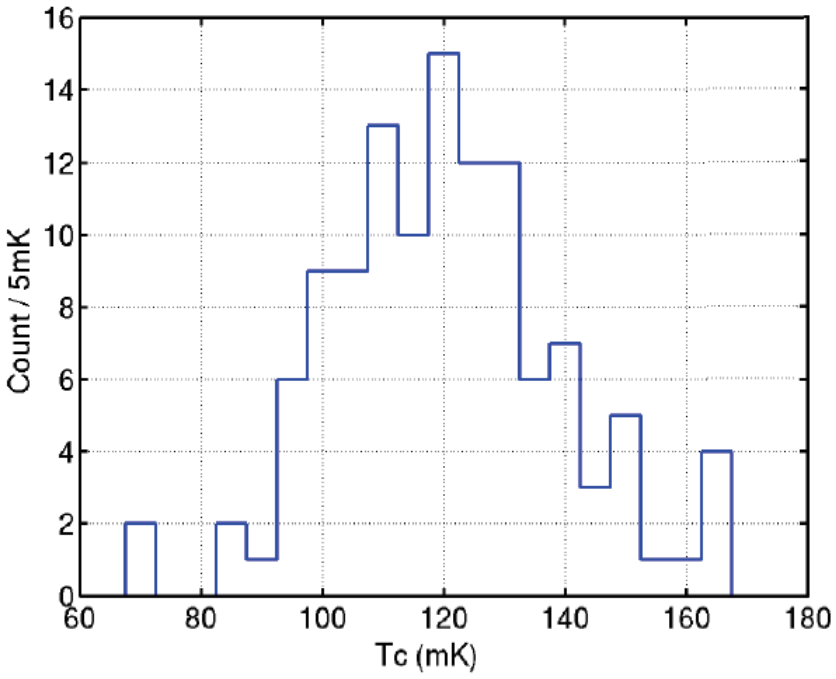

Figure 5.3: Variation of superconducting transition temperature (T_c) among as-fabricated phonon measurement channels corresponding to different detectors used in CDMS-II experiment. Figure taken from [306].

In addition to there being T_c variation among detector batches, T_c variations across the surface of individual detector are also existent. A proxy deposition is

simultaneously done over a thin wafer while tungsten thin film is being deposited over the crystal, and is subjected to cryogenic testing to obtain a "map" of T_c variation as existing in the film deposited on crystal, as shown in Fig. 5.4. The T_c variations (existing on the crystal) are normalized out by implanting the film with magnetic ^{56}Fe ions, and using the proxt T_c map to estimate the dosage of the implanted impurities (Presence of magnetic impurities in the film affect the T_c of the TES) [317–319]. After implantation, the proxy wafer and the crystal is again cryogenically tested to verify that the T_c variations have indeed been removed (and may still be rejected if they do not meet standards).

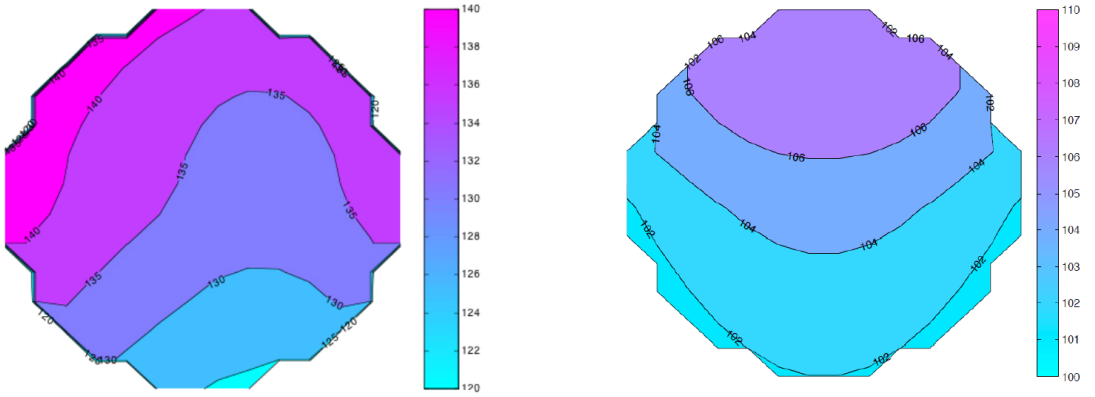

Figure 5.4: LEFT: Variation of tungsten T_c (in mK) within a single test-wafer. The map is generated after cryogenic measurements. The variations are normalized out by doping magnetic ^{56}Fe ions (via an ion implantation step). RIGHT: The variation in T_c within the same test-wafer after ion implantation step. Figure taken from [306].

Although the above mentioned procedures to rectify the variations in film T_c reproducible, it is an extremely costly and time consuming option (2 set of cryogenic measurements at ∼80mK and one ion-implantation step carried out through specialized service providers), and precludes feasibility for an experiment of ∼1ton detector

mass.

5.2 Addressing Fabrication Problems

The following section describes the efforts taken in the CDMS detector fabrication lab at TAMU to study, understand and resolve the above mentioned problems affecting the feasibility for a 1ton scale experiment.

5.2.1 Improving Crystal Polishing Rate

As mentioned above, the step of crystal polishing is inherently time consuming (A detailed description of the polishing step is provided in Appendix K.2). The throughput rate is further depreciated because there is only one external service provider being used for crystal polishing, and the requirements for a polished crystal is extremely stringent. To overcome the problem, additional instruments were installed at TAMU allowing polishing of the silicon/germanium crystals, as shown in Fig. 5.5.

In addition to simply improving the throughput rate, an involvement in polishing steps also provides an improved insight to control, review and improve the polishing step, like, development of post-polish cleaning method at TAMU and recent addition of heavy chemical etching (suggested by Stanford fabrication lab).

5.2.2 Reducing the Variations in Quasiparticle Trap Properties

This section outlines the efforts taken at the CDMS detector fabrication lab at TAMU to improve the probability of quasiparticle tunneling, from aluminum films (quasiparticle traps) into the tungsten TES. Future effort may aim to obtain processing parameters allowing for deposition of aluminum thin film with increased quasiparticle diffusion length, mentioned in future studies section (Section 5.4).

As described in Appendix K.4, the aluminum thin film (which collects quasi-

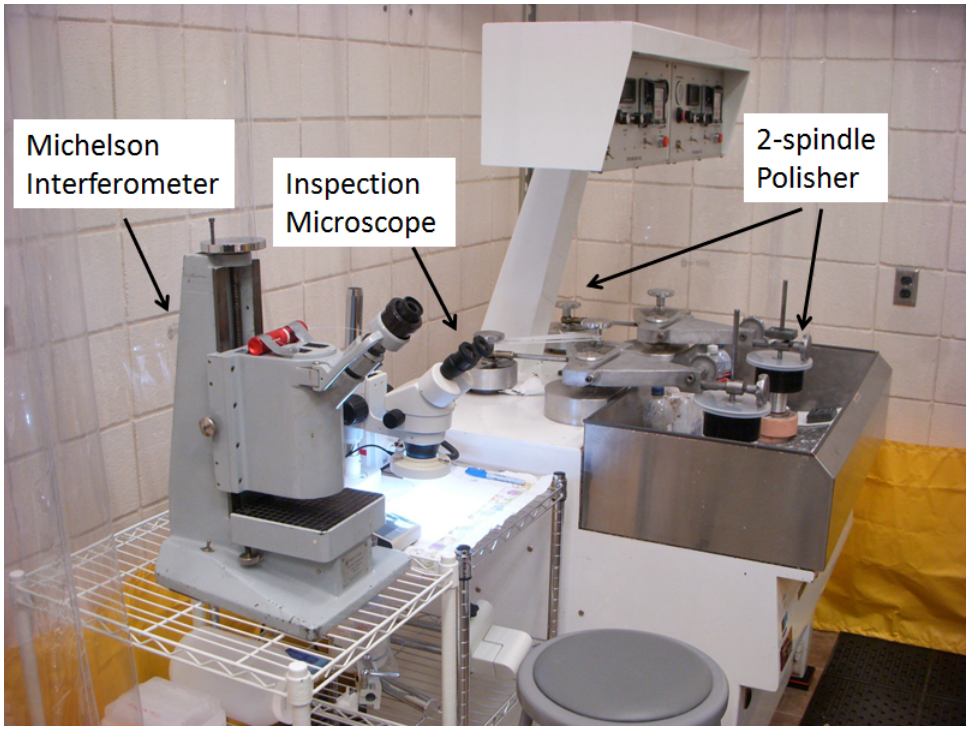

Figure 5.5: To improve the throughput rate of polished crystal the following were installed in the CDMS detector fabrication lab at TAMU: A 2-spindle polisher (to polish crystals), inspection microscope (to verify that polished crystals are scratch-free) and a table-top michelson interferometer (to verify surface flatness). Figure taken from [306].

particles and funnels them into the TES) is immediately covered by a thin layer of tungsten (it is done while the substrate is in vacuum. In the description below it is referred as the first tungsten layer). To allow a proper diffusion of quasiparticles, the second tungsten layer (on which TES are patterned) is required to make a nice contact with the first tungsten layer, as shown in Fig. 5.6. The reason for developing such a design is described in Appendix K.4 and Appendix K.6. While it is possible for the TES to directly make contact with the aluminum film through the small vertical area of 300nm height, the quasiparticle tunneling through such a contact is deemed to be extremely unreliable because the exposed aluminum face is of small

area, and would form a stable oxide layer which may not be removed by performing a RF etch before depositing the second tungsten layer (the argon gas ions performing the etch action strike in a direction perpendicular to the substrate surface; RF-etch is further described in Appendix J.2.2). However, this RF etch (performed before depositing second tungsten layer) easily removes the weakly bound tungsten oxide on top of the first tungsten layer, and ensures a nice contact of it with the second tungsten layer. Thus, it is *assumed* that the low quasiparticle tunneling probability may not be ascribed to the presence of oxide layer between the quasiparticle traps and the second tungsten layer (containing the TES).

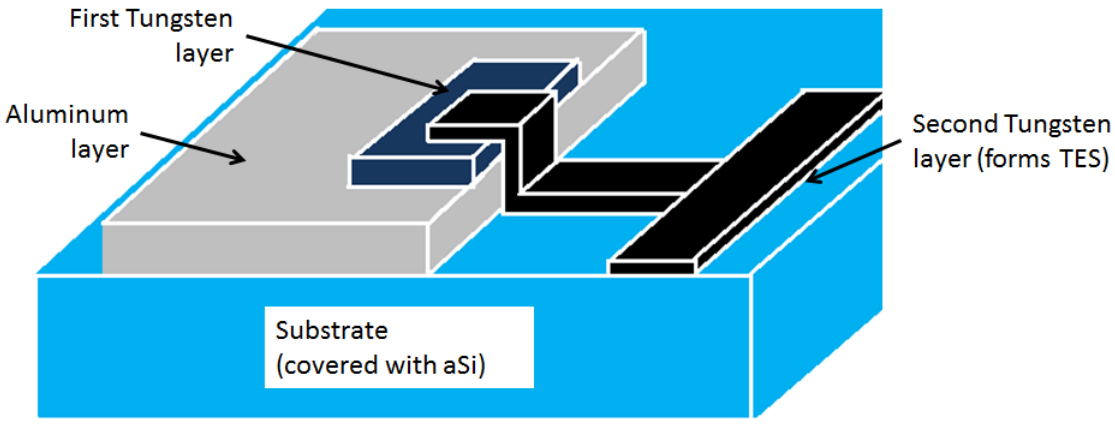

Figure 5.6: A schematic of contact between the aluminum quasiparticle-collection layer, through which the quasiparticles diffuse into the first tungsten layer (deposited immediately after the aluminum layer without letting the substrate be exposed to atmospheric oxygen. The aluminum layer is itself deposited after covering the crystal surface with a thin layer of amorphous silicon, or aSi). If the first tungsten layer is not deposited immediately after the aluminum layer without exposing the latter to oxygen, then a stable, passive layer of aluminum oxide would form, preventing the diffusion of quasiparticles to TES. The figure is not to scale.

A possible source of this problem was revealed by studying similar circuits fabri-

cated on silicon wafer, studied using scanning electron microscope (SEM). It relates to the fact that wet (chemical) etching is isotropic in nature. When etching the aluminum film, lying below the tungsten film, the isotropic nature of wet-etch process creates an undercut, as shown in Fig. 5.7. It is necessary to nullify the effect of undercut in aluminum film by repeating a tungsten etch (on the first tungsten layer). If this tungsten etch is not done completely and the tungsten overhang remains, then it prevents a conformal deposition of second tungsten layer connecting the aluminum quasiparticle traps with the TES. Such a feature was found existing in test wafers prepared using the same etch "recipes" used to fabricate CDMS-II detectors (the existence of such feature on CDMS-II detectors themself hasn't been verified). By increasing the "tungsten overhang" etch time, an optimized etch recipe was developed by the group, allowing a conformal deposition of second tungsten layer. A schematic diagram, and physical observation made on samples are shown in Fig. 5.8.

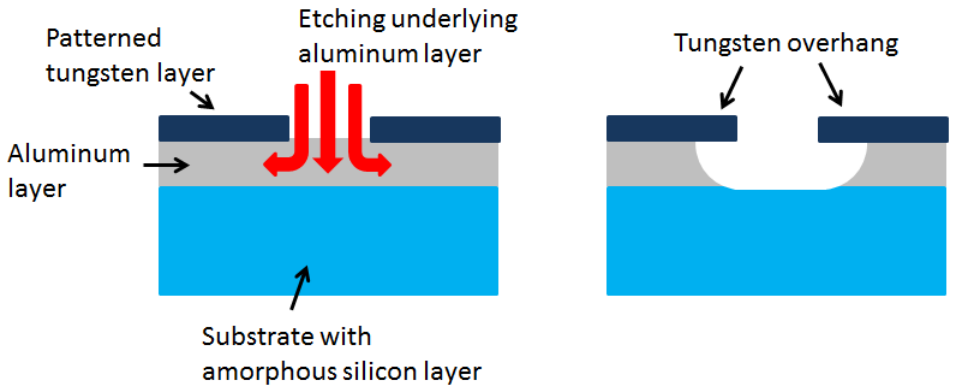

Figure 5.7: The aluminum layer is etched after the tungsten layer has been etched. Isotropic etching of aluminum layer creates an overhanging tungsten structure.

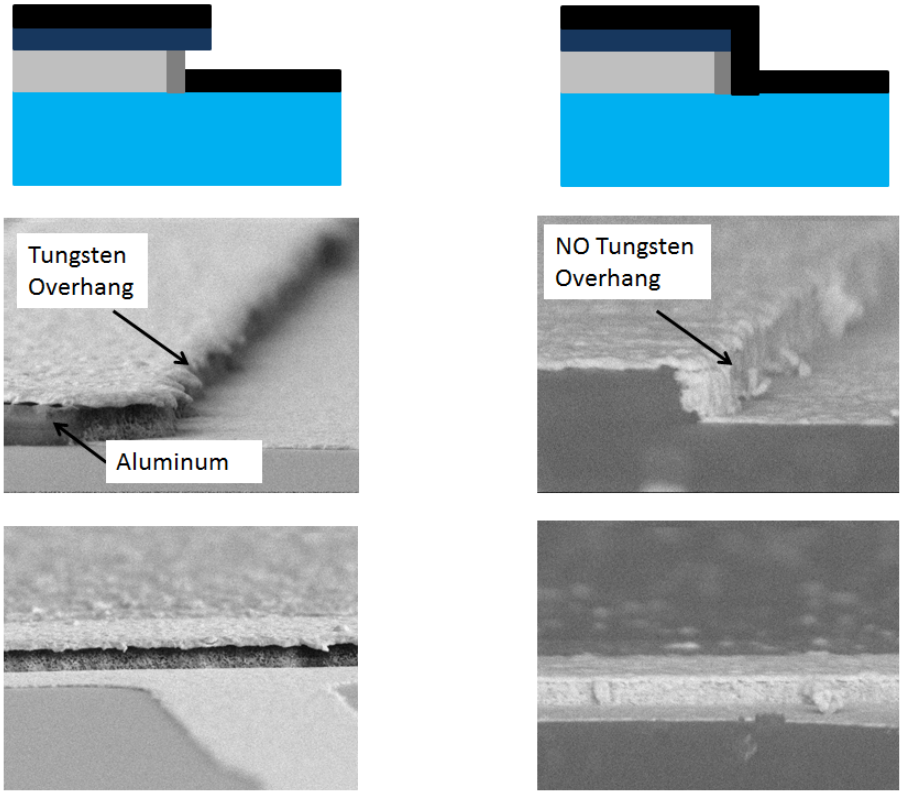

Figure 5.8: In the schematic (top row), the crystal, with amorphous silicon layer (blue) is shown in blue, the aluminum film is shown in light grey, first tungsten layer in dark blue and second tungsten layer in black. Due to exposure of aluminum to atmospheric oxygen, a stable, vertical layer of aluminum oxide is *assumed* to be present, shown in dark gray. LEFT: Schematic (top row) and SEM images corresponding to deposition of second tungsten layer without a full removal of overhang from first tungsten layer. In this case, there is a bare contact between the wall of aluminum film (or aluminum oxide) and the second tungsten layer. RIGHT: A conformal deposition after overhand etch optimization. The figures in top row are not to scale. The remaining 4 SEM figures have different scales. Thus, it is removed for keeping the figures unambiguous despite being placed beside each other.

5.2.3 Reducing the Variations in TES Properties

The variation in TES properties can mainly arise due to variation in superconducting transition temperature (T_c) across the substrate surface and due to variation

in TES width.

5.2.3.1 Reducing the Variations in TES T_c

Variations in T_c is primarily attributed to presence of contaminants, especially oxygen and water vapor (existing inside the deposition chamber), or as oxide layer on top of the substrate (where tungsten layer is to be deposited). In addition to performing a thorough substrate cleaning (described in Appendix K.3), the additional measures implemented to reduce contamination are described below.

SEGI: The organization of thin film deposition system at TAMU (called SEGI, because it was originally developed by the Semiconductor Engineering Group Inc.), itself allows for film deposition in an environment with reduced contamination levels. The deposition system consists of two separate chambers, called "Load Lock" and the "Processing Chamber", as shown in Fig. 5.9. The processing chamber is the main unit where thin film deposition is done. It has a flat-bed design, i.e. the target and substrate and arranged in parallel horizontal planes, separated by a certain, adjustable distance. When not in use, it is always kept at high vacuum ($\sim 10^{-7} torr$) through a cryo pump. To load substrate inside the processing chamber, they are put inside the load lock and carried from atmospheric pressure (760 torr) to $\sim 10^{-3} torr$ using a rotary pump, and then to $\lesssim 10^{-5} torr$ using a turbo pump (backed by rotary pump). Doing so reduces the amount of oxygen and water vapor in the load lock, which may diffuse to processing chamber during the brief time they are opened to each other to allow the transfer of substrate to the processing chamber. A high purity argon gas source is used to transfer the argon gas, through steel pipes, to the deposition chamber (argon is used to create plasma, and assist in thin film deposition, via sputtering. Sputtering is described in Appendix J.1). Since the substrate needs to be transferred back to load lock after the processing is done, it is imperative to

keep load lock under vacuum even when a thin film deposition is being done inside the processing chamber. To retrieve the substrate after the processing is over and it is transferred back to the load lock, the load lock is flushed with pure nitrogen up to atmospheric pressure. Once the substrate is retrieved, the idle load lock is again pumped back to $\lesssim 10^{-5} torr$ using the rotary and turbo pump. These set of operations ensure a low contamination level inside the processing chamber of thin film deposition system.

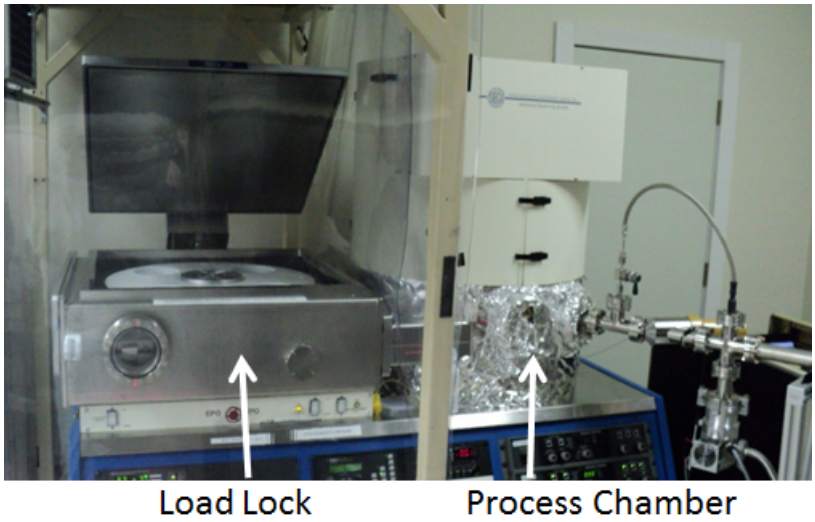

Figure 5.9: The semi-automated, Semiconductor Engineering Group Inc (SEGI) sputter deposition system at CDMS detector fabrication lab in TAMU, contains 2 separate chambers; the "Load Lock" where the user may load upto 4 crystals and 4 wafers for simultaneous processing, and a "Process chamber" where actual thin film deposition occurs. The opening of load lock, through which the substrate is put inside the machine, is encased in a class-100 clean tent. The plumbing on extreme right connect to the in-situ residual gas analyzer (RGA).

RGA: To monitor the concentration of the contaminant gases inside the deposition chamber, an in-situ residual gas analyzer (RGA) is attached. Deposition is not

done if the contaminant concentration is qualitatively high.

Aluminum Bury: Despite the above precautions, there will always be some equilibrium level of contaminants inside the system. To suppress the levels immediately before thin film deposition, the processing chamber is coated with a layer of aluminum (essentially carrying out an aluminum thin film deposition, but without any substrate inside the chamber). This process is called "Aluminum Bury". The contaminants, like oxygen, water vapor and products from decomposition of pump oil vapors are physically or chemically trapped by the deposited aluminum layer. The deposition is done at high argon pressure so that the aluminum atoms get diffused across entire chamber as they collide with argon atoms. Fig. 5.10 shows a reduction in chamber contamination levels after an aluminum bury.

Target Cleaning: Since the multiple thin film deposition targets (silicon, aluminum and silicon) are present in same deposition chamber, it is possible for the target surface to trap contaminants (present inside the processing chamber), while the machine is not being actively used. To prevent deposition of these contaminants, the initial 25sec of deposition is done on a "shutter" which prevents the exposure of the substrate to the target. After 25sec, the shutter is opened and the deposition is allowed to proceed.

Rotation Speed: Once loaded inside the deposition chamber, the substrate rotates in a horizontal plane and crosses the target (placed horizontally, at a height of $\sim$3inch above the substrate) after a certain time. Every time it crosses below the target, it gets a "coating" of thin film, comprising of sputtered target atoms. The example below illustrates that in such a process, the thickness of deposited film depends on the substrate rotation speed.

Example: Consider that the film deposition rate is 1nm/sec (under certain process parameters), for every second spent by substrate below the target. However, the

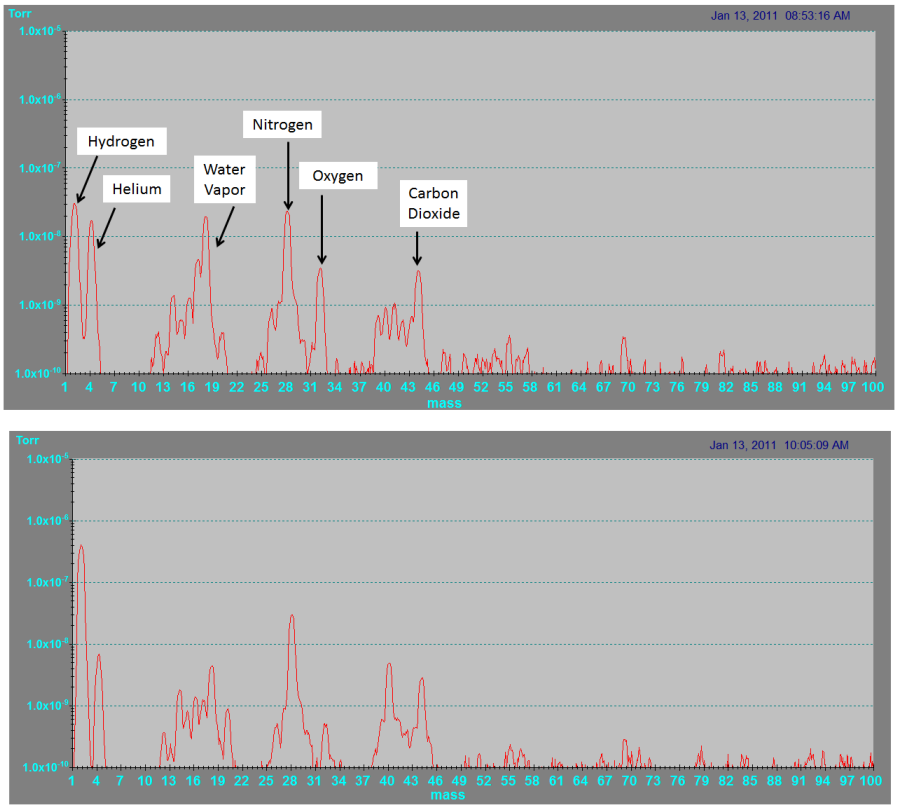

Figure 5.10: Comparison of gas levels in deposition chamber, before and after aluminum bury. A reduction in water vapor and oxygen levels is found, along with suppression of gases with heavy molecular mass (formed from the decomposition of pump oil vapors)

target is shaped as a circular sector with an angle of 120°, and only a third of total rotation time is spent below the target. Consider the two cases, each executing a "film deposition recipe" with a deposition time of 50sec.

- For a slow rotation speed of 3rpm, the substrate will make $2\frac{1}{3}$ rotations within the allocated time, spending $6\frac{2}{3}$sec under the target in each rotation. In reality though, depending on its initial location inside the processing chamber (as shown in Fig. 5.11), it passes under the target either 2 times (right case) or 3 times (left case), getting a film deposition of either 13.3nm (right case) or

20nm (left case).

- For a slow rotation speed of 20rpm, the substrate will make $16\frac{2}{3}$ rotations within the allocated time, spending 1sec under the target in each rotation. In reality though, depending on its initial location inside the processing chamber (as shown in Fig. 5.11), it passes under the target either 16 times (right case) or 17 times (left case), getting a film deposition of either 16nm (right case) or 17nm (left case).

It may be argued that once the total deposition time (the "deposition recipe") is fixed, one may opt for a slower rotation speed, such that the substrate undergoes integral rotations within the allocated time. While above is a valid argument, it is the very process of determining the recipe which suffers a setback due to variation in film thickness.

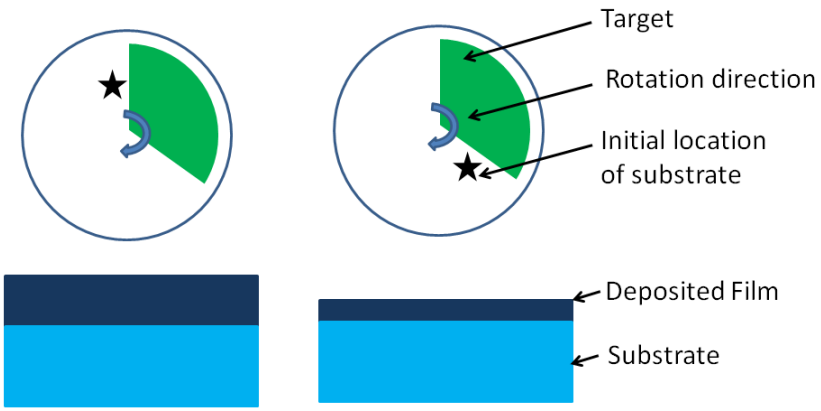

Figure 5.11: Before the actual process of film deposition starts, if the substrate is placed before the target (LEFT), the thickness of deposited film will always be greater than, or equal to the thickness of film deposited on substrate, if placed after the target (RIGHT). The difference in film thickness for the two cases depends inversely on the rotation speed.

Resistance Measurements: During deposition of the second tungsten thin film (forming the TES) on the crystal, a simultaneous deposition is made on a silicon test wafer. Since the film on test wafer and crystal is simultaneously deposited, it is expected that both the film will have similar T_c. Additionally, it is recognized that for this test wafer, its film resistance closely relates to its T_c. Thus, the crystals with varying TES T_c can be identified by performing a room temperature 4-probe sheet-resistance measurement of tungsten thin film deposited on the test wafer (4-probe measurement is described in [346]). This helps in reducing wastage of both time and money (in performing cryogenic testing) on crystals which are expected to have large T_c variation and be unsuitable for use in CDMS experiment.

Results: With the above mentioned efforts, the detector fabrication group at TAMU was able to make detectors on germanium crystals with a full-width variation of ∼8mK across detector surface (described in Table 5.1), as compared to ∼20-25mK full-width variations observed in detectors fabricated outside TAMU, shown in Fig. 5.4. Although, this result is based on only 3 fabricated detectors (with more detector testing in queue, and would be described in future theses), the confidence in the conclusion that the group at TAMU was able to reduce variations in T_c of tungsten film is based on results obtained from depositions done on test wafers. The result, shown in Table 5.2, imply an achievement of ∼1.5mK full-width variation in tungsten T_c within one wafer, and ∼5mK full-width variation among different wafers. With such a low variation in T_c of tungsten film, both within a crystal and among different batches, it is possible to exclude the time and cost intensive steps of performing 2 set of cryogenic measurements at ∼80mK and one ion-implantation step (originally done for each crystal to homogenize the effect of T_c variations).

Table 5.1: The T_c for 4 phonon measurement channels, fabricated on germanium crystals at TAMU. All measurements are in mK. "-" means that due to certain wiring problems, a successful reading was not obtained.

Detector	T_c(Channel-A)	T_c(Channel-A)	T_c(Channel-A)	T_c(Channel-D)
G22A	93	87	85	-
G34C	-	99	98	96
G38C	86	91	88	-

Table 5.2: The minimum and maximum T_c of tungsten film (deposited over amorphous silicon layer) in a test wafer. All of the deposition were done using same process parameters and staggered over several days. All measurements are in mK. "-" means that due to certain problems, a reading was not obtained.

Sample Name	T_c(Minimum)	T_c(Maximum)
008G23	98	-
008G25	96	-
008H23	99.5	-
008H24	96.5	95
008H25	91	92.5
008I03	98.6	-
008I04	93.3	-
008I05	97	98.5

5.2.3.2 Reducing the Variations in TES width

From SEM studies of the phonon sensor pattern deposited on the crystals, it was observed that the width of TES vary radially; TES with largest width ($\sim 3\mu m$) exist near the center and those with minimal width ($\sim 2\mu m$) near the periphery. A study on the topic is ongoing, and a detailed analysis may be presented in future theses.

5.3 Additional Studies Performed at TAMU

This section describes two of the additional fabrication related efforts undertaken at TAMU, other than the above mentioned efforts aimed at fabricating CDMS de-

tectors with homogeneous set of properties.

5.3.1 Amorphous Silicon Deposition Parameters

The amorphous silicon (aSi) thin film, deposited first on a cleaned substrate helps in reducing the occurrence of surface events [232, 327] (surface events are described in Section 3.3.3, and are undesirable because they form a major background to WIMP analysis) and also prevents the chemical etching of underlying germanium substrate in certain fabrication steps, described in Appendix K.5 and Appendix K.7. If there are voids in the amorphous silicon film, then the underlying germanium substrate can get etched/pitted when exposed to chemicals. It is desirable to prevent such occurrences because the possible affect of such features on WIMP analysis is unknown.

An etch pit study was done at TAMU to ascertain the deposition parameters for which less voids are formed in the amorphous silicon layer. In the study, the amorphous silicon layer is deposited over another layer of silicon dioxide (SiO_2), and treated with Hydrofluoric acid (HF). Wherever there is a void, the HF will move through it and etch the underlying SiO_2, forming a "crater". A schematic is shown in Fig. 5.12. Also shown are the results of the study. It was found that there are multiple craters when the amorphous silicon film was deposited at 2kW or at 1kW, but as few as 1-crater/cm^2 in film deposited at 500W.

5.3.2 Relation Between T_c and Sheet-Resistance

In a ZIP detector, the tungsten thin film (forming the TES) is deposited on a layer of amorphous silicon. As an intermediary step to achieving this goal, the fabrication group at TAMU performed studies on tungsten thin films deposited immediately over polished, cleaned silicon test wafer (without an intermediate thin film of amorphous silicon). For such an arrangement, it was found that the sheet-resistance of the

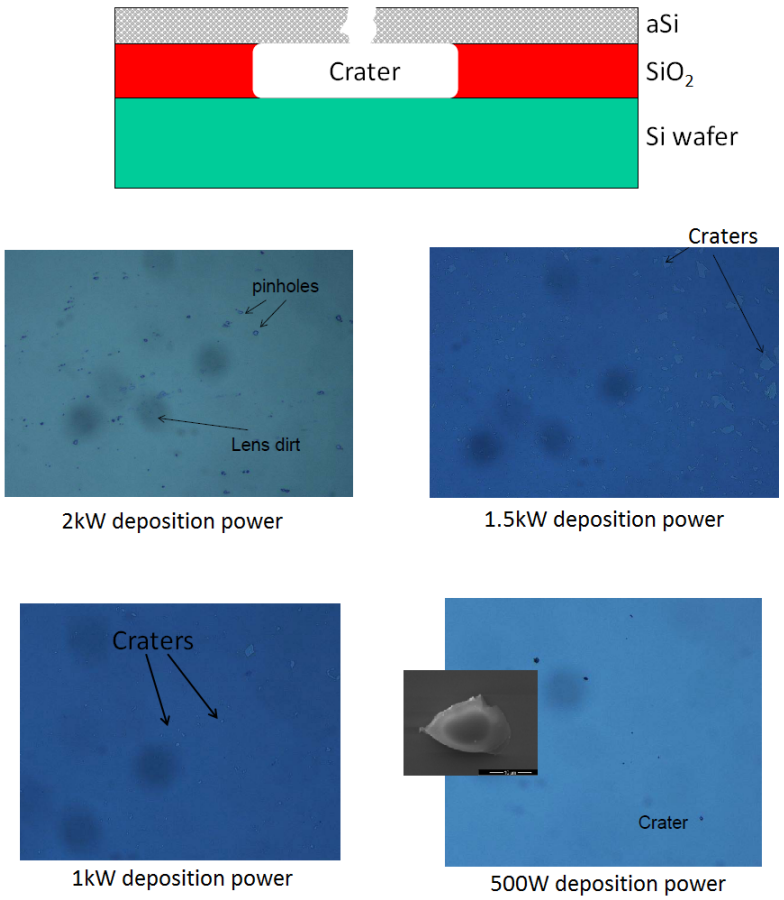

Figure 5.12: A schematic showing the formation of "craters" in silicon dioxide (SiO_2) bed-layer wherever there is a hole in the above amorphous silicon (aSi) layer. Also shown are the results of etch pit study as the deposition power for aSi layer is varied from 2kW to 500W. As few as 1-crater/cm^2 was found in film deposited at 500W. Some wafer cleavage dust is also found (and cross verified using SEM). Figure taken from [307].

deposited tungsten thin film correlates with its T_c, as shown in Fig. 5.13. For ZIP detectors fabricated on silicon substrate, where it may be viable to remove the layer of amorphous silicon, this result can be used to search for new set of deposition parameters allowing the tungsten film to have a sheet-resistance, and thus, a different T_c.

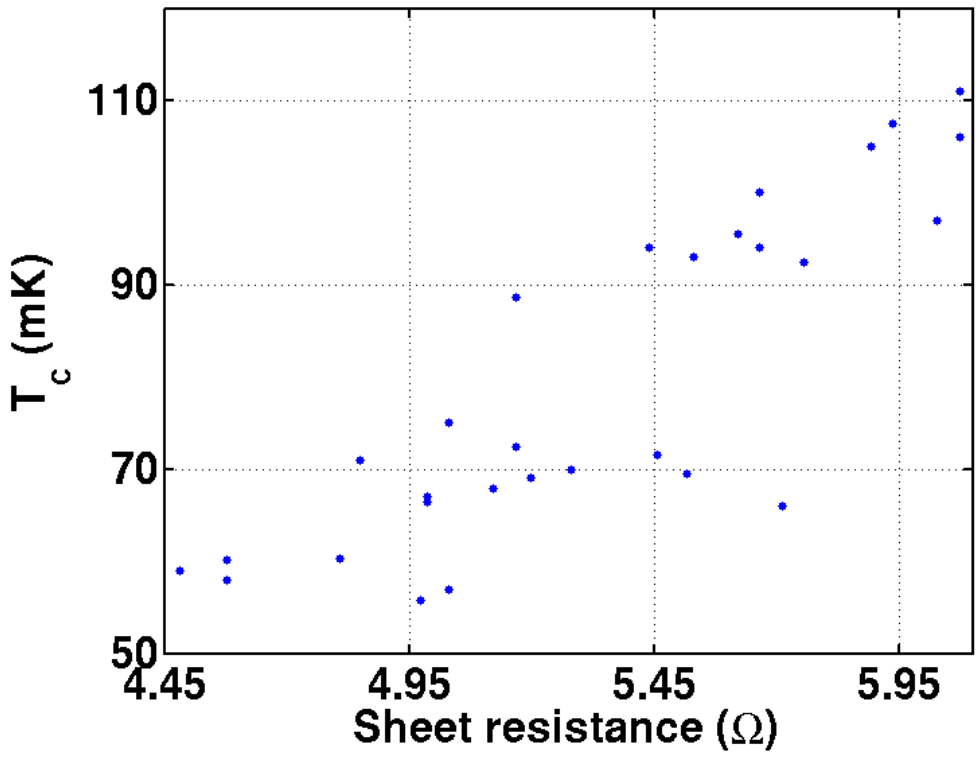

Figure 5.13: Variation of T_c with sheet resistance of tungsten thin film deposited directly on silicon test wafers, without an additional layer of amorphous silicon. All films are of 40±4nm thickness.

5.4 Future Efforts

The section lists some of the possible future efforts and studies which can be done to address the fabrication issues, or to simply study and understands the processes (outlined in this section and Appendix J, K) and related systematics in greater details.

5.4.1 Characterizing the Polishing Process

Although a heavy chemical etch is done to remove surface defects after the crystal grinding, there may be surface damages occurring due to the polishing step itself.

It may be due to using a polishing pad beyond its lifetime, or simply because of an inherent nature of the polishing process. Since the defects act as charge traps, it is desirable to understand if they at all form, the mechanism for their formation and the depth from surface up to which they extend. One is also restricted to not perform a heavy chemical etch, as this may destroy the quality of polished surface, but there may exist possibilities to perform a light etch (like, etch the germanium crystal in Hydrofluoric acid, or, HF) to remove the top few atomic layers which suffer the greatest bruise from polishing induced defect. Additionally, it has been mentioned that the quality of deposited films depend on the morphology of substrate surface (Appendix J.3), and it would be desirable to quantify the latter after the polishing process.

5.4.2 Characterizing the Wet-Cleaning Process

The optimality of cleaning process depends on its ability to remove metallic and organic contaminants from the surface. This may be quantified by mass-spectroscopy studies and verifying that the substrate surface is indeed cleansed of impurities. Additionally, it is suggested in [324,325] that cleaning germanium by using Hydrochloric acid (HCl) might be a better option to pursue, that using Hydrofluoric acid (HF). The effect of change in cleaning procedure on the quality of deposited tungsten films may be studied.

5.4.3 Additional improvements in Thin Film Deposition

Since the process of thin film deposition itself involves different stages, various suggestions relating to each step are separately mentioned.

5.4.3.1 Aluminum Bury

The first optimization of time period for "aluminum bury" was based on results from RGA suggesting that a 12:30minute deposition is sufficient to reduce the chamber contamination levels. However, the deposition chamber has gone multiple processing ever since the study. Additionally, it was realized that RGA reading may change over ∼4 hours if it left switched off and connected to the chamber. Hence, a new study may be warranted.

5.4.3.2 RF Etch

The aim of RF etch is to remove the oxide layer on top of substrate before a thin film of either amorphous silicon (aSi), or tungsten is deposited. The process may be quantified. A possible method may be to perform mass-spectroscopic studies and to achieve the depth of surface oxide layer formed for both cases (or, to obtain a theoretical estimate based on suitable models), followed by obtaining the RF etch rate, and using the two to rationalize the etching time used. RF etch process may also create surface defect if a high etching power is used. But, a low etching power won't create the desired effect. Whether the currently used RF etch power is high enough to cause surface damage and/or whether the induced surface roughness helps in nucleation of subsequently deposited thin films; this needs to be studied.

5.4.3.3 Amorphous Silicon

It is observed that film deposition at 500W is much better in quality than the ones deposited at higher power. Studies on films deposited using even lower power can be done. However, lowering deposition power increases the deposition time which may increase the chance for chamber contaminations to enter the aSi or subsequent deposited film. These considerations may be used to optimize the deposition power

(and deposition time) of aSi film. A study of temporal evolution of chamber contamination (using RGA) would be helpful to this cause.

5.4.3.4 Aluminum Film Deposition

The quasiparticle diffusion time (time before a quasiparticle diffuses in aluminum film before it recombines into Cooper pairs) for aluminum film deposited by CDMS is inferred to be $\sim 3.3\mu s$ [235, 236]. However, similar devices fabricated by CRREST collaboration have a measured diffusion time of $\sim 100\mu s$ [352]. Thus, there exists huge opportunities for improvements in properties of deposited aluminum film. One of the suggested methods to improve aluminum film properties is to apply a negative bias to the substrate when an aluminum film deposition is done. Additional bombardment by argon ions may promote formation of aluminum film with larger grain size. AFM studies of the grain size can be done to obtain data on grain size. Another possibility may be to change the design from using a large rectangular shaped aluminum fin (to collect phonons to form quasiparticles which are then diffused to TES) to a set of rectangular fingers promoting a 1-dimensional diffusion of quasiparticles (rather than a 2-dimensional diffusion across rectangular fin), as shown below in Fig. 5.14.

5.4.3.5 First Tungsten Layer Deposition

The first tungsten layer is the one which is directly deposited on top of aluminum layer. A primary reason for including it in the design is that when a RF-etch is done before deposition of TES tungsten layer, then the aluminum may backsputter and get deposited in the regions where TES would be fabricated. The presence of aluminum affects the T_c of TES [330]. This may be verified for the film deposition unit at TAMU.

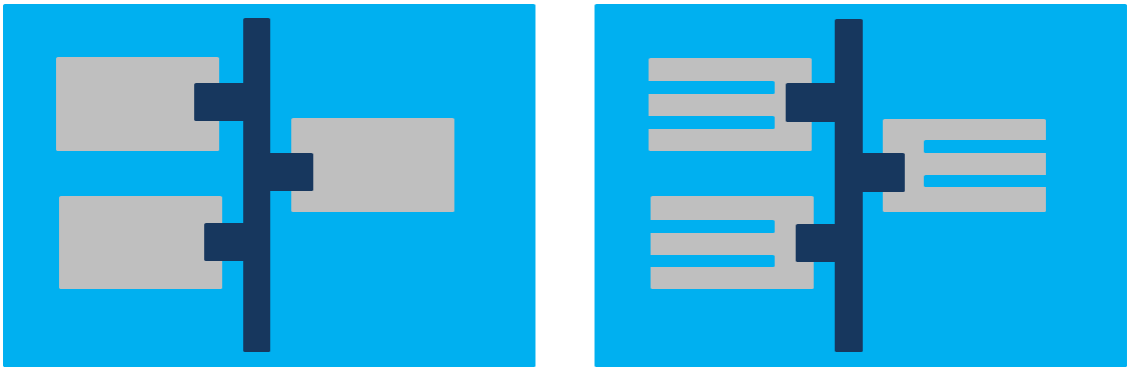

Figure 5.14: Suggested modification in design of aluminum fins (grey) that interact with phonons, form quasiparticles and funnel them to TES (dark blue). A top view is shown. The existing design allows a two-dimensional diffusion of quasiparticles, allowing a possibility for them to spend more time in aluminum film, rather than quickly diffusing to TES. This is prevented in the suggested design.

5.4.3.6 Second Tungsten Layer Deposition

The second tungsten layer is the one on which TES are patterned. Apart from simply performing T_c studies, various other studies may be performed on the tungsten layer, as described below:

- The tungsten film deposited on aSi do not undergo phase transformations (from as-deposited β to α phase) [316]. Thus, the tungsten TES may exist as a layer with heterogeneous thin film properties. The theoretical repercussions of such an assumption on the characteristics and performance of TES may be studied.

- The crystal microstructure is affected by the substrate roughness (Appendix J.3). A study on variation of tungsten film properties due to variation in roughness of aSi is suggested.

- It is known that CDMS TES have an undesirable property of becoming thermally "phase separated", i.e. instead of the entire TES having same tempera-

ture (and resistance), some portions of it are driven normal, while other may lie on superconducting edge, or even be superconducting. Such a behavior may be avoided if the films have high thermal conductivity. Thus, future efforts may also aim to optimize film deposition parameters to obtain large thermal conductivity. The effect of design change (as suggested in Fig. 5.14) in preventing/promoting thermal phase separation may also be evaluated. Additionally, since all previous CDMS detector also employed the method of T_c-tuning, the correlation of the procedure with propensity of TES to phase separate may also be studied. Such a studies supports the need for a fabrication procedure that does not involve ion implantation.

- A fascinating study would be to perform SEM measurement (obtaining visual changes in the concentration of quasiparticles and/or electrons) as the detectors are operated, and/or to perform a point contact spectroscopy to obtain the distribution of T_c of the tungsten film. These measurements can be done on both test wafer and the CDMS ZIP detector.

- The phenomenon of superconductivity initially develops within the grain and eventually crosses over the grain boundaries, leading to the bulk. Thus it is natural to assume that the grain size of deposited film plays a crucial role in TES characterization. The variation of T_c, T_c-width and thermal conductivity may be studied as a function of grain size.

- A study on the variation of T_c with film thickness (for similar deposition parameters), or with deposition parameters (for same film thickness) can be performed.

- The superconducting transition width of the TES also contributes to the noise

[270], which increases the noise bandwidth and forms a major part of total noise at high frequencies. Future studies may also concentrate towards characterizing the T_c-width rather than simply obtaining the T_c of the tungsten film.

- The existent method to explore thin film stress relies on bending of thin wafer upon which the film is deposited. However, this method would not work when the film is deposited on thick crystals, as used b CDMS. A new method to measure film stress of thick substrate may be developed by correlating the force required to penetrate a sharp needle in the film (or, film hardness) to the film stress. A compressively stressed film would be harder to penetrate, as compared to a film with tensile stress.

6. CONCLUSION

The dissertation searches for existence of cosmogenically produced fractionally charges particles, also called LIPs, using the events recorded by the CDMS collaboration, recorded using ZIP detectors installed underground in Soudan Underground Labs. Although previous attempt to search for LIPs have been done [8–10], these attempts are limited to study of LIPs with fractional charge $\gtrsim 1/6$. The result presented in the dissertation is a first attempt towards performing similar searches up to small fractional charges of *e/200*. The result from this analysis suggest non-observation of LIP-induced events. However, the analysis does find few events which are weakly rejected as being LIP-induced. Being an "almost" background free analysis, such a close rejection allows speculation for considering the observed events as possibly LIP-induced. Thus, the analysis definitely finishes with a request for future improvements to either verify the observed events are LIP-induced, or to reject them with greater confidence. The result for this analysis, based on the observations, is shown in Fig. 6.1. It presents the minimum value of LIP flux incident on detectors, excluded with 90% confidence. Also, to mention, the total background estimate for this analysis is 0.078 ± 0.078.

In addition to performing the LIPs analysis, the dissertation also presents results from studies performed to homogenize the characteristics of fabricated detector. Such an effort is required to reduce the extremely high cost for production of a successful ZIP detector which may be installed in Soudan Underground Labs. The cost estimate for such a production is $\sim$\$350k per detector, and includes the material, fabrication and testing cost scaled suitably to account for the fact that only $\sim$30% of fabricated detectors have suitable characteristics to be used for scientific studies. The variation

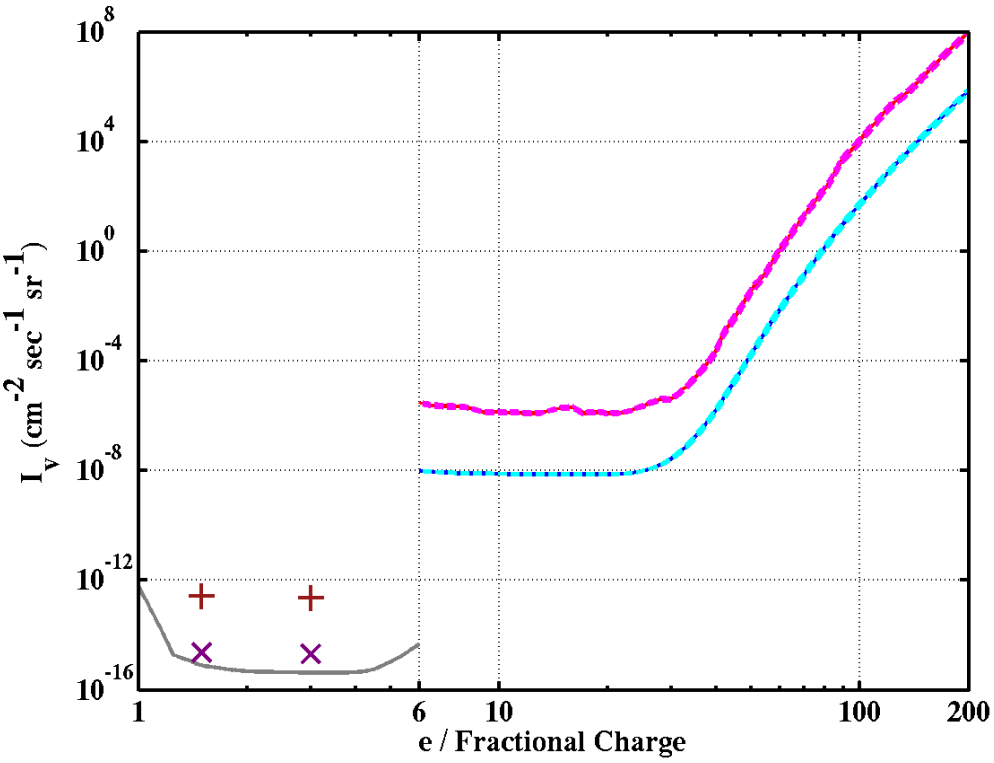

Figure 6.1: The 90% confident exclusion plot for LIP flux (lower bound to excluded LIP flux) corresponding to different fractional charges, incident on Tower-2 and Tower-4, based on the LIPs analysis. The two set of results correspond to analysis performed using "old" tracking criteria (red, with 1σ error in broken, magenta lines) and the new tracking criteria (blue, with 1σ error in broken, cyan lines). 1σ error bars, in broken lines, are also shown, but they get hidden due to the enormity of ordinate scales. The 90% Confidence Level limits for LIP flux from MACRO (grey), LSD (maroon +) and Kamiokande (purple X) are also shown (based on data from [10]).

in detector properties is mainly related to the variations in the superconducting transition temperature (T_c) of tungsten thin film. Existent detectors display a variation in T_c with a full width of 20-25mK. This is reduced to a variation with full width of $\sim$8mK. Multiple cost and time intensive steps (employing cryogenic testing of fabricated detectors and ion implantation process) are currently employed to reduce

existent inhomogeneities in T_c. By developing the fabrication procedure itself to remove these uncertainties, additional cost and time reduction in detector fabrication is obtained. Along with the 3 fold (and more) reduction in variation of detector characteristics, an increased rate for detector fabrication of $\sim$80% was observed (against existing 30% success rate). Lastly, through SEM based studies, a previously unoptimized fabrication procedure is brought to light, wherein presence of overhanging structures cause an improper connection between the aluminum quasiparticle traps and the tungsten transition edge sensors. Although non-quantified, it is believed that the improper connection may greatly reduce the ZIP detector sensitivity towards measurement of low energy signals. The fabrication procedure is developed to remove this impropriety. Although multiple success is obtained, the vastness of the detector fabrication procedure still leaves ample room for future developments on topics mentioned or not-mentioned in current dissertation.

REFERENCES

[1] G. Jungman, M. Kamionkowski, K. Griest, Physics Reports **267**, 195 (1996), arXiv:hep-ph/9506380v1, doi: 10.1016/0370-1573(95)00058-5

[2] J. Ellis, K. A. Olive, in *Particle Dark Matter: Observations, Models and Searches*, edited by G. Bertone (Cambridge, UK; New York : Cambridge University Press, 2010), pp. 142-163

[3] P. A. M. Dirac, Proceeding of Royal Society London **A133**, 60 (1931), doi: 10.1098/rspa.1931.0130

[4] L. B. Okun, M. B. Voloshin, V. I. Zakharov, Physics Letters **B138**, 115 (1984), doi: 10.1016/0370-2693(84)91884-7

[5] R. Foot, H. Lew, R. R. Volkas, Journal of Physics **G19**, 361 (1993), doi: 10.1088/0954-3899/19/3/005

[6] B. Holdom, Physics Letters **B166**, 196 (1986), doi: 10.1016/0370-2693(86)91377-8

[7] P. C. Kim, E. R. Lee, I. T. Lee, M. L. Perl, V. Halyo, D. Loomba, Physical Review Letters **99**, 161894 (2007), doi:10.1103/PhysRevLett.99.161804

[8] M. Aglietta, P. Antonioli, G. Badino, C. Castagnoli, A. Castellina *et al.*, Astroparticle Physics **2**, 29 (1994), doi: 10.1016/0927-6505(94)90015-9

[9] M. Mori, Y. Oyama, A. Suzuki, K. Takahashi, M. Yamada *et al.*, Physical Review **D43**, 2842 (1991) , doi: 10.1103/PhysRevD.43.2843

[10] M. Ambrosio, R. Antolini, A. Baldini, G. C. Barbarino, B. C. Barish *et al.*, arXiv:hep-ex/0402006 (2004)

[11] Z. Ahmed, D. S. Akerib, S. Arrenberg, C. N. Bailey, D. Balakishiyeva *et al.*, Science /bf 327, 1619 (2010), arXiv:0912.3592, doi: 10.1126/science.1186112

[12] D, S. Akerib, M. S. Armel, M. J. Attisha, L. Baudis, D. A. Bauer *et al.*, Nuclear Instruments and Methods in Physics Research **A520**, 105 (2004), doi: 10.1016/j.nima.2003.11.253

[13] D, S. Akerib, J. Alvaro-Dean, M. S. Armel, M. J. Attisha, L. Baudis *et al.*, Nuclear Instruments and Methods in Physics Research **A520**, 116 (2004), doi: 10.1016/j.nima.2003.11.256

[14] J. Beringer, J. F. Arguin, R. M. Barnett, K. Copic, O. Dahl *et al.*, Physical Review **D86**, 010001 (2012), doi: 10.1103/PhysRevD.86.010001

[15] J. Jaeckel, A. Ringwald, arXiv:1002.0329v1 (2010)

[16] A. A. Prinz, Ph.D. Dissertation, Stanford University, Stanford, California, USA (2001)

[17] S. Davidson, S. Hannestad, G. Raffelt, Journal of High Energy Physics **5**, 003 (2000), arXiv:hep-ph/0001179v2, doi: 10.1088/1126-6708/2000/05/003

[18] R. Foot, H. Lew, Modern Physics Letters **A8**, 3767 (1993), arXiv:hep-ph/9307328, doi: 10.1142/S0217732393003500

[19] J. C. Maxwell, Philosophical Transactions of the Royal Society of London **155**, 459 (1865), doi: 10.1098/rstl.1865.0008

[20] P. Curie, Sances de la Socit Franaise de Physique (Paris), 76 (1894)

[21] J. Preskill, Annual Review of Nuclear and Particle Science **34**, 461 (1984)

[22] A. M. Polyakov, Journal of Experimental and Theoretical Physics Letters **20**, 194 (1974)

[23] G. 't Hooft, Nuclear Physics **B79**, 276 (1974), doi: 10.1016/0550-3213(74)90486-6

[24] H. Georgi, S. L. Glashow, Physical Review Letters **32**, 438 (1974), doi: 10.1103/PhysRevLett.32.438

[25] J. C. Pati, A. Salam, Physical Review **D10**, 275 (1974), doi: 10.1103/PhysRevD.10.275, 10.1103/PhysRevD.11.703.2

[26] M. Ambrosio, R. Antolini, G. Auriemma, D. Bakari, A. Baldini *et al.*, European Physical Journal **C25**, 511 (2002), arXiv:hep-ex/0207020, doi: 10.1140/epjc/s2002-01046-9

[27] J. L. Pinfold, AIP Conference Proceedings **1304**, 234 (2010), doi: 10.1063/1.3527206

[28] K. Kinoshita, R. Du, G. Giacomelli, L. Patrizii, F. Predieri *et al.*, Physical Review **D46**, 881 (1992). doi: 10.1103/PhysRevD.46.R881

[29] J. L. Pinfold, R. Du, K. Kinoshita, B. Lorazo, M. Regimbald *et al.*, Physics Letters **B316**, 407 (1993), doi: 10.1016/0370-2693(93)90346-J

[30] E. Witten, Physics Letters **B86**, 283 (1979), doi: 10.1016/0370-2693(79)90838-4

[31] F. A. Bais, arXiv:hep-th/0407197v2 (2004)

[32] C. N. Yang, Physical Review **D1**, 2360 (1970), doi: 10.1103/PhysRevD.1.2360

[33] J. L. Rosner, arXiv:hep-ph/0108195v6 (2001)

[34] S. L. Adler, Physical Review **177**, 2426 (1963), doi: 10.1103/PhysRev.177.2426

[35] J. S. Bell, R. Jackiw, Nuovo Cimento **A60**, 47 (1969), doi: 10.1007/BF02823296

[36] B. R. Holstein, American Journal of Physics **61**, 142 (1993), doi: 10.1119/1.17328

[37] R. Delbourgo, A. Salam, Physics Letters **B40**, 381 (1972), doi: 10.1016/0370-2693(72)90825-8

[38] T. Eguchi, P. G. O. Freund, Physical Review Letters **33**, 1251 (1976), doi: 10.1103/PhysRevLett.37.1251

[39] L. Alvarez-Gaume, E. Witten, Nuclear Physics **B234**, 269 (1984), doi: 10.1016/0550-3213(84)90066-X

[40] D. Choudhury, U. Sarkar, Physics Letters **B268**, 96 (1991), doi: 10.1016/0370-2693(91)90929-K

[41] E. Takasugi, M. Tanaka, Physical Review **D44**, 3706 (1991), doi: 10.1103/PhysRevD.44.3706

[42] J. Baumann, J. Kalus, R. Gahler, W. Mampe, Physical Review **D37**, 3107 (1988), doi: 10.1103/PhysRevD.37.3107

[43] K. Durstberger-Rennhofer, T. Jenke, H. Abele, Physical Review **D84**, 036004 (2011), doi: 10.1103/PhysRevD.84.036004

[44] A. Arvanitaki, S. Dimopoulos, A. A. Geraci, J. Hogan, M. Kasevich, Physical Review Letters **100**, 120407 (2008), doi: 10.1103/PhysRevLett.100.120407

[45] K. S. Babu, R. R. Volkas, Physical Review **D46**, 2764 (1992), doi: 10.1103/PhysRevD.46.R2764

[46] G. Bressi, G. Carugno, F. Della Valle, G. Galeazzi, G. Ruoso, G. Sartori, Physical Review **A83**, 052101 (2011), doi: 10.1103/PhysRevA.83.052101

[47] C. S. Unnikrishnan, G. T. Gillies, Metrologia **41**, S125 (2004), doi: 10.1088/0026-1394/41/5/S03

[48] K. S. Babu, R. N. Mohapatra, Physical Review **D42**, 3866 (1990), doi: 10.1103/PhysRevD.42.3866

[49] E. R. Williams, J. E. Faller, H. A. Hill, Physical Review Letters **26**, 721 (1971), doi: 10.1103/PhysRevLett.26.721

[50] J. C. Zorn, G. E. Chamberlain, V. W. Hughes, Physical Review **129**, 2566 (1963), doi: 10.1103/PhysRev.129.2566

[51] G. Barbiellini, G. Cocconi, Nature **329**, 21 (1987), doi: 10.1038/329021b0

[52] C. Broggini, C. Giunti, A. Studenikin, arXiv:1207.3980v1 (2012)

[53] J. Bernstein, M. Ruderman, G. Feinberg, Physical Review **132**, 1227 (1963), doi: 10.1103/PhysRev.132.1227

[54] G. G. Raffelt, Physics Reports **320**, 319 (1999), doi: 10.1016/S0370-1573(99)00074-5

[55] C. Giunti, A. Studenikin, Physics of Atomic Nuclei **72**, 2089 (2009), arXiv:0812.3646v5, doi: 10.1134/S1063778809120126

[56] S. A. Abel, J. Jaeckel, V. V. Khoze, A. Ringwald, Physics Letters **B666**, 66 (2008), arXiv:hep-ph/0608248v2, doi: 10.1016/j.physletb.2008.03.076

[57] K. R. Dienes, C. F. Kolda, J. March-Russell, Nucl.Phys. **B492**, 104 (1997)

[58] D. Lüst, S. Stieberger, Fortschritte der Physik **55**, 427 (2007), arXiv:hep-th/0302221, doi: 10.1002/prop.200310335

[59] S. A. Abel, B. W. Schofield, Nuclear Physics **B685**, 150 (2004), arXiv:hep-th/0311051, doi: 10.1016/j.nuclphysb.2004.02.037

[60] S. Abel, J. Santiago, Journal of Physics **G30**, R83 (2004), arXiv:hep-ph/0404237, doi: 10.1088/0954-3899/30/3/R01

[61] B. Batell, T. Gherghetta, Physical Review **D73**, 045016 (2006), doi: 10.1103/PhysRevD.73.045016

[62] R. Blumenhagen, S. Moster, T. Weigand, Nuclear Physics **B751**, 186 (2006), doi: 10.1016/j.nuclphysb.2006.06.005

[63] J. Polchinski, *String Theory* (Cambridge, UK; New York, NY : Cambridge University Press, 1998), Vol. I and II

[64] M. Cicoli, M. Goodsell, J. Jaeckel, A. Ringwald, arXiv:1103.3705v2 (2011)

[65] R. Essig, P. Schuster, N. Toro, Physical Review **D80**, 015003 (2009), doi: 10.1103/PhysRevD.80.015003

[66] M. Ahlers, H. Gies, J. Jaeckel, J. Redondo, A. Ringwald, Physical Review **D76**, 115005 (2007), arXiv:0706.2836v1 doi: 10.1103/PhysRevD.76.115005

[67] E. Masso, J. Redondo, Physical Review Letters **97**, 151802 (2006), arXiv:hep-ph/0606163, doi: 10.1103/PhysRevLett.97.151802

[68] K. R. Dienes, C. F. Kolda, J. March-Russell, Nuclear Physics **B492**, 104 (1997), arXiv:hep-ph/9610479, doi: 10.1016/S0550-3213(97)00173-9

[69] F. Bruemmer, J. Jaeckel, V. V. Khoze, Journal of High Energy Physics **06**, 037 (2009), arXiv:0905.0633v1, doi: 10.1088/1126-6708/2009/06/037

[70] P. H. Adrian, arXiv:1301.1103 (2013)

[71] C. Hearty, J. E. Rothberg, K. K. Young, A. S. Johnson, J. S. Whitaker *et al.*, Physical Review Letters **58**, 1711 (1987), doi: 10.1103/PhysRevLett.58.1711

[72] C. Hearty, J. E. Rothberg, K. K. Young, A. S. Johnson, J. S. Whitaker *et al.*, Physical review **D39**, 3207 (1989), doi: 10.1103/PhysRevD.39.3207

[73] S. Davidson, B. Campbell, D. C. Bailey, Physical Review **D43**, 2314 (1991), doi: 10.1103/PhysRevD.43.2314

[74] E. Golowich, R. W. Robinett, Physical Review **D35**, 391 (1987), doi: 10.1103/PhysRevD.35.391

[75] R. Akers, G. Alexander, J. Allison, K. Ametewee, K. J. Anderson *et al.*, Zeitschrift für Physik **C67**, 203 (1995), doi: 10.1007/BF01571281

[76] P. Abreu , W. Adam, T. Adye, I. Azhinenko, G.D. Alekseev *et al.*, Physics Letters **B396**, 315 (1997), doi: 10.1016/S0370-2693(97)00152-4

[77] U. D. Jentschura, Annals of Physics **326**, 516 (2011), arXiv:1011.5453v1, doi: 10.1016/j.aop.2010.11.011

[78] T. Mitsui, R. Fujimoto, Y. Ishisaki, Y. Ueda, Y. Yamazaki *et al.*, Physical review Letters **70**, 2265 (1993), doi: 10.1103/PhysRevLett.70.2265

[79] A. Badertscher, P. Crivelli, W. Fetscher, U. Gendotti, S. Gninenko *et al.*, Physical Review **D75**, 032004 (2007), arXiv:hep-ex/0609059v2, doi:10.1103/PhysRevD.75.032004

[80] A. Czarnecki, Acta Physica Polonica **B30**, 3837 (1999), arXiv:hep-ph/9911455v1

[81] G.S. Adkins, R.N. Fell, J.R. Sapirstein, Annals of Physics **295**, 136 (2002), doi: 10.1006/aphy.2001.6219

[82] S. G. Karshenboim, International Journal of Modern Physics **A19**, 3879 (2004), arXiv:hep-ph/0310099, doi: 10.1142/S0217751X04020142

[83] S. N. Gninenko, N. V. Krasnikov, V. A. Matveev, A. Rubbia, Physics of Elementary Particles and Atomic Nuclei **37**, 321 (2006), doi: 10.1134/S1063779606030038

[84] A. Czarnecki, S. Karshenboim, arXiv:hep-ph/9911410 (1999)

[85] J. Govaerts, M. Van Caille, Physics Letters **B381**, 451 (1996), doi: 10.1016/0370-2693(96)00623-5

[86] G. S. Atoyan, S. N. Gninenko, V. I. Razin, Y. V. Ryabov, Physics Letters **B220**, 317 (1989), doi: 10.1016/0370-2693(89)90059-2

[87] A. A. Prinz, R. Baggs, J. Ballam, S. Ecklund, C. Fertig *et al.*, Physical Review Letters **81**, 1175 (1998), arXiv:hep-ex/9804008, doi: 10.1103/PhysRevLett.81.1175

[88] J. Jaeckel, M. Jankowiak, M. Spannowsky, Physics of the Dark Universe **2**, 111 (2013), arXiv:1212.3620, doi: 10.1016/j.dark.2013.06.001

[89] S. Chatrchyan , V. Khachatryan, A. M. Sirunyan, A. Tumasyan, W. Adam *et al.*, Physical Review **D87**, 092008 (2013), arXiv:1210.2311v2, doi: 10.1103/PhysRevD.87.092008

[90] W. E. Lamb, R. C. Retherford, Physical Review **72**, 241 (1947), doi: 10.1103/PhysRev.72.241

[91] P. A. M. Dirac, Proceeding of Royal Society London **A117**, 610 (1928), doi: 10.1098/rspa.1928.0023

[92] G. W. Bennett, B. Bousquet, H. N. Brown, G. Bunce, R. M. Carey *et al.*, Physical Review **D73**, 072003 (2006), arXiv:hep-ex/0602035, doi: 10.1103/PhysRevD.73.072003

[93] K. Hagiwara, A. D. Martin, D. Nomura, T. Teubner, Physics Letters **B649**, 173 (2007), arXiv:hep-ph/0611102, doi: 10.1016/j.physletb.2007.04.012

[94] R. Pohl, A. Antognini, F. Nez, F. D. Amaro, F. Biraben *et al.*, Nature **466**, 213 (2010), doi: 10.1038/nature09250

[95] U. D. Jentschura, S. Kotochigova, E. Le Bigot, P. J. Mohr, B. N. Taylor, Physical Review Letters **95**, 163003 (2005), doi: 10.1103/PhysRevLett.95.163003

[96] P. J. Mohr, B. N. Taylor, D. B. Newell, Review of Modern Physics **80**, 633 (2008), arXiv:0801.0028, doi: 10.1103//RevModPhys.80.633

[97] A. Pineda, arXiv:1108.1263 (2011)

[98] J. L. Cervantes-Cota, G. Smoot, AIP Conference Proceedings **1396**, 28 (2011), arXiv:1107.1789v2, doi: 10.1063/1.3647524

[99] P. A. R. Ade, N. Aghanim, C. Armitage-Caplan, M. Arnaud, M. Ashdown *et al.*, arXiv:1303.5076v1 (2013)

[100] K. S. Babu, R. R. Volkas, Physical Review **D46**, 2764 (1992), arXiv:hep-ph/9208260, doi: 10.1103/PhysRevD.46.R2764

[101] M. Pospelov, J. Pradler, Annual Review of Nuclear and Particle Science **60**, 539 (2010), doi: 10.1146/annurev.nucl.012809.104521

[102] E. W. Kolb, D. Seckel, M. S. Turner, Nature **314**, 415 (1985), doi: 10.1038/314415a0

[103] J. Yang, M. S. Turner, G. Steigman, D. N. Schramm, K. A. Olive, The Astrophysical Journal **281**, 493 (1984), doi: 10.1086/162123

[104] D. Puy, M. Signore, New Astronomy Reviews **43**, 185 (1999), doi: 10.1016/S1387-6473(99)00011-1

[105] R. H. Cyburt, B. D. Fields, K. A. Olive, Journal of Cosmology and Astroparticle Physics **0811**, 12 (2008), arXiv:0808.2818, doi: 10.1088/1475-7516/2008/11/012

[106] K. A. Olive, E. D. Skillman, The Astrophysical Journal **617**, 29 (2004), arXiv:astro-ph/0405588, doi: 10.1086/425170

[107] R. Foot, M. J. Thomson, R. R. Volkas, Physical Review **D53**, 5349 (1996), arXiv:hep-ph/9509327, doi: 10.1103/PhysRevD.53.R5349

[108] R. Foot, R. R. Volkas, Physical Review **D61**, 043507 (2000), arXiv:hep-ph/9904336, doi: 10.1103/PhysRevD.61.043507

[109] A. D. Dolgov, arXiv:hep-ph/0306154 (2003)

[110] G. Mangano, G. Miele, S. Pastor, O. Pisanti, S. Sarikas, Physics Letters **B708**, 1 (2012), arXiv:1110.4335v1, doi: 10.1016/j.physletb.2012.01.015

[111] R. N. Mohapatra, L Z. Rothstein, Physics Letters **B247**, 593 (1990), doi: 10.1016/0370-2693(90)91907-S

[112] S. Davidson, M. Peskin, Physical Review **D49**, 2114 (1994), arXiv:hep-ph/9310288, doi: 10.1103/PhysRevD.49.2114

[113] E. Castorina, U. Franca, M. Lattanzi, J. Lesgourgues, G. Mangano *et al.*, Physical Review **D86**, 023517 (2012), arXiv:1204.2510v3, doi: 10.1103/PhysRevD.86.023517

[114] Z. Berezhiani, A. Dolgov, I. Tkachev, arXiv:1211.4937v2 (2012)

[115] E. W. Kolb, M. S. Turner, T. P. Walker, Physical review **D34**, 2197 (1986), doi: 10.1103/PhysRevD.34.2197

[116] P. D. Serpico, G. G. Raffelt, Physical Review **D70**, 043526 (2004), arXiv:arXiv:astro-ph/0403417v2, doi: 10.1103/PhysRevD.70.043526

[117] W. Hu, S. Dodelson, Annual Review of Astronomy and Astrophysics **40**, 171 (2002), arXiv:astro-ph/0110414, doi: 10.1146/annurev.astro.40.060401.093926

[118] D. Samtleben, S. Staggs, B. Winstein, Annual Review of Nuclear and Particle Science **57**, 245 (2007), arXiv:0803.0834v1, doi: 10.1146/annurev.nucl.54.070103.181232

[119] J. C. Mather, D. J. Fixsen, R. A. Shafer, C. Mosier, D. T. Wilkinson, The Astrophysical Journal **512**, 511 (1999), arXiv:astro-ph/9810373, doi: 10.1086/306805

[120] D. J. Fixsen, A. Kogut, S. Levin, M. Limon, P. Lubin *et al.*, arXiv:0901.0555v1 (2009)

[121] A. A. Penzias, R. W. Wilson, The Astrophysical Journal **142**, 419 (1965), doi: 10.1086/148307

[122] G. F. Smoot, C. L. Bennett, A. Kogut, E. L. Wright, J. Aymon *at al.*, The Astrophysical Journal **396**, L1 (1992)

[123] J. B. Peterson, G. S. Griffin, M. G. Newcomb, D. L. Alvarez, C. M. Cantalupo *et al.*, arXiv:astro-ph/9910503 (1999), doi: 10.1086/312576

[124] A. Miller, J. Beach, S. Bradley, M. J. Devlin, R. Caldwell *et al.*, The Astrophysical Journal Supplementary series **140**, 115 (2002), arXiv:astro-ph/0108030, doi: 10.1086/339686

[125] S. Padin, M. C. Shepherd, J. K. Cartwright, R. G. Keeney, B. S. Mason *et al.*, Publication of the Astronomical Society of the Pacific **114**, 83 (2002), arXiv:astro-ph/0110124v1, doi: 10.1086/324786

[126] N. W. Halverson, E. M. Leitch, C. Pryke, J. Kovac, J. E. Carlstrom *et al.*, The Astrophysical Journal **568**, 38 (2002), arXiv:astro-ph/0104489, doi: 10.1086/338879

[127] S. Hanany, P. Ade, A. Balbi, J. Bock, J. Borrill *et al.*, The Astrophysical Journal **545**, L5 (2000), arXiv:astro-ph/0005123, doi: 10.1086/317322

[128] B. P. Crill, P. A. R. Ade, D. R. Artusa, R. S. Bhatia, J. J. Bock *et al.*, The Astrophysical Journal Supplementary series **147**, 527 (2002), arXiv:astro-ph/0206254, doi: 10.1086/376894

[129] C. L. Bennett, M. Halpern, G. Hinshaw, N. Jarosik, A. Kogut *et al.*, The Astrophysical Journal Supplementary series **148**, 1 (2003), arXiv:arXiv:astro-ph/0302207v3, doi: 10.1086/377253

[130] E. Komatsu, K. M. Smith, J. Dunkley, C. L. Bennett, B. Gold *et al.*, The Astrophysical Journal Supplementary series **192**, 18 (2011), arXiv:1001.4538v3, doi: 10.1088/0067-0049/192/2/18

[131] N. Jarosik, C. L. Bennett, J. Dunkley, B. Gold, M. R. Greason *et al.*, The Astrophysical Journal Supplementary series **192**, 14 (2011), arXiv:1001.4744, doi: 10.1088/0067-0049/192/2/14

[132] J. L. Weiland, N. Odegard, R. S. Hill, E. Wollack, G. Hinshaw *et al.*, The Astrophysical Journal Supplementary series **192**, 19 (2011), arXiv:1001.4731, doi: 10.1088/0067-0049/192/2/19

[133] D. Larson, J. Dunkley, G. Hinshaw, E. Komatsu, M. R. Nolta *et al.*, The Astrophysical Journal Supplementary series **192**, 16 (2011), arXiv:1001.4635, doi: 10.1088/0067-0049/192/2/16

[134] B. Gold, N. Odegard, J. L. Weiland, R. S. Hill, A. Kogut *et al.*, The Astrophysical Journal Supplementary series **192**, 15 (2011), arXiv:1001.4555, doi: 10.1088/0067-0049/192/2/15

[135] C. L. Bennett, R. S. Hill, G. Hinshaw, D. Larson, K. M. Smith *et al.*, The Astrophysical Journal Supplementary series **192**, 17 (2011), arXiv:1001.4758, doi: 10.1088/0067-0049/192/2/17

[136] R. A. Bunker, Ph.D. Dissertation, University of California, Santa Barbara, California, USA (2011)

[137] L. Page, C. Jackson, C. Barnes, C. Bennett, M. Halpern *et al.*, The Astrophysical Journal **585**, 566 (2003), arXiv:astro-ph/0301160, doi: 10.1086/346078

[138] G. Hinshaw, M. R. Nolta, C. L. Bennett, R. Bean, O. Doré *et al.*, The Astrophysical Journal Supplementary series **170**, 288 (2007), arXiv:astro-ph/0603451v2, doi: 10.1086/513698

[139] G. Hinshaw, J. L. Weiland, R. S. Hill, N. Odegard, D. Larson *et al.*, The Astrophysical Journal Supplementary series **180**, 225 (2009), arXiv:0803.0732v2, doi: 10.1088/0067-0049/180/2/225

[140] E.L. Wright, G. Hinshaw, C.L. Bennett, arXiv:astro-ph/9510102v1 (1996), doi: 10.1086/309927

[141] C. Bennett, R. S. Hill, G. Hinshaw, M. R. Nolta, N. Odegard *et al.*, The Astrophysical Journal Supplementary series **148**, 97 (2003), arXiv:astro-ph/0302208v2, doi: 10.1086/377252

[142] C. L. Reichardt, P. A. R. Ade, J. J. Bock, J. R. Bond, J. A. Brevik *et al.*, The Astrophysical Journal **694**, 1200 (2009), arXiv:0801.1491, doi: 10.1088/0004-637X/694/2/1200

[143] M. L. Brown, P. Ade, J. Bock, M. Bowden, G. Cahill *at al.*, The Astrophysical Journal **705**, 978 (2009), arXiv:0906.1003v3, doi: 10.1088/0004-637X/705/1/978

[144] R. K. Sachs, A. M. Wolfe, The Astrophysical Journal **147**, 73 (1967), doi: 10.1007/s10714-007-0448-9

[145] J. Silk, The Astrophysical Journal **151**, 459 (1968), doi: 10.1086/149449

[146] U. Seljak, M. Zaldarriaga, The Astrophysical Journal **469**, 437 (1996), arXiv:astro-ph/9603033, doi: 10.1086/177793

[147] A. Lewis, A. Challinor, A. Lasenby, The Astrophysical Journal **538**, 473 (2000), arXiv:astro-ph/9911177,

[148] D. Scott, A. Moss, arXiv:0902.3438v2 (2009)

[149] A. Melchiorri, A. Polosa, A. Strumia, Physics Letters **B650**, 416 (2007), arXiv:hep-ph/0703144v2, doi: 10.1016/j.physletb.2007.05.042

[150] Y. B. Zeldovich, R. A. Sunyaev, Astrophysics and Space Science **4**, 301 (1969)

[151] R. A. Sunyaev, Y. B. Zeldovich, Comments on Astrophysics and Space Science **4**, 173 (1972)

[152] C. Burrage, J. Jaeckel, J. Redondo, A. Ringwald, Journal of Cosmology and Astroparticle Physics **11**, 2 (2009), arXiv:0909.0649v1, doi: 10.1088/1475-7516/2009/11/002

[153] C. L. Carilli, G. B. Taylor, Annual Review of Astronomy and Astrophysics **40**, 319 (2002), arXiv:astro-ph/0110655, doi: 10.1146/annurev.astro.40.060401.093852

[154] S. L. Dubovsky, D. S. Gorbunov, G. I. Rubtsov, Letters to Jounal of Experimental and Theoretical Physics **79**, 1 (2004), arXiv:hep-ph/0311189v2, doi: 10.1134/1.1675909

[155] D. Kirkman, D. Tytler, N. Suzuki, J. M. O'Meara, D. Lubin, The Astrophysical Journal Supplementary Series **149**, 1 (2003), arXiv:astro-ph/0302006v1, doi: 10.1086/378152

[156] C. Ma, E. Bertschinger, The Astrophysical Journal **455**, 7 (1995), arXiv:astro-ph/9506072, doi: 10.1086/176550

[157] S. L. Dubovsky, D. S. Gorbunov, Physical Review **D64**, 123503 (2001), arXiv:astro-ph/0103122, doi: 10.1103/PhysRevD.64.123503

[158] M. Ahlers, Physical Review **D80**, 023513 (2009), arXiv:0904.0998v1, doi: 10.1103/PhysRevD.80.023513

[159] A. G. Riess, A. V. Filippenko, P. Challis, A. Clocchiattia, A. Diercks *et al.*, The Astronomical Journal **116**, 1009 (1998), arXiv:astro-ph/9805201, doi: 10.1086/300499

[160] S. Perlmutter, G. Aldering, G. Goldhaber, R. A. Knop, P. Nugent *et al.*, The Astrophysical Journal **517**, 565 (1999), arXiv:astro-ph/9812133, doi: 10.1086/307221

[161] M. Kowalski, D. Rubin, G. Aldering, R. J. Agostinho, A. Amadon *et al.*, The Astrophysical Journal **686**, 749 (2008), arXiv:0804.4142, doi: 10.1086/589937

[162] P. P. Kronberg, Reports on Progress in Physics **57**, 325 (1994), doi: 10.1088/0034-4885/57/4/001

[163] R. N. Mohapatra, S. Nussinov, International Journal of Modern Physics **A7**, 3817 (1992), doi: 10.1142/S0217751X92001708

[164] M. I. Dobroliubov, A. Yu. Ignatiev, Physical Review Letters **65**, 679 (1990), doi: 10.1103/PhysRevLett.65.679

[165] S.I. Blinnikov, N.V. Dunina-Barkovskaya, Monthly Notices of the Royal Astronomical Society **266**, 289 (1994)

[166] G.G. Raffelt, *Stars as Laboratories for Fundamental Physics* (Chicago, IL : University of Chicago Press, 1996)

[167] J. Jaeckel, E. Masso, J. Redondo, A. Ringwald, F. Takahashi, arXiv:hep-ph/0605313 (2006)

[168] J. Jaeckel, E. Masso, J. Redondo, A. Ringwald, F. Takahashi, Physical Review **D75**, 013004 (2007), arXiv:hep-ph/0610203, doi: 10.1103/PhysRevD.75.013004

[169] E. Masso, J. Redondo, Journal of Cosmology and Astroparticle Physics **09**, 015 (2005), arXiv:hep-ph/0504202, doi: 10.1088/1475-7516/2005/09/015

[170] R. N. Mohapatra, S. Nasri, Physical Review Letters **98**, 050402 (2007), arXiv:hep-ph/0610068, doi: 10.1103/PhysRevLett.98.050402

[171] P. Brax, C. van de Bruck, A. C. Davis, Physical Review Letters **99**, 121103 (2007), arXiv:hep-ph/0703243, doi: 10.1103/PhysRevLett.99.121103

[172] P. Jain, S. Mandal, International Journal of Modern Physics **D15**, 2095 (2006), arXiv:astro-ph/0512155, doi: 10.1142/S0218271806009558

[173] A. K. Ganguly, P. Jain, S. Mandal, S. Stokes, Physical Review **D76**, 025026 (2007), arXiv:hep-ph/0611006, doi: 10.1103/PhysRevD.76.025026

[174] J. E. Kim, Physical Review **D76**, 051701 (2007), arXiv:0704.3310, doi: 10.1103/PhysRevD.76.051701

[175] E. Masso, J. Redondo, Physical Review Letters **97**, 151802 (2006), arXiv:hep-ph/0606163, doi: 10.1103/PhysRevLett.97.151802

[176] J. Redondo, arXiv:0807.4329 (2008)

[177] J. Huh, J. E. Kim, J. Park, S. C. Park, Physical Review **D77**, 123503 (2008), arXiv:0711.3528v4, doi: 10.1103/PhysRevD.77.123503

[178] J. F. Beacom, H. Yuksel, Physical Review Letters **97**, 071102 (2006), arXiv:astro-ph/0512411v2, doi: 10.1103/PhysRevLett.97.071102

[179] P. Sizun, M. Cassé, S. Schanne, B. Cordier, arXiv:astro-ph/0702061 (2007)

[180] J. Knodlseder, V. Lonjou, P. Jean, M. Allain, P. Mandrou *et al.*, Astronomy & Astrophysics **411**, L457 (2003), arXiv:astro-ph/0309442, doi: 10.1051/0004-6361:20031437

[181] P. Jean, J. Knoedlseder, V. Lonjou, M. Allain, J. Roques *et al.*, Astronomy & Astrophysics **407**, L55 (2003), arXiv:astro-ph/0309484, doi: 10.1051/0004-6361:20031056

[182] J. Knödlseder, P. Jean, V. Lonjou, G. Weidenspointner, N. Guessoum *et al.*, Astronomy & Astrophysics **441**, 513 (2005), arXiv:astro-ph/0506026, doi: 10.1051/0004-6361:20042063

[183] G. Weidenspointner, C.R. Shrader, J. Knoedlseder, P. Jean, V. Lonjou *et al.*, Astronomy & Astrophysics **450**, 1013 (2006), arXiv:astro-ph/0601673, doi: 10.1051/0004-6361:20054046

[184] G. Weidenspointner, J. Knoedlseder, P. Jean, G.K. Skinner, J. Roques *et al.*, arXiv:astro-ph/0702621 (2007)

[185] P. Jean, J. Knodlseder, W. Gillard, N. Guessoum, K. Ferriere *et al.*, Astronomy & Astrophysics **445**, 579 (2006), arXiv:astro-ph/0509298, doi: 10.1051/0004-6361:20053765

[186] C. D. Dermer, R. J. Murphy, arXiv:astro-ph/0107216 (2001)

[187] M. Cassé, B. Cordier, J. Paul, S. Schanne, The Astrophysical Journal **602**, L17 (2004), arXiv:astro-ph/0309824, doi: 10.1086/381884

[188] G. Bertone, A. Kusenko, S. Palomares-Ruiz, S. Pascoli, D. Semikoz, Physics Letters **B636**, 20 (2006), arXiv:astro-ph/0405005, doi: 10.1016/j.physletb.2006.03.022

[189] H. Goldberg, L. J. Hall, Physics Letters **B174**, 151 (1986), doi: 10.1016/0370-2693(86)90731-8

[190] K. Cheung, T. C. Yuan, Journal of High Energy Physics **03**, 120 (2007), arXiv:hep-ph/0701107, doi: 10.1088/1126-6708/2007/03/120

[191] D. Feldman, Z. Liu, P. Nath, Physical Review **D75**, 115001 (2007), arXiv:hep-ph/0702123, doi: 10.1103/PhysRevD.75.115001

[192] M. Ahlers, H. Gies, J. Jaeckel, J. Redondo, A. Ringwald, Physical Review **D77**, 095001 (2008), arXiv:0711.4991, doi: 10.1103/PhysRevD.77.095001

[193] J. Jaeckel, Physical Review Letters **103**, 080402 (2009), arXiv:0904.1547v1, doi: 10.1103/PhysRevLett.103.080402

[194] H. Gies, J. Jaeckel, Journal of High Energy Physics **08**, 63 (2009), arXiv:0904.0609v1, doi: 10.1088/1126-6708/2009/08/063

[195] H. Gies, J. Jaeckel, A. Ringwald, Europhysics Letters **76**, 794 (2006), arXiv:hep-ph/0608238v1, doi: 10.1209/epl/i2006-10356-5

[196] H. Gies, J. Jaeckel, A. Ringwald, Physical Review Letters **97**, 140402 (2006), arXiv:hep-ph/0607118v1, doi: 10.1103/PhysRevLett.97.140402

[197] F. Sauter, Zeitschrift für Physik **69**, 742 (1931)

[198] W. Heisenberg, H. Euler, Zeitschrift für Physik **98**, 714 (1936), arXiv:physics/0605038

[199] J. Schwinger, Physical Review **82**, 664 (1951), doi: 10.1103/PhysRev.82.664

[200] L. Lilje, E. Kako, D. Kostin, A. Matheisen, W. D. Moeller *et al.*, Nuclear Instruments and Methods in Physics Research **A524**, 1 (2004), arXiv:physics/0401141, doi: 10.1016/j.nima.2004.01.045

[201] R. Corsini [CLIC Study Group Collaboration], Nuclear Physics B - Proceedings Supplements **154**, 137 (2006), doi: 10.1016/j.nuclphysbps.2006.01.053

[202] R. Cameron, G. Cantatore, A. C. Melissinos, G. Ruoso, Y. Semertzidis *et al.*, Physical Review **D47**, 3707 (1993), doi: 10.1103/PhysRevD.47.3707

[203] E. Zavattini, G. Zavattini, G. Ruoso, E. Polacco, E. Milotti *et al.*, Physical Review Letters **96**, 110406 (2006), arXiv:hep-ex/0507107v3 doi: 10.1103/PhysRevLett.96.110406

[204] S. J. Chen, H. H. Mei, W. T. Ni, Modern Physics Letters **A22**, 2815 (2007), arXiv:hep-ex/0611050, doi: 10.1142/S0217732307025844

[205] B. Dobrich, H. Gies, Europhysics Letters **87**, 21002 (2009), arXiv:0904.0216v2, doi: 10.1209/0295-5075/87/21002

[206] E. A. Uehling, Physical Review **48**, 55 (1935), doi: 10.1103/PhysRev.48.55

[207] E. R. Williams, J. E. Faller, H. A. Hill, Physical Review Letters **26**, 721 (1971), doi: 10.1103/PhysRevLett.26.721

[208] D. F. Bartlett, S. Loegl, Physical Review Letters **61**, 2285 (1988), doi: 10.1103/PhysRevLett.61.2285

[209] M. L. Perl, E. R. Lee, D. Loomba, Annual Review of Nuclear and Particle Science **59**, 47 (2009), doi: 10.1146/annurev-nucl-121908-122035

[210] M. Marinelli, G. Morpurgo, Physics Reports **85**, 161 (1982), doi: 10.1016/0370-1573(82)90053-9

[211] P. F. Smith, Annual Review of Nuclear and Particle Science **39**, 73 (1989), doi: 10.1146/annurev.ns.39.120189.000445

[212] M. Marinelli, G. Morpurgo, Physics Letters **B137**, 439 (1984), doi: 10.1016/0370-2693(84)91752-0

[213] P. F. Smith, G. J. Homer, J. D. Lewin, H. E. Walford, W. G. Jones, Physics Letters **B197**, 447 (1987), doi: 10.1016/0370-2693(87)90418-7

[214] P. F. Smith, G. J. Homer, J. D. Lewin, H. E. Walford, W. G. Jones, Physics Letters **B171**, 129 (1986), doi: 10.1016/0370-2693(86)91012-9

[215] W. G. Jones, P. F. Smith, G. J. Homer, J. D. Lewin, H. E. Walford, Zeitschrift für Physik **C43**, 349 (1989), doi: 10.1007/BF01506530

[216] G. J. Homer, P. F. Smith, J. D. Lewin, S. J. Robertson, J. U. D. Langridge *et al.*, Zeitschrift für Physik **C55**, 549 (1992), doi: 10.1007/BF01561292

[217] G. S. Larue, J. D. Phillips, W. M. Fairbank, Physical Review Letters **46**, 967 (1981), doi: 10.1103/PhysRevLett.46.967

[218] L. W. Jones, Reviews of Modern Physics **49**, 717 (1977), doi: 10.1103/RevModPhys.49.717

[219] D. Joyce, P. Abrams, R. Bland, C. Hodges, R. T. Johnson *et al.*, Physical Review Letters **51**, 731 (1983), doi: 10.1103/PhysRevLett.51.731

[220] M. L. Savage, R. W. Bland, C. L. Hodges, J. L. Huntington, D. C. Joyce *et al.*, Physics Letters **B167**, 481 (1986), doi: 10.1016/0370-2693(86)91305-5

[221] V. Halyo, P. Kim, E. R. Lee, I. T. Lee, D. Loomba *et al.*, Physical Review Letters **84**, 2576 (2000), arXiv:hep-ex/9910064, doi: 10.1103/PhysRevLett.84.2576

[222] I. T. Lee, S. Fan, V. Halyo, E. R. Lee, P. C. Kim *et al.*, Physicl Review **D66**, 012002 (2002), arXiv:hep-ex/0204003, doi: 10.1103/PhysRevD.66.012002

[223] P. C. Kim, E. R. Lee, I. T. Lee, M. L. Perl, V. Halyo *et al.*, Physical Review Letters **99**, 161804 (2007), doi: 10.1103/PhysRevLett.99.161804

[224] J. J. Beatty, S. Westerhoff, Annual Review of Nuclear and Particle Science **59**, 319 (2009), doi: 10.1146/annurev.nucl.58.110707.171154

[225] P. Langacker, G. Steigman, Physical Review **D84**, 065040 (2011), doi: 10.1103/PhysRevD.84.065040

[226] K. Irwin, G. Hilton, Topics in Applied Physics **99**, 63 (2005), doi: 10.1007/10933596_3

[227] V. Mandic, Ph.D. Dissertation, University of California, Berkeley, California, USA (2004)

[228] J. Filippini, Ph.D. Dissertation, University of California, Berkeley, California, USA (2008)

[229] T. Bruch, Ph.D. Dissertation, Universität Zürich, Zürich, Switzerland (2010)

[230] Z. Ahmed, Ph.D. Dissertation, California Institute of Technology, Pasadena, California, USA (2012)

[231] J. Kiveni, Ph.D. Dissertation, Syracuse University, Syracuse, New York, USA (2012)

[232] S. Golwala, Ph.D. Dissertation, University of California, Berkeley, California, USA (2000)

[233] J. Sander, Ph.D. Dissertation, University of California, Santa Barbara, California, USA (2007)

[234] K. Sundqvist, Ph.D. Dissertation, University of California, Berkeley, California, USA (2012)

[235] M. Pyle, Ph.D. Dissertation, Stanford University, Stanford, California, USA (2012)

[236] S. Hertel, Ph.D. Dissertation, Massachusetts Institute of Technology, Cambridge, Massachusetts, USA (2012)

[237] K. McCarthy, Ph.D. Dissertation, Massachusetts Institute of Technology, Cambridge, Massachusetts, USA (2013)

[238] T. Shutt, Ph.D. Dissertation, University of California, Berkeley, California, USA (1993)

[239] D. Moore, Ph.D. Dissertation, California Institute of Technology, Pasadena, California, USA (2012)

[240] R. Clarke, Ph.D. Dissertation, Department of Physics, Stanford University, Stanford, California, USA (1999)

[241] T. Saab, Ph.D. Dissertation, Stanford University, Stanford, California, USA (2002)

[242] R. W. Ogburn, Ph.D. Dissertation, Stanford University, Stanford, California, USA (2008)

[243] S. W. Nam, Ph.D. Dissertation, Stanford University, Stanford, California, USA (1998)

[244] M. Brigida, C. Favuzzi, P. Fusco, F. Gargano, N. Giglietto *et al.*, Nuclear Instruments and Methods in Physics Research **A533**, 322 (2004), doi: 10.1016/j.nima.2004.05.127

[245] B. Cabrera, M. Pyle, R. Moffatt, K. Sundqvist, B. Sadoulet, arXiv:1004.1233v1 (2010)

[246] D. S. Akerib, M. S. Armel-Funkhouser, M. J. Attisha, C. N. Bailey, L. Baudis *et al.*, Physics Review **D72**, 052009 (2005), arXiv:astro-ph/0507190, doi: 10.1103/PhysRevD.72.052009

[247] B. L. Dougherty, Physical Review A **45**, 2104 (1992), doi: 10.1103/PhysRevA.45.2104

[248] G. Wang, Journal of Applied Physics **107**, 094504 (2010), doi: 10.1063/1.3354095

[249] K. D. Irwin, Applied Physics Letters **66**, 1998 (1995), doi: 10.1063/1.113674

[250] A. G. Kozorezov, A. F. Volkov, J. K. Wigmore, A. Peacock, A. Poelaert, R. den Hartog, Physical Review **B61**, 11807 (2000), doi: 10.1103/PhysRevB.61.11807

[251] N. E. Booth, Applied Physics Letters **50**, 293 (1987), doi: 10.1063/1.98229

[252] Y. P. Varshni, Physica **34**, 149 (1967), doi: 10.1016/0031-8914(67)90062-6

[253] G. F. Knoll, *Radiation Detection and Measurement* (New York, NY : Wiley, 2000)

[254] J. Lindhard, M. Scharff, H. E. Schiott, Matematisk-Fysiske Meddelelser Konglige Danske Videnskabernes Selskab **33**, 1 (1963)

[255] J. Lindhard, V. Nielsen, M. Scharff, Matematisk-Fysiske Meddelelser Konglige Danske Videnskabernes Selskab **36**, 10 (1968)

[256] W. Sasaki, M. Shibuya, Journal of the Physical Society of Japan **11**, 1202 (1956), doi: 10.1143/JPSJ.11.1202

[257] K. D. Irwin, S. W. Nam, B. Cabrera, B. Chugg, B. A. Young, Review of Scientific Instruments **66**, 5322 (1995), doi: 10.1063/1.1146105

[258] B. Cabrera, Nuclear Instruments and Methods in Physics Research **A444**, 304 (2000), doi: 10.1016/S0168-9002(99)01402-3

[259] T. Saab, R. M. Clarke, B. Cabrera, R. A. Abusaidi, R. Gaitskell, Nuclear Instruments and Methods in Physics Research **A444**, 300 (2000), doi: 10.1016/S0168-9002(99)01401-1

[260] B. S. Neganov, V. N. Trofimov, Journal of Experimental and Theoretical Physics **28**, 328 (1978)

[261] P. N. Luke, Journal of Applied Physics **64**, 6858 (1988), doi: 10.1063/1.341976

[262] H. Maris, Physical Review **B41**, 9736 (1990), doi: 10.1103/PhysRevB.41.9736

[263] H. Maris, S. Tamura, Physical Review **B47**, 727 (1993) doi: 10.1103/PhysRevB.47.727

[264] S. Tamura, J. A. Shields, J. P. Wolfe. Physical Review **B44**, 3001 (1991), doi: 10.1103/PhysRevB.44.3001

[265] S. Tamura, H. Maris, Physical Review **B31**, 2595 (1985), doi: 10.1103/PhysRevB.31.2595

[266] S. Tamura, Physical Review **B31**, 2574 (1985), doi: 10.1103/PhysRevB.31.2574

[267] M. E. Huber, P. A. Neil, R. G. Benson, D. A. Burns, A. M. Corey *et al.*, IEEE Transactions On Applied Superconductivity **11**, 4048 (2001), doi: 10.1109/77.947383

[268] R. P. Welty, J. M. Martinis, IEEE Transactions on Applied Superconductivity **3**, 2605 (1993), doi: 10.1109/77.233523

[269] T. Minotani, K. Enpuku, Y. Kuroki, Journal of Applied Physics **82**, 457 (1997), doi: 10.1063/1.365838

[270] J. N. Ullom, W. B. Doriese, G. C. Hilton, J. A. Beall, S. Deiker emphet al., Applied Physics Letters **84**, 4206 (2004), doi: 10.1063/1.1753058

[271] B. Rossi, *High Energy Particles* (New York, NY : Prentice-Hall, 1952)

[272] W. W. M. Allison, J. H. Cobb, Annual Review of Nuclear and Particle Science **30**, 253 (1980), doi: 10.1146/annurev.ns.30.120180.001345

[273] N. Bohr, Philisophical Magazine **25**, 10 (1913), doi: 10.1080/14786440108634305

[274] N. Bohr, Philosophical Magazine **30**, 581 (1915), doi: 10.1080/14786441008635432

[275] H. Bethe, Annalen der Physik **397**, 325(1930), doi: 10.1002/andp.19303970303

[276] U. Fano, Annual Review of Nuclear Science **13**, 1 (1963), doi: 10.1146/annurev.ns.13.120163.000245

[277] H. Bichsel, Review of Modern Physics **60**, 663 (1988), doi: 10.1103/RevModPhys.60.663

[278] J. F. Ziegler, Journal of Applied Physics **85**, 1249 (1999), doi: 10.1063/1.369844

[279] H. Bichsel, Nuclear Instruments and Methods in Physics Research **A562**, 154 (2006), doi: 10.1016/j.nima.2006.03.009

[280] CDMS Internal Notes, http://cdms.berkeley.edu/wiki/doku.php?id=detectors:soudan:home#towers_1-5, last-acessed: Nov-14-2013

[281] U. Fano, Physical Review **72**, 26 (1947), doi: 10.1103/PhysRev.72.26

[282] E. D. Palik, G. Ghosh, *Handbook of Optical Constants of Solids* (San Diego, CA : Academic Press, 1998)

[283] Online reference, http://physics.nist.gov/PhysRefData/FFast/html/form.html, last-acessed: Nov-14-2013

[284] Online reference, http://physics.nist.gov/PhysRefData/XrayMassCoef/tab3.html, last-acessed: Nov-14-2013

[285] Online reference, http://henke.lbl.gov/optical_constants/asf.html, last-acessed: Nov-14-2013

[286] Online reference, http://henke.lbl.gov/optical_constants/getdb2.html, last-acessed: Nov-14-2013

[287] V. Lucarini, K. Peiponen, J. J. Saarinen, E. M. Vartiainen, *Kramers-Kronig Relations in Optical Materials Research* (Berlin, Germany; New York, NY : Springer, 2005)

[288] CDMS Internal Notes, http://titus.stanford.edu/cdms_restricted/Soudan/R125-128/ebook/121015_2/zeroPointNoiseResolution.html, last-acessed: Nov-14-2013

[289] CDMS Internal Notes, http://titus.stanford.edu/cdms_restricted/Soudan/R125-128/ebook/121008/phon_reso.html, last-acessed: Nov-14-2013

[290] Online reference, http://www.nist.gov/data/PDFfiles/jpcrd22.pdf, last-acessed: Nov-14-2013

[291] Online reference, http://physics.nist.gov/cgi-bin/Star/compos.pl?, last-acessed: Nov-14-2013

[292] Online reference, http://www.nist.gov/pml/data/comp.cfm, last-acessed: Nov-14-2013

[293] R. Agnese, A. J. Anderson, M. Asai, D. Balakishiyeva, R. Basu Thakur *et al.* (unpublished)

[294] CDMS Internal Notes, http://titus.stanford.edu/cdms_restricted/Soudan/R125-128/ebook/120823/LIPsSearch_CheckGammaMC.html, last-acessed: Nov-14-2013

[295] CDMS Internal Notes, http://titus.stanford.edu/cdms_restricted/Soudan/R125-128/ebook/120926/LIPsSearch_GammaBackground.html, last-acessed: Nov-14-2013

[296] CDMS Internal Notes, http://titus.stanford.edu/cdms_restricted/Soudan/R125-128/ebook/120517/LipsStarttime.html, last-acessed: Nov-14-2013

[297] CDMS Internal Notes, http://titus.stanford.edu/cdms_restricted/Soudan/R125-128/ebook/120829_2/DatStatistic.html, last-acessed: Nov-14-2013

[298] CDMS Internal Notes, http://titus.stanford.edu/cdms_restricted/Soudan/R125-128/ebook/090701/Trig_Eff_c58/TriggerEfficiencies_c58.html, last-acessed: Nov-14-2013

[299] CDMS Internal Notes, http://titus.stanford.edu/cdms_restricted/Soudan/R125-128/ebook/121219_2/LipThresholdUncertainty3.html, last-acessed: Nov-14-2013

[300] CDMS Internal Notes, http://titus.stanford.edu/cdms_restricted/Soudan/R125-128/ebook/121023/lips_1keV.html, last-acessed: Nov-14-2013

[301] CDMS Internal Notes, http://titus.stanford.edu/cdms_restricted/Soudan/R125-128/ebook/130204/track_gamma.html, last-acessed: Nov-14-2013

[302] CDMS Internal Notes, http://titus.stanford.edu/cdms_restricted/Soudan/R125-128/ebook/130915/low_ener_reso4.html, last-acessed: Nov-14-2013

[303] CDMS Internal Notes, http://titus.stanford.edu/cdms_restricted/Soudan/R125-128/ebook/130916/low_ener_reso5.html, last-acessed: Nov-14-2013

[304] CDMS Internal Notes, http://titus.stanford.edu/cdms_restricted/Soudan/R125-128/ebook/121015/lips_eff.html, last-acessed: Nov-14-2013

[305] CDMS Internal Notes, http://titus.stanford.edu/cdms_restricted/Soudan/R125-128/ebook/121012/yield_phon_reso.html, last-acessed: Nov-14-2013

[306] CDMS Internal Notes, https://docs.sanfordlab.org/docushare/dsweb/Get/Document-73463/110817GEODMS4Review.pdf, last-acessed: Nov-14-2013

[307] CDMS Internal Notes, https://docs.sanfordlab.org/docushare/dsweb/Get/Document-68574/110317HarrisTAMUFabUpdate.pdf, last-acessed: Nov-14-2013

[308] S. M. Rossnagel, I. C. Noyan, C. Cabral, Journal of Vacuum Science & Technology B: Microelectronics and Nanometer Structures **20**, 2047 (2002), doi: 10.1116/1.1506905

[309] I. C. Noyan, T. M. Shaw, C. C. Goldsmith, Journal of Applied Physics **82**, 4300 (1997), doi: 10.1063/1.366237

[310] P. Petroff, T. T. Sheng, A. K. Sinha, G. A. Rozgonyi, F. B. Alexander, Journal of Applied Physics **44**, 2545 (1973), doi: 10.1063/1.1662611

[311] I. A. Weerasekera, S. I. Shah, D. V. Baxter, K. M. Unruh, Applied Physics Letters **64**, 3231 (1994), doi: 10.1063/1.111318

[312] T. J. Vink, W. Walrave, J. L. C. Daams, A. G. Dirks, M. A. J. Somers, K. J. A. van den Aker, Journal of Applied Physics **74**, 988 (1993), doi: 10.1063/1.354842

[313] J. Ligot, S. Benayoun, J. J. Hantzpergue, Journal of Vacuum Science & Technology A **19**, 798 (2001), doi: 10.1116/1.1355759

[314] C. E. Wickersham, J. E. Poole, K. E. Palmer, Journal of Vacuum Science & Technology B **4**, 1339 (1986), doi: 10.1116/1.583455

[315] F. Meyer, D. Louchier, V. Stambouli, C. Pellet, C. Schwebel, G. Gautherin, Applied Surface Science **38**, 286 (1989), doi: 10.1016/0169-4332(89)90549-7

[316] A. E. Lita, D. Rosenberg, S. Nam, A. J. Miller, D. Balzar *et al.*, IEEE Transactions on Applied Superconductivity **15**, 3528(2005), doi: 10.1109/TASC.2005.849033

[317] B. A. Young, T. Saab, B. Cabrera, J. J. Cross, R. M. Clarke, R. A. Abusaidi, Journal of Applied Physics **86**, 6975 (1999), doi: 10.1063/1.371781

[318] A. A. Abrikosov, L. P. Gor'kov, Soviet Physics - Journal of Experimental and Theoretical Physics **12**, 1243 (1961)

[319] W. A. Roshen, J. Ruvalds, Physical Review **B31**, 2929 (1985), doi: 10.1103/PhysRevB.31.2929

[320] Y. G. Shen, Y. W. Mai, Journal of Materials Science **36**, 93 (2001), doi: 10.1023/A:1004847009613

[321] B. A. Young, S. W. Nam, P. L. Brink, B. Cabrera, B. Chugg *et al.*, IEEE Transactions on Applied Superconductivity **7**, 3367 (1997), doi; 10.1109/77.622094

[322] M. Fritts, Ph.D. Dissertation, University of Minnesota, Minneapolis, Minnesota, USA (2011)

[323] CDMS Internal Notes, https://confluence.slac.stanford.edu/display/CDMS/Ge_Detectors_Documentation, last-acessed: Nov-14-2013

[324] S. Sun, Y. Sun, Z. Liu, D. Lee, S. Peterson, P. Pianetta, Applied Physics Letters **88**, 021903 (2006), doi: 10.1063/1.2162699

[325] J. Kima, J. McVittiea, K. Saraswata, Y. Nishia, S. Liub, S. Tanb, ECS Transactions **3**, 1191 (2006), doi: 10.1149/1.2355913

[326] S. Sioncke, M. Lux, W. Fyen, M. Meuris, P. W. Mertens, A. Theuwis, Solid State Phenomena **134**, 173 (2008), doi: 10.4028/www.scientific.net/SSP.134.173

[327] T. Shutt, J. Emes, E. E. Haller, J. Hellmig, B. Sadoulet *et al.*, Nuclear Instruments and Methods in Physics Research **A444**, 340 (2000), doi: 10.1016/S0168-9002(99)01379-0

[328] Y. Xie, B. Bhushan, Wear **200**, 281 (1996), doi: 10.1016/S0043-1648(96)07275-4

[329] Y. Samitsu, Nanotechnology **4**, 236 (1993), doi: 10.1088/0957-4484/4/4/010

[330] K. D. Irwin, Ph.D. Dissertation, Stanford University, Stanford, California, USA (1995)

[331] H. Geng, *Semiconductor Manufacturing Handbook* (New York, NY : McGraw-Hill, 2005)

[332] K. R. Williams, R. S. Muller, Journal of Microelectromechanical Systems **5**, 256 (1996), doi: 10.1.1.120.3130

[333] V. S. Smentkowski, Progress in Surface Science **64**, 1 (2000), doi: 10.1016/S0079-6816(99)00021-0

[334] M. V. R. Murty, Surface Science **500**, 523 (2002), doi: 10.1016/S0039-6028(01)01586-2

[335] H. R. Koenig, L. I. Maissel, IBM Journal of Research and Development **14**, 168 (1970), doi: 10.1147/rd.142.0168

[336] M. Ohring, *The Materials Science of Thin Films* (Boston, MA : Academic Press, 1992)

[337] D. W. Hoffman, Journal of Vacuum Science & Technology **A12**, 953 (1994), doi: 10.1116/1.579073

[338] R. J. Wilson, B. L. Weiss, Vacuum **42**, 719 (1991), doi: 10.1016/0042-207X(91)90167-H

[339] L. W. Barron, M.S. Thesis, Rochester Institute of Technology, Rochester, New York, USA (2005)

[340] S. Wolf, *Silicon Processing for the VLSI Era* (Sunset Beach, CA : Lattice Press, 2002), Vol. 4

[341] H. Onoda, T. Narita, K. Touchi, K. Hashimoto, Journal of Vacuum Science & Technology **B14**, 2645 (1996), doi: 10.1116/1.588999

[342] C. Kylner, Thin Solid Films **348**, 222 (1999), doi: 10.1016/S0040-6090(98)01398-4

[343] O. Buchmueller, R. Cavanaugh, A. De Roeck, M. J. Dolan, J. R. Ellis *et. al*, arXiv:1110.3568v1 (2011)

[344] D. Speller (private communication, 2013)

[345] C. James, Physics Education **2**, 315 (1967), doi:10.1088/0031-9120/2/6/002

[346] L. B. Valdes, Proceedings of the IRE **42**, 420 (1954), doi: 10.1109/JRPROC.1954.274680

[347] Online reference, http://encyclopedia2.thefreedictionary.com/Glow+Discharge, last-acessed: Nov-14-2013

[348] Online reference, http://www.glow-discharge.com/?Physical_background:Glow_Discharges, last-acessed: Nov-14-2013

[349] A. Fridman, L. A. Kennedy, *Plasma Physics & Engineering* (Boca Raton, FL : CRC Press, 2004)

[350] J. A. Thornton, D. W. Hoffman, Thin Solid Films **171**, 5 (1989), doi: 10.1016/0040-6090(89)90030-8

[351] Y. Sekino, T. Kimura, K. Inokuchi, Y. Sano, M. Sakuta, Japanese Journal of Applied Physics **27**, L2183 (1988), doi: 10.1143/JJAP.27.L2183

[352] M. Loidl, S. Cooper, O. Meier, F. Probst, G. Safran *et al.*, Nuclear Instruments and Methods in Physics Research **A465**, 440 (2001), doi: 10.1016/S0168-9002(01)00621-0

[353] CDMS Internal Notes, http://cdms.berkeley.edu/cdms_restricted/detectors/detsubsysnotes/0201/0201003/ZIPtechnicalreview21.pdf, last-acessed: Nov-14-2013

[354] CDMS Internal Notes, http://cdms.berkeley.edu/cdms_restricted/detectors/detsubsysnotes/0407/0407002/ZIPbatch16recipe.html, last-acessed: Nov-14-2013

APPENDIX A

SEARCH FOR MAGNETIC MONOPOLES

As yet no firm experimental evidence for monopoles has been found. Cosmic-ray experiments have also searched for monopoles but so far it hasn't been detected. For example, the MACRO (Monopole, Astrophysics and Cosmic Ray Observatory) detector in the Gran Sasso National Laboratory has set stringent upper limits [26]. At CERN [27], the search for magnetic monopoles using dedicated detectors began in 1961 with a counter experiment to sift through the secondary particles produced in protonnucleus collisions at the PS (Proton Synchrotron). Over the following years, searches took place at the Interacting Storage Rings and at the SPS (Super Proton Synchrotron). At the LEP (Large Electron Positron) collider, the hunt for monopoles in e+ e- collisions was carried out in two experiments: MODAL (the Monopole Detector at LEP), deployed at intersection point I6 on the LEP ring [28]; and the OPAL monopole detector, positioned around the beam pipe at the OPAL (Omni-Purpose Apparatus at LEP) intersection point [29]. These established new limits on the direct production of monopoles. On 2 December 2009, the LHC's (Large Hadron Collider) seventh experiment was approved, the Monopole and Exotics Detector At the LHC (MoEDAL) [27]. Its prime motivation is to search for the direct production of the magnetic monopole at the LHC.

APPENDIX B

EXPERIMENTAL CHARGE QUANTIZATION LIMITS IN SM PARTICLES

The mechanisms for charge dequantization described in Section 2.3.2 cause neutrons and/or neutrinos to develop electromagnetic charge. This also affect the charge neutrality of matter. These effects can be experimentally studied and constrained [5, 47].

Consider the Standard Model with massive Dirac neutrinos. The charge dequantization ensues in this case [5] (regardless of number of generations) via

$$Q = Q_{SM} + \epsilon\,(B - L)\,/2 \tag{B.1}$$

This result implies that both quarks and leptons have non-standard electric charges. Since the (B - L) value of the hydrogen atom is zero, it will be electrical neutrality despite the presence of above form of charge dequantization. However, neutrons are no longer electrically neutral. Assuming charge conservation and the validity of the CPT theorem, this parameter has to be below $3{\cdot}10^{-21}$ [41]. Experiments on the neutrality of neutrons yield the stringent bound [42, 43] $\epsilon_{neutron} < 1.8{\cdot}10^{-21}e$ There are propositions to increase the sensitivity of experiments by 2 orders of magnitude using Ramsey spectroscopy [43], and by 7 orders of magnitude using atom interferometry techniques [44].

Dequantization of electron charge through the first 2 sets of possibilities in Eq. (2.16), may cause a loss in charge neutrality of bulk matter. Experimental investigations of the neutrality of matter impose an upper limit [46]: $\epsilon_{p-e} < 10^{-21}e$. Constraints on non-neutrality of matter can also be obtained from requiring that the

radial electric field near the earth's surface be less than about 100 Vm^{-1}, yielding $\epsilon < 10^{-27}e$ [45, 48]. Unfortunately this bound assumes that the number of protons in the earth equals the number of electrons, so it cannot be taken as rigorous.

For neutrinos, the electric charge is zero and there are no electromagnetic interactions at tree-level. However, such interactions can arise at the quantum level from higher order loop Feynman diagrams corresponding to perturbative expansion of the SM interaction. Charge dequantization due to Eq. (2.16) also causes the neutrinos in two out of the three generations to have nonzero electric charge.

By assuming electric-charge conservation in beta-decay [45, 50], a constraint on the charge of the electron neutrino, $\epsilon_{\nu_e} < 4{\cdot}10^{-17}e$ is obtained (This upper limit is naturally guided by the upper limit on sum of neutron and proton charge obtained from charge-neutrality experiments). Similarly, agreement between the theoretical and measured cross-sections for $\nu_\mu - e^-$ scattering (which would include a contribution from photon exchange if ν_μ had nonzero charge) constrains $\epsilon_{\nu_\mu} < 10^{-9}e$ [45].

If the fractional charge is due to the last option in Eq. (2.16), then there will be a charge difference between electron and muon. By studying the one-loop photonic contribution to the anomalous magnetic moments of electron and muon, the constraint on difference of charge between them, $\epsilon < l0^{-6}e$ must be imposed in order to preserve the precision of the agreement between the standard theoretical predictions and the measured values for these quantities [5, 45].

Stricter but less certain bounds on neutrino charge can be obtained from cosmological and astrophysical consideration [5, 16, 45]. Charged relic neutrinos would impart a thermal electric mass to the photon, leading to an effective long-distance violation of Gauss's law (or, equivalently Coulombs law), for which the experimental evidence implies $\epsilon < 10^{-12}e$ [49]. Additionally, in models where ν_μ and ν_τ are charged and massless, massive plasmon states in red giant stars can decay into charged $\nu\bar{\nu}$

pairs, which subsequently escape and increase the cooling rate of star so fast that it can delay helium ignition. From the lack of observational evidence of this effect, the bound $\epsilon < 2{\cdot}10^{-14}e$ is obtained [45, 52]. The decay process was first considered in [53] as a possible source of energy loss of the Sun. The requirement that the energy loss does not exceed the solar luminosity, gave $\epsilon_\nu < 6{\cdot}10^{-14}e$ [54, 166]. A bound of $\epsilon_\nu < 10^{-19}e$ is obtained from the observation of electron neutrinos from supernova SN 1987A [45, 51].

Additional discussion on neutrino, including discussions on the neutrino electric charge, can be found in [55].

APPENDIX C

SEARCHES IN BULK MATERIALS

Cosmic rays can interact with bulk materials on Earth and create FCPs trapped inside them. A negative FCP could be held in bulk matter by the coulomb attraction of a nucleus. If it is heavy, it could be in a low Bohr orbit so that it forms a compact object with the nucleus. A positive FCP may itself act as a nucleus, collecting electrons and being held in the solid by molecular forces. The following discussion follows that in [209].

Alternately, one can also study for presence of FCPs in ancient meteoritic materials. Meteorites that come from asteroids may be a particularly rich source of FCPs for several reasons. These meteorites form out of asteroidal surface material that comes loose when asteroids collide. During the formation of the Solar System, asteroids had chemically and electrically active surfaces that may have attracted FCPs. The FCPs produced in early universe would have got incorporated in carbonaceous chondritic meteorites which are some of the most primordial sources of materials inside the solar system (at over 4.5 Gyrs old) [7]. Additionally, it is also believed that they have undergone very little processing since formation. Many asteroids, once formed, are chemically and thermally stable; thus, FCPs collected on an asteroid's surface would remain on that surface [209].

While terrestrial matter is abundant, suitable material may lie far below the Earth's surface. If the FCP is heavier than the nuclei of ordinary matter, during the course of the Earth's geological history, most FCPs would have descended deep within the Earth [209]. No searches have been carried out on material from the Moon because of the scarcity of such material. Also, there is no strong reason to expect

material from the Moon's surface to be particularly rich in FCPs [209].

Another special aspect of bulk matter searches is that the sought FCP is always part of a sample of solid or liquid matter. Thus, the total sample charge is the sum of FCPs and the entirety of the charges from ions or electrons that are not neutralized. The searches can be done using Levitometer (discussed in Section C.1) or Millikan liquid drop based experiments (discussed in Section C.2). These searches provide a sensitive upper limit on the ratio of FCPs mass density to Baryon mass density and can be compared to similar limits obtained from WMAP (discussed in Appendix F.3.4).

C.1 Levitometer Based Searches

Fractionally charged particles can be searched using Levitometer [210, 211]. A sample that may contain a FCP is magnetically suspended in vacuum. An oscillating electric field is applied to the sample, and the resulting motion is observed and measured. Various searches are performed using ferromagnetic levitometer [212–216] and superconducting levitometer [217]. All ferromagnetic levitometer searches reported null results. Although a presence of fractional charge of $\left(\frac{e}{3}e\right)$ was observed in niobium sphere [217], others have failed to find it in larger niobium sample [218]. The current consensus is that the conclusions drawn in [217] were wrong.

C.2 Millikan Liquid Drop Method

In the Millikan liquid drop method for detection of FCPs [219,220], a liquid drop with a radius r ranging from 3 to $15\mu m$ is made to fall under gravity through a measurement region containing still or precisely regulated flowing gas, usually air. The measurement region also contains a horizontal, alternating electric field E. A schematic diagram of the setup is shown in Fig. C.1. Within a few milliseconds, the drop reaches its vertical, downward terminal velocity, $v_{vert-term}$, defined by Stokes'

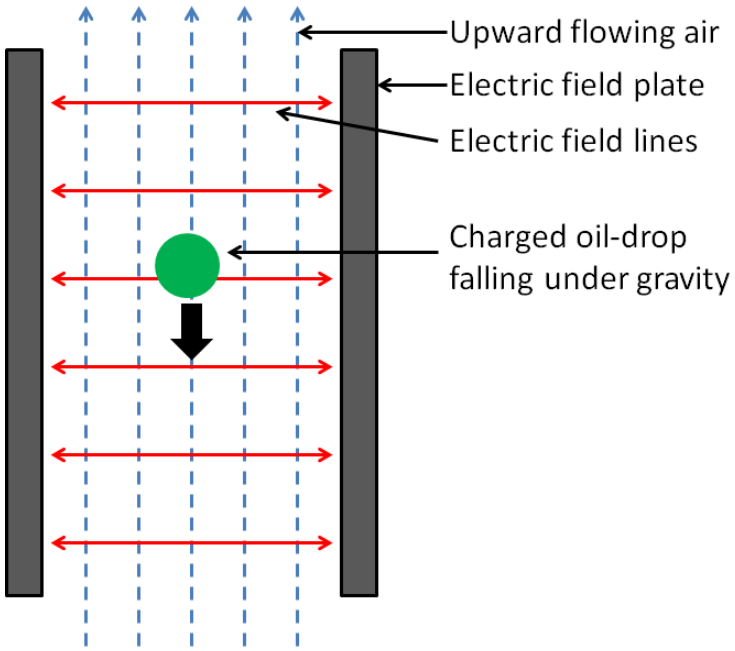

Figure C.1: Schematic of the modern Millikan liquid drop method used to search for fractional charge elementary particles [209, 222].

law,

$$v_{vert-term} = \frac{mg}{6\pi\eta r} \tag{C.1}$$

where m is the drop mass, g is the gravitational acceleration, and η is the viscosity of the gas. Given the liquid density ρ, and $m = \frac{4}{3}\pi r^3$, the drop radius r can be calculated from $v_{vert-term}$. The alternating electric field E causes the drop to have an alternating, horizontal, terminal velocity, $v_{horiz-term}$, which depends on the charge of drop Q

$$v_{horiz-term} = \frac{EQ}{6\pi\eta r} \tag{C.2}$$

The setup has been used to detect FCPs in bulk matter (sea water [219] and mercury [220]), silicon and mineral oil [221–223] and meteorites [223]. The final experiment searched for fractional charge in a 1.5%-by-mass suspension of carbona-

ceous chondrite meteorite dust in light mineral oil. This experiment ran continuously for three years and detected no fractional charge in 42.5 million fluid drops with a total mass throughput of 259 mg of mineral oil and 3.9 g of meteoritic material [223]. The results are shown in Fig. C.2.

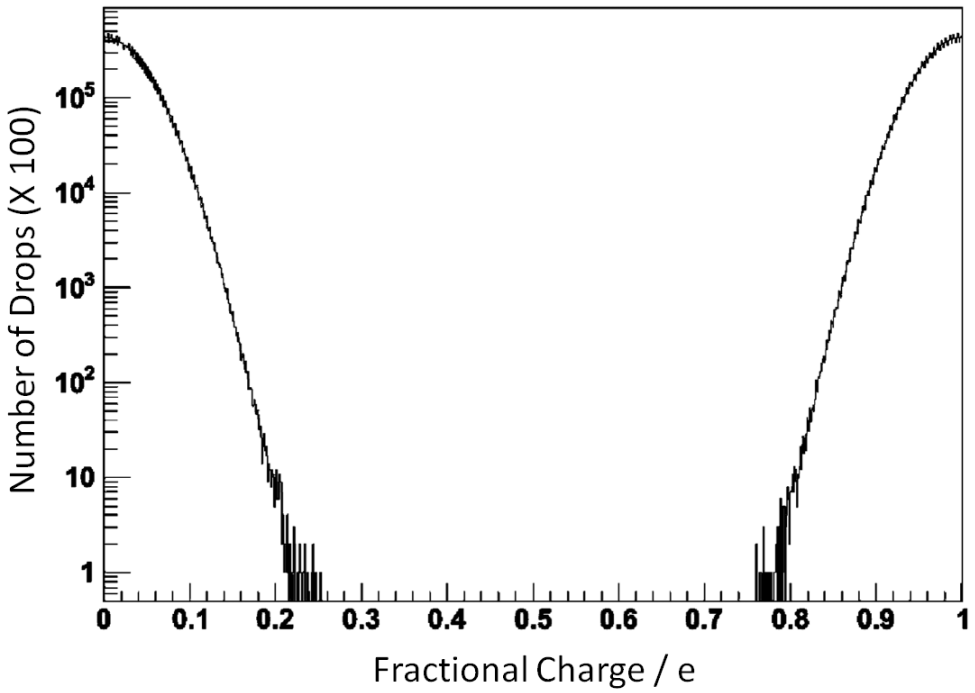

Figure C.2: The result for search of FCPs in meteoritic materials [209, 223]. The sensitivity of experiment reduces for fractional charges close to an integer. For $\mid Q_{total} - n \mid > 0.25$, where n is any integer (i.e. in the region suffiently far away from any integer value), the experiment strongly rejects the presence of FCPs

By comparing these limits to those from models where massive, negatively charged FCPs get bound to light nuclei during Big Bang Nucleosynthesis (BBN, described in Appendix D) and survive further annihilation, a strong exclusion on "mass-charge" parameter space of FCPs is obtained. It excludes FCPs with $q \gtrsim 0.01e$ and mass $M \gtrsim 1GeV$ [225].

APPENDIX D

BIG BANG NUCLEOSYNTHESIS (BBN)

Big Bang Nucleosynthesis (BBN) is a widely accepted model describing conditions in the early universe ($t \simeq 0.1s - 10^4 s$ after the Big Bang, with temperatures ranging from few MeV to 10keV) covering time periods carrying the universe starting from a period with neutron-proton statistical equilibrium with no other nuclear species up to a period with significant presence of helium. It is a standardized theoretical framework with which the abundances of light nuclei formed in the early Universe (bulk of ^{4}He and D as well as good fractions of ^{3}He and ^{7}Li)can be predicted with high reliability. All the other elements are believed to have been produced either by stars or by cosmic rays. BBN consideration can be used to put constraints on allowable "mass-charge" parameter space for FCPs, as discussed in Appendix F.3.3. This appendix describes BBN in sufficient details to help readers understand the processes and rationale behind obtaining those constraints. For a general review on BBN, the following may be referred [14, 101].

BBN asserts that nuclear and fundamental particle properties (e.g. masses, couplings, cross-sections and lifetimes) are the same today as they were in the early universe. The nuclear reaction cross-sections obtained in labs are used to predict the start and evolution of various nuclear reactions as the universe expanded and cooled. Standard BBN calculations rely on the following assumptions [101]:

- The expanding Universe following the Big Bang is spatially isotropic and homogeneous. It is in a radiation-dominated epoch.
- The Universe starts out hot enough for the protons and neutrons to be in

thermal equilibrium, such that they are approximately in equal numbers

- The fundamental particles and their interactions are governed by the SM and the baryon asymmetry (absence of antibaryons) already exists.

- Nuclear and fundamental particle properties (e.g., masses, couplings, cross-sections and lifetimes) are the same today as they were in the early universe when BBN took place.

BBN is almost a parameter free theory depending solely on the baryon number density n_B, the number of relativistic degrees of freedom during BBN N_{eff}, and the lepton asymmetry in the electron neutrino sector. All the parameters can be obtained by different astronomical and/or high energy experiments (like, measurement of Cosmic Microwave Background (CMB) and accelerator based results constraining lepton asymmetry). Thus, BBN predictions can be used as a counter-check to verify results from different astronomical measurements. More importantly, deviations from BBN predictions signal the possibility for presence of undiscovered interactions between fundamental particles and/or new set of fundamental particles. Thus, it can be used to exclude a large portion of charge-mass parameter space for FCPs in models with/ without a hidden-sector photon.

As mentioned, BBN makes predictions for the primordial abundances of the light elements (D, ^{3}He, ^{4}He and ^{7}Li) based upon few input parameters including the number of relativistic particle species present when the temperature of the universe was above $\sim$1MeV. Assuming that the framework of SM holds, the BBN predictions closely match the observed abundances. A critical modification due to presence of additional particles (outside the SM) is that the predicted abundance of ^{4}He is affected. Thus, restriction on parameters of new particle will apply to maintain compatibility between theoretical and observed values, as discussed below. The

discussion below follows from [16].

During the BBN era, the universe's rate of expansion is guided by relativistic particles (the ratio of baryon to photons is $\sim 6{\cdot}10^{-9}$ [101]). It is given by [102]

$$\frac{\dot{R}}{R} = \left(\frac{8\pi\rho G_N}{3}\right)^{\frac{1}{2}} \tag{D.1}$$

and the rate of cooling is given by [103]

$$t = 2.42{g_*}^{-\frac{1}{2}}T^{-2} \tag{D.2}$$

where R is the cosmic scale factor, G_N is Newton's constant, ρ is the energy density, t is time in seconds, T is the temperature in MeV, and g_* counts the effective degrees of freedom. g_* is computed as [103]:

$$g_* = \sum_B g_B \left(\frac{T_B}{T_\gamma}\right)^4 + \frac{7}{8}\sum_F g_F \left(\frac{T_F}{T_\gamma}\right)^4 \tag{D.3}$$

where g_B (g_F) is the number of helicity states of the boson (fermion), T_B (T_F) is the temperature of the species. The sum runs over particles and antiparticles with $M \lesssim 1MeV$. The factor of $\left(\frac{7}{8}\right)$ accounts for the different statistics of fermions in comparison to bosons. For similar temperature, the energy density of fermions is smaller than that for bosons by a factor of $\left(\frac{7}{8}\right)$. As an example, in the SM, $g_* = 2 + \left(\frac{7}{8}\right)(4+6) = 10.75$ from photons, $e^+ - e^-$, and $\nu_i - \bar{\nu}_i$ (assuming all neutrinos are light). The energy density ρ is proportional to g_* via [102]

$$\rho = \frac{\pi^2 g_* T_\gamma^4}{30\hbar^3 c^3} \tag{D.4}$$

Thus the rate of expansion depends strongly on the number of light species present

(that are not significantly colder than the photons) during BBN.

During the evolution of universe, any particle can be thermally produced with equal probability if the temperature of universe if larger than mass of the particle. However, if the annihilation rate of particle from a particular species is slower than rate of expansion of universe, its number will stop evolving (it will "freeze out"). This is because the expansion of universe makes it increasingly difficult for particles to interact and annihilate each other. However, if the interactions among particles are stronger to prevent freeze out, while the temperature of universe becomes less than mass of some particle species, they become non-relativistic and their concentration begins to fall down, following Boltzmann statistics. For $T > 0.7MeV$, the weak reactions

$$\begin{aligned} p + e^- &\leftrightarrow n + \nu_e \\ n + e^+ &\leftrightarrow p + \bar{\nu_e} \\ n &\leftrightarrow p + e^- + \bar{\nu_e} \end{aligned} \tag{D.5}$$

keep neutrons and protons in chemical equilibrium. Since the temperature of universe is lower than mass of neutron (and proton), the neutron to proton ratio decreases rapidly following Boltzmann statistics [101]

$$\frac{n}{p} = exp\left(-\frac{\Delta m}{T}\right) \tag{D.6}$$

where Δm is the neutron-proton mass difference. Below $T \lesssim 0.7MeV$, the weak reaction rates fall below the rate of expansion, and the *(n/p)* ratio becomes frozen (The expansion rate of universe goes as $\sim T^2$, and the weak interaction rate goes as $\sim T^5$. Below a certain temperature, the expansion rate is higher than weak interaction

rate [101]). Starting with equal numbers of protona dn neutrons at high temperature, from $T \sim 940MeV$ to $T{\sim}0.7MeV$, the *(n/p)* ratio falls exponentially to (1/6) [101].

After the freeze-out, the *(n/p)* ratio decreases further because free neutron is not a stable particle. It decays with a lifetime of 885.7s. This reduction continues till the temperature drops to $T{\sim}0.085MeV$, after which the nucleosynthesis starts with formation of Deuteron nuclei. Although Deuteron binding energy is 2.22MeV, the formation of nuclei is delayed due to photodissociation by overwhelmingly large number of photons with energies higher than the deuteron binding energy. Once the temperature drops to 0.085MeV, the exponential Boltzmann suppression of such photons is sufficient to allow formation of Deuteron nuclei and ignite more nuclear reactions. At these temperatures, the neutron-to-proton ratio drops to $\sim 1/7$ [101].

Neutron decay stops once it is used to form Deuteron nuclei. Through multiple nuclear reactions shown in Fig. D.1 [104], neutrons and protons are combined to generate light nuclei. ^{4}He nucleus has the highest binding energy and is most stable among the generated nuclei. Almost all neutrons end up as 4He nucleus [101]. For every two neutrons and fourteen protons (because *(n/p)*=(1/7)),or, 16 baryons, one helium nucleus and twelve protons are obtained. Thus, about (4/16), or, 25% of the baryons by mass are converted to helium. Denoting ^{4}He mass fraction as Y_p, the predictions from BBN suggest: $Y_p = 0.2486{\pm}0.0002$ [105], and the value inferred from astrophysical considerations are $Y_p = 0.249{\pm}0.009$ [106]. Presence of extra FCP species should be such that the concordance between theoretical BBN prediction and observed Helium abundance is maintained.

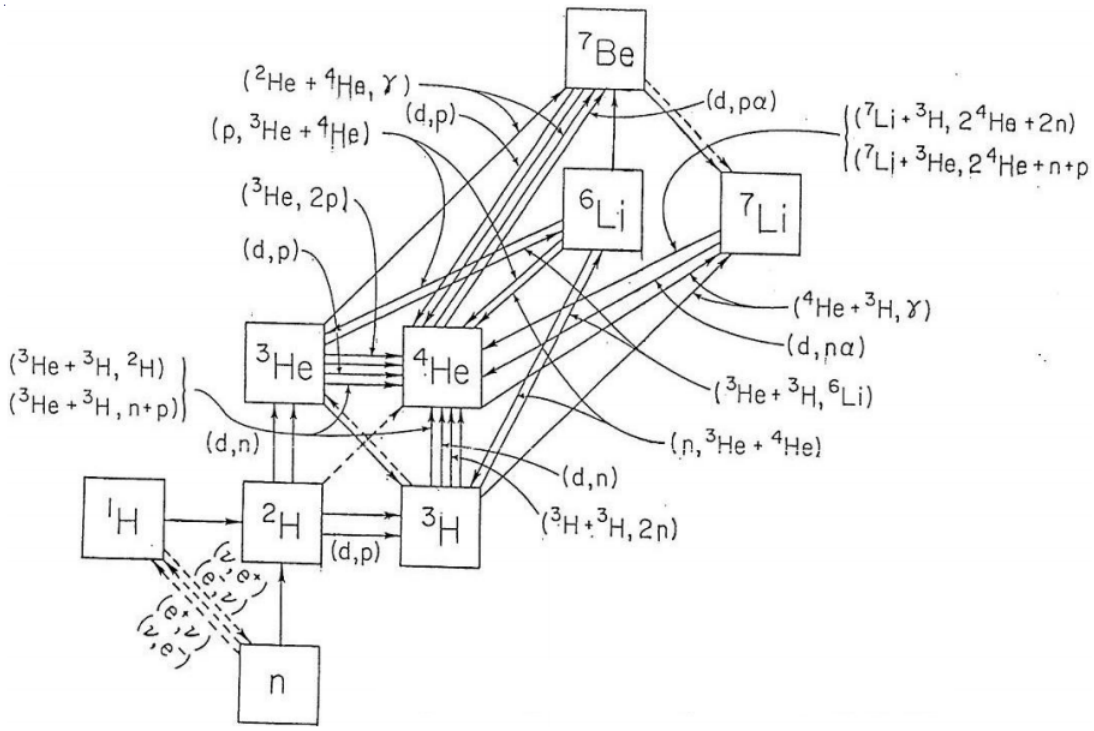

Figure D.1: Nuclear reactions guiding the evolution of primordial light nuclei during BBN [104]

APPENDIX E

COSMIC MICROWAVE BACKGROUND (CMB)

The Big Bang, heralding the creation of universe, was a violent event involving high temperatures. Such high temperatures would be associated with plasma of different SM particles and high energy thermal photons. As universe expands and cools, the energy of these thermal photons also reduces. When the universe has sufficiently expanded and cooled to allow the electromagnetically charged particles to fall into a bound state with each other, these photons get decoupled from the plasma and become free to move throughout the universe. As the universe continues to expand, they continue to reduce in energy. These free streaming photons found everywhere and coming in every direction is the Cosmic Microwave Background (CMB) radiation that providing credibility to theories like the Big Bang model of creation of universe, spatial isotopy of universe and inflation [14,117,118,121]. CMB consideration can be used to put constraints on allowable "mass-charge" parameter space for FCPs, as discussed in Appendix F.3.4. This appendix describes CMB in sufficient details to help readers understand the processes and rationale behind obtaining those constraints.

The CMB radiation was accidentally discovered in 1965 by Penzias and Wilson. Current measurements associate this uniform glow of microwave radiations with a characteristic temperature of $2.725 \pm 0.001K$ [119]. Since these are thermal photons, the frequency distribution of the CMB radiation closely matches a blackbody radiation. These measurements can only be made with absolute temperature devices, such as the FIRAS instrument on the COBE satellite [119]. Such measurements of the spectrum are consistent with a blackbody distribution over more than three decades

in frequency (with some recent evidence for deviation at low frequencies [120]).

Another observable quantity inherent in the CMB is the variation in temperature (or intensity) from one part of the microwave sky to another. They are attributed to the small matter density perturbations in cosmic photon-baryon plasma before CMB photons decoupled. These perturbations grew through gravitational instability into the objects (stars, galaxies, clusters and superclusters of galaxies) we observe today. Subsequent to this epoch, CMB photons propagated freely through the universe except cooling (red-shifting) under the cosmic expansion. However, at the time of their decoupling, photons released from different regions of space experience slightly different gravitational due to matter density perturbations. Since photons redshift as they climb out of gravitational potentials, photons from some regions redshift slightly more than those from other regions, giving rise to temperature anisotropy in the CMB.

Since the rst detection of CMB anisotropies by the COBE satellite ($\Delta T/T \sim 6 \cdot 10^{-6}$) [122], there have been multiple efforts to refine measurements of the CMB anisotropy and its polarization modes by ground-based telescopes (e.g., VIPER [123] and TOCO [124]) , interferometers (e.g., CBI [125] and DASI [126]), as well as balloonborn instruments (e.g., MAXIMA [127] and BOOMERANG [128]). However, it is the data from the satellite-borne Wilkinson Microwave Anisotropy Probe (WMAP) [129] that has provided a detailed all-sky map of the anisotropy through which multiple inferences about the evolution and particle content of universe may be tested Since the same physical laws as SM of particle physics should also apply to the universe, CMB also provides test for the SM.

The following description on the collection, processing and analysis of WMAP data is obtained from [136]. For further details, the following may be referred [130–135].

In the WMAP satellite, microwave radiation is collected using a pair of back-to-back $\gtrsim 2m^2$ Gregorian-style telescopes that feed a series of horns attached to radiometers designed to make multi-frequency differential measurements of the CMB radiation [137]. Rather than measure the absolute temperature of the CMB, the temperature differences between two points in the sky separated by 180° are measured. The instrument aboard WMAP is commonly referred to as a Differential Microwave Radiometer (DMR). The DMR design has the advantage that it is insensitive to the radiative properties of its host satellite, making it largely insensitive to a variety of nontrivial systematic temperature variations. To provide an analogy, it is similar to how the noise performance of a transistor-based amplifier is improved when the transistors share a common substrate (and therefore, temperature). WMAP orbits the Sun in the Sun-Earth L_2 Lagrange point where it is partially shielded from solar radiation. It rotates and precesses quickly enough for its DMR to scan microwave-temperature differences over ∼30% of the sky every hour. Due to its orbit, however, the instrument requires six months in order to access the entire sky, resulting in highly redundant scans of the entire sky in five different frequencies. The WMAP collaboration have released data four times, once after the first fully operational solar orbit (WMAP first-year data [129]) and once every two years since then (WMAP 3-year [138], 5-year [139], and 7-year data [131]).

The data for each frequency band are converted to an all-sky map that is typically displayed in a Mollweide equal-area projection in Galactic coordinates, with the temperature differences given in units of CMB thermodynamic temperature [140] (The Mollweide projection is a type of coordinate transformation commonly used for maps of the globe or the sky. It accurately represents area while tending to distort angles and shapes. For CMB anisotropy maps, the galactic plane runs horizontally through the middle of the map). The maps created include the primordial-temperature differ-

ences from the surface of last scattering ("primary anisotropy"), and also the features due to diffuse galactic emission, point sources such as planets and nearby galaxies. Additionally, a large dipole signature caused by the motion of the Earth relative to the cosmic rest frame also shows up in the temperature map. The reason the maps are recorded at five different frequencies is to remove the undesirable foreground features. The technique for extracting the primary anisotropy is described in [141] and results in a single map like the one shown in Fig. E.1.

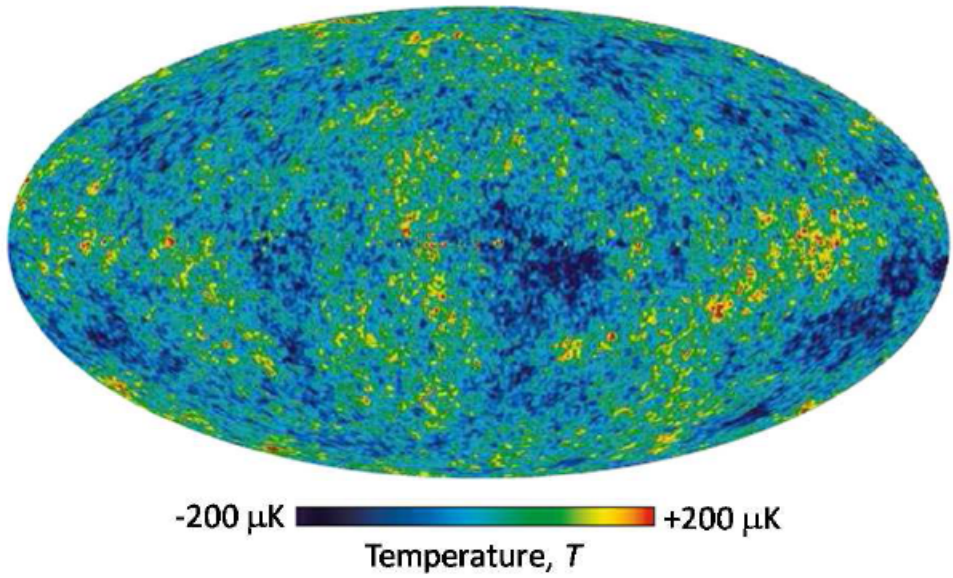

Figure E.1: The Wilkinson Microwave Anisotropy Probe 5-year data all-sky map of the cosmic microwave background primary anisotropy. A Mollweide equal-area projection is used to display the entire sky in galactic coordinates, with temperature differences given in units of thermodynamic temperature. Figure taken from [139].

In order to fit a cosmological model to CMB data, the primary-anisotropy map

is (typically) decomposed into spherical harmonics, Y_{lm};

$$T(\hat{n}) = \sum_{l,m} a_{lm} Y_{lm}(\hat{n}) \tag{E.1}$$

where $\hat{n}$ is a unit direction vector and represents the angular position of a map pixel. The angular power spectrum at multipole moment l is given by an average over the moments m;

$$C_l = \frac{1}{2l+1} \sum_{m=-l}^{l} \mid a_{lm} \mid^2 \tag{E.2}$$

The power spectrum is usually plotted as a function of l in terms of the squared temperature anisotropy, and is shown in Fig. E.2

$$(\Delta T_l)^2 = l(l+1)C_l/2\pi \tag{E.3}$$

The error bars in Fig. E.2 show the power spectrum derived from the WMAP 7-year CMB data for multipoles up to $\gtrsim$1000 [130], augmented with higher multipole moments derived from data obtained by the ACBAR [142] and QUaD [143] experiments. The spectrum can be thought of as the amount of power stored in small- and large-scale fluctuations in the CMB temperature, where low multipole moments represent large angular scales (e.g., $l < 100$ corresponds to $\theta \gtrsim 2^\circ$) and high multipole moments represent relatively small angular scales (e.g., $l > 1000$ corresponds to $\theta \lesssim 0.2^\circ$). These temperature differences represent fluctuations in the temperature of the surface of last scattering which corresponds to the matter-density fluctuations in the early Universe. These perturbations eventually evolve into the structures we see today. The presence of extra FCP components perturb the matter-density fluctuation. By requiring that the perturations be within limits of error, constraints on FCP properties can be put.

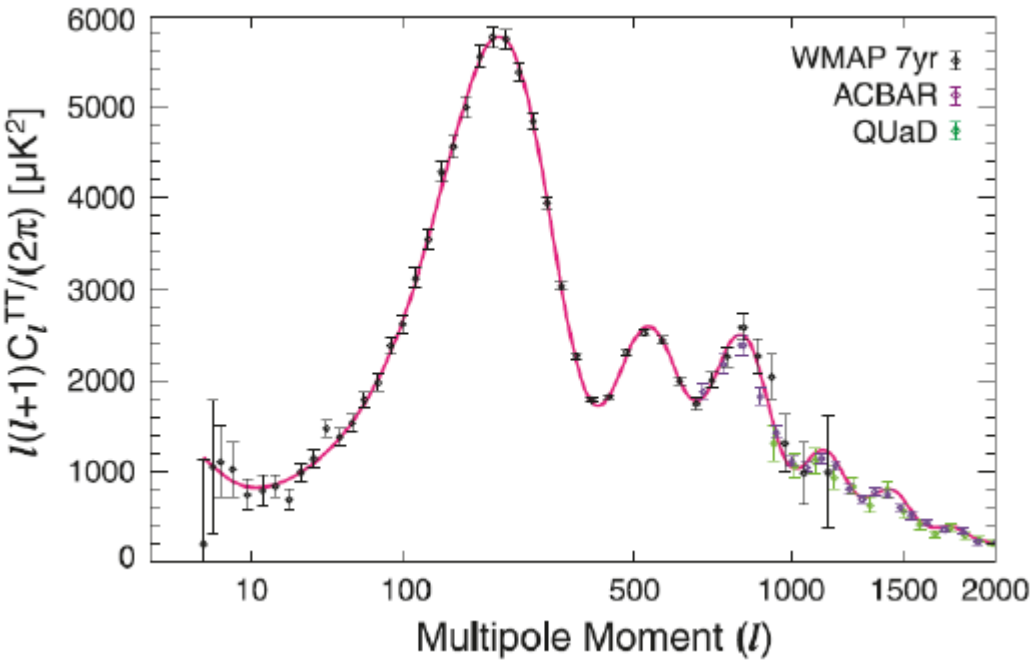

Figure E.2: The angular power spectrum of CMB primary temperature anisotropy as a function of multipole moment. The black error bars up to $l \simeq 1200$ are derived from the WMAP 7-year data [133], while the lighter colored error bars for $l \geq 690$ are derived from data obtained by the ACBAR [142] and QUaD [143] experiments. The solid curve represents the best-fit ΛCDM model to only the WMAP data [130, 136].

Fig. E.2 also shows a best fit cosmological model to the WMAP data. However, before discussing the details of the best-fit cosmological model, it is instructive to qualitatively explore the structure of the power spectrum. For the first two thousand multipole moments the shape is primarily due to three effects: the Sachs-Wolfe effect [144], acoustic oscillations, and Silk damping [145]. For purpose of this dissertation, only acoustic oscillations are described. The following discussion (and extra details not described here) follows the review by Scott and Smoot in [14] and from [136].

The peaked structure of the power spectrum for $l \gtrsim 100$ is due to acoustic oscillations in the baryon-photon fluid prior to recombination. Acoustic oscillations can be understood as a competition between the tendency for baryonic matter to clump

as it falls into gravity wells caused by the initial gravitational perturbations, and the tendency for the radiation pressure of the tightly coupled photon background to oppose the clumping. These pre-recombination oscillations in the tightly coupled baryon-photon fluid cause time variations in the fluid temperature with a frequency characteristic of the speed of sound in the fluid. Following recombination, the photon decouples from the plasma and the phases of the acoustic oscillations freeze out. This causes angular correlations in CMB temperature fluctuations, resulting in the formation of peaks seen in the CMB power spectrum. A CMB model with FCPs provide extra terms guiding the acoustic oscillations. By requiring that the presence of additional FCPs do not cause deviation from observed CMB spectrum, constraints on FCP parameter space can be applied.

The power spectrum's acoustic peaks are sensitive to several cosmological parameters. An open Universe has peaks shifted toward higher multipoles relative to a closed geometry. Furthermore, the absolute and relative amplitudes of the first three peaks is highly sensitive to the baryonic and nonbaryonic matter densities in the early Universe. For example, a larger value of baryonic density causes the baryon-photon fluid to fall deeper into the initial gravitational perturbations, thereby enhancing the compressional acoustic oscillations (odd numbered peaks) relative to the anticompressional acoustic oscillations (even numbered peaks).

Fitting a specific cosmological model to the CMB power spectrum is complicated by the subtle interplay of the many effects that give rise to its shape. Cosmologists have developed a number of sophisticated computer programs to calculate theoretical models and perform likelihood fits to the power spectrum (e.g. cmbfast [146], camb [147], and recfast [148]). The best-fit curve in Fig. E.2 makes use of several such codes in concert to find the simplest known model that reasonably fits the WMAP 7-year power spectrum. The best-fit parameters for the so-called minimal ΛCDM and their

1σ errors taken from [133]. For purpose of this dissertation, the most important fit parameter is the Baryon density ($10^2\Omega_b h^2 = 2.249^{+0.056}_{-0.057}$) (implying that only $\sim 4.5\%$ of entire universe is composed of baryons.)

APPENDIX F

"MASS-CHARGE" EXPERIMENTAL CONSTRAINTS ON EXOTIC FRACTIONALLY CHARGED PARTICLES

Several regions of the charge-mass parameter space for exotic FCPs can be excluded based upon the available experimental evidence. Based on nature of experiments, the constraints described in the following subsections may broadly be categorized as originating from high energy experiments (in Appendix F.1), precision optical experiments (in Appendix F.2) , cosmological (in Appendix F.3) and astrophysical considerations (in Appendix F.4). The results described in this appendix assume a FCP as a particle with only electromagnetic interaction. It may change if the particle gets its fractional charge due to the mechanism described in Section 2.4, as described in sections below. It is pointed out to readers that the unlike Fig. 2.2 which uses inverse of ratio of fractional charge to charge of electron, the plots below use the ratio of fractional charge of particle to the charge of electron. This is done to maintain similarity between the format in which the results are presented in the dissertation to the format in which they are presented in relevant papers.

Fig. F.1 below shows all the constraints in a single plot.

F.1 Constraints from High Energy Experiments

The high energy experiments constraining the properties of FCPs can be broadly classified in to two categories. One set of experiments generate FCPs through high energy reaction (by impinging protons, electrons, etc. on fixed target) and subsequently detecting them. The sensitivity to detection of FCPs through such experiments is severely limited by probability to generate such particles. Sensitive detectors

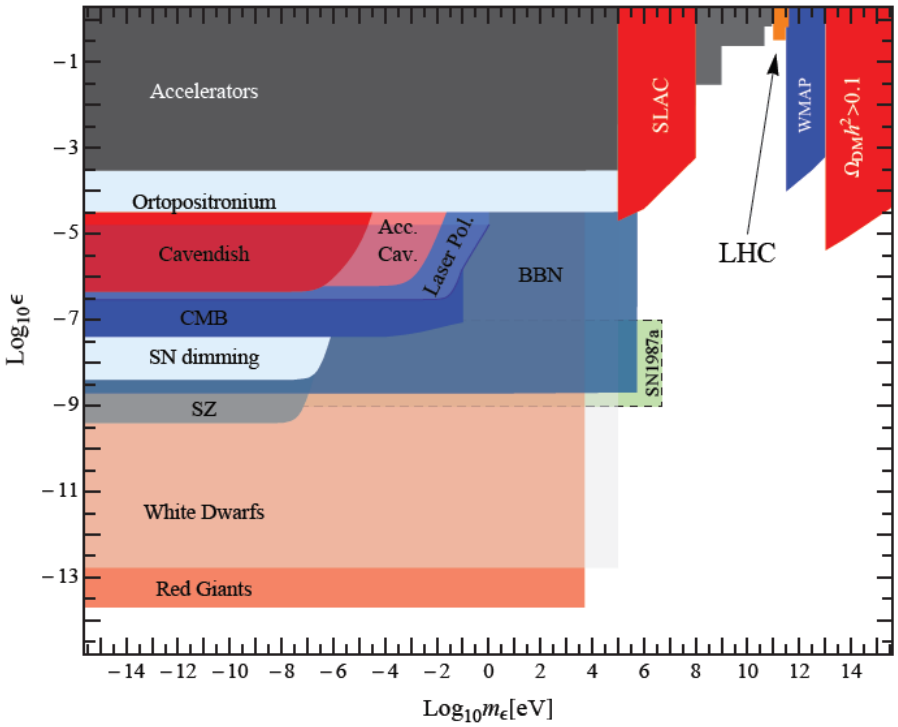

Figure F.1: Constraints on "mass-charge" parameter space for FCPs from various high-energy experiments, precision optical experiments, cosmological and astrophysical considerations [15, 17, 88]. Each of the constraints (and more) are described in this appendix.

and intricate analysis may be employed to enhance the detection of corresponding particle signature once they are generated. The probability to generate FCPs decreases quadratically with the fractional charge (due to reduction in electromagnetic interaction cross-section. In reality, a competitive process enhancing the production rate is due to electromagnetic showers generated within the target). In addition to above, one may only search for particles with mass as allowed by energy of incident beam. Thus, these experiments search for FCPs with low mass and high charge, and are sensitive only to stable FCPs which may survive the time difference between production and measurement. The second set of high energy experiments study the

decay properties of SM particles and negate the existence of FCPs, whose generation would otherwise cause discordance between theoretical predications and observed results. Multiple high energy experiments are described below.

Constraints on properties of FCPs are set based on results from accelerator experiments, schwinger pair-production considerations, muon (g-2) and Lamb shift experiments and by studying the Orthopositronium decay. The results apply both to models with and without hidden sector photon [73].

F.1.1 Accelerator Based Experiments

The Anomalous Single Photon (ASP) [71, 72] search at SLAC studies $e^+ + e^- \rightarrow \gamma + X$, where X is any weakly interacting particle that escape detection. After subtracting contribution from the three neutrino flavors, the limit on the cross-section for the production of FCPs is $\sigma \sim 0.049pb$. It rules out particles with charge $\epsilon > 0.08e$ for masses $M \gtrsim 10GeV$ [16, 73].

Analysis of the data from a proton beam dump experiment, E613, at Fermilab rules out charges between $l0^{-l}e$ and $10^{-2}e$ for $M < 200MeV$ [16, 74].

An electron beam dump experiment at SLAC, which sought to detect neutrino-like particles, has been re-analyzed in the context of trident production ($e^- + N \rightarrow e^- N fcp^+ fcp^-$) and detection ($fcp^{+/-} N \rightarrow fcp^{+/-} N e^+ e^-$) of FCPs, resulting in the exclusion of $\epsilon > 3{\cdot}10^{-4}e$ for $M < 200keV$, and $\epsilon > 3{\cdot}10^{-2}e$ for masses up to 1GeV [16, 73].

Data from the Large Electron Positron (LEP) collider may be analyzed to search for FCPs [17]. These are limits are weaker because the coupling of FCPs with Z-boson is suppressed by a $\sin^2(\theta_W)$ factor. A search for FCPs with $\epsilon = 2/3$ was performed by OPAL using 1991-93 data [17, 75, 76], which rules out $\epsilon \geq 2/3$ for mass $M < 84GeV$. This bound could be extended to the kinematic limit of mass $M < 100GeV$, by

assuming that a particle with $1 > \epsilon > 2/3$ would be seen as such in the detector. By requiring that FCPs do not contribute more than the 2σ error to the invisible width of the Z-boson at LEP1, the LEP bound can be extended to $\epsilon < 0.24$ for mass $M > 45GeV$ (this bound assumes that particles with $1/4 < \epsilon < 2/3$ would escape detection by looking like noise events in the detector, and not be misidentified as ϵ=1 tracks) [17].

A dedicated experiment uniquely suited to the production and detection of FCPs has been carried out at SLAC [87]. The experiment is located near the positron-production target of the SLAC Linear Collider (SLC), which acts as source for FCPs. The high-intensity, short-duration pulses of the SLC beam allow background reduction by requiring the expected signal to occur within a narrow window surrounding the arrival time of each pulse. Scintillation counters are employed to detect signals as small as a single scintillation photon originating from interaction with produced FCPs. Analysis of the data rules out a region of mass and charge, establishing, for example, a 95% confidence upper limit on electric charge of $4.1{\cdot}10^{-5}e$ for FCPs of mass 1MeV and $5.8{\cdot}10^{-4}e$ for mass 100MeV.

Fractionally charged particles can be searched for at the Large Hadron Collider (LHC) by looking for particles in the muon chamber that leave faint tracks because of their subelectronic charges. Such an analysis has recently been performed by CMS [89]. Particles with electric charge $\pm 2e/3$ with masses below 310 GeV, and those with charge $\pm e/3$ with masses below 140 GeV are excluded at 95% confidence. Their results, along with the constraints obtained from different accelerator based experiments are shown in Fig. F.2. One can see that the LHC fills in a gap in the region $100GeV \leq M \leq 390GeV$. Alternatively, the process $pp{\rightarrow}mu^{+}mu^{-}$ may also be considered. The 1-loop contributions to the Z and photon propagators arising from a FCP could give rise to measurable features in the $mu^{+}mu^{-}$ invariant mass

distribution. However, the current sensitivity is not sufficient to obtain new bounds [88].

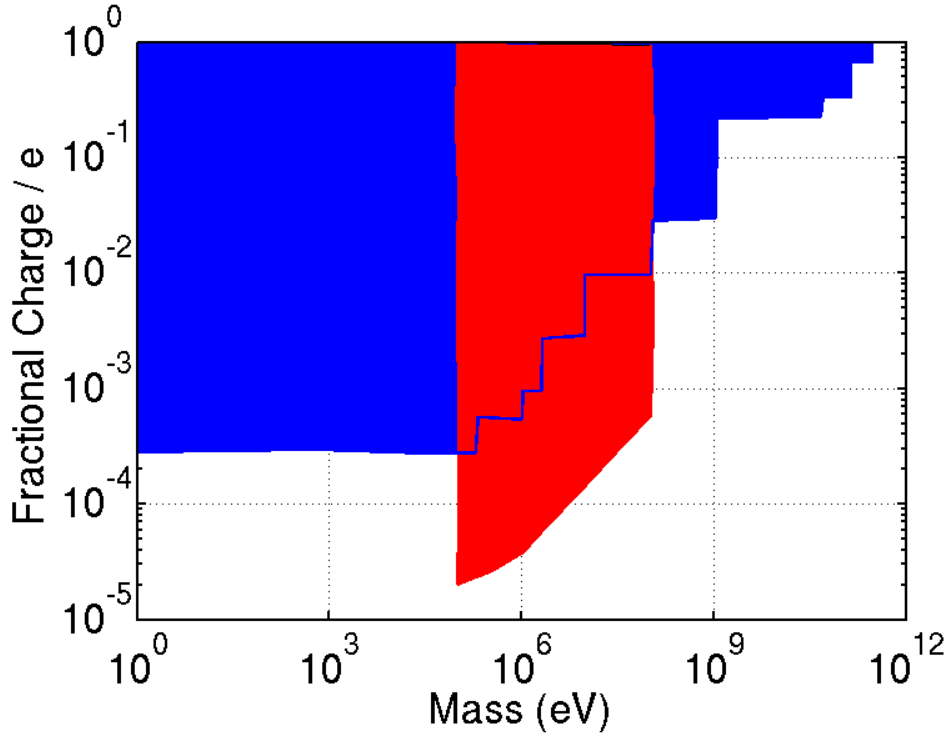

Figure F.2: The blue shaded region shows the "mass-charge" parameter space exclusion for FCPs from analysis of various accelerator based experiments [17, 89]. The red shaded region shows the exclusion from dedicated experiment done at SLAC to search for FCPs [87].

F.1.2 Schwinger Pair-production

Quantum electrodynamics predicts that electron-positron pairs are produced from vacuum in strong electric fields [197–199]. A sizeable rate for spontaneous $e^+ - e^-$ pair production requires extraordinary strong electric field strengths E of order or

above the critical value (with $\hbar = c = 1$)

$$E_c^e \equiv \frac{m_e^2}{e} \simeq 1.3 \cdot 10^{18} V/m \tag{F.1}$$

Acc cavity eqn (1) for which the work of the field on a unit charge e over the Compton wavelength of the electron, $\bar{\lambda_e} = \frac{1}{m_e}$, equals the electron's rest mass me. The process can be viewed as quantum tunneling, giving rise to an exponential field dependence, $\sim exp(-\pi E_c^e/E)$, which exhibits the nonperturbative structure in eE [195]. However, if FCPs with fractional charge ϵe exist in nature, their corresponding critical field,

$$E_c^{\epsilon e} \equiv \frac{m_\epsilon^2}{\epsilon e} \simeq \left(4.98 \cdot 10^6 V/m\right) \left(\frac{1}{\epsilon}\right) \left(\frac{m_\epsilon}{eV}\right)^2 \tag{F.2}$$

may be much smaller and they may be copiously produced with electric fields reachable at currently developed accelerators.

Typical parameters for a time varying electric field in TESLA accelerator $E_{amplitude} \sim (35 - 150) MV/m$ and ν (oscillation frequency)=1GHz [200, 201]. Under these conditions, and assuming that the frequency is much smaller than the rest mass of the FCP, the dominant contribution to the pair-production rate is given by the Schwinger formula [199]. By removing normal dissipative energy loss from cavity, and attributing the remainder as loss due to production of FCPs, constraints on properties of FCPs can be placed as shown in Fig. F.3 [195].

F.1.3 Lamb Shift and (g-2) Experiment

Each particle can be attributed a magnetic moment which is usually expressed in terms of the g-factor. For a free, elementary particle, the Dirac equation predicts g=2 [91]. Due to quantum interactions between particle and electromagnetic vacuum, this classical result differs from the experimental value by a small fraction. The

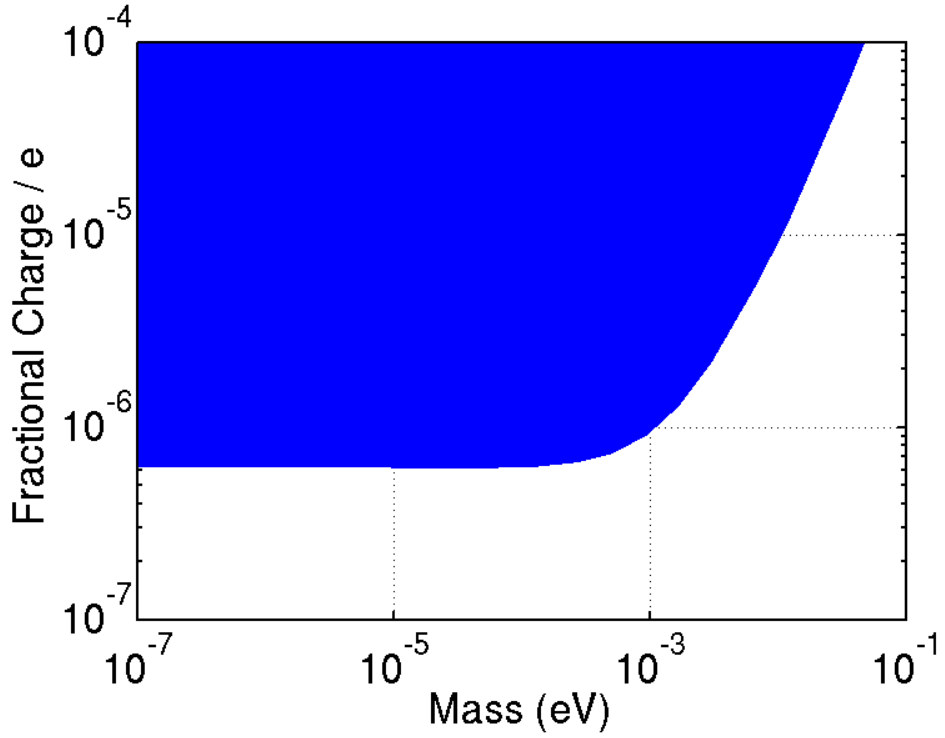

Figure F.3: The blue shaded exclusion limit arises from the bound on the energy loss caused by Schwinger pair production of FCPs in accelerator cavities developed for TESLA ($E_0 = 25MV/m$, $L_{cav} = 10cm$) [193, 200]. In near future ($E_0 = 50MV/m$, $L_{cav} = 10cm$), the bounds can be improved by factor of 4.

fractional difference is the anomalous magnetic moment, denoted as a and defined as a=(g-2)/2.

The Lamb shift [90] is a primarily observed as the small difference in energy between two energy levels $^2S_{1/2}$ and $^2P_{1/2}$ of the hydrogen atom in quantum electrodynamics (QED). This difference is approximately 1063MHz. According to Dirac theory, the $^2S_{1/2}$ and $^2S_{1/2}$ levels should have the same energies. However, the interaction between the electron and the fluctuation of electromagnetic vacuum perturbs the coulomb potential of atomic hydrogen and causes a tiny energy shift of the $^2S_{1/2}$ level.

Experimental deviation from theoretically calculated value of Lamb shift and anomalous magnetic moment signifies presence of unaccounted particles that affect the properties of electromagnetic vacuum. Therefore, these experiments form a nice platform to search for new physics beyond SM.

Recently, two experiments involving these quantum electrodynamics (QED) effects have been in disagreement with theory [77]. The muon anomalous magnetic moment $a_\mu = (g_\mu - 2)/2$ has been measured as $a_{\mu,exp} = 11659208.0 \cdot 10^{-10}$ [92], in 3.4σ disagreement with some of the latest theoretical analyses $a_{\mu,exp} = 11659180.4 \cdot 10^{-10}$ [93].

Muonic hydrogen Lamb shift experiment have been done with aim of determining the proton radius [94, 97]. Assuming QED theory to be correct, the value $r_p = 0.84184(67)fm$ is inferred for the root-mean-square proton charge radius corresponding to the transition ${}^2S_{1/2} \Leftrightarrow {}^2P_{1/2}$ in muonic hydrogen [77]. This value of the proton radius is in disagreement with the value obtained in the same way mainly from hydrogen and deuterium spectroscopy [95], which is the basis of the CODATA value [96], $r_p = 0.8768(69)fm$. The most recent and accurate measurement of the proton radius from electron scattering [97] yields a value of $r_p = 0.879(8)fm$. The two experimental are in excellent mutual agreement but differ from the theoretically calculated muonic hydrogen value by 5.0 standard deviations.

The muon anomalous magnetic moment is numerically small because the correction induced by a hypothetical virtual particle is a two-loop eect. However, for the muonic hydrogen Lamb shift, the contribution of a FCP is a one-loop correction Fig. F.4. Regardless, both of the most recent QED experiments involving muons [92, 94] are in disagreement with theory. The discrepancies have the "same sign", i.e. the experimental values are larger than theoretical estimates.

Since the current experimental limits show the muon anomalous magnetic moment and the Lamb shift discrepancy to have the same sign, an additional virtual

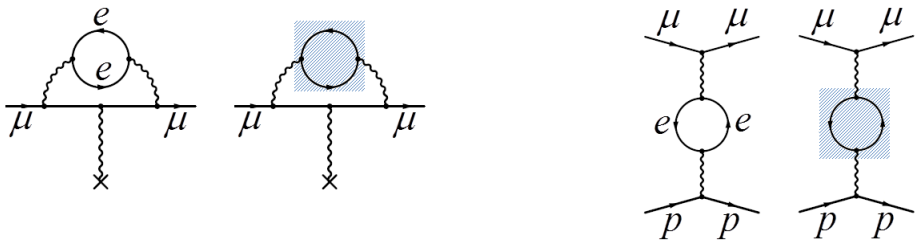

Figure F.4: LEFT: Vertex correction to the muon anomalous magnetic moment with an additional vacuum-polarization insertion in the photon line due to electron-positron loop and other non-QED virtual process including virtual FCPs. RIGHT: Vacuum polarization correction to the muonic hydrogen Lamb shift due to electron-positron loop and extra corrections from non-QED virtual process

excitation of a FCP field producing theoretical enhancement in both eects may be a valid explanation for the discrepancy.

By focusing on FCPs and not treating hypothetical supersymmetric models, it is concluded that a simple modication of the vacuum polarization function due to a FCP cannot simultaneously explain both discrepancies observed for the muon anomalous magnetic moment and for the muonic hydrogen Lamb shift without signicantly distorting the proton radius inferred from electronic hydrogen [77]. Fractionally charged particles could explain the muon anomalous magnetic discrepancy while having a negligible eect on the muonic Lamb shift, but not vice versa. This stands in contrast to limits presented in [17] which were based only from Lamb-shift measurements and not on (g-2) results.

F.1.4 Orthopositronium Decay

Limits on FCPs may be applied by studying decay of Ortho-positronium (o-Ps) [78–80]. Positronium (Ps) is the bound state positron and electron. This makes it the lightest known "atom", which at the current level of experimental and theoretical precision is bound and self-annihilates through the electromagnetic inter-

action [81]. This makes positronium an ideal system for testing the accuracy of bound state Quantum Electrodynamics (QED) calculations [82]. Due to the odd-parity under Charge transformation, the triplet (1^3S_1) state of Ps (orthopositronium, o-Ps), decays predominantly into three photons with a lifetime in vacuum of $\tau_{o-Ps} = 142.05ns$ [79]. The singlet (1^3S_0) state (parapositronium, p-Ps) decays predominantly into two photons with a lifetime in vacuum of $\tau_{p-Ps} = 125ps$ [79]. The longer lifetime of o-Ps gives an enhancement factor $\sim 10^3$ in the sensitivity towards potential new interactions not accommodated in the SM [83].

Evidence for new physics can be searched for by focusing on o-Ps $\rightarrow$ invisible decays (invisible decays mean photonless decays which are not accompanied by energy deposition in a hermetic calorimeter) [79]. In the SM, the invisible decays comprise of o-Ps decay into a neutrino-antineutrino pair with a branching ratio of $6.6{\cdot}10^{-18}$ [84, 85]. Therefore, an evidence for invisible decays with branching ratio $\sim 10^{-7}$ would signal the presence of new physics (like, predicting the existence of extra-dimensions, FCPs, a new light vector gauge boson, or mirror particles which could be candidates for dark matter [79]). Atoyan et al. performed the first experiment to search for invisible decay channels of o-Ps [86] which was repeated by Mitsui et al. [78]. The current limit on branching ratio is Br(o-Ps$\rightarrow$invisible)¡$4.2{\cdot}10^{-7}$ [79]

The theoretical prediction for the decay rate of o-Ps into a pair of fcp^+fcp^- particles with fractional chargeϵe is [80]:

$$\Gamma(o-Ps{\rightarrow}fcp^+fcp^-) = \epsilon^2 \frac{m_e \alpha^6}{6} \sqrt{1 - \frac{m_f cp^2}{m_e^2}} \left(1 + \frac{m_f cp^2}{2m_e^2}\right) \tag{F.3}$$

FCPs can be searched for in o-Ps decays by comparing above with the measured bound on the maximum decay rate of o-Ps into invisible particles, Γ(o-Ps$\rightarrow$invisible) $< 4.2{\cdot}10^{-7}.\Gamma(o-Ps \rightarrow \gamma\gamma\gamma)$. The resulting curve is shown in Fig. F.5 below [79].

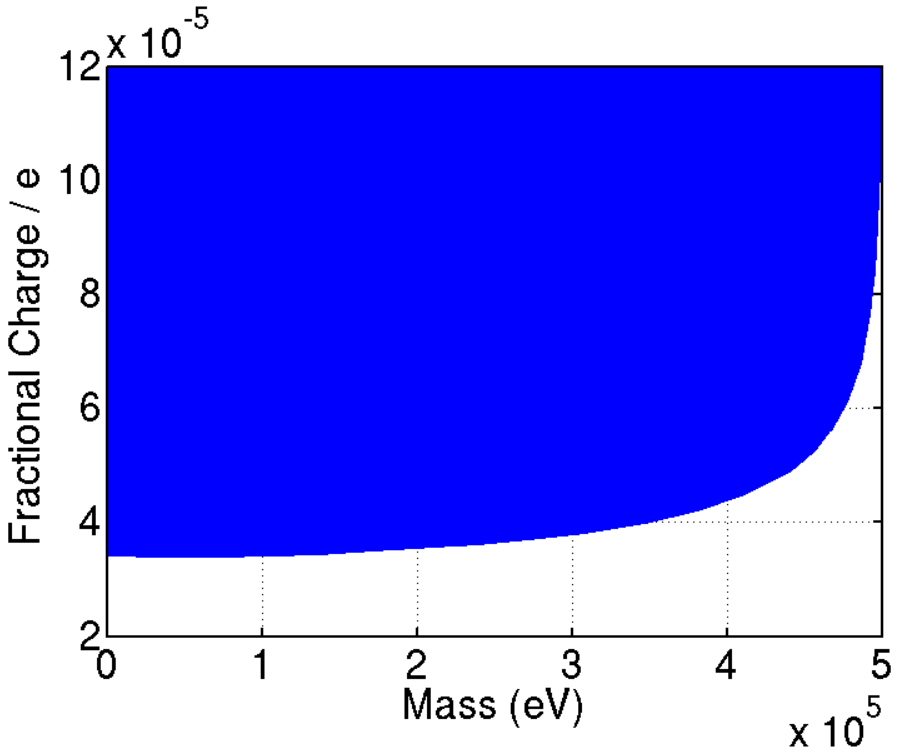

Figure F.5: Excluded "Masscharge" parameter space from study of possible o-Ps decay into FCPs.

F.2 Constraints from Precision Optical Experiments

Strong electromagnetic fields offer a new window to particle physics. Experiments involving strong fields have a new-physics discovery potential which is partly complementary to accelerator experiments. Particle physics effects in strong fields result from the macroscopic spatial extent of the fields which can support coherent phenomena. If the mass of the new particles is sufficiently low, processes can become non-perturbative in the external field, significantly enhancing the discovery potential. Thus, laser experiments can be used as a powerful laboratory tool to shed light on hidden sectors with potentially tiny couplings to photons. In presence of magnetic field, laser photon can decay into FCPs which may be detected via multiple effects.

Constraints on properties of FCPs are set through inferences from laser based experiments measuring vacuum dichroism and birefringence and "Cavendish" like electromagnetic experiments.

F.2.1 Vacuum Dichroism and Birefringence

In QED, photon may decay into an electron-positron, $\gamma \to e^+e^-$, in an external magnetic eld. However, due to the large electron mass, a huge magnetic field is needed to observe the effect. For a light FCP, the decay may happen at lower magnetic field. This decay depends on angle between polarization vector of photon and the direction of applied magnetic field. Thus, the two polarizations decay at a different rate. If a linearly polarized beam of light is sent into a region with magnetic field with equal beam intensity in parallel and perpendicular direction to magnetic field, then the above decay mechanism would cause a difference in intensity of two polarizations as the light exits. This causes a rotation of direction of polarization, and is called vacuum dichroism [196].

In addition to photon decay, the photon can couple to virtual FCPs. This coupling is different for the polarization of light parallel and perpendicular to direction of magnetic field. This brings a difference in refractive index for the two polarizations of light and induces ellipticity in an initially unpolarized light. This phenomenon is called vacuum birefringence [196].

Limits on vacuum dichroism and birefringence from laser polarization experiments such as BFRT [202], PVLAS [203], and Q&A [204] can be used to constrain the parameter space for FCPs [192, 196]. The results are shown below in Fig. F.6. Incidentally, an anomalous ellipticity signal (for magnetic field of 5T) was reported which is only marginally compatible with the other data for larger masses $M \gtrsim 0.1eV$ within the hypothesis of FCPs. Thus, the corresponding PVLAS interpretation is

that the signal results from an instrumental artifact.

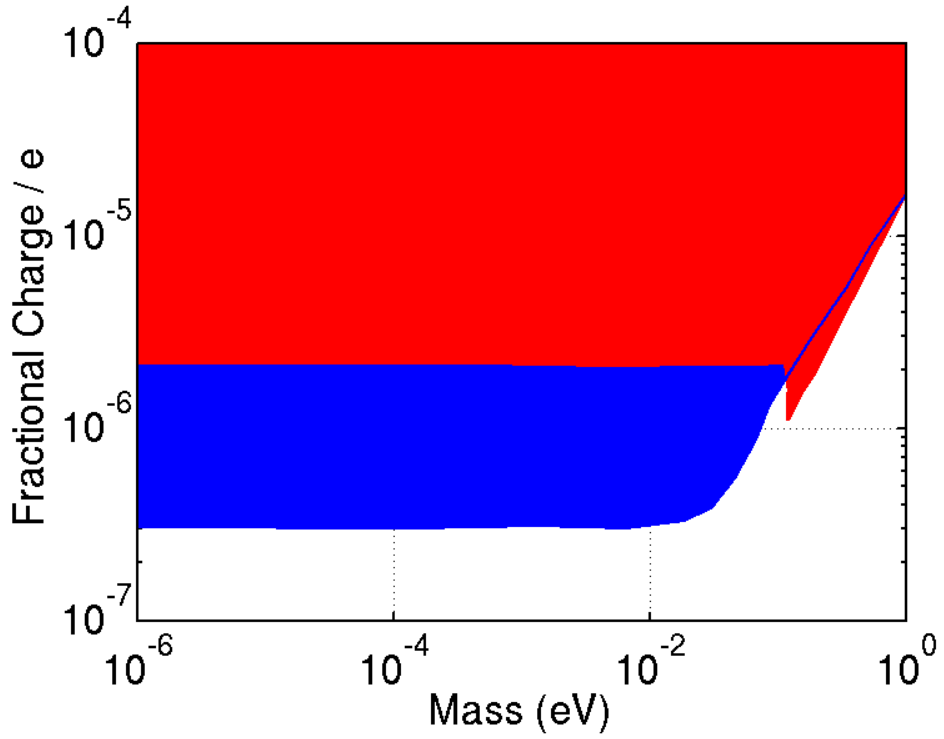

Figure F.6: The blue shaded region represent the excluded "mass-charge" from vacuum birefringence experiments and applies only to pure FCPs. Improvements in above sensitivities can be achieved by interferometric measurements (using gravitational wave interferometers) [205]. The red shaded region represent the excluded "mass-charge" from vacuum dichroism considerations and applies only to FCPs arising from kinetic mixing [193]. [194] describes procedure to test for pure FCPs, but hasn't been experimentally performed. The results from these experiments can also be used to constrain the coupling between normal and hidden sector photon [192].

F.2.2 Test of Coulombs Law (Cavendish-like Experiments)

Cavendish-like experiments form one of the most sensitive tests of the Coulomb potential. The idea behind this experiment is that the field inside a sphere is zero (and the potential constant) if and only if the potential has a 1/r form. Thus, the

potential difference between a charged outer sphere and an uncharged inner sphere is zero if and only if the electric potential has the Coulomb form. Deviations from this form would lead to a non-vanishing potential difference that can be measured [193]. Fractionally charged particles cause a deviation from Coulomb's law via their effect on the vacuum polarization, particularly through the Uehling potential [206]. The presence of a non-vanishing vacuum polarization modifies the form of Coulomb electric potential.

In the simplest version of the Cavendish experiment, there are two concentric spheres. The outer sphere is charged to a certain voltage, and then the voltage difference to the uncharged inner sphere is measured. This primary setup has evolved into a more complicated one involving several spheres. The latest and most precise [207, 208] uses four spheres with radii $d > c > b > a$. A very high voltage is applied between the outer two and the voltage difference is measured between the innermost pair. By requiring consistency between experimental measurements, the parameter space of FCPs can be constrained [193]. The result is shown below in Fig. F.7

F.3 Constraints from Cosmological Considerations

From considerations based on standard cosmological model [98], we may derive additional bounds on the mass-charge parameters of FCPs. The constraints are guided by requiring that the relic density of FCPs be insufficient to overclose the universe, their presence should not result in too large of an effective mass for the photon, incorporation of FCPs does not cause disagreement between the BBN (Big Bang Nucleosynthesis) predictions and measured primordial abundances of the light elements. Similarly, the cosmological models with FCPs should not predict a CMB (Cosmic Microwave Background) spectrum which is inconsistent with the one observed. The dimming of light from distant supernovae also limits the parameters

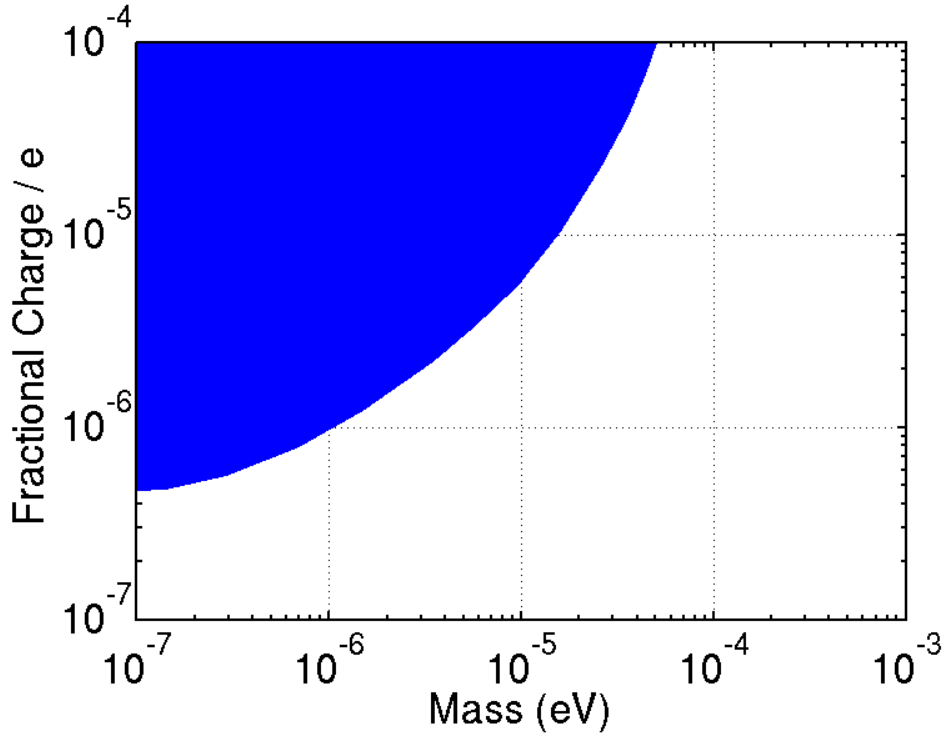

Figure F.7: The blue shaded region corresponds to the "mass-charge" parameter space exclusion obtained from the Cavendish type tests of Coulomb's law [193].

for these particles. In the last section, the allowed parameter range for FCPs as a possible solution to the observed 511keV cosmic-ray anomaly is discussed.

F.3.1 Critical Density of Universe

The standard cosmological model [98] suggests that the universe is flat. Thus, it is expected that the relic density of FCPs, ρ_{fcp} does not exceed the critical density ρ_c that would make the universe flat ($\rho_c = \left(\frac{3H^2}{8\pi G}\right) = 1.88{\cdot}10^{-29}h^2 g/cm^3$ [16, 18], where h is 1/100 of the Hubble constant in $km.sec^{-1}.Mpc^{-1}$). For this criteria to hold, the mass of FCPs must either have a mass smaller than ∼100eV, or its population must have been greatly reduced via annihilation, or its interaction with normal-matter sectors must have been out of thermal equilibrium [16]. FCPs can go out of

equilibrium is the total interaction rate (sum of annihilation by $fcp^+fcp^- \rightarrow \gamma\gamma$ and scattering due to $fcpe \rightarrow fcpe$), which is lower for a higher mass FCP, is less than expansion rate of universe [73].

Assuming for the moment the absence of a hidden sector photon (i.e. the FCPs exists without there being any hidden sector photon), the FCPs with mass greater than that of electron will annihilate to pair produce electron-positron. In this case, the requirement that ρ_{fcp}/ρ_c be less than 1 leads to the bound $M < 2{\cdot}10^3(q/e)GeV$ [73], assuming the particles are in thermal equilibrium with normal sector matter (this criteria is met as long as $M < l0^{l5}(q/e)^2Gev$ [73]). For $M < m_e$, the dominant annihilation process is $fcp^+fcp^- \rightarrow \gamma\gamma$, and the corresponding bound is $M < 10^3(q/e)^2GeV$ [16, 163]. The results again hold as long as thermal equilibrium is maintained, requiring $q > 10^{-9}e$ [163].

If hidden-sector photon exists, then the FCPs can annihilate to produce these hidden photons. Due to extra decay chains, less severe constraints follow on the properties of FCPs (as compared to when hidden photons are absent). The corresponding bounds (that apply under thermal equilibrium) get relaxed to $M < 10^5\alpha' GeV$, where α' is the coupling constant with the hidden sector bosons. If $\alpha' < 1/10$, then $M < 10TeV$ applies, along with the criteria of thermal equilibrium ($M < l0^{l5}(q/e)^2Gev$) [163].

Fig. F.8 show the constraints on "mass-charge" parameter space of FCPs due to above consideration, in models without and with hidden sector photons (paraphotons).

F.3.2 Thermal Mass of Photon

The presence of relic light, FCPs spread throughout the universe amounts to a thermal bath with $T \sim 2^\circ K$ [16, 100]. It forms a background plasma through which

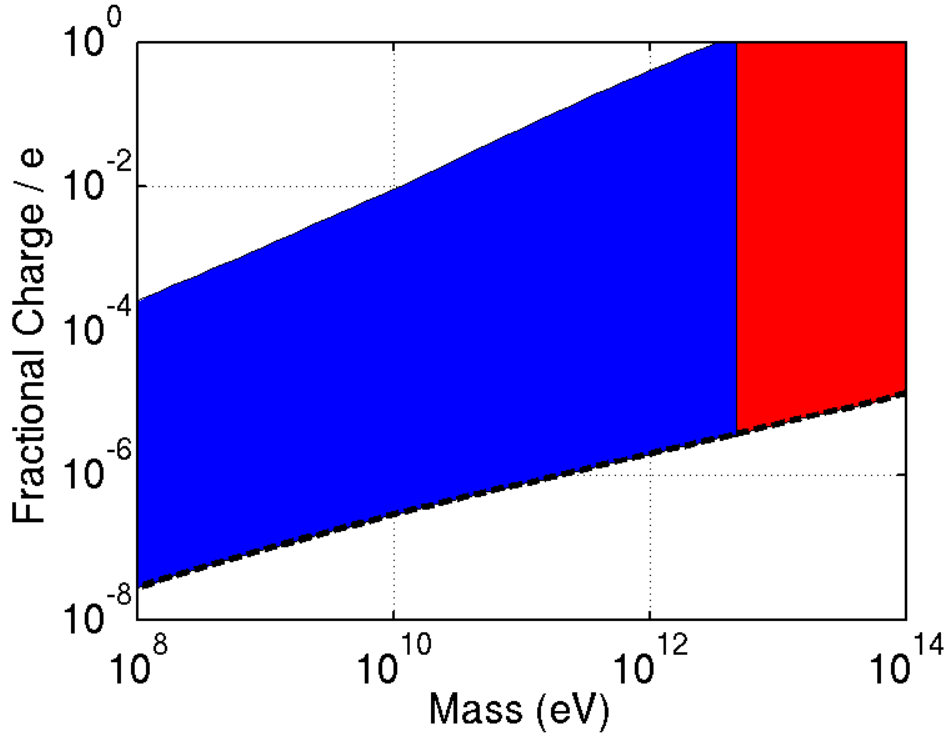

Figure F.8: The blue shaded region (including the region hidden below the red shaded area) is excluded by requiring the relic abundance of FCPs to be less than critical density, in models without paraphoton. The red shaded region shows the exclusion region in models with paraphoton (assuming $\alpha' = 0.1$). Below the dashed black line, the FCPs cannot be thermally produced in the Early Universe [73].

the photons must traverse. Due to electromagnetic interaction with the plasma, the photons will acquire a thermal electric mass $m_{el,thermal}$, which will manifest itself experimentally as a long-range violation of Gauss's law (or equivalently, Coulomb's law). Comparing the lowest-order contribution to $m_{el,thermal}$ (from the 1-loop vacuum polarization diagram with internal propagators taken at finite temperature) and experimental tests of Gauss's law limiting $m_{el,thermal} < 10^{-25} GeV$ [49], FCPs with $q > 10^{-l2}e$ for $M < 10keV$ are excluded [100].

F.3.3 Big Bang Nucleosynthesis (BBN)

Big Bang Nucleosynthesis (BBN) [14, 101] is a widely accepted model describing conditions in the early universe ($t \simeq 0.1s10^4s$ after the Big Bang, with temperatures ranging from few MeV to 10keV) covering time periods carrying the universe starting from a period with neutron-proton statistical equilibrium with no other nuclear species up to a period with significant presence of helium. It is a standardized theoretical framework with which the abundances of light nuclei formed in the early Universe (bulk of ^{4}He and D as well as good fractions of ^{3}He and ^{7}Li)can be predicted with high reliability. All the other elements are believed to have been produced either by stars or by cosmic rays. It is almost a parameter free theory depending solely on the baryon number density, n_b, the number of relativistic degrees of freedom during BBN, N_{eff}, and the lepton asymmetry in the electron neutrino sector. Further details on BBN are discussed in Appendix D.

(Describing BBN briefly) As the universe expands, it cools. At a given time, all particles with mass smaller than temperature of universe are thermally generated. The particles may interact and annihilate as long as the probability for them to find each is reduced due to expanding universe, or, as long as the interaction rate is larger than expansion rate. The expansion rate during BBN is guided by relativistic fermionic and bosonic species at a given time (during BBN, the universe is radiation dominated with $\sim 10^9$ photons for every baryonic matter [101]). At $T \lesssim 0.7MeV$, the expansion of universe is faster than weak interactions, causing a freeze-out of *(n/p)* ratio at 1/6 [101]. After the freeze-out, the *(n/p)* ratio decreases further because free neutron is not a stable particle (it decays with a lifetime of 885.7sec). This reduction continues till the temperature drops to ∼0.085MeV and the *(n/p)* ratio becomes 1/7 [101]. Subsequently, nuclear reactions start and combine protons and

neutrons to form light nuclei. If the universe is populated by SM particles, then the predicted evolution of baryonic concentration within the framework of BBN closely matches the abundance of those elements as inferred from astrophysical calculations. Thus, any variation to SM should be such that the concordance of BBN predictions (under new model) with experimental observations is not broken.

The amount of each light element produced in the BBN framework depends on the neutron to proton ratio (the nucleon to photon ratio is used as a free parameter which can be measured from the Cosmic Microwave Background [99]). To obtain a prediction of ^{4}He abundance (and abundance of other lighter nuclei), it is necessary that neutrons and protons evolve in correct ratio. The neutron to proton ratio depends strongly on the temperature at which the weak reactions freeze out. This depends upon the expansion rate, which in turn depends on the number of light species. As an example, consider if there are extra light, relativistic species present during BBN in addition to SM particles. Presence of extra light species increases the energy density and expansion rate. A greater expansion rate means that the nuclear reactions based weak interactions will freeze out at a higher temperature. Thus, the *(n/p)* ratio freezes at a higher value. Since most of the available neutrons get bound into ^{4}He, its abundance will increase. Thus, a change in ^{4}He abundance can be related to a change in the effective degree of freedom, g_* during BBN [102]

$$\Delta Y_p \cong 0.19 \log_{10} \left(g_* / g_*^{SM} \right) \tag{F.4}$$

where Y_p is the mass fraction of ^{4}He. Traditionally, the number of degrees of freedom is expressed in terms of the equivalent number light neutrino species $N_{\nu*}$, with $N_{\nu*}$ and g_* related by $N_{\nu*} = (4/7)(g_* - 5.5)$. Restricting Y_p between 0.24 and 0.26 corresponds to $2.6 < N_{\nu*} < 4$ [101].

In applying above relation between g_* and primordial ^{4}He abundance, the assumptions of BBN need to be considered. BBN predictions assume that the fundamental particles and their interactions are governed by SM with $leptonasymmetry < 0.15$ [109, 110, 113]. Any unknown/ undiscovered particle or reaction mechanism which might directly affect the weak reaction rates, or for larger lepton asymmetry, the production of light elements are affected [107, 108]. Decays or annihilations of a heavy standard model neutrino would also impact light element abundances. In such cases it is necessary to define an effective number of degrees of freedom g_{eff} (or equivalent number of light neutrino species $N_{\nu,eff}$) based upon the model's prediction for the abundance of ^{4}He, and compare them to the bounds from astrophysical observation of ^{4}He abundance. Assuming that neutrinos cannot decay or annihilate, and that nothing in the model under consideration would affect the rate of the weak reactions (i. e., assuming $g_{eff} = g_*$), limits on FCPs may be derived.

From above constraints on N_{eff}, one may conclude that a FCP which is relativistic and remains in thermal equilibrium at BBN cannot be a massive Dirac particle. A Dirac particle corresponds to 2 neutrino particle (due to its two spin states). With 3 standard model neutrinos existing, BBN constraints only allow for existence of one extra light neutrino-like degree of freedom. Since the coupling between FCPs and ordinary particles will keep them in thermal equilibrium if $q > 10^{-8}e$ for $m < m_e$ [17, 111], the FCPs with these properties are excluded to maintain concordance with BBN predictions ([17] cites the limit of $q > 2.1{\cdot}10^{-9}e$ as the region excluded for FCPs with mass $M \lesssim m_e$. This result is similar to above result which is obtained from a simple consideration, but is more quantitaive and errors are better controlled). Similar bounds hold for models with hidden sector photon (paraphoton) [112]. However, the above mentioned limits can be relaxed if the lepton asymmetry is allowed to increase (i.e. if we deviate from the assumptions used to construct the BBN framework) [114].

The constraints on FCPs from BBN considerations are shown in Fig. F.9 below.

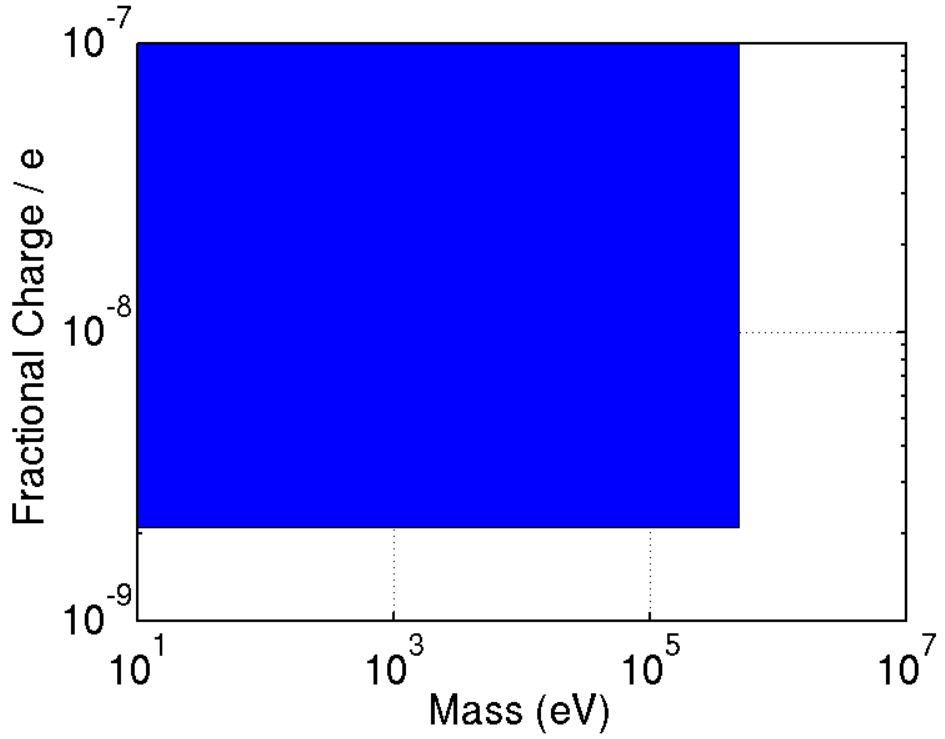

Figure F.9: The blue shaded region corresponds to the "mass-charge" parameter space excluded from BBN considerations [17, 112].

The above construction of BBN framework studies the presence of undiscovered, light, relativistic species during BBN era as particles which are in thermal equilibrium with neutrinos. However, if the particles are fractionally charged, then they predominantly interact with the electromagnetic plasma. It is found that the BBN effects of these particles disfavor masses below about 2MeV. However, masses in the approximate range of 410 MeV actually have the opposite effect of lowering Y_p without significantly affecting deuterium. Therefore, the concordance between the predicted and observed ^{4}He and ^{2}H abundances is slightly improved [114–116].

F.3.4 Cosmic Microwave Background (CMB)

The Big Bang, heralding the creation of universe, was a violent event involving high temperatures. Such high temperatures would be associated with plasma of different SM particles and thermal photons. As universe expands and cools, the energy of these thermal photons would also reduce. Finally, as electromagnetically charged particles fall into a bound state with each other, these photons would be free to move throughout the universe, and will continue to reduce in energy as the universe expands. These free streaming photons found everywhere and coming in every direction is the CMB (Cosmic Microwave Background) [14, 117, 118] radiation that providing credibility to theories like the Big Bang model of creation of universe, spatial isotopy of universe and inflation [121]. A detailed discussion of CMB is given in Appendix E. Here, we describe relevant details which may be used to constrain parameter space for FCPs.

The CMB radiation was accidentally discovered in 1965 by Penzias and Wilson. Current measurements associate this uniform glow of microwave radiations with a characteristic temperature of $2.725 \pm 0.001 K$ [119]. Since these are thermal photons, the frequency distribution of the CMB radiation closely matches a blackbody radiation. These measurements can only be made with absolute temperature devices, such as the FIRAS instrument on the COBE satellite [119]. Fractionally charged particles with $M \lesssim eV$ can be pair-produced by CMB photons after they get decoupled from plasma (via $\gamma\gamma \to fcp\bar{fcp}$). Such a process leads to an energy-dependent depletion of the CMB, whose energy spectrum has been measured with $\sim 10^{-5}$ accuracy by FIRAS. By fitting to the FIRAS data a maximum limit of $Y = n_{fcp}/n_\gamma \lesssim 6{\cdot}10^{-5}$ (up to 3σ confidence) is obtained, for $M_{fcp} \sim 0.1 eV$. This is shown in Fig. F.10 below.

Constraints on properties of light, FCPs can be applied by requiring consistency

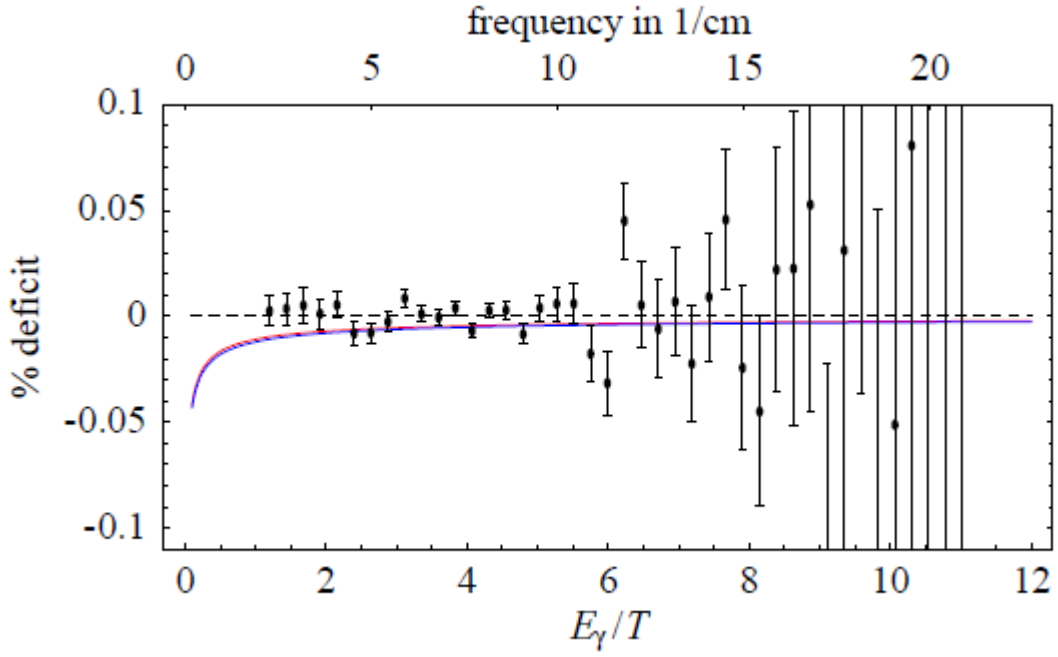

Figure F.10: FIRAS data compared to the energy-dependent depletion of the CMB spectrum due to $\gamma\gamma \to fcp\bar{fcp}$. The distortion in the photon energy spectrum is plotted for fermion (scalar) FCPs with $M_{fcp} = 0.1eV$ and $q = 10^{-7}e$ ($q = 1.7{\cdot}10^{-7}e$), chosen such that the two cases give roughly equal effects, excluded at about 3 standard deviations [149].

between FIRAS measurements with possible modifications in CMB energy spectrum from introduction of FCPs (Separate results are obtained if the FCP is treated as a scalar or fermion) [149]. Since the constraints from assumption of FCP as a scalar particle is more conservative, it is shown below in Fig. F.11.

When photons from the CMB pass through galaxy clusters, there is a small probability that they will interact with the high energy cluster-electrons. The low energy CMB photons can be Thomson scattered up to higher energies, distorting the CMB spectrum. This is the Sunyaev-Zel'dovich (SZ) effect [150, 151]. An important property of the SZ effect is that, because on average the CMB photons gain energy when scattered, the spectral shape of the SZ effect is a decrement in the temperature of

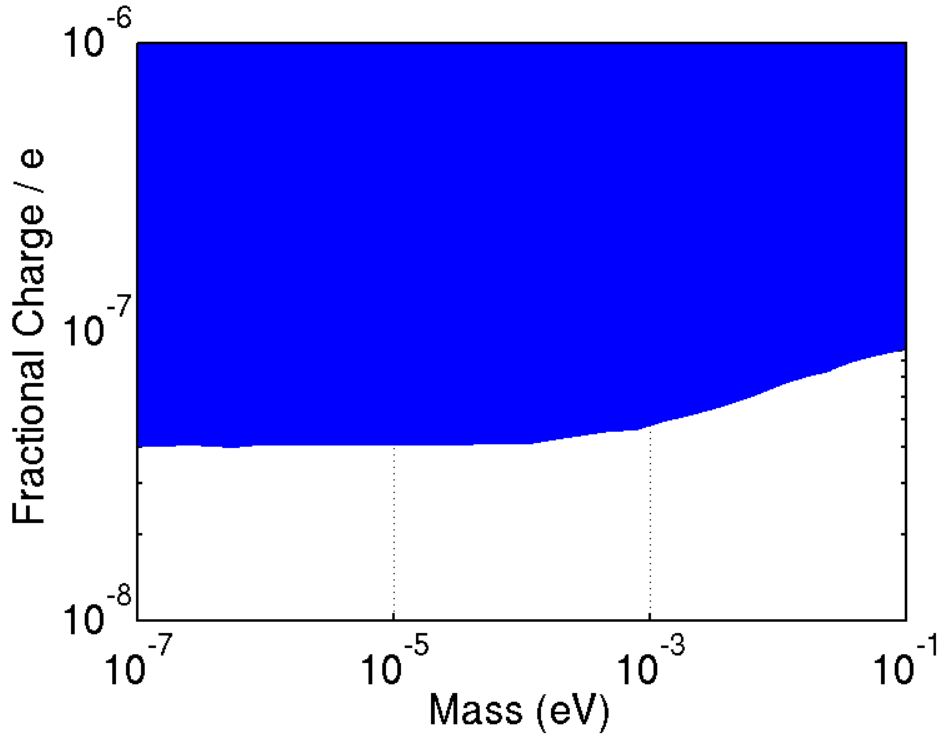

Figure F.11: The blue shaded region is excluded by requiring match within allowed variations in the CMB energy spectrum, assuming FCPs as scalar particles. The excluded limits drops further down by a factor of 2 for fermionic FCPs [15, 149].

the CMB at low frequencies, and an increment at high frequencies, crossing through a null at around 217GHz.

A photon loss mechanism contribution to the SZ effect is due to conversion of CMB photons into virtual or real FCPs as they pass through magnetic field of cluster of galaxies [152]. Clusters of galaxies are some of the largest objects in the universe; a typical cluster contains $\sim 10^3$ galaxies in a region $\sim 2Mpc$ in radius. The magnetic fields of these clusters are relatively well understood [153], and it is common to model these magnetic fields as being made up of a large number of equally sized magnetic domains. Within each domain the magnetic field is constant, and the magnitude of the magnetic field strength is constant over the whole cluster, but within each domain

the direction of the magnetic field vector is essentially a random variable. Photons passing through such clusters may interact with the cluster magnetic field and convert into real or virtual MCPs. This loss of photons would look like a contribution to the SZ effect of the form

$$\frac{\Delta T}{T} = \frac{1 - e^{-x}}{x} \frac{\Delta I}{I_0} \tag{F.5}$$

where I_0 is the photon flux from the CMB, ΔI is the flux decrement due to MCPs and $x = \omega / T_{CMB}$, and ω is the photon energy and T_{CMB} is the temperature of the CMB radiation today. The best constraints would come from a cluster for which both the SZ effect and the properties of its magnetic field have been directly measured. This is uniquely the case for the Coma cluster (Abell 1656) which lies at a redshift z = 0.023. By requiring that the decrement in flux of CMB photons is not larger than the observed SZ effect, constraints on the parameter space of FCPs may be put [152]. The constraints vary depending on hidden sector coupling strength. In Fig. F.12, the constraint corresponding to model with a very weakly coupled, or without a hidden sector photon is shown.

Another observable quantity inherent in the CMB is the variation in temperature (or intensity) from one part of the microwave sky to another. They are attributed to the small matter density perturbations in cosmic photon-baryon plasma before CMB photons decoupled. These perturbations grew through gravitational instability into the objects (stars, galaxies, clusters and superclusters of galaxies) we observe today. Subsequent to this epoch, CMB photons propagated freely through the universe except cooling (red-shifting) under the cosmic expansion. However, at the time of their decoupling, photons released from different regions of space experience slightly different gravitational due to matter density perturbations. Since photons redshift as they climb out of gravitational potentials, photons from some regions redshift

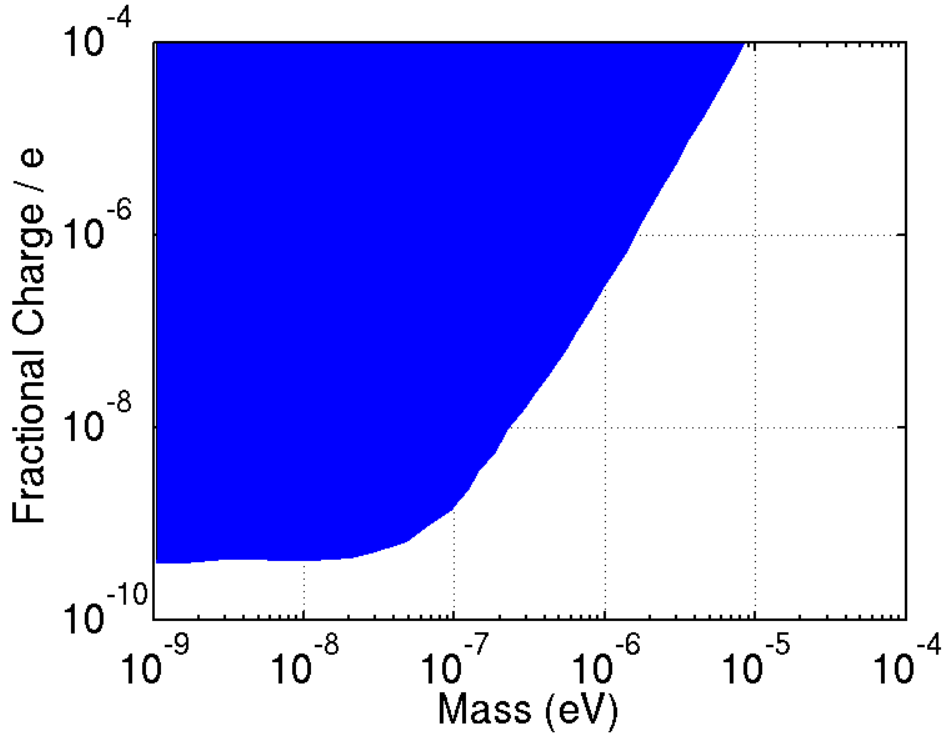

Figure F.12: The blue shaded region corresponds to excluded "mass-charge" parameter space for FCPs by requiring that the decrement in flux of CMB photons is not larger than the observed SZ effect. It is applicable for models with a very weak hidden sector coupling, or no hidden sector (paraphoton) present [152].

slightly more than those from other regions, giving rise to temperature anisotropy in the CMB.

The data from the satellite-borne Wilkinson Microwave Anisotropy Probe (WMAP) [129] that has provided a detailed all-sky map of the anisotropy, as shown in Fig. F.13. Multiple inferences about the evolution and particle content of universe may be tested using the all-sky CMB anisotropy map. Since the same physical laws as SM of particle physics should also apply to the universe, the anisotropy structure in CMB also provides test for the SM. In order to fit a cosmological model to CMB data, the primary-anisotropy map [141] is (typically) decomposed into spherical harmonics,

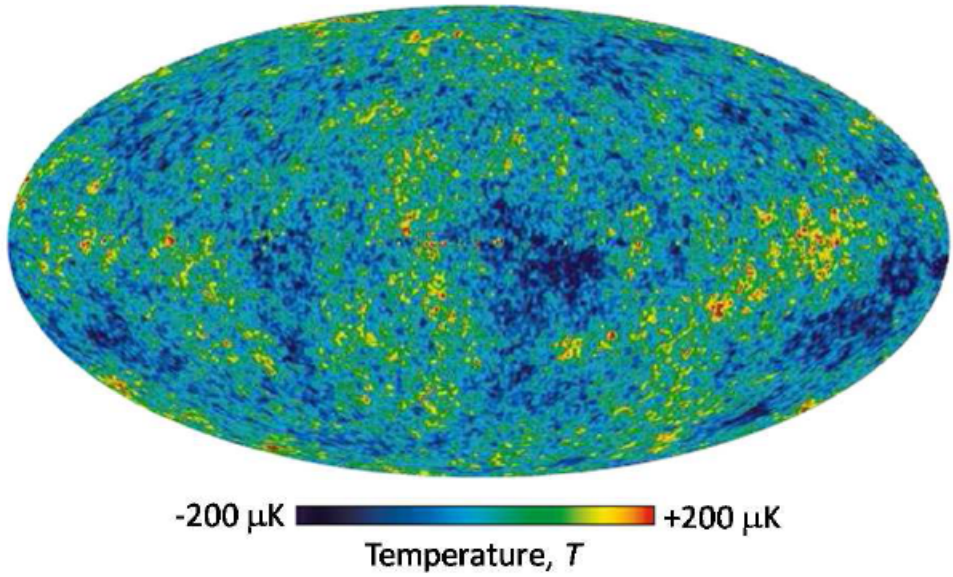

Figure F.13: The Wilkinson Microwave Anisotropy Probe 5-year data all-sky map of the cosmic microwave background primary anisotropy. A Mollweide equal-area projection is used to display the entire sky in galactic coordinates, with temperature differences given in units of thermodynamic temperature. Figure taken from [139].

Y_{lm};

$$T(\hat{n}) = \sum_{l,m} a_{lm} Y_{lm}(\hat{n}) \tag{F.6}$$

where $\hat{n}$ is a unit direction vector and represents the angular position of a map pixel. The angular power spectrum at multipole moment l is given by an average over the moments m;

$$C_l = \frac{1}{2l+1} \sum_{m=-l}^{l} \mid a_{lm} \mid^2 \tag{F.7}$$

The power spectrum is usually plotted as a function of l in terms of the squared temperature anisotropy, and is shown in Fig. F.14

$$(\Delta T_l)^2 = l(l+1)C_l/2\pi \tag{F.8}$$

The error bars in Fig. F.14 show the power spectrum derived from the WMAP 7-year CMB data for multipoles up to $\gtrsim$1000 [130], augmented with higher multipole moments derived from data obtained by the ACBAR [142] and QUaD [143] experiments. The spectrum can be thought of as the amount of power stored in small and large-scale fluctuations in the CMB temperature. Also shown in Fig. F.14 is a best fit cosmological model that produces CMB predictions matching closest with the observation.

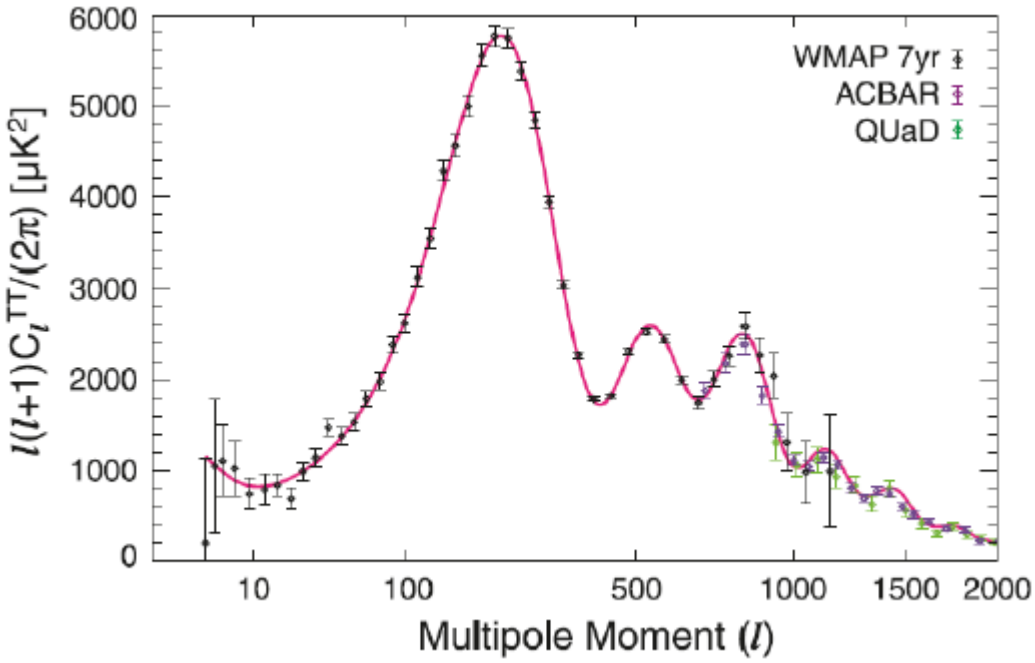

Figure F.14: The angular power spectrum of CMB primary temperature anisotropy as a function of multipole moment. The black error bars up to $l \simeq 1200$ are derived from the WMAP 7-year data [133], while the lighter colored error bars for $l \geq 690$ are derived from data obtained by the ACBAR [142] and QUaD [143] experiments. The solid curve represents the best-fit ΛCDM model to only the WMAP data [130, 136]. Figure taken from [130].

Since there is a part of the parameter space for the FCPs where they do not

decouple from the acoustic oscillations of the baryon-photon plasma at recombination, the effect of these particles on the CMB anisotropy spectrum may be similar to the effect of baryons [157]. To measure the effect of presence of FCPs on CMB anisotropy, cosmological models with particles of electric charge $q \sim 10^{-6}e - 10^{-1}e$ and mass $M \sim 10^{-3}GeV - 10^{2}GeV$ can be studied [154]. It is done by extending the set of kinetic equations [156] for the linear perturbations in the primordial plasma to account for the presence of FCPs. The equations for the baryonic component are extended to account for elastic scattering off FCPs. A similar set of kinetic equations are added for the fractionally charged component. They are also included while measuring contributions to the energy-momentum tensor. The Compton scattering off FCPs is negligible, since the corresponding cross-section is suppressed by the fourth power of the charge q.

A large region of the "mass-charge" parameter space for the FCPs exists where their effect on the CMB spectrum is similar to the effect of baryons. Fig. F.15 shows the CMB spectrum with best fit cosmological model compared to a new model with FCPs. Requiring concordance between predictions from new model with FCPs and observed CMB anisotropy and assuming the standard Big Bang Nucleosynthesis (BBN) value for the baryon abundance, $\Omega_B h_0^2 = 0.0214 \pm 0.0020$ [155], the new model constrains their abundance of FCPs to be $\Omega_{FCP} h_0^2 < 0.007$ [154]. Here, Ω represents the ratio of density of a particular component to critical density of universe.

Using the LeeWeinberg formula, the limit $\Omega_{FCP} h_0^2 < 0.007$ can be converted into the bound on the parameter space for FCPs. The results are different for models with and without a hidden-boson (paraphoton) [154], shown in Fig. F.16 below.

The above limit is especially interesting for the models without paraphoton, where it excludes most part of the window with not very heavy particles and substantial electric charges. To completely close the window, sensitivity to FCP abundance

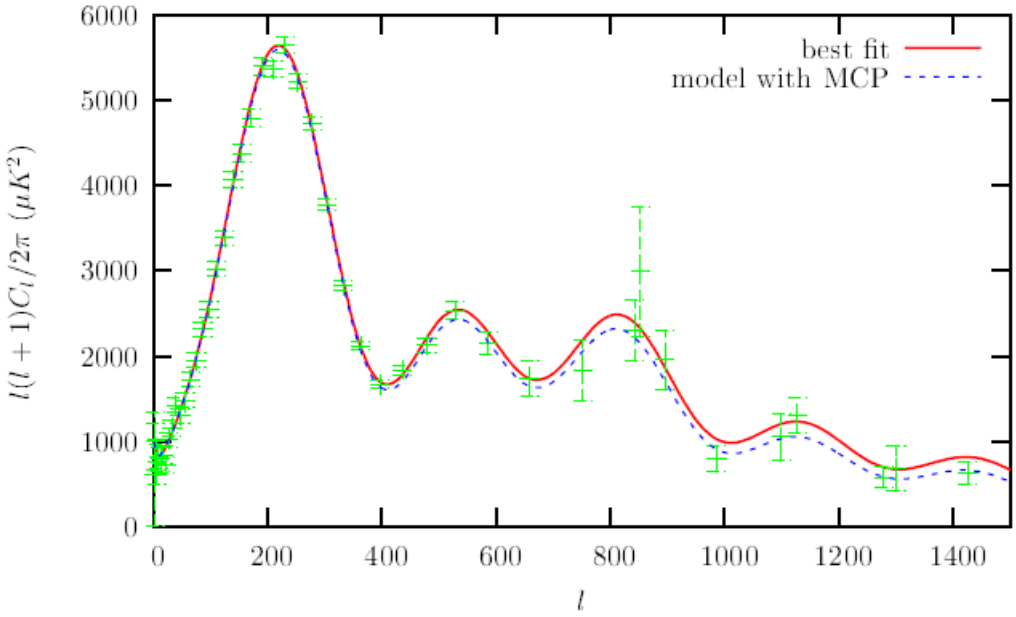

Figure F.15: The two different CMB anisotropy spectra are compared with extended WMAP dataset. Solid line represents the best fit model without FCPs, $\Omega_B h_0^2 = 0.022$. Dashed line corresponds to model with $\Omega_B h_0^2 = 0.014$, $\Omega_B h_0^2 = 0.007$ [154]

at the level of $\Omega_{FCP} h_0^2 \sim 3{\cdot}10^{-4}$ would be required, which cannot be achieved with future CMB experiments due to inaccuracy in determination of the baryon abundance from the BBN [154]. Thus, the rest of this window will need future accelerator and/or laboratory experiments to get explored. Additionally, While the above criteria allows for a model with $\Omega_B h_0^2 = 0.014$, $\Omega_B h_0^2 = 0.007$ to be consistent with WMAP data, the null result from FCP searches in bulk matter sets a much lower limit for this ratio in region of experimental sensitivity (described in Appendix C.2).

F.3.5 Supernovae Dimming

The parameters for FCPs can be constrained by their effect on the luminosity-redshift relation of type 1a supernovae in the standard cosmological model [158]. Analogous to the SZ effect for CMB photon (discussed in above subsection), the

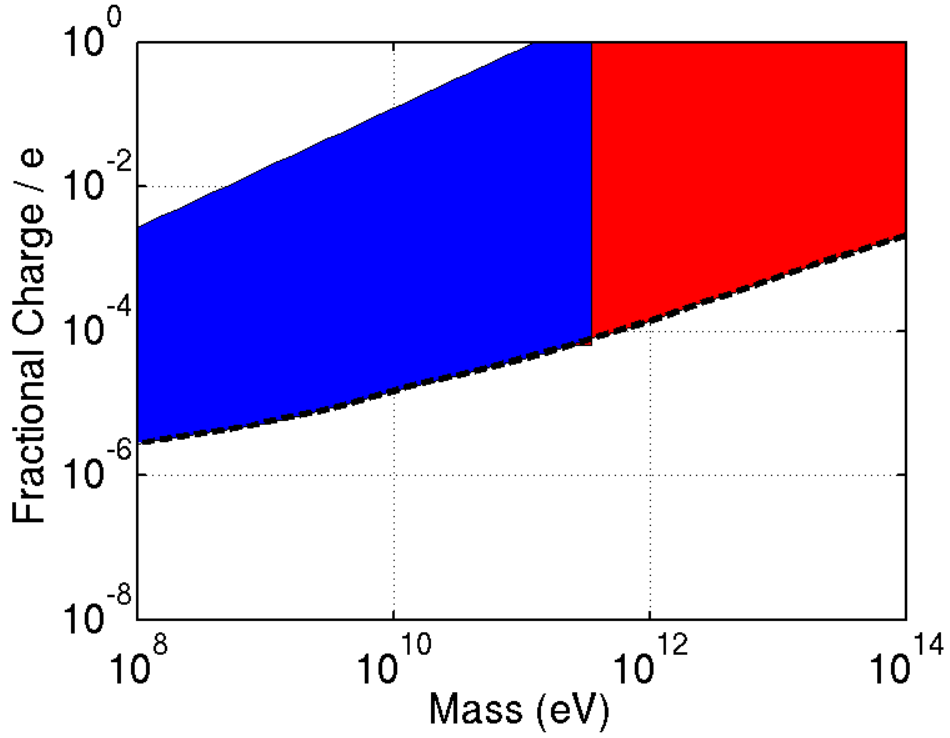

Figure F.16: The region above the black dashed line represents FCPs that are coupled to baryons. Requiring that the presence of FCPs do not contribute to WMAP anisotropies beyond possible errors, the blue shaded region (including the region hidden below red shade) corresponds to the "mass-charge" parameter space excluded in models without a paraphoton. The red shaded region corresponds to the "mass-charge" parameter space excluded in models with a paraphoton [154]

interaction of photons from distant supernovae with intergalactic magnetic field can cause reduction in photon intensity via photon decay into FCPs. This affects to increase the luminosity distance measurements of cosmological standard candles like type Ia supernovae (SNe) [159–161]. The luminosity distance d_L at redshift z is defined as

$$d_L(z) = \sqrt{\frac{L}{4\pi F}} \tag{F.9}$$

where L is the luminosity of the standard candle (assumed to be sufficiently well-known) and F the measured flux. If the flux from a source at redshift z is attenuated

by a factor *P(z)* the observed luminosity distance increases as

$$d_L^{obs}(z) = \frac{d_L(z)}{\sqrt{P(z)}} \tag{F.10}$$

Pair production of MCPs by star light via photon decay in the inter-galactic (IG) electron plasma and magnetic field dominates in the high-frequency ($m_\epsilon \ll \omega$) and strong field limit ($m_\epsilon^2 \ll \epsilon e B_{IG}$), with an average IG magnetic field strength B_{IG} of the order of 1nG [162]) and ω is the energy of photon. It is found that for FCP mass of $m \lesssim 10^{-7} eV$, the pair production rate is independent of mass. To ensure consistency with supernovae dimming, an upper bound of $\epsilon \lesssim 6.4{\cdot}10^{-9} e$ for scalar FCPs with mass $M \lesssim 10^{-7} eV$ is obtained. For fermionic particles, the corresponding limit is $\epsilon \lesssim 3.5{\cdot}10^{-9} e$. For larger masses $M \gtrsim 10^{-7} eV$, the pair-production rate becomes mass-dependent [158]. Constraints from above requirement are shown in Fig. F.17 below. [2.5-fig16] = constraints from SN dimming [Fig3 of V-IMP-lips-review]

F.3.6 511keV Line from Galactic Center

The SPI/INTEGRAL detectors observe sharp γ-ray peak at 511keV from the galactic bulge [180–185]. A most probable reason is attributed to positronium decay [177]. Despite existence of mechanism for astrophysical production of positron in galaxy (like, supernovae, black holes) [186–188], they turn out to be inappropriate to explain the intensity of the positron annihilation flux in the concerned emission region. This is because the intensity from the astrophysical sources like black holes and supernovae are expected to be more spread out than observed.

To explain the anomaly, it is suggested that dark matter is composed (partly, if not whole) of O(MeV) massive FCPs [177] (the idea of heavy FCP as a dark matter (DM) candidate was suggested about 25 years ago [189] and it has been revived recently [190, 191]). If the mass of such a dark matter particle is less than the

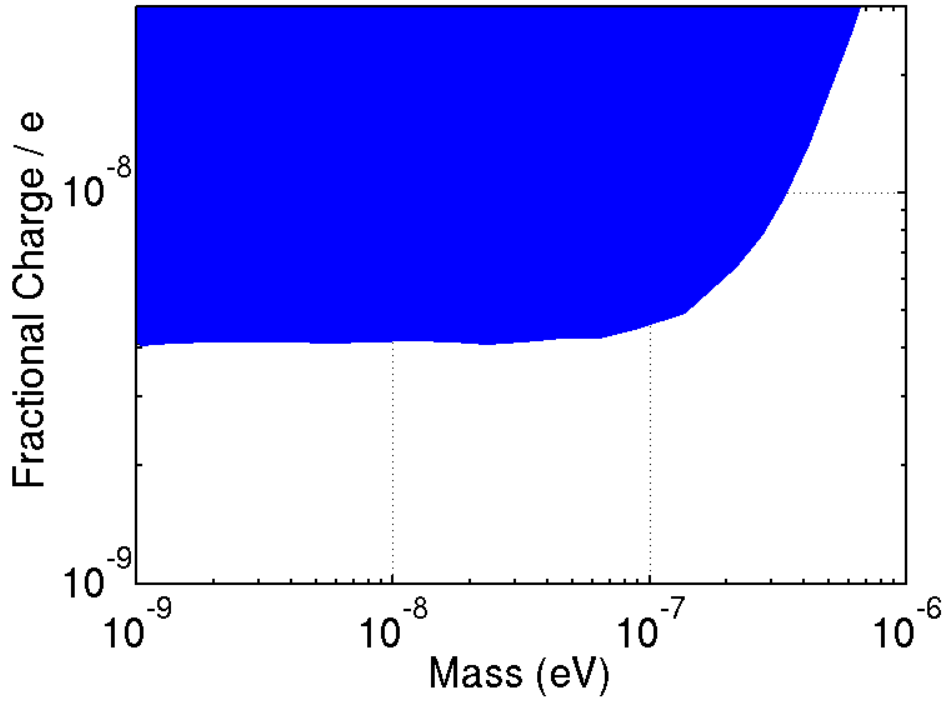

Figure F.17: The blue shaded region corresponds to "mass-charge" parameter space exclusion for pure FCPs from Supernova dimming consideration [15]

muon mass, the low velocity annihilations can produce electron-positron pairs. The mass and charge of FCP can be constrained such the theoretically predicted flux of 511keV gammas (generated from positron annihilation, where in the positrons themselves form due to annihilation of FCPs) is concordant with the observed flux. The result is shown in Fig. F.18 [177].

F.4 Constraints from Astrophysical Considerations

Stellar cores are sites of high temperature containing plasma of photons and electromagnetically charged particles. If FCPs exist, they would be produced in the dense stellar plasma. For FCPs with $M \lesssim 1MeV$ (the cutoff below which $fcp^+fcp^- \rightarrow e^+e^-$ is kinematically forbidden) and $q \lesssim 10^{-3}e$, the rate of annihilation

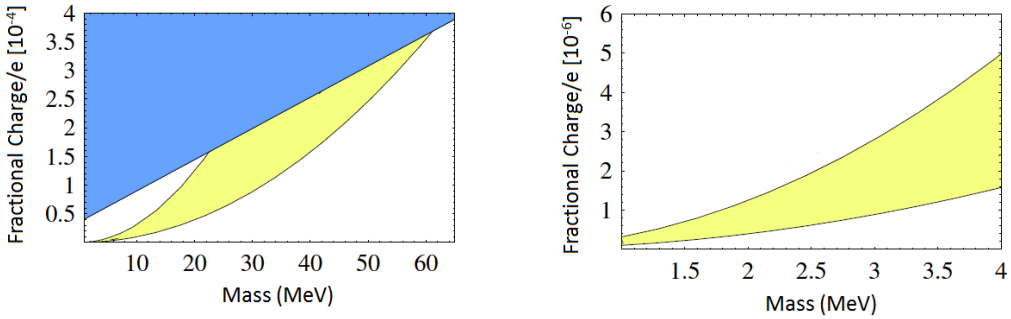

Figure F.18: LEFT: The plausible "mass-charge" parameter space for FCPs shown in yellow shaded region is based on 511keV Galactic emission line, having an observed ray-profile of full width at half maximum of $\sim 6^\circ$ with a $4^\circ - 9^\circ$ 2σ confidence interval [177]. The blue region corresponds to the parameter space excluded by search for FCPs at SLAC [87]. RIGHT: Same curve is expanded for region $m \lesssim 4MeV$ based on recently given strong constraints on the light DM mass [178, 179]. By requiring that $\rho_{fcp}/\rho_{crit} < 1$, this region is ruled out in models without paraphoton, as discussed in Appendix F.3.1

of FCPs within a star has been shown to be negligible compared to their rate of production [163]. Depending on their parameters, the FCPs can either be trapped within the star, or they can escape. For latter case, it creates a new energy loss pathway which substantially alters the evolution of star (sun, red giants, white dwarfs and supernovae) from astronomically observed pathway. Several bounds have been derived on the basis of these effects, shown below in Fig. F.19. Unless otherwise indicated, it is assumed there is no hidden-sector photon into which FCP particle-antiparticle pairs can annihilate.

F.4.1 Energy Loss From Sun

The sun is less sensitive to FCP emission than other stars. Solar bounds have been obtained from studies of its lifetime, helioseismology and the neutrino flux. But even though its properties are better known and the data is more precise the resulting constraints are weaker [15]. By requiring that the power emitted in the form

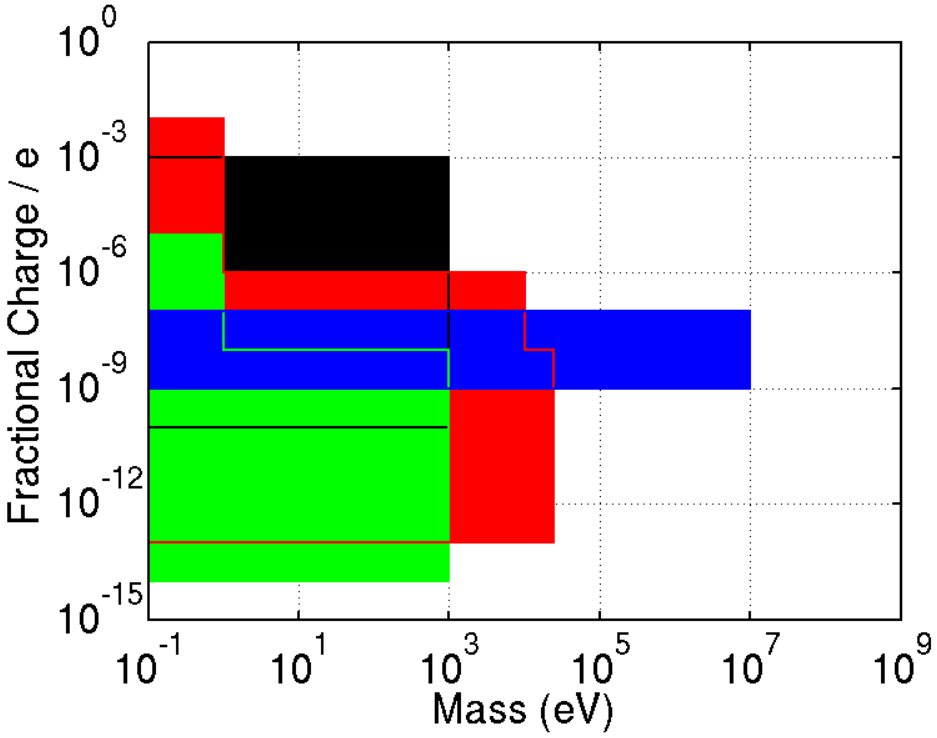

Figure F.19: The blue shaded region corresponds to "mass-charge" parameter space exclusion for pure FCPs from Astrophysical considerations [15–17]. The black shaded region/curve corresponds to constraints from studying energy loss from sun. The green shaded region/curve corresponds to constraints from Red Giants, the red region/curve from White Dwarfs and the blue region/curve from Supernova SN1987A

of escaping FCPs does not exceed the power radiated as photons (assuming the FCPs do not become trapped), an estimate of their production rate of within the sun leads to the exclusion of the charges $l0^{-10}e < q < 10^{-3}e$ for masses $M < 1keV$ [16, 163].

F.4.2 Red Giants and Horizontal Branch Stars

The following discussion on red giants and horizontal branch stars has been referred from [17]. At the end of the main-sequence evolution of normal stars, the hydrogen in the inner part has been consumed, leaving the star with a core consisting mainly of helium. In low-mass stars, this helium core reaches degeneracy before it

is hot and dense enough to be ignited. This process is very dependent on density and temperature of the star. Therefore, the core mass at helium ignition as implied by the color-magnitude diagrams of several globular clusters implies a limit on any new energy-loss channel. After helium ignition, the stars move to the horizontal branch (HB) where they burn helium in their core. A new energy-loss mechanism will lead to an accelerated consumption of nuclear fuel, shortening the helium-burning lifetime which can be "measured" by number counts of HB stars in globular clusters.

To constrain new model modifying the plasmon decay modes, the helium-ignition argument provides far more restrictive limits than the helium-burning lifetime argument because the plasmon decay is more effective in the degenerate red-giant core. On the other hand, axion losses by the Primakoff process are more effective in the nondegenerate cores of HB stars so that the helium-burning lifetime argument yields more restrictive limits. The emission of milli-charged particles is a special case in that both arguments yield comparable limits [166].

For a red giant (where the plasmon mass is $m_\gamma \simeq 2keV$ [73]), FCPs with $M \simeq 1keV$ contribute to the energy loss of the star. Requiring that the energy loss rate does not exceed the nuclear energy production rate excludes values of fractional charge greater than $10^{-14}e$ [16, 73]. The excluded region extends as far as $10^{-8}e$ (for $M = 1keV$) or $10^{-5}e$ (for $M = 1eV$), above which the FCPs become trapped in the star and no longer contribute to the energy loss. However, they contribute to the efficiency of heat conduction within the red giant, and the requirement that their contribution be less than that from convective heat transport extends the exclusion region to $2{\cdot}10^{-3}e$ [16, 164].

F.4.3 White Dwarfs

The observed population of hot, young white dwarfs is consistent with cooling by surface emission of photons and by volume emission of neutrinos produced by plasmon decay via standard model interactions [17, 165, 166]. By requiring that the additional neutrino emission not cool the white dwarfs faster than observed, a bound on the neutrino magnetic moment, $\mu_\nu < 10^{-11}\mu_B$ (where $\mu_B = e/2m_e$) can be set [165]. Similar criteria can be used to generate bounds for FCPs, as the plasmon decay into FCP pairs will contribute to the rate of cooling of white dwarfs. For the present theory of white dwarf cooling to remain consistent with the observed luminosity distribution, particles must be excluded over the range $10^{-13}e < q < 10^{-2}e$ (for $M < 1eV$), $10^{-13}e < q < 10^{-6}e$ (for $1eV < M < 10keV$), and $10^{-13}e < q < 10^{-8}e$ (for $10keV < M < 25keV$) [16, 73, 164].

F.4.4 Supernova SN 1987A

The stellar energy-loss argument can be applied to SN 1987A where the number of neutrinos detected at Earth agree roughly with theoretical expectations [17]. If there are other free streaming particles contributing to the cooling of the proto neutron star, this will reduce the neutrino fluxes and the duration of the neutrino signal. Their production would divert energy from neutrino generation in a supernova. The experimental observation of neutrinos from SN 1987A provides an upper bound to the amount of energy that could have been lost to FCPs, which allows exclusion of charge range $10^{-9}e < q < 10^{-7}e$ for $M < 10MeV$ [111] (The upper limit of $q < 10^{-7}e$ is because particles with larger charges are trapped inside the star and do not contribute to energy loss) [16, 17].

F.4.5 Constraints for Hidden Sector Models

The following discussion on astronomical constraints for hidden sector models has been referred from [16].In a universe with hidden-sector photons (γ') that couple to FCPs with a strength α' close to α, bounds from the energy loss of stars are more stringent than those calculated in the absence of a hidden-sector photon [16]. Within the helium core of a star, hidden-sector photons will be generated through Compton scattering off thermally populated FCPs ($fcp\gamma \rightarrow fcp\gamma'$). If the mass of FCP satisfies $M > 100eV$, the mean free path of γ'(s) in the star's outer region will be greater than that of normal photons, and the star will cool by emitting γ'(s) more readily than ordinary photons [112]. Requiring that the rate of γ' production via Compton scattering in the helium core be smaller than the ratio of normal-photon luminosity to surface temperature leads to the bound $M \lesssim 0.4 + 0.02\ln(q/e)MeV$, from consideration of red giants [112]. A similar argument applied to the sun [112] yielding a less stringent but more reliable bound $M \lesssim 40 + 2\ln(q/e)keV$.

F.4.6 Limitations to Astrophysical Bounds

It should be noted that while the stellar bounds are very strong, they are also vulnerable. They can be considerably relaxed if the couplings to photons effectively depend on environmental conditions such as the temperature and matter density [167, 168]. It can also be relaxed depending on hidden sector models [66, 169–176].

As example, in models containing more than one paraphoton with at least one paraphoton being exactly massless and one light, $keV \gg M_{\gamma'} \neq 0$, the prohibitively strong astrophysical bounds on the fractional charge, $q \lesssim 2{\cdot}10^{-14}e$, for $M \lesssim fewkeV$, arising from energy loss considerations of stars discussed in above subsections can be considerably relaxed [56]. In a simple model analyzed in [67], there are two paraphotons: one massless and one light, and the fermion transforms in the bifun-

damental representation of these two $U(1)$ factors with charge $(0, e, -e)$ under the visible and the two hidden sector $U(1)$ factors, respectively. In vacuum, the fermion acquires an electric charge ϵ due to a kinetic-mixing between the photon and the two paraphotons. However, this electric charge is reduced in the stellar plasma by a multiplicative factor $\frac{m_{\gamma'}^2}{\omega_p^2}$, where $\omega_p \simeq fewkeV$ is the plasma frequency. This charge screening mechanism is caused by a partial cancellation between two paraphotons interacting with the bifundamental fermion [56,67]. Such models are generic in open string models with hidden D-brane sectors, since hidden sector fields arising from open strings stretched between hidden sector branes naturally fall into the bifundamental represention of the two hidden sector $U(1)$'s [56].

APPENDIX G

ADDITIONAL DETAILS ON CDMS IONIZATION SIGNAL

In addition to the details on ionization signal generation and measurement mentioned in Section 3.1, a complete discussion warrants additional details on the transport, readout electronics, noise characteristics, processing and calibration of obtained signal, etc. Since these are important details, but do not directly relate to the results discussed in the dissertation, they are mentioned in this appendix.

G.1 Charge Trapping

Even though the population of free charge is extremely suppressed (e.g., at 20mK, the Boltzmann suppression factor is $\sim e^{5800}$ [232]), there exists an additional mechanism that causes trapping of ehp generated from interaction with the penetrating particle. Trapped signal are not collected at electrodes and provide an incorrect estimate of energy lost by incoming particle inside the substrate. At cryogenic temperatures, it might be expected that since the charge carriers are not freely available, they fill the (otherwise) charged impurity sites. However, at such low temperatures, it is energetically favorable for the electrons from donor impurities inside the semiconductor to fall onto acceptor sites instead of remaining bound to the donor sites. This results in formation of ionized donors and acceptors, forming very shallow energy levels, just above the valence band (or below the conduction band), and acting as efficient traps for the ehp. If left this way, ehp collection in the semiconductor crystal is greatly reduced because they will bind with the charged impurities rather than getting measured [232]. Other mechanisms for bulk trapping are discussed in [234].

An additional trapping is due to "Sidewall trapping". At the bare cylindrical surfaces of the crystal, the periodicity in atomic arrangement in lost and the energy levels become much harder to predict. The irregularity in spatial topology and presence of dangling bonds at the sidewall create a highly irregular band structure in which drifting charges get trapped. The loss in ionization collection due to sidewall trapping can go as low as less than 10% of charges getting collected.

G.2 Detector Neutralization

When charges have collected in either the bulk or external surfaces, the drift field of the crystal is significantly reduced, and also altered in direction. A weakened field promotes more trapping in a runaway process, and the detector becomes unusable. Thus it is necessary to "neutralize" the traps.

One possible method to overcome charge trapping is by applying an extremely large ionization bias so large that drifting charges acquire too much kinetic energy and do not get trapped. However, doing so creates lot of phonons that would swamp the intrinsic phonon signal (The corresponding mechanism is discussed in Section 3.2.1.3). The other method is by neutralizing the ionized impurities.

The detectors are neutralized by exposing the crystal to a Light Emitting Diode (LED) while keeping low temperature and with no external bias applied. Photons from the LED produce ehp. In the absence of an external drift field, these newly created free charges either recombine or get trapped on ionized impurities. An ionized impurity with a trapped charge carrier is no longer able to trap other charges formed when detector is in active operation. To maintain the neutralization, it is necessary to keep the detector well below the activation temperature of the impurity levels, both during and after baking to maintain neutralization; which is easy since the activation temperature is $\sim 140K$ [232].

The detector neutralization, obtained using LEDs, is not stable when the detector is biased (i.e. when an external electric field is applied). Some of the traps are emptied during the particle interactions, degrading the charge collection efficiency with time. The time span over which this degradation becomes important depends on the event rate. For CDMS detectors detecting WIMP at very low event rate, neutralization can hold for around 8 hours for silicon (and longer for germanium substrates) [227]. This allows for an efficient data collection without worrying about the related problem.

G.3 Anisotropic Charge Transport

Another complication associated with operation at cryogenic temperatures relates to anisotropic transport of charges inside the silicon and germanium crystals. Silicon and germanium are indirect bandgap materials, and the location of conduction band minimum is different from the location of valence band maximum in the energy-momentum space. Under application of an electric field, the electrons (holes) move in a direction corresponding to the minimum (maximum) in the conduction (valence) band. At high temperatures, the charges are scattered by the thermal population of phonons and exhibit an average drift along the direction of applied electric field. At cryogenic temperatures, this scattering mechanism is absent and despite the direction of applied electric field, the charges travel along the direction of band minimum/maximum. This causes an anisotropic charge transport [256]. In particular, conduction of electrons occurs in band minima along the $\langle 111 \rangle$ direction in germanium and the $\langle 100 \rangle$ direction in silicon. In the case of holes, the band minima are all in the center of the Brillouin zone with larger mobility along $\langle 100 \rangle$ direction in both cases.

Since the $\langle 111 \rangle$ directions are not mutually orthogonal to each other, it implies

that regardless of direction of applied electric field, in a germanium substrate there will be electrons which will move out from the location of interaction as they drift under external electric field. Using similar arguments and by noting that the $\langle 100 \rangle$ directions are orthogonal to each other, the electrons in a silicon crystal will move along the direction of electric field (and will not spread out) only if the electric field is applied in similar $\langle 100 \rangle$ direction. Lastly, since the valence band has maximum in the center of the Brillouin zone, they will always move along the direction of applied field.

A detailed discussion is provided in [236].

G.4 Concentric Designed and Negatively Biased Electrodes

Due to the anisotropic movement of electron under the external electric field and the conceptual mismatch of such a measurement technique with the primary objective of ZIP detectors (DM detection), it is preferable to measure the holes formed inside the crystal from an interaction with a penetrating particle. The ZIP detectors are primarily employed for the detection of WIMP. However, an active detector would respond to all possible kind of events and not simply the events from WIMP interaction within the substrate. The set of all these "other" events are collectively termed as "Backgrounds".

A possible background in WIMP detection is the presence of electromagnetic gammas and high energy electrons. Having a low penetration distance within the silicon or germanium crystal, these events are quickly absorbed within few millimeters from the curved surface of cylindrical detector. However, a valid WIMP interaction has an uniform probability of occurrence within the cylindrical substrate. Thus, possible background rejection (with small loss in efficiency to detect valid WIMP signal) is obtained by rejecting events occurring within a few millimeters from the

curved surface. It is due to this reason that two concentric ionization electrodes are patterned on one of the face of the cylindrical crystal, shown in Fig. 3.1. An inner electrode covers ∼85% of the detector surface, enclosed by an outer, annular ring of 3mm width (The geometry of inner charge electrode is also designed to ensure that there is no variation in "Ramo field" with depth from the crystal surface. These variations arise by presence of grounded copper surface of housings in which the detectors are placed, mentioned in Appendix I.4). Events occurring close to the curved surface create holes at corresponding location. These holes are collected by outer annular electrode. As mentioned above, these events are rejected in a WIMP analysis. To measure holes, the charge electrodes are negatively biased.

Instead of measuring holes, if the electrons are measured, then the anisotropic charge transport may cause a larger signal in inner electrode even if an event occurs near the curved surface. Similarly, a large signal in outer electrode may occur even if there the event occurred in the inner bulk of the crystal.

G.5 Ionization Signal Readout

As mentioned in the above section, the CDMS-II ZIP-detector measures ionization using two concentric electrodes fabricated on one of the flat side of the cylindrical substrate. The ionization measurement is done by applying a bias voltage of -3V (-4V) on electrodes fabricated on one face on cylindrical shaped germanium (silicon) crystal, while keeping the other face grounded. The section below details the circuitry associated with measurement of these charges, shown in Fig. G.1. These measurements are done independently for the inner and outer charge signals. The following discussions are referred from [231, 232, 239, 242].

The ZIP ionization electrodes are biased through a large bias resistance (R_b) of 40K-Ohm. The high bias resistance prevents dissipation of charge signal over the

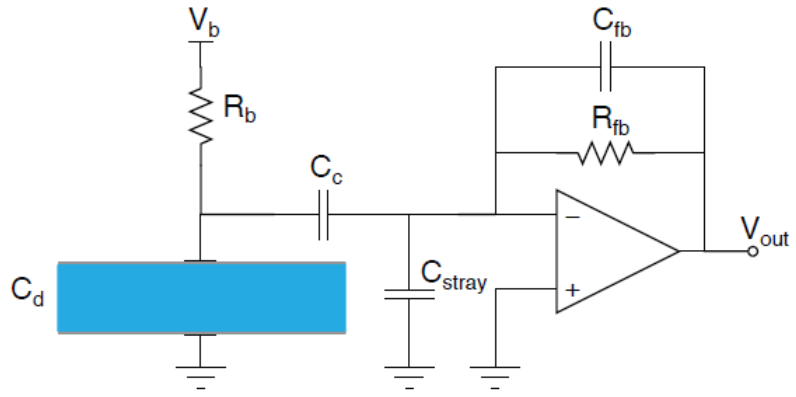

Figure G.1: Schematic of charge readout circuit. The detector (blue) has capacitance $C_d = 93pF$ for the inner electrode (36pF for the outer). The phonon face is held at ground, while the charge faced is biased through $R_b = 40M\Omega$, typically at $V_b = -3V$ for germanium. This DC bias is decoupled from the amplifier through $C_c = 300pF$. Charge collected across the detector is measured by the image charges transferred to the feedback capacitor $C_{fb} = 1pF$, which then drains through the feedback resistor, $R_{fb} = 40M\Omega$, with characteristic time of $40\mu s$. The stray capacitance to ground, $CC_s \equiv 75pF$ is comparable to the detector capacitance, but still small relative to C_c, causes a small loss in charge signal. Figure taken from [239].

time scale of the pulse. To ensure that the electrodes are well coupled to the readout for fast pulses, they are capacitively coupled to a Field Effect Transistor (FET) amplifier. Each electrode is connected to a coupling capacitor $C_c = 300pF$, which passes the fast charge pulse, but keeps the bias and the amplifier decoupled.

As the charges (from interaction of particle with the crystal) drift across the crystal under the effect of applied electric field, image charges are induced on the metalized charge electrodes. According to Ramo's theorem, the charge induced is equal to the charge drifted. Charge collected across the detector crystal quickly transfers to the feedback capacitor C_{fb} (through the action of a charge amplifier) producing a voltage measurement. This is the measured ionization pulse. However, in reality, a fraction of the charge signal is lost in the capacitive coupling causing the

charge induced at the feedback capacitor is less than the induced image charge. The stray (parasitic) capacitance C_s incorporates several different components including relative capacitance of inner and outer electrodes, capacitance to neighboring detectors and the detector housing [242]. Since the charge carrier drift velocities at 50mK are 20-40 mm/μs [245] and the amplifier response time is sufficiently fast, the rise time of the pulse is essentially instantaneous relative to the 0.8μs sampling time of the Analog to Digital Converter (ADC). The relatively quick response of the ZIP ionization measurement makes the ionization-pulse start time the most accurate indicator of when a scattering event occurred.

The ionization pulse decays as the feedback capacitor drains through the feedback resistor R_{fb}, producing an exponential falling edge of the voltage pulse. The fall-time $\tau_f = 40\mu s$ of the pulse is determined by the $R_{fb} = 40M - Ohm$ and $C_{fb} = 1pF$. The feedback capacitor, set in parallel with the feedback resistor, acts as a high-pass filter with time constant $\sim 40\mu s$ and slowly dissipates the charge. The ionization pulses therefore have a very fast risetime set by the amplifier response, and a fall time set by the feedback resistance and the feedback capacitance (of $\sim 40\mu s$).

The transimpedance (complex impedance) of this system is given by [229]

$$A(\omega) = \frac{R_{fb}}{1 + j\omega R_{fb} C_{fb}} \tag{G.1}$$

where $\omega = 2\pi f$ is the frequency of the fourier analogous of the time dependent input signal.

G.6 Ionization Signal Noise Characteristics

Although the CDMS read out set up is a low-noise transimpedance, the FET amplifier contributes a to substantial amount of noise in the overall charge signals. The dominant theoretical contributions to the voltage noise in this system comes

primarily from the amplifier's first-stage Junction Field Effect Transistor (JFET), measured to be typically $0.5nV/sqrtHz$ [227] referenced to the input, and from the feedback and bias resistors. Since the FETs are rendered nonoperational at temperatures below ∼100K, they must be thermally isolated from the rest of the readout circuit and the detector. Rather than sitting at 20mK stage of the cryostat (which maintains the detectors at ∼50mK), the FETs are coupled to the 4K stage of the cryostat, where they are allowed to self heat to their optimal operating temperature of ∼130K (the physical location of FETs in the experimental setup is described in Appendix I.4).

Other sources of noise include the current noise from the JFET, fluctuation in detector leakage current due to shot noise (i.e., Poisson fluctuations in the number of thermal ehp contributing to the current)and microphonic effects from the wiring. These nonfundamental noise sources (in particular microphonic pickup) can vary significantly by detector, leading to nearly a factor of 2 variation in the reconstructed charge resolution for each detector from 0.25-0.50keV [239]. In practice, there is also a very large contribution from pickup of ambient noise, which has been reduced by the use of an radio-frequency shielded experimental enclosure and a careful grounding scheme. Fig. G.2 shows the charge noise noise for one of the germanium detectors.

Given the charge collection and observed signal sizes, this leads to a baseline resolution of σ ∼0.4-0.7keV for germanium detectors, and a much higher resolution of σ ∼1keV for silicon detectors.

G.7 Charge Signal Processing Pipeline

The analysis pipeline takes the raw traces recorded by the DAQ (discussed in Appendix I.6)for each event and produces reconstructed quantities describing the pulse characteristics (like, estimating the energy deposited as ionization). For the

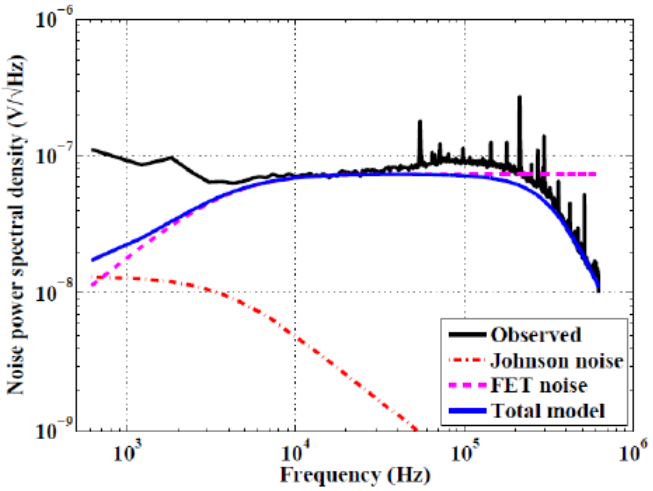

Figure G.2: Measured ionization noise spectrum in the inner charge electrode (for one of the germanium detectors) overlaid with model predictions. The noise spectrum is rolled off at high frequencies by a low pass filter. The total contribution from the Jonhson and FET noise well match the shape of the measured charge noise at high frequency. Figure taken from [231].

data being analyzed in this dissertation, it is processed using the processing package "BatRoot", implemented using C++/ROOT.

G.7.1 Optimal Filter Reconstruction of Charge Amplitudes

The amplitudes of the charge pulses for the inner and outer channels are reconstructed simultaneously using a 2-component template for each pulse [228, 232]. This procedure takes into account the cross-talk between the inner and outer charge channels and produces an amplitude estimate that maximizes the signal-to-noise given the fixed pulse shape set by the charge readout circuit (a charge pulse template) and the measured charge noise for each data series. In performing the fit, a search within the time window of [-100,+10]μs of the event trigger for germanium, and [-50,+10]μs for silicon is performed. The start time that maximizes the summed reconstructed inner and outer amplitudes is used. The time-window used for reconstruction is in-

fluenced by the fact that event trigger is generated using phonon pulses (discussed in Appendix I.5), and since phonon pulses are slower than charge pulses, it is more natural to expect charge pulses to be present earlier than the trigger time. Second, the phonon speed in silicon is almost double of speed in germanium ($\sim$5mm/μs in germanium and $\sim$8mm/μs in silicon [231]). So, it is natural to expect that the time-difference between the charge pulse and event trigger will be smaller for silicon detector.

G.7.2 Time Domain Fit to Charge Amplitudes

A second, time domain fit to the charge pulse is performed for highly saturating events, excluding samples which saturate the ADC. This reconstruction is primarily used to identify high-energy α interactions in order to constrain contamination of the detectors and surrounding materials.

G.8 Preliminary Charge Energy and Position Calibration

Following initial pulse reconstruction by BatRoot, the charge energies are calibrated in physical units using calibration lines of known energy from an in situ ^{133}Ba source, also normalizing out any position dependence in ionization signal. An example of calibration procedure for one of the germanium detectors is shown in Fig. G.3. It shows the uncalibrated charge energies for data from the ^{133}Ba source, as a function of Y -position in the detector (The y-position is reconstructed from the phonon delay, ydel, described in Section 3.2.3). Variations of $\sim$5-10% with position are observed in the reconstructed energy of the 356keV ^{133}Ba γ-line. The position of this line as a function of (xdel,ydel) is fit to a polynomial form and defines the position dependence in charge calibration. After normalizing out this difference, The overall amplitude of the charge signal is scaled to physical units, i.e., 356keV using the ^{133}Ba spectral feature. Similar calibration is done using the 384 keV γ-line.

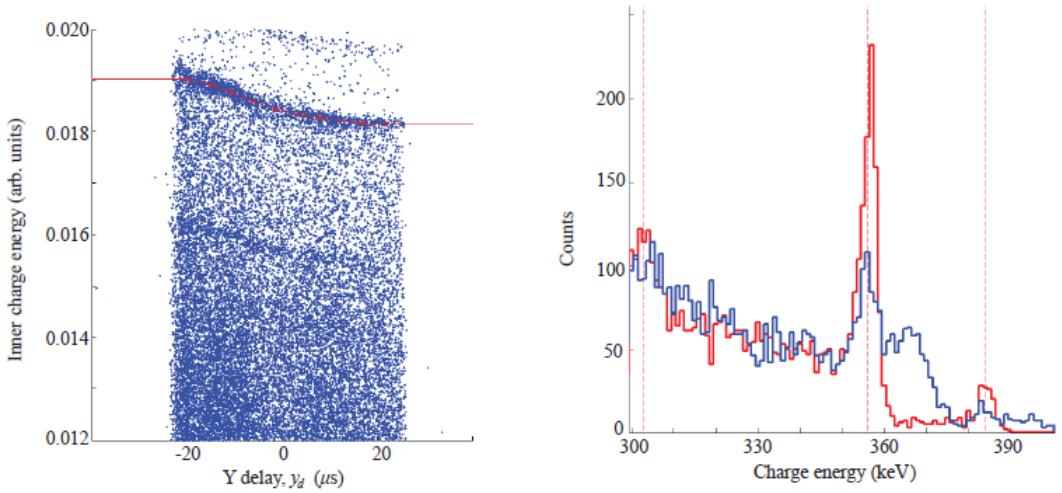

Figure G.3: Position-based calibration of charge energy. The 356keV ^{133}Ba line appears as a concentration of events above which only the weaker 384keV line is seen. LEFT: These events are selected, following which their position dependence is obtained (red line). RIGHT: Observed charge energy spectrum before (blue) and after (red) applying the position-dependent charge calibration and preliminary absolute calibration. The dashed lines show the location of the expected emissions from the source. After correction, a clear 356keV peak is observed. Figure taken from [239].

For Silicon ZIP detectors, the probability of containment of 356keV line from ^{133}Ba inside the small detector mass is minimal. The inner electrode is then calibrated using 356keV events shared with neighboring germanium detectors which are already calibrated. In the absence of a charge line, the calibrations of the inner and outer electrode are assumed to be equal and no charge position correction is performed [228]. However, a direct calibration of the nuclear-recoil energy scale in silicon is also possible using a strong resonance in the ^{28}Si neutron scattering cross-section, which appears as a corresponding feature in the ^{252}Cf calibration spectrum just above 20keV [136, 247].

At energies $\lesssim$10keV, the X and Y delays cannot be reliably determined (discussed in Appendix G.7) and the charge position correction is not effective. However, at

these energies read out noise begins to dominate over the $\lesssim$10% systematic position variations, so application of the charge position correction would not improve the reconstructed resolution even with improved position estimators at low energy. A position independent energy calibration for the germanium detectors at low energy can be done using the 1.3keV and 10.4keV lines present after the neutron activation of the detectors by ^{252}Cf calibrations (^{71}Ge is produced by thermal neutron capture during neutron calibrations and decays by electron capture to ^{71}Ga with a half-life of $\sim$11 days. Most of the time, this decay proceeds via capture of a K-shell electron, followed by emission of 10.36keV of energy in x-rays and Auger electrons. A smaller fraction of the time, $\sim$10%, the decay proceeds via an L-shell capture, giving 1.29keV in energy).

APPENDIX H

ADDITIONAL DETAILS ON CDMS PHONON SIGNAL

In addition to the details on phonon signal generation and measurement mentioned in Section 3.1, a complete discussion warrants additional details on the transport, readout electronics, noise characteristics, processing and calibration of obtained signal, etc. Since these are important details, but do not directly relate to the results discussed in the dissertation, they are mentioned in this appendix. An additional interesting study relates to usage of phonon timing to discriminate valid WIMP signals against possible backgrounds. Since it does not relate to the entire dissertation topic, it is not discussed, even in this appendix. Interested readers may refer to various other dissertation from CDMS collaboration relating to WIMP search efforts [228–231].

H.1 Phonon Propagation

As a recoiling electron or nucleus relaxes, it deposits energy in phonon system causing emission of the "primary phonons" as high-energy optical phonons at the Debye frequency ($\sim$10 THz). In addition to primary phonons, ehp are formed from particle interaction. As the ehp drift under external electric field, an additional population of Neganov-Luke phonons are created during the 0.1μs it takes to for the carriers to drift across the crystal. These phonons are emitted with frequencies well below the Debye frequency (0.1-0.6THz) [248].

The four main processes contributing to the phonon scattering as it propagates in the crystal include phonon-carrier scattering, phonon-phonon scattering, phonon-impurity scattering and anharmonic phonon decay [262, 263]. Phonon-carrier and

phonon-phonon scattering are essentially negligible at mK and sub-mK temperatures, since there are no free carriers or phonons outside of the location of particle interaction in the crystal. The athermal phonons however are subject to two types of scattering, both of which become stronger with increasing phonon frequency: isotopic scattering and anharmonic decay [264]. The isotopic scattering is a elastic, isotropic Rayleigh scattering of phonons on the isotopic impurities with a larger scattering rate for larger frequencies (ν^4 frequency dependence). The anharmonic decay occurs when a higher-energy phonon splits into two lower-energy phonons. The decay rate has a frequency dependence of ν^5 for longitudinal acoustic phonon modes. The rates for longitudinal acoustic phonons at low temperatures (3K) and 1THz are 1.23105s^1 in silicon and 1.62106s^1 in germanium [265, 266]. The rates for transverse phonons are very anisotropic, and can approach the rates for longitudinal phonons only in certain directions.

Since the two processes described above are strongly frequency-dependent, the mean free path of high-frequency phonons is very small (order of mm, for THz primary phonon frequency). The anharmonic decay quickly reduces the high frequency phonons to $\sim$1.6THz, at which isotope scattering begins to dominate. After a few μs of quasi-diffusive propagation, these phonons decay sufficiently that their mean free path is on order of the crystal dimension ($\nu \lesssim$1THz). At this point, the phonons are ballistic and propagate within detector without additional scattering [229].

In addition to primary and Luke phonons, recombination phonons are also generated. They are formed at energies of a few tenths of an electron volt (1eV=241.799THz), but down-convert rapidly through interaction with the metal films (aluminum) at the detector surface [228, 242].

H.2 QET Bias Circuit

For a successful measurement of QETs, it is necessary to operate it under a negative ETF loop. It can be applied by operating the TES in a voltage-biased configuration. The voltage bias is maintained by connecting a shunt resistor ($R_{sh} = 25m\Omega \ll R_{TES} \sim 0.2\Omega$) in parallel with the TES, as shown in Fig/ H.1. The current source is actually a voltage source in series with a 1kΩ bias resistor kept at room temperature [231]. Since the bias resistor is much larger than other resistance involved, it acts as a current source of $\left(\frac{V_{bias}}{7k\Omega}\right)$In this configuration, the bias voltage is tuned so that the Joule heating ($P = I_{TES}V_b$) due to the bias current self-heats the electron system in the TES to the desired operating point along its transition. Typically, the TES array is biased only partway up the transition, with $R_{TES} \equiv 100 - 200m\Omega$.

In biasing the TES, they are first allowed to cool down to superconducting state, without any external current flowing through them. A large bias voltage is initially applied to make them transition from superconducting to normal state. The bias is then reduces to bring the TES on its transition edge.

H.3 SQUID Readout Circuit

The current through the voltage biased QETs changes as they interact with phonons. The change in current through the TES is read out with a single-stage SQUID array, as shown in above Fig. H.1. A more complete description of the dc-SQUID used by CDMS are described in [267, 268].

The TES is connected in series with an input coil of inductance L_i, which converts the change in I_{TES} into a change in flux through the SQUID array. Although the SQUID array provides an extremely sensitive magnetometer, its response is highly nonlinear and the array must be operated in closed-loop mode to increase its dynamic

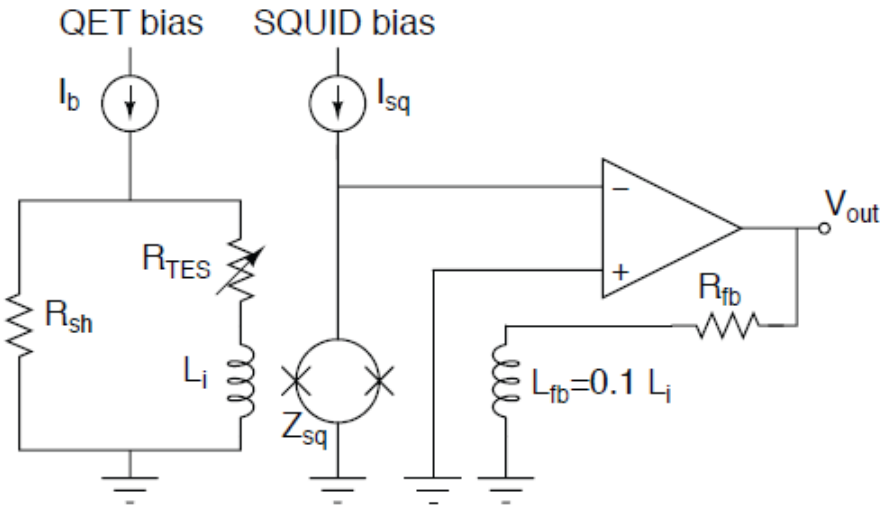

Figure H.1: Schematic of phonon readout circuit. The TES, typically operated at $R_{TES} \sim 100 - 200m\Omega$, is wired in series with the input coil, $L_i = 250nH$ and voltage biased by connecting a shunt resistor, $R_{sh} = 25m\Omega$. At output end, the amplifier adjusts the current through the feedback coil, $L_{fb} = L_i/10$, to cancel the flux change through the SQUID array (represented here as a single SQUID, Z_{sq}) from the input coil, giving a factor of 10 gain in the feedback current. This is measured as voltage across $R_{fb} = 1.2k\Omega$. Figure taken from [239].

range. In this mode, a negative feedback signal is applied through the feedback coil of inductance L_{fb} to cancel the change in flux through the SQUID. However, the feedback coil contains only 1/10th as many turns as the input coil, leading to a factor of 10 gain in the output current of the amplifier, leading to an output voltage across feedback resistance ($R_{feedback} \sim 1k\Omega$) of $V_{out} = 10 \cdot I_{TES} \cdot R_{feedback}$.

The phonon DC offsets, The difference between the raw phonon trace's baseline and zero is are a measure of the SQUID and TES stability. If the offset is greater than ~0.2V, it indicates that the SQUID has likely lost its stable lock point, compromising the SQUID noise performanc [231]. If at any point during the data set a detector channels DC offset is greater than 0.2V, the data set is paused and all of the SQUIDs are relocked to restore stable SQUID operation.

H.4 Phonon Signal Noise Characteristics

The phonon readout noise is determined by the Johnson noise of the shunt resistor, the noise current in the SQUID array, and the intrinsic noise of the TES, which is due to both fluctuations in the charge carriers (Johnson noise) and thermal fluctuations in the conductance between the electron system in the TES and the substrate. Detailed discussion of these theoretical noise sources for the CDMS TESs can be found in [227, 242, 249].

In practice, since the shunt resistor is heat sunk to the 600mK stage rather than base temperature, Johnson noise from R_{sh} dominates, giving white noise at $\equiv 15pA/\sqrt{Hz}$, rolled off at high frequencies with a 50-100kHz time constant (guided by the self-inductance of the input coil, L_i), and the effective input resistance at the input end, $\equiv R_{TES}$). Resonances in the SQUID arrays [231, 269] typically push the roll-off to higher frequencies, ∼200-300kHz. The superconducting transition width of the TES also contributes to the noise [270], which increases the noise bandwidth and forms a major part of total noise at high frequencies. Fig. H.2 shows the predicted and observed noise in phonon channels. Given the phonon collection and observed signal sizes, this leads to a baseline resolution of σ ∼0.1-0.2keV for silicon detectors and σ ∼0.4-0.7keV for germanium detectors.

H.5 Phonon Signal Processing Pipeline

The analysis pipeline takes the raw traces recorded by the DAQ (discussed in Appendix I.6)for each event and produces reconstructed quantities describing the pulse characteristics (like, estimating the energy deposited as phonon, phonon start-time, etc.). For the data being analyzed in this dissertation, it is processed using the processing package "BatRoot", implemented using C++/ROOT.

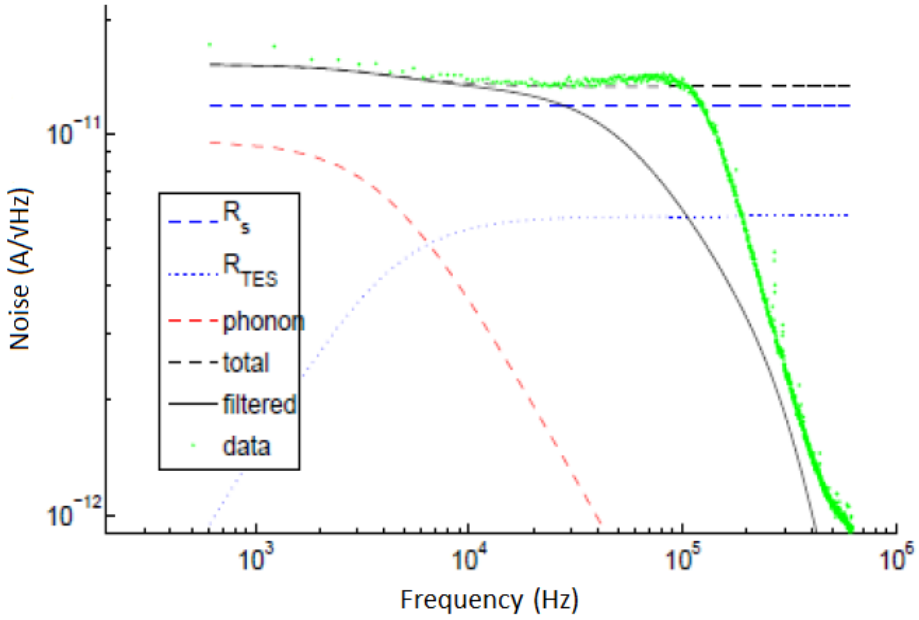

Figure H.2: The predicted and observed noise in a ZIP detector phonon channel. The major contribution the phonon noise is from shunt resistance. The discrepancy at around 100 kHz is from SQUID resonances which extends the noise bandwidth beyond the L/R cutoff. Figure taken from [231]. R_s and R_TES is the noise from the shunt resistor and the phonon channel respectively. "Phonon" represents the noise due to thermal fluctuations in the conductance between the electron system in the TES and the substrate.

H.5.1 Optimal Filter Reconstruction of Phonon Amplitudes

Phonon amplitudes are reconstructed using a single template optimal filter algorithm. Details on "optimal-filter" and the template fitting procedure may be referred from [231, 232]. This procedure produces an amplitude estimate that maximizes the signal-to-noise given the fixed pulse shape set (a phonon pulse template) and the measured phonon noise for each data series. The start time that provides the best fitting is used. However, unlike charge pulses, the observed pulse shape also include additional position dependencies arising from variation in the properties of the QETs (both spatially, and variation with energy deposited in detector). This leads to a 10-

20% systematic variations in the reconstructed pulse amplitude with position, and needs to be corrected [230].

H.5.2 Nonparametric Reconstruction of Phonon Pulse Shape

Unlike the determination of charge start from the charge optimal filter (discussed in Appendix G.7), the phonon pulse start time is determined with a time-domain algorithm. As mentioned above, there are position and energy dependent variations in the phonon pulse shape relative to the optimal filter template. Thus, a start-time estimate based on optimal filter reconstruction would have similar variations.

The details on "Walk" algorithm are referenced from [236]. The "Walk" algorithm is used to determine the start-time corresponding to the phonon pulse. Before applying the algorithm, the phonon pulse is smoothed using a variable low-pass Butterworth filter. Then, starting from the peak of the pulse, an algorithm walks towards earlier times, and records the first time at which the pulse height goes below a certain percentage of the amplitude. The timings mentioned in Eq. (3.11) are obtained when the pulse height is 20% of its amplitude.

The Walking algorithm assumes two conditions, that the amplitude of the noise is much smaller than the amplitude of the pulse, and the slope of the rising edge is relatively steep. If either of these two conditions fails, then the rising edge will be non-monotonic due to noise fluctuations adding to the original pulse shape. A Walk algorithm searching for, say, 20% timing information, will report a value corresponding to the first instance of a 20% point which may fluctuate due to presence of noise. An example of the pathology is shown in Fig. H.3, which is more dominant at low energies. To offset the problem, a pulse-specific variable, low pass filter is used that allows smoothening of the noisy, raw phonon pulse depending on its signal-to-noise content. The rising edge of the filtered phonon pulse is monotonic for all energy

scales, and a better estimate of 20% timing, used in Eq. (3.11), is obtained. Also shown in Fig. H.3 is the result from fitting done on similar pulse smoothed using a variable low pass filter. An original discussion on "Walk" algorithm can be found in [236].

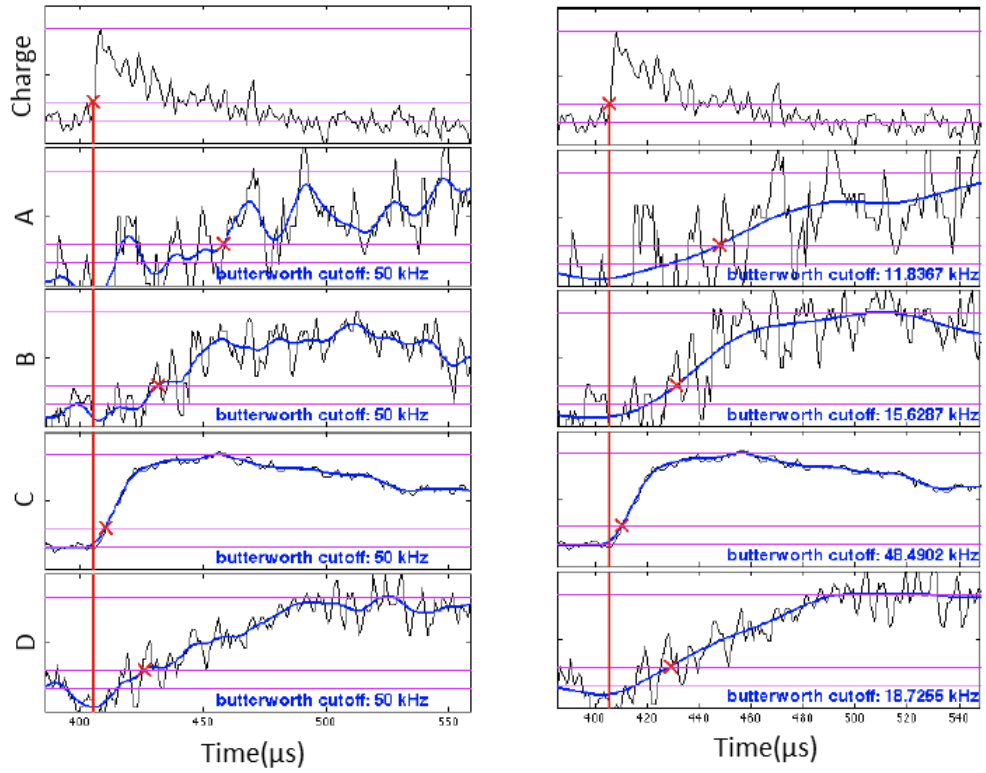

Figure H.3: The same event processed using constant cutoff Butterworth filter (LEFT), and pulse-specific filter (RIGHT), before finding the 20% times. The high-frequency noise is greatly suppressed for the latter case. The 'signal-to-noise' quantity is simply the ratio between the pulse amplitude and the noise rms (as measured by the first 500 bins of the corresponding trace), which is then mapped into a Butterworth cutoff frequency using an empirically-defined mapping function. Figure taken from [236].

Although the usage of a variable, low pass filter is able to reduce the fluctuations

in estimation of phonon start-time, it is still apparent that low energy signal suffer from larger variation in phonon timings, than high energy phonon pulses. Thus, the delay based position estimates get increasingly uncertain for low energy events. However, phonon amplitude based position estimation suffers from less variation at low energy. This is because the noise induced fluctuations in estimation of phonon energy also reduces with energy, as shown explicitly by Eq. (4.20) in Section 4.2.4.

H.5.3 Time Domain Fit to Phonon Pulses

This description is provided for completeness. The quantities from Time Domain Fit is not used in the analysis described in this dissertation.

BatRoot also provides a reconstruction of the pulse amplitude and start time determined from a time-domain fit to each phonon pulse. This procedure accounts for the phonon pulse shape variation with position and provides significantly less position variation in the reconstructed pulse amplitudes than the optimal filter fit, prior to position-dependent calibration. It also provides improved signal-to-noise in the reconstructed pulse timing at the cost of potential systematic errors arising from misparameterization of the pulse shape.

H.6 Preliminary Phonon Energy and Position Calibration

The preliminary phonon energy calibration consists of two stages. First, a relative calibration between the 4 phonon sensors is performed using ^{133}Ba calibration data. For the relative calibration, the distributions of the phonon partition in each sensor are aligned to ensure that on average all sensors contribute equally to the summed phonon energy, as shown by left figure in Fig. H.4. Such a procedure ensures that the box-plots (described in Section 3.2.3) does not look crooked/misaligned. The summed energy is then scaled using the precalibrated ionization energy (calibration of ionization energy is discussed in Appendix G.8) to ensure that the mean ionization

yield is equal to unity for electromagnetic recoil type events for evens depositing large energy ($\gtrsim$10keV), as shown by the right figure in Fig. H.4.

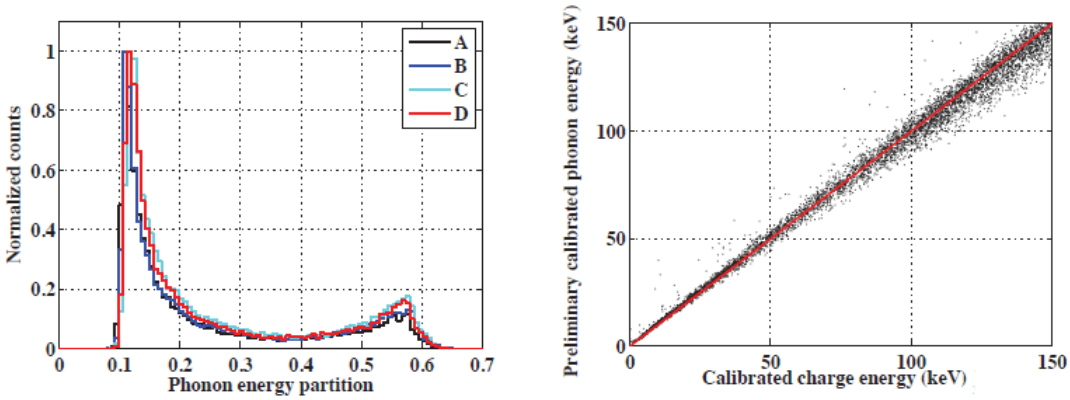

Figure H.4: Phonon calibration for one of the germanium detector. LEFT: Relative calibration done by requiring that on average all sensors contribute equally to the summed phonon energy. RIGHT: Preliminary absolute phonon calibration is performed by requiring the phonon energy to match the precalibrated charge energy for electromagnetic recoils type events (with yield of unity). Figure taken from [239].

H.7 Position Correction of Phonon Quantities

After this preliminary calibration, significant variations (∼10-20%) in the reconstructed energy with position and energy remains (as described in Appendix H.5.1). These additional position dependencies arise due to spatial variation in the properties of the QETs. The variations get induced during the fabrication of phonon sensors over the germanium or silicon crystal, discussed in Section 5.1.2 and Section 5.1.3. The process of normalizing out the variations in phonon traces arising due to variation in QET properties is called "Position Correction". While it is required to normalize out the lateral variations (caused due to QETs), the correction procedure should not normalize out the variation in phonon properties due to occurrence of

event at different depth (from the crystal surface) inside the detector (z-dependent variation in phonon quantities helps in WIMP analysis background rejection). In addition to position dependence, there are also variations in pulse shape with energy. The main causes for this energy dependency in ZIP detectors is the loss of detection sensitivity of phonon sensors to large energy signals, discussed in Section 3.2.2.2. A detailed discussion on position correction algorithm is described in [230]. This subsection provides a brief description of the correction procedure.

The basic idea behind implementing position correction is to compare the phonon parameter values for each event against a look-up table which describes the variation of mean values of these parameters with the location and energy of the event. By factoring out the trends expressed in the look-up table, one normalizes out from phonon measurements the extraneous trends due to variation in QET behavior. The look-up table is empirically created using the calibration dataset. A separate table is defined for each ZIP detector and for each of the four phonon sensors. Once created, the table (and correction) is applied to other dataset which is used for WIMP, or LIPs search. The look-up table is created by ganging together a bunch of events of similar energy which would have occurred at similar physical location inside the detector, obtaining the average value associated with different phonon quantities for these events and studying the variation of the average quantity for set of events occurring at different location inside the detector. The quantitative definition of the variable emulating the location of event occurrence inside the detector and of the criteria "events occurring at similar location in the detector" is empirically constructed to obtain a good correction performance. An optimization is also performed to decide on the number of events (of similar energy, and occurring at similar location inside the detector) which should be ganged up to get the average value associated with different phonon quantities.

For an event requiring correction, its phonon quantities are appropriately scaled by the correction factor (C),

$$C = \frac{Mean_{All}}{Mean_{NN}} \tag{H.1}$$

where $Mean_{All}$ is the mean of a phonon quantity over all events used to generate a look-up table, and $Mean_{NN}$ is the mean of same phonon quantity at the emulated location where the event (requiring correction) has occurred, as obtained from the look-up table.

However, for energies $\lesssim$10keV, the delay-based position estimators have poor signal to noise (as shown in Appendix H.5.2), and the position-based correction no longer improves the resolution.

APPENDIX I

DETECTOR INSTALLATION AT THE SOUDAN UNDERGROUND LAB

Since the primary objective of CDMS-II experiment is to search for WIMPs, the experiment is designed, and installations performed around the objective of reducing background to the corresponding search. A primary background to WIMP search effort is the neutron background. This is because the neutrons produce nuclear recoils that cannot be distinguished from WIMP-induced nuclear recoils. Thus, a sensitive WIMP search experiment requires shielding to prevent neutrons from reaching the detectors. A detailed description of detector installation at SUL can be found in [227, 231, 239]. The details provided below are referred from the same.

I.1 Soudan Underground Lab (SUL)

Neutrons can be of radiogenic or cosmogenic origin. Radiogenic neutrons result from radioactive decays in the materials surrounding the detectors. Cosmogenic neutrons result from showers containing neutrons induced by cosmic rays. They can be produced by the interaction of high energy, cosmic muons with materials surrounding the detectors, through spallation (muon-induced nuclear disintegration) or various secondary processes within muon-induced hadronic and electromagnetic showers. The neutrons produced are of MeV energies and can produce keV nuclear recoils in the detectors. Since the cosmic muons are highly penetrating, the cosmogenic neutron background is especially troublesome. To sufficiently shield the experiment from cosmogenic neutrons, it is necessary to reduce the flux of comic muons and associated particle showers. Such a reduction is efficiently obtained by opting for underground operation. It is for this reason that CDMS-II experiment

was operated in the Soudan Underground Laboratory (SUL) in northern Minnesota. The lab is on the 27th level of a decommissioned iron mine, at a depth of 714 m below the surface. The rock overburden at the SUL provides a reduction in cosmic ray flux that is equivalent to 2090 meters of water overburden, reducing the muon flux by a factor of $5{\cdot}10^4$ relative to the flux at the surface (the remaining muon flux is <1 per minute), as shown in Fig. I.1. This reduction in muons is accompanied by a corresponding reduction in muon induced particle showers.

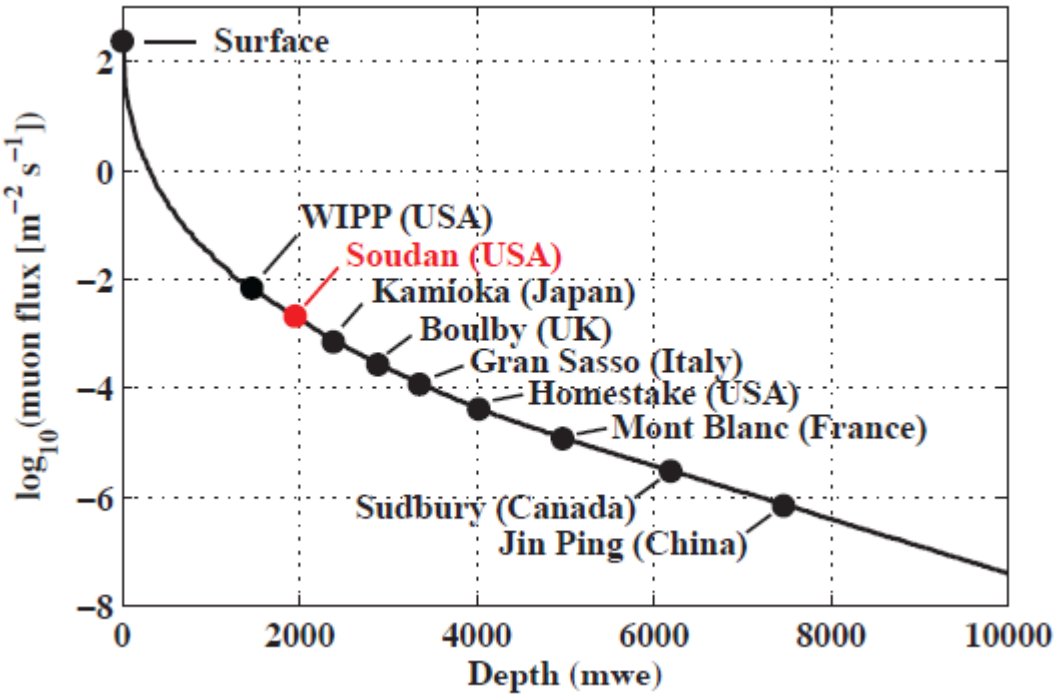

Figure I.1: Muon flux versus depth for a selection of underground laboratories. At a depth of 2090 meters water equivalent (mwe), the muon flux at Soudan is suppressed by more than 4 orders of magnitude relative to the surface. Figure taken from [239]

To ensure a successful operation of the experiment, additional facilities are needed. The Soudan 2 cavern was excavated in order to accomodate the special infrastruc-

tures needed to support CDMS-II experiment [229], as shown in Fig. I.2. Since the detectors are operated at cryogenic temperatures, the cryogenic control systems was developed to allow a stable operation of experiment for extended period of time. The required set of equipments such as pumps, plumbing, thermometry, electronic control systems, etc. are housed on a "cryopad". A clean-room is needed to prevent even trace amount of radioactive dust (from mine, or from radon in air) to settle on the detectors. The surrounding rocks in Soudan mine contain 238U, 232Th and 40K at a concentration of 0.17±0.06ppm, 0.89±0.20ppm and 0.79±0.04ppm respectively [233]. The walls of mine are coated with 2.5cm thick shortcrete and have the respective concentrations of 0.78±0.06ppm, 3.21±0.20ppm and 0.91±0.04ppm [233]. So, a class-10000 clean room is constructed, adjacent to the cryopad, within which the experiment is run. It also provides a receiver filter shielding for a low-electrical-noise environment, and is called as "RF room". Once the signals are obtained from the detector, various manipulations are needed, which can be done at room temperature. An "electronics room" is set-up containing necessary electronics to configure, operate the experiment, and acquire, record the data. Additionally, it is necessary to automate the process to allow detector operation and control during times when the access to SUL is not available.

I.2 Shielding

With the reduction in cosmogenic neutron flux by opting for underground operation, it is necessary to reduce the remaining flux of cosmogenic and radiogenic neutrons. Additionally, an active detector, being respondent to all type of events, will also record the events triggered by electromagnetic interaction of radioactive gammas and betas with the detector. Thus, it becomes necessary to add multiple layers of active and passive shielding around the detectors to reduce the occurrence

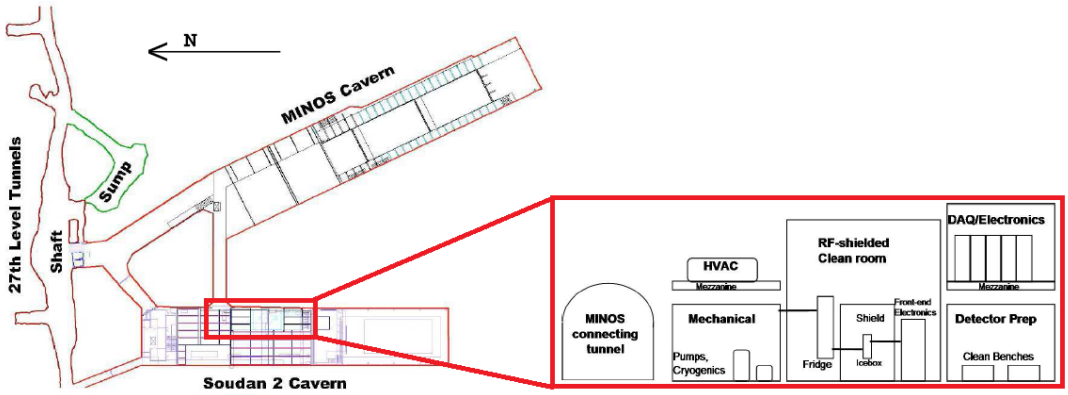

Figure I.2: Left: A layout of SUL on the 27th level of Soudan mine. CDMS experiment resides in Soudan 2 cavern (length 71.6m, height 11.2m). Right: A schematic view of the CDMS layout in the Soudan 2 cavern, looking East. The mechanical section is also called Cryopad, containing necessary equipment for cryogenic operation. The RF-shield clean room, or RF room houses detectors, the fridge and necessary shield. Detector pulses go to the DAQ, or electronics room. Figure taken from [233].

of such events, or be able to tag if an event is caused by these backgrounds. These are shown in Fig. I.3

I.2.1 Active Shield: Veto

To reject the muon flux that is not stopped by the rock overburden (which can interact with the nuclei of other elements surrounding the detector and produce neutrons), the detector volume is completely surrounded by an outermost layer of a shield that consists of an active scintillator veto made up of 40 overlapping panels (BICRON BC-408), as shown in Fig. I.3. The panels are arranged so that adjacent panels have a slight overlap and they cover the entire experimental setup. Acrylic light guides direct the scintillation photons in the panels to the attached photo multiplier tubes (Hamamatsu R329-02). The scintillator panel and light guide are wrapped in mylar foil for light isolation. The veto system also includes a source of blue light, transported to each panel with an optical fiber. Periodic pulsing of

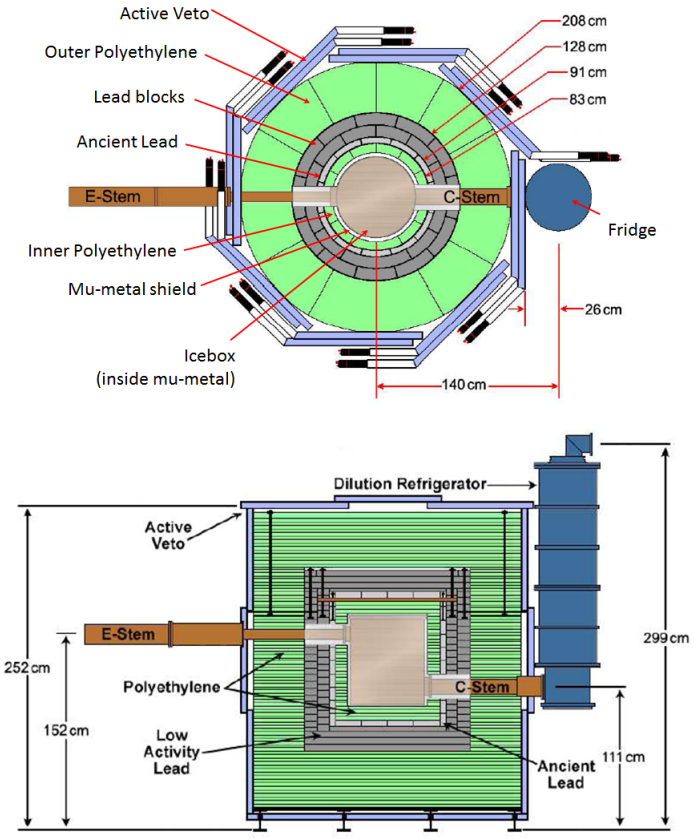

Figure I.3: Schematic top and side view of the shielding around the detector (kept inside set of nested copper cans called Icebox). The e-stem contains connection carrying electrical signals to/from detector. The C-stem contains connections to the dilution refrigerator. Figure taken from [233].

the blue light source (between data acquisition runs) allows calibration checks of the PMTs. Details about the architecture and design of the veto can be found in [136].

The scintillator thickness is 5 cm, allowing a minimum ionizing muon depositing $2MeVg^{-1}cm^2$ to deposit sufficient energy ($\sim$10 MeV) that it can be distinguished from the more prevalent Compton scattering of radiogenic γ-rays that appear at lower energy ($\lesssim$2MeV). This allows incoming muons to be tagged with $\sim$99.7% efficiency, while avoiding the large loss of livetime that would result if muons could not be

distinguished from the 600 Hz rate of Compton scatters in the veto [136, 233].

I.2.2 Passive Shield

Directly inside the active scintillator veto lie several layers of passive shielding with aim to reduce event occurrence due to natural radioactivity (radiogenic neutron and γ), an outer layer of polyethylene, two layers of lead, and an inner layer of polyethylene, shown in Fig. I.3. The ordering of the passive shielding was determined by Monte Carlo simulations to be optimal in terms of suppression of neutron background. Although, the shielding is designed to surround the detectors completely, there are a small holes in the outer lead shield, allowing exposure of the detectors to gamma and neutron calibration sources (^{133}Ba for gammas and ^{252}Cf for neutrons). Such dataset is useful to characterize the performance of detector.

The 40cm thick outer polyethylene layer acts as a neutron moderator reducing the energy of external neutrons sufficiently that they do not produce nuclear recoils above the detector threshold. The high concentration of hydrogen in polyethylene layer is efficiently able to extract energy out of incident neutrons.

The lead is an element with high atomic number. High concentration of electrons effectively attenuates external γs. The layers of lead comprise of an 18cm thick outer layer and an inner 4.5cm thick layer of "ancient lead". Recently smelted Lead blocks contain trace concentrations of ^{210}Pb, which has a half-life of 22.3 yrs and is a decay product of natural Uranium found in the ores used to produce the Lead. In contrast, the ancient lead used in CDMS was recovered from a sunken ship near Nantes, France [246], and the ^{210}Pb has decayed sufficiently that its concentration is negligible. So, the ancient lead layer is used to attenuate gamma backgrounds from radioactive isotopes in the outer lead.

The 10cm thick innermost layer of polyethylene serves as an additional neutron

moderator, primarily moderating neutrons produced from fission and (α,n) processes in the Lead shield. The inner moderator provides additional screening against the neutrons that might have penetrated the outer polyethylene layer (or simply created inside the outer polyethylene layer). The neutrons, being extremely massive in comparison with Lead atom, can continue to elastically bounce of against the Lead shield without significant loss of energy. Thus, without an inner layer, the neutrons will continue to bounce and interact multiply with the detectors.

Immediately inside the innermost polyethylene layer is a 2mm thick mu-metal shield, kept at room temperature that shields the inner volume from external magnetic fields. The magnetic fields can affect the performance of SQUIDs, which are used to measure the phonon signal (discussed in Appendix I.4). Thus, this layer of passive shielding is not inherent to reducing background, but to ensure an operation of the entire experiment. Immediately inside the mu-metal shield are the nested copper cans containing the detectors. Although the ZIP detectors are are kept under vacuum, the radioactivity levels from air in the SUL is relatively high (due to ^{222}Rn): $\sim$700Bq/m^3. Any substantial amount of air inside the shield will significantly increase the rate of Compton scattering background from γs. To reduce this background, the region between the outer copper can and the mu-metal is purged continuously with N_2 boil-off from a dewar of liquid nitrogen. This purge was observed to reduce the Compton scatter rate from γs by a factor of $>$4 in the 10-100keV region [228].

The following brief discussion does not relate to detector installation at SUL, but plays a crucial role in reducing backgrounds observed by detector. In order to complete the discussions presented in this section which emphasizes on steps taken to reduce background levels, the following fact is presented. Radon may contribute to background in an additional manner. During the period of detector fabrication,

decays from the ambient radon in atmosphere implant ^{210}Pb less than a micron into the detector surface. Low energy radioactive emissions from decay of ^{210}Pb forms a background to the experiment. It is for this reason that the detectors are kept in a Radon free environment during fabrication

I.3 Cryogenics

Once the possible sources of background have been checked through active and passive shielding, additional hardware needs to be installed to allow cryogenic cooldown of detectors to ∼40mK. Since this introduces extra materials in vicinity of active detector, it is also necessary to ensure that they do not introduce radioactive backgrounds.

The CDMS experiment achieves its low base temperature required for the operation of the ZIP detectors by using the 400S ^{3}He-^{4}He dilution refrigerator, from Oxford Instruments, which delivers a cooling power of 400 W at 100 mK and a base temperature below 10 mK with no external load. The fridge is made of steel which is not radio-pure and contains some residues of Uranium, Thorium and ^{60}Co. To prevent the detectors from operation in radioactive environment, they are mounted inside a separate unit comprising of nested copper cans, which is termed as "Icebox". To reduce the levels of radioactivity near the detector, The icebox and inner concentric cans consist of oxygen-free high thermal conductivity (OFHC) copper. All materials within the icebox were screened for radioactivity with a high-purity germanium detector to measure or place limits on the level of contamination. Comparison of the observed spectrum with simulation indicates that ^{238}U and ^{232}Th in the inner concentric copper cans dominate the Compton rate at low-energy due to the large mass of the cans (260kg) within the inner volume. The background measurement using the ZIP detectors themselves provides the most sensitive determination of the

radioactive contamination of the experimental apparatus. Comparison with simulations indicates that the concentration of ^{238}U and ^{232}Th in the cans is 0.18-0.01ppb and 0.56-0.06ppb, respectively [229].

The fridge is positioned outside the shielding and attached to the icebox through a series of concentric copper tubes that make up the "cold stem" or c-stem. The innermost icebox concentric copper can, within which the detectors are mounted is cooled by a commercial Oxford dilution refrigerator. The fridge has several cold stages within the outer vacuum chamber (OVC), which provide isolation from room temperature to the ∼40 mK base temperature at the detectors. Each stage is connected to a corresponding copper can within the icebox by the cold stem. An outer shield is maintained at 77K by a liquid nitrogen bath, while an additional inner 4K shield is maintained by the liquid helium bath. The dilution refrigerator maintains the innermost copper can of icebox (mixing chamber) at 40mK. Between the 4K and mixing chamber stages, there are two intermediary stages kept at ∼800mK (called "still") and at ∼130mK (called "cold plate"), and the mixing chamber at ∼40 mK.

The dilution fridge continuously cycles the ^{3}He-^{4}He mixture through the dilution unit, allowing long periods of stable operation at desired base temperature. To prevent blockages in the circulation loop, the mixture is cycled through external liquid Nitrogen and liquid Helium cold traps, as well as the internal liquid Helium cold trap supplied by Oxford. This cycling removes any contamination that enters the mixture due to small, undetected leaks or outgassing of materials. All three of these traps are cleaned regularly during normal operation, generally on a monthly interval.

The detectors are read out through a corresponding "electronics stem" (or, e-stem) which exits the icebox on the side opposite the cold stem. The electronics stem allows the detector wiring to exit the shield and is cooled by a Gifford-McMahon

cryocooler at the 77K and 4K stages, without the need for an additional liquid cryogen bath. This cooling unit intercepts the heat load from the detector wiring, which otherwise causes the detector temperature to increase from 45mK to ∼4K. Although, the cryocooler is connected to the e-stem through flexible copper couplings designed to maintain excellent thermal conductivity and limit the transmission of mechanical vibration, the vibrations introduced by the cryocooler were found to cause microphonic pickup on the charge channels for several detectors.

I.4 Cold Hardware

The detector support structure, wiring, and cryogenic amplifiers within in the icebox and electronics stem are known as the "cold hardware". They are necessary to operate the experiment at a low base temperature. The whole assembly, is mounted by a fixture designed to minimize the heat conducted and radiated into the cold stages. The cold hardware components are constructed with low radioactivity materials namely kapton and a low-activity custom solder.

The cold hardware components are assembled into "towers", shown in Fig. I.4, which contain the detectors and cold readout electronics. The ZIP detectors are enclosed in hexagonal high-purity Copper housings and supported with three cirlex clamps on the top and the bottom face. The detectors are stacked in sets of 6 to form the lower portion of the towers. The housings within the tower do not have lids and are positioned so that the detectors face each other with a vacuum ∼2mm spacing (This close spacing between detector faces allows efficient tagging of multiple-detector scatters from surface events occurring on neighboring detector faces. Such a discrimination is helpful in WIMP analysis, where a valid signal is expected to interact with just one detector). As a detector is stacked above others inside the tower arrangement, it is rotated by 60° corresponding to its neighbor (lower

placed detector) in an anticlockwise manner (for Tower2) or clockwise manner (other towers).

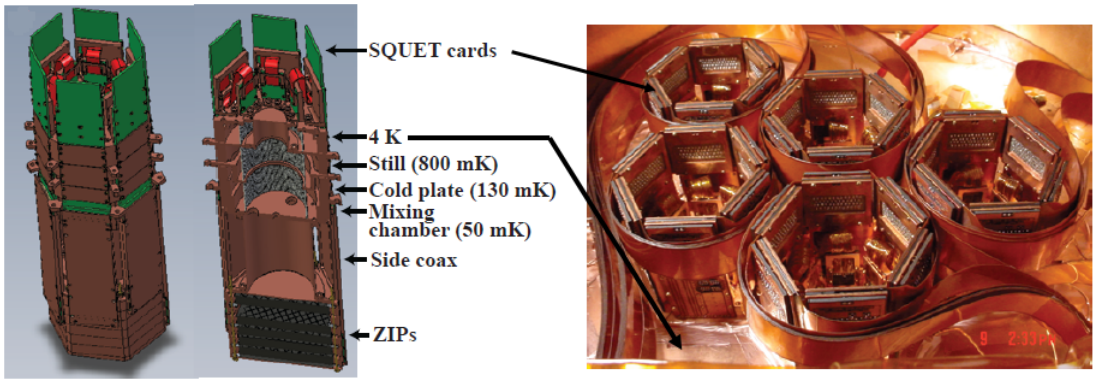

Figure I.4: CAD drawing of assembled tower and cross-sectional view specifying the temperature stages and cold hardware components. Photograph showing the 5 towers installed in the Soudan icebox. The SQUET cards at the top of the towers and the striplines are visible above the 4 K radiation shield. Figure taken from [239].

Each detector is connected to readout electronics via a detector interface board (DIB), shown in Fig. I.5a, which is attached to the inside of the detector housing along the substrate flat. It provides wirebonding pads that are connected directly to the bias lines on the detector. Two infrared LEDs, which are used to neutralize the detectors (as described in Appendix G), are also soldered to the top of the DIB. Above the detector stack, the upper portion of the tower is heat sunk to each of the successive cold stages (mixing chamber, cold plate, still, 4K bath), and thermally isolated from the remaining stages by a central graphite support structure. Radiation shields within the tower minimize infrared radiation emitted at the upper stages from reaching the detectors at base temperature.

A "side coax", shown in Fig. I.5b, contains 16 vacuum coax lines that electrically

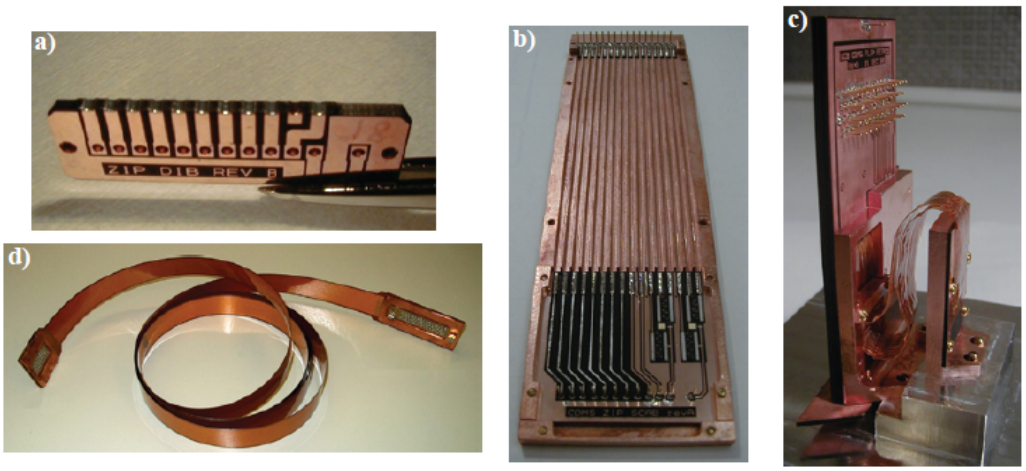

Figure I.5: Photographs of various cold hardware components: (a) DIB, (b) Side coax, (c)SQUET board, (d) stripline. Figure taken from [239].

connected the DIB of each detector to the base temperature stage of their tower. Each face of the hexagonal tower carries the bias and signal wires of one of 6 detector (Thus, the wires are of different lengths). The side coax also contains the coupling capacitors and bias and feedback resistors for the ionization readout, described in Appendix G.5. Heat sinking the resistors at base temperature reduces their Johnson noise contribution to the ionization readout.

The SQUET cards, shown in Fig. I.5c, is positioned at the top of the tower. It is a combination of two electronic circuit boards that houses the SQUID arrays for phonon signal amplification (described in Appendix H.3), and the first-stage JFETs for charge signal amplification (described in Appendix G.5) of a single detector. The SQUIDs are heat sunk to the still stage at ∼800mK to reduce the Johnson noise of the shunt resistors and the SQUID noise. The JFET charge amplifiers are heat sunk to the 4K stage. The FETs themselves sit on a Kapton membrane which allows them to self-heat to ∼140K, where the optimal noise (∼0.5 nV/$\sqrt{Hz}$ at 10 kHz) is obtained [227]. The two cards are joined by a flexible cable composed of twisted-

pair superconducting niobium wires sandwiched between layers of Kapton tape. The wires connecting the SQUETs and the side coaxes reside in vacuum coax channels, are tensioned to reduce microphonic noise, and are heat-sunk along the way to reduce thermal load on the side coaxes at base temperature.

The upper portion of the SQUET card connects to the "striplines", shown in Fig. I.5d, which provide a connection to the room temperature electronics through the e-stem. Each stripline is a flexible, 2.5cm wide, 3m long ribbon cable consisting of copper traces sandwiched between dual ground planes with Kapton as the dielectric. The striplines are heat sunk at 4K and 77K and pass through a copper radiation shield (to limit the heat flow from room temperature to 4K stage) as they pass through the e-stem and are connected to 50-pin hermetic connectors on the electronics stem breakout box (e-box) at room temperature.

I.5 Warm Electronics

The "warm electronics", located in the RF room at room temperature, take the signals exiting the e-box, provide second-stage amplification and signal conditioning, wait for an event trigger, digitize and record the corresponding detector timestreams.

The front end boards (FEBs) connect directly to the 50-pin connectors on the e-box and house the second-stage amplifier chain and biasing circuits for the cold electronics. The FEBs are operated from the electronics room by a fiber-optic-linked GPIB controller. A fiber-optic GPIB extender connects the GPIB Interface Box to the data-acquisition computers, electrically isolating the front-end digital control.

The amplified charge and phonon signal from the FEBs are connected to receiver-trigger-filter (RTF) boards in the electronics room, which removes baseline offsets for the phonon channels and applies an analog 336kHz 2-pole Butterworth anti-aliasing filter. A Butterworth filter has a frequency response which is maximally

flat below a pre-determined cut-off frequency, and decays to zero at the frequencies above the cut-off. A summed charge pulse is generated from the inner and outer charge channels, while a summed phonon pulse is generated from the 4 phonon inputs by the RTF board. These summed traces are used to issue triggers according to thresholds set by software at run-time. Although multiple phonon and charge triggers are generated, for the data analyzed in this dissertation, the P_{lo} is used to determine whether or not to record the event. The P_{lo} trigger represents if an event with sufficient phonon energy has occurred in any detector that the event should be measured, and is typically set at 10-15σ above the baseline phonon noise to prevent spurious triggerring from time-dependent noise.

The trigger logic board (TLB) accepts signals from the RTF boards and corresponding signals from the active scintillator veto and generates a "global trigger" if either the P_{lo} trigger is issued for any detector (indicating presence of an event with non-noise induced phonon energy in one of the detectors), the scintillation panels of active shield issues simultaneous triggers in multiple panels (indicating that multiple panels show high energy deposition. These triggers are conditioned and controlled by LeCroy discriminators which compares the PMT pulse heights to a software predefined threshold and issue triggers for veto panels whose signal exceeds threshold), or if it is a trigger randomly generated by the data acquisition software, or DAQ, to monitor detector noise (DAQ is discussed in the next section).

When a global trigger is issued, the DAQ computers read out the digitized signal for each detector channel and veto channel. The phonon and charge channels are digitized by 14-bit Struck SIS 3301 analog-to-digital converters (ADCs), which provide a sampling rate of 1.25MS/s and buffer a 2048 sample long time stream with the trigger at the 512th sample. Similarly, the veto signals are recorded by 12-bit Joerger VTR812 ADCs, which record 1024 samples at 5MS/s. However, since the

raw veto signals are extremely short in duration (order of ∼10ns), these signals are reshaped by a pulse-stretching filter network before digitization.

All of the above trigger signals are also recorded by a set of Struck SIS 2400 time-to-digital converters (TDC), and is separately held in a circular buffer with 1μs resolution. For each event recorded to disk, a record of the times and hit pattern for the 4 triggers immediately preceding the event as well the 5 triggers immediately after are stored. A slower DAQ system records phonon offsets (helps monitoringing loss in stable operation of SQUID, affecting phonon measurements) and mean trigger rates (helps monitoring changes in detector noise causing increased event rate for similar trigger level) as well as various experimental conditions and stores these data to disk separately throughout the data taking.

I.6 Data Acquisition

The Soudan DAQ, described in detail in [233], is controlled by a "run control" server which manages the configuration and operation of the experiment, an "event builder," which acquires and records the data for each event, and a run control GUI which allows control and configuration of the experiment. Each component is implemented in Java or C++ and runs on dedicated servers within the electronics room at the SUL. The run control GUI is a Java-based network application which can be used to monitor the experiment remotely, or directly control the experiment from the local network at the mine.

The largest overhead during data acquisition results from acquiring traces and recording them to disk. For the 5-tower operation, the maximum rate at which all the traces for each event could be recorded was 20Hz, corresponding to a data rate of 12MB/s. Although this is well above the ∼0.1Hz trigger rate recorded in WIMP search data, it limits the rate of calibration events that can be recorded, increasing

the time which must be spent acquiring calibration data. To improve the data rate during the high-rate ^{133}Ba calibrations, the DAQ was operated in "selective readout" mode, where traces were recorded only for detectors that issued a P_{lo} trigger. In this configuration, data rates of up to 70Hz are possible, reducing the time needed for calibration by a factor of 3.5. For the WIMP search data as well as the lower-rate ^{252}Cf neutron calibrations, data is recorded in full readout mode, where traces are read out for each detector regardless of trigger information to ensure that particle-induced events falling under the trigger thresholds are recorded.

I.7 Analysis Pipeline

The analysis pipeline takes the raw traces recorded by the DAQ for each event and produces reconstructed quantities describing the pulse characteristics. The data recorded to disk by the DAQ at Soudan is compressed, backed up to tape in the mine, and transferred to Fermilab for the primary data processing. The analysis pipeline for charge pulses is described in Appendix G.7 and Appendix G.8. The analysis pipeline for phonon pulses is described in Appendix H.5 and Appendix H.6.

APPENDIX J

THIN FILM DEPOSITION (VIA SPUTTERING) AND CHARACTERISTICS

Sputter deposition is a technique for deposition of thin film using sustained glow discharge, or plasma. Since the film deposition is not due to occurrence of any chemical reactions at the substrate surface, sputtering is referred as being part of "Physical Vapor Deposition" technique for film deposition. The sections below describe the sputtering process, and few of the characteristics of thin film.

J.1 Plasma and Sputtering

Sputter deposition can be based on two main principles, the formation of a sustained glow discharge (a plasma) - either using a direct-current (DC) or radio-frequency (RF) voltage bias, and on the particle-particle collision involving an elastic transfer of momentum. A detail review on sputtering can be found in [333, 334, 336].

J.1.1 Formation of DC Plasma

The simplest type of glow discharge is a direct-current (DC) glow discharge. In its simplest form, it consists of two electrodes in a cell held at low pressure (0.110 torr; about 1/10000th to 1/100th of atmospheric pressure), and electric potential of several hundred volts applied between them. The cell is typically filled with inert gases, like neon, argon, xenon, but other gases can also be used.

A small fraction gas atoms exist in equilibrium due to processes like thermal collisions between atoms, or by keeping an externally heated element to promote ionizatin of atoms, or due to interaction with high energy particles (cosmic rays, background γ rays). Under the affect of field existing between the electrodes, the positively charged ions and the negatively charged electrons are driven towards the oppositely charged

electrodes. Due to the comparatively small mass of electrons (as compared to mass of ions), they quickly gain kinetic energy and collide with other atoms as they drift, ionizing them. More electrons are also ejected as the positively charged ions collide with the negatively charged electrode which contribute to the plasma buildup (this also creates ejection of atoms off from the electrode surface, and the process is called "Sputtering". It is discussed in next section, Appendix J.1.3). However, an other possibility is that the ions and electrons may recombine to form neutral atom. For sufficiently high voltage between the electrode, the rate of ionization exceeds the rate of recombination, and a sustained plasma of conducting, charged particles is formed.

Fig. J.1 shows the different regions in a DC plasma [348, 349]. These are formed due to the variation in ion and electron density at different distance from the cathode, described below:

- The Aston Dark Space (1) is a thin region close to the cathode. The electrical field is strong in this region accelerating the electron away from the cathode. The electrons in the Aston dark space outnumber the positive ions in this region, but their density and energy ($\sim$1eV) is too low to efficiently excite the gas, it consequently appears dark.

- In the Cathodic Glow (2), next to the Aston dark space, the electrons are energetic enough to excite the neutral atoms during collisions, and has a relatively high ion density. The cathodic glow sometimes masks the Aston dark space as it approaches the cathode very closely.

- The Cathode/Crooks/Hittorf dark space (3) is a relatively dark region that has a strong electric field and a relatively high ion density (providing the majority of current). The acceleration of electron leads to ionization rather than electronic recombination. Thus, it appears dark. The majority potential dif-

ference between the two electrodes is across this narrow region surrounding the cathode. Hence, the it is also called "Cathode Fall".

- The Negative Glow (4) has the brightest intensity of the entire discharge. The high electron density at end of the cathode dark space results in decrease of electric field (and electron energy). This promotes electronic recombination over ionization. Electrons carry almost the entire current in the negative glow region, due to their high mobility.

- The Faraday dark space (5) separates the negative glow from the positive column. At the end of the negative glow, the electrons have lost most of their energy, excitation and ionization processes cease to exist. This is the start of the next dark region.

- The Positive Column (6) is a luminous region that forms due to reduction of plasma density in the Faraday dark space, causing an increase in the electric field. The electric field is just large enough to maintain the degree of ionization to reach the anode.

- The Anodic glow (7) is slightly brighter than the positive column due to an increased concentration of positively charged ions repelled by anode. But, it is not always observed.

- The Anode dark space (8) or anode sheath is the space between the anode glow and the anode itself. Due to the repulsion of ions from the anode, this region has a net negative space charge. An absence of ions reduce the electronic recombination rate, and the region appears dark.

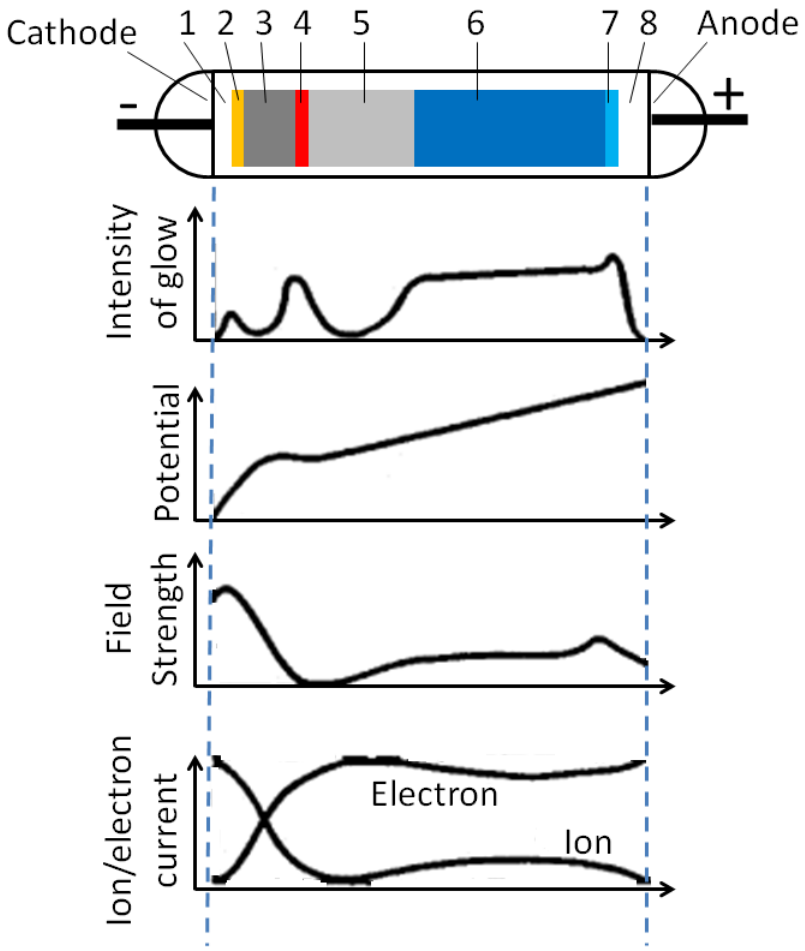

Figure J.1: Different region of DC plasma between cathode and anode. Going from cathode(LEFT) to anode(RIGHT), there is (1)Aston Dark Space, (2)Cathodic Glow, (3) Cathode/Crookes/Hittorf Dark Space, (4)Negative Glow, (5)Faraday Dark Space, (6)Positive Column, (7)Anodic Glow, (8)Anode Dark Space. Figure taken from [347]

J.1.2 Formation of RF Plasma

Another method to form a plasma is by applying an alternating, radio-frequency (RF; typically, 13.56MHz) bias to the electrodes, instead of a constant DC bias (a detailed sicussion can be found in [335]). Due to the change in direction of voltage, the electric field between the electrodes change, and free electrons are trapped between

the electrodes for a longer period, creating more ionization. Thus, RF biased plasma can be generated even by applying a lower voltage and/or under a low gas pressure. Free ions do not contribute to creating further ionization because their heavy mass prevents them to gain sufficient kinetic energy to create ionization within the small time period after which the RF bias changes its polarity, for applied RF frequency $\gtrsim$1MHz. For similar reasons, the contribution to plasma buildup, from electrons which are ejected as the ions strike the electrode, is also negligible.

Since the direction of bias always changes, there is no concept of a "cathode" and "anode", as it was in the case of DC plasma. A dark space is formed near both electrodes. It is mentioned above that the contribution to ionization is due to free electrons existing between electrodes. For a typical design of thin film deposition machine, the entire body is grounded (and acts like an electrode). Thus, the entire space inside the machine glows as a RF plasma is formed.

Although no external DC bias is applied when creating a RF plasma, it (a DC bias) may get induced. When an electrode is positively biased under one-half cycle of the RF bias, the electrons profusely move off into the electrode, owing to their high mobility. However, in the next half, negatively biased cycle, very few ions are able to strike the electrode, owing to their extremely low mobility. After a few cycles, the electrode develops a negative charge (in comparison to the plasma) and repels the electrons, till the flux of electrons and ions hitting the surface is equal. If the electrode surface area is large, then more ions can hit the surface, and so a lower negative voltage develops on the electrode, and vice versa. It is shown that [335]

$$\left(\frac{Voltage_A}{Voltage_B}\right) = \left(\frac{Area_B}{Area_A}\right)^4 \tag{J.1}$$

where, A, B denote the two electrodes, $Area$ denotes there respective electrode area

and *Voltage* denotes the induced DC voltage on each of the area. Thus, one may note that by making one of the electrodes much smaller than the other electrode, a greater voltage is developed across it, making the ions hit the corresponding electrode with higher kinetic energy (and causing a larger ejection of atoms from it). However, an exact relation is also dependent upon the electrode geometry and their placement inside the thin film deposition chamber.

One final comment on the usability of RF plasma; There is no particular "cathode" or "anode" in RF plasma (only by changing the relative size of them electrodes, the one with smaller area acts as the sputter target electrode), and in each cycle the electrons and ions strike both the electrodes. This allows it to be used for creating plasma (and for sputtering purposes), when one of the electrode is (or, is covered with) an insulating material. If a negative DC bias is instead applied, then the electrode will simply keep on collecting positively charged ions, till it develops sufficient charge to repel the charged ions, and killing the plasma.

J.1.3 Sputtering

In the previous sections describing DC plasma (Appendix J.1.1) and RF-plasma (Appendix J.1.2), it is mentioned that immediately next to the electrode, there is a region comprising of positively charged ions with a huge electric potential gradient. The ions, under the effect of the potential gradient, gain large kinetic energy and strike the electrode, causing one/multiple of the following effects, shown in Fig. J.2:

- Production of photons (visible, or x-rays)
- Embedding of the incident ion inside the electrode
- Ejection of electrons. Since the electrode is negatively charged, the electrons are repelled off.

- Ejection of atom(s)/ ion(s)/ radical(s) of material comprising the electrode, or of incident ion.

The ejection of target material due to collision with incident ion is called "Sputtering". Note that in RF etching, both electrodes experience sputtering. However, by designing the electrodes such that one is much larger in area than the other; the one with smaller area is sputtered, while the ions may elastically bounce-off, or simply produce photons when interacting with the electrode of larger area.

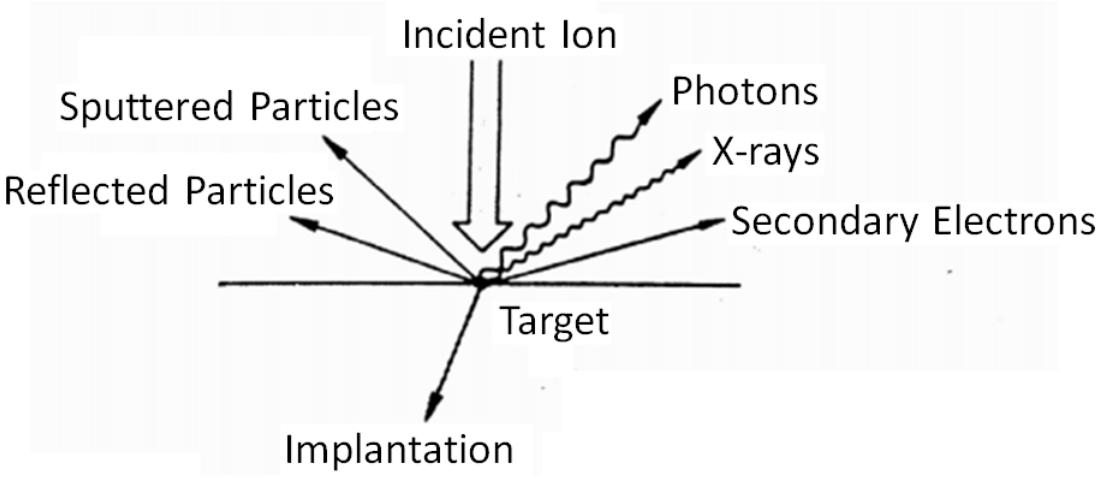

Figure J.2: Most general of outcomes as a target material is hit by an incident ion. The ejection of neutral, positive or negative charged atom(s) of target material, is called "Sputtering".

J.2 Sputter Deposition and Sputter Etching

In the sputtering process, atoms are dislodged from a "target" electrode, and deposited on the surface of oppositely placed electrode (where a semiconductor substrate may be placed, which needs to be coated with a thin film). Thus, depending on usage of the process, it may be said that either sputtering caused a deposition of

thin film on the substrate, or it caused an etching of the target (in general, one never says that the target is being etched off. Description of sputter etching is provided below.)

J.2.1 Sputter Deposition

The atoms released from the target electrode diffuses across the plasma and arrives at the opposite electrode, where the substrate requiring a thin film deposition is placed. During deposition, the incident target species strike the wafer surface, get adsorbed and diffuse across the surface. They may either settle into a particular location (forming a growth island), or may desorp from the surface. Additional atoms may coagulate with existing islands or impart energy to it to cause the entire island to desorp. Thus, if the energy of each atom incident on the substrate surface is large, then they are more likely to diffuse across the surface and settle at a location which is already nucleated, rather than creating a new island. The atoms will also be more likely to arrange themselves to fit to the crystal structure of the existing island. If the substrate is heated, then they may also use the thermal energy of the substrate to the same effect. Finally, as these islands nucleate and grow independent of one another, they finally merge with each other and growth continues in a columnar manner. Thus, one gets a polycrystalline film structure.

A few parameters that affect the quality of the deposited thin film are described below. These are the main parameters used by fabrication group at TAMU to control the quality of deposited thin film. In addition to them, there are multiple other parameters which affect film deposition characteristics, like, substrate roughness, crystal direction normal to the deposition surface, lattice spacing between two atoms on the substrate surface, deposition temperature and even the geometry of deposition chamber ([337] studies the effect of various parameters on the stress in thin film).

J.2.1.1 Deposition power

A higher deposition power means that the voltage across the cathode dark space and the current flowing through it is large. This implies that a larger amount of ions are impinging on the target electrode, and with greater kinetic energy. Thus, more atoms are sputtered (increased deposition rate), with a higher energy (as compared to low deposition power). A large deposition rate also causes less impurities to be trapped inside the film.

J.2.1.2 Gas pressure

A higher deposition pressure means that an atom sputtered from the target will undergo more collisions with the gas before it reaches the substrate. Also, more of the gas ions will hit the target and cause more atoms to be sputtered. If the mass of gas is more or comparable to the mass of sputtered atom, then the atom loses energy and less of it arrives at the substrate with a low energy. If the mass of sputtered atom is much more than the mass of gas, it doesn't loose much of energy in the collisions, but the rate of atom arrival at the substrate increases.

J.2.1.3 Substrate bias

A larger, negative bias on the substrate promotes impingement by positively charged ions. If the material being deposited has a tendency to form positively charged ion inside the plasma, then the ions are also attracted to the substrate. This increases the deposition rate and the energy with which it arrive at surface. Since Argon is generally used inside the thin film deposition chamber as the processing gas, which exists as Ar^+ inside the plasma, it also hits the substrate surface, imparting additional energy to the deposited atoms to increase their surface mobility, improving film adhesion, and acting to sputter etch any oxide layers which may be present on

the substrate surface.

J.2.2 Sputter Etching

As mentioned above, it instead of target, the substrate is placed at the cathode, then it will be etched. However, since the substrate used by CDMS is semiconducting silicon/germanium crystal, a RF plasma based etching has to be used.

J.2.3 Advantages and Disadvantages of Sputtering

The following are the advantages of sputtering:

- There is a better correlation between the process parameter and the outcome (quality of film). This also allows for repeatability in film quality, including control on intrinsic and extrinsic microstructure.
- The thickness of film is uniform across the substrate. Thickness control is easy since it is proportional to deposition time.
- It is easier to deposit multiple films, alloys (with same stoichiometry as target) and insulators. Using a suitable system, all of the operations can also be done within a single unit without cross-contamination.
- Better film adhesion.
- Possibility of in-situ cleaning (using RF-etch and/or negative biased substrate).
- Due to usage of high energy atoms, one obtains denser film.
- Due to interaction with the gas atoms/ions (used to create plasma), the film deposition is isotropic, i.e. the sputtered atom can strike substrate surface at any angle. This allows for a better step coverage.

The disadvantages of sputtering are:

- Source material must be available in sheet form.
- Deposition rate are usually $\lesssim$4nm/s.
- Except for short runs, the substrate heats up due to bombardment by ions. It is necessary to cool the substrate.
- The substrate may attain radiation damage during RF etching. If a thin film layer is required to be deposited after RF etching, then the rough substrate surface may hamper mobility of atom (leading to a film with small grain size).

J.3 Properties of Sputter Deposited Thin Film

The measurable film properties of a sputter deposited thin film depend on the "crystal microstructure", which in turn depends upon a number of different factors, like machine design, process parameters, substrate conditions and composition [338], as shown in Fig. J.3. Barring considerations to machine design (which is fixed for a given machine) and substrate conditions (by assuming that for different iterations one is given substrate with similar surface features), it is the process parameter which plays a major role in determining the properties of deposited thin film.

The crystal microstructure is not the same as crystal structure. The crystal structure is related to the constitution of the material, the relationship between unit cell and crystal spacing. The microstructure is defined by the relationship between crystalline grains and grain size, and includes both intrinsic and extrinsic components [339]. Intrinsic microstructure includes within-grain parameters such as grain composition and free electron concentration. Extrinsic microstructure primarily concerns the size, shape, orientation and phase of grains, as well as the topography of the deposited film and of the substrate surface on which the film was deposited.

The structure of a metallic thin film can be described by the standard zone

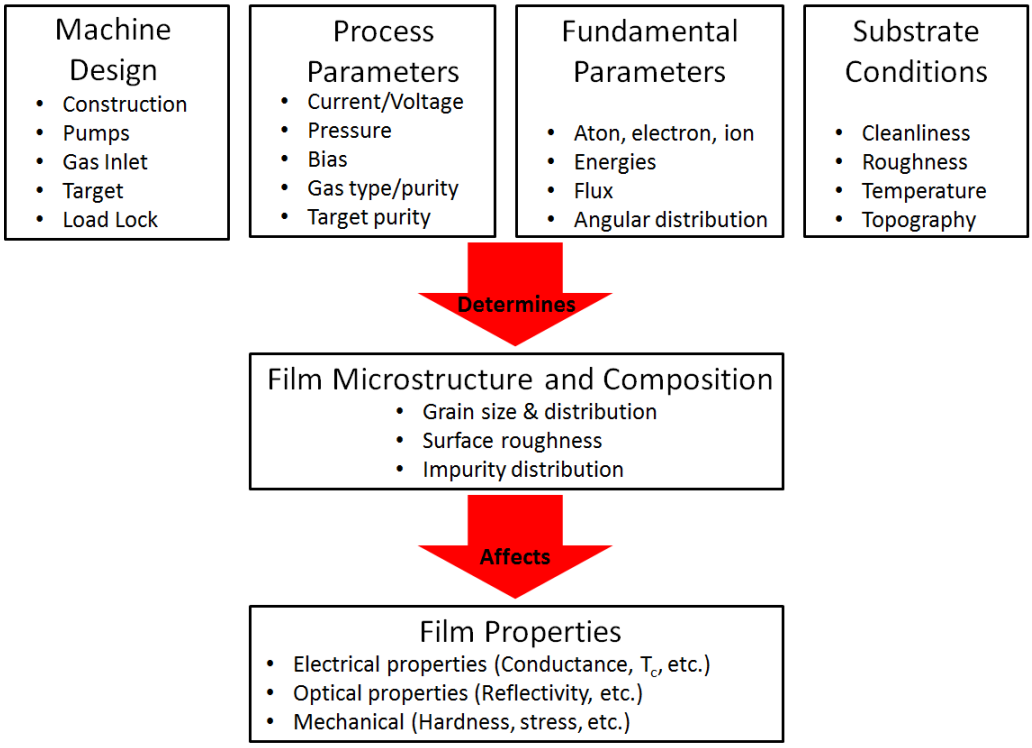

Figure J.3: Summary of Sputter Parameters impacting Film Microstructure. T_c refers to the film's superconducting transition temperature. Figure taken from [339].

diagram (SZD), shown below in Fig. J.4 [336]. The SZD relates temperature and process pressure for a metallic coating. Sputtered films typically reside in either Zone 1 or Zone T. Interpretation of the SZD diagram, described below, is referred from [339].

Zone 1 films deposited at high pressure and low power are fibrous, but porous, and typically demonstrate tensile stress. The Grains are columnar, but separated by voids, and thus, are less dense. Due to low deposition rate, there is a higher gaseous impurity incorporation. These films exhibit tensile stress.

Zone T (transition region) films are ones deposited at low pressure and high power and tend to form structures that are very densely packed containing fibrous grains with low ductility [336]. This is due to the enhanced energy and directionality of

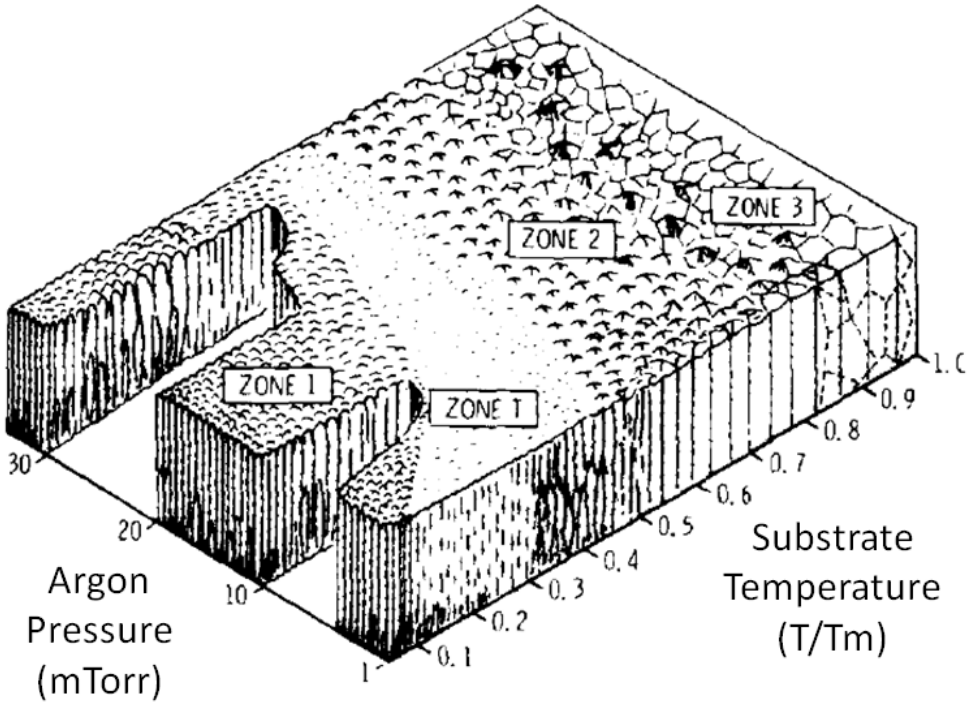

Figure J.4: The Standard Zone Diagram for Metallic Thin films relating the crystal microstructure with the deposition pressure and substrate temperature, other factors being same [336, 350]. T_m refers to the substrate melting point. Figure taken from [339].

atoms in the vapor phase. Atomic peening, or packing via gas atoms colliding with the growing film, ensures the high density of the film, typically along with compressive stress levels [340]. Grains tend to be small, with domed surface topography and low levels of surface roughness [336]. The high rate of deposition causes relatively low levels of gas impurity incorporation into the film, and promote good electrical conductivity and specular reflectivity [336]. Moving to zone 2 and zone 3, the influence of bulk diffusion increases and recovery and/or recrystallization limits the intrinsic stresses in this region.

The effect of temperature on microstructure is related to how close the deposition

temperature is to the melting point of the deposited material [336]. The higher the temperature, the more is the mobility of deposited atoms on the substrate surface. This results in larger grains that have a smoother surface, but with a tendency for facets to grow between grains. At lower temperatures, the film is much denser, with surface roughness a function of film thickness [340].

The crystal structure and topography of the substrate also affects the structure of the deposited thin film. To this effect, it was demonstrated that the roughness of underlying substrate gets transferred to sputtered aluminum thin films and affects the reflectivity of the film [341], deposition of identical films onto different substrate materials was shown to result in varying grain size, resistivity, stress, and hardness [342] and the superconducting transition temperature, film stress and crystalline phase transition of tungsten thin film was shown to depend on the substrate up on which the deposition was done [316]. The crystal orientation of the underlying substrate can also alter the preferred grain orientation of sputtered films [336].

APPENDIX K

ZIP DETECTOR FABRICATION STEPS

The appendix provides a description of various processing step covered by a germanium/silicon crystal to convert it into a ZIP detector, obtained from [323]. In addition to being fabricated, the detector should also satisfy various quality checks and cryogenic measurements before it is deemed suitable for use in CDMS experiment. The set of checks are described in other CDMS theses [227, 241, 322]. To optimize the steps, they are first performed on silicon (sometimes, germanium) wafers. Thus, the processing steps mentioned below also apply to wafers (except the steps of alignment, grinding and polishing, which is not done by CDMS), even though it may not be explicitly mentioned below.

Following the procurement of high purity, low defect density crystals from the corresponding vendor, it passes through the following fabrication steps, described below. Although the general order of fabrication steps remain almost the same, the exact sequence of operations carried out in each of the processing step may change depending on the charge and phonon sensor circuit design used by CDMS (during the corresponding period); Indeed, the circuit patterns have changed over the years (described in multiple CDMS theses [227, 228, 230, 231, 235, 236]), and so have the sequence of operations. The specific details on fabrication of CDMS-II detectors can be found in [353, 354].

K.1 Alignment, Grinding and Scribing

As described in Section 3.5, flats are made in crystal along different directions, facilitating detector handling and alignment (while arranging them in vertical stacks,

or "towers, inside the CDMS setup, as decribed in Appendix I.4). Depending on their location, the flats also help in identifying the crystallographic orientation. Since crystals cleave along the crystallographic planes, it is necessary to obtain them through x-ray diffraction measurements. This helps in defining the exact location of major flats on an otherwise circular symmetric faces of cylindrical crystal volume. Thus, the process of alignment and grinding (of flats) is carried out one after another.

After the above steps, a "crystal name" (an identifying marker) is scribed on one of the major flats using a diamond-tipped scribe. The scribing is done such that the crystal laying on the table with the label correct way up (upright and not inverted), the side of crystal in contact with the table is closer to the original seed end of the boule (A boule is the initial cylindrical shaped chunk of single crystal, from which smaller pieces are cut. An individual piece forms the substrate for ZIP detectors). This, bottom side of crystal is called "side-2", and the other, top side is called the "side-1" of the crystal.

This step is currently done by an external service providers. To speed up the process (and prevent it from becoming possible bottleneck and reduce the fabrication speed), the detector fabrication group at TAMU is developing the x-ray alignment and grinding capabilities.

K.2 Polishing

ZIP detectors employ 40-300nm thick sensors pholithographically fabricated on metallic films (described later in this appendix). To obtain thin film deposition with uniform thickness and for a successful lithography step, it is necessary that any surface irregularities (like scratches, dents, chips, shown in Fig. 5.2) on the crystal be removed, it is polished to a surface roughness much less than the minimum thickness of any metallic film deposited on it ($\sim$1nm), and the maximum topographical

variation in surface height should be of the same size (or less) as the smallest pattern/feature on the sensor circuit ($\sim 2\mu m$). The terms "Polishing" as used here refers to a set of process done one after another, and include:

- Heavy Chemical Etch
- Banking
- Lapping
- Coarse Polishing
- Fine Polishing
- Post Polish Cleaning

K.2.1 Heavy Chemical Etch

The crystal surface from the previous grinding step is badly damaged. The damaged locations act as charge trapping sites and need to be removed before the crystal is deemed usable for the CDMS experiment. Additionally, the grinding step is done through external providers and it would be desirable to ensure that possible surface contaminants (from detector handling in an unknown environment) are removed, especially radon (found in atmosphere), and its decay product, ^{210}Pb. Events induced by radioactive decay of these contaminants act as significant backgrounds in a WIMP search analysis. To address these concerns, the 100-200μm from the entire outer surface of the crystal is chemically etched off by dunking the it in a mixture of 1000ml 70% Nitric acid (HNO_3), 200ml of 49% Hydrofluoric acid (HF) and 50ml of glacial acetic acid (CH_3COOH).

K.2.2 Banking

This step involves filing off the crystal edges to create a smooth bank at the corner. This prevents the crystal from slicing off user's skin (with its sharp edge) while it is handled. It also prevents the chipping of crystal edges as the polishing pads move over the crystal surface (during Coarse and Fine Polishing), and additional tear/wear of polishing pad by rubbing against sharp crystal edge. While it is desirable to have a banked edge, it should not be done too deep or too angled (creating a loss of active detector material). Thus, the step of banking is carried out only whe required.

K.2.3 Lapping

Lapping is a coarse polishing, done using slurry made from $9\mu m$ alumina powder, to remove larger features (deep scratches, indentions, etc.), done manually for a few minutes on a glass surface.

K.2.4 Coarse Polishing

Coarse polishing is done using colloid made from $1\mu m$ alumina, with acidic chemical component, and corresponding polishing pads. The main purpose of this step is to remove all scratches and leave a flat surface, but covered with sleeks (a hair-line scratch). Surface flatness is checked by inspecting the crystal surface through a Michelson interferometer, as shown in Fig. 5.5. For a red light source of wavelength (λ) $\sim$650nm, observance of $\leq$3-rings across the crystal surface ensures its flatness to $\lesssim 2\mu m$. After achieving desired surface flatness, the crystal is taken through a second polishing step, using similar slurry, but using softer, medium "nap" polishing pad (The pads used for polishing vary by the height of their fiber, known as the nap and by the stiffness or resiliency of the fiber). The latter step doe not/negligibly affects crystal surface flatness. A discussion on the effect of particle size, polishing

pad and contact pressure in free abrasive polishing process can be found in [328,329].

K.2.5 Fine Polishing

The crystal achieves a high surface finish (without even a single scratch/ sleek/ dents/ pits) after the fine polishing step done using a colloid made from 70nm silica, and "high nap" polishing pads.

K.2.6 Post Polish Cleaning

Post polish cleaning is necessary to ensure a complete removal of macroscopic slurry particles, dirt, etc. particles which are attached to crystal surface through Van der Walls force [326] (except trace quantities of metallic and/or organic residue, which are removed through chemical cleaning mentioned in the next section, Appendix K.3), and to obtain a "visibly" clean crystal surface. Since the crystal polishing at Stanford in done through external service providers, but done by the group itself at TAMU, the following post-polishing procedure mentioned below was developed at TAMU itself (with help from the fabrication group at Stanford). At TAMU, this step is always followed by a chemical cleaning step, mentioned in next section, Appendix K.3.

The post-polish cleaning step involves:

- Wiping slurry particles off from the curved surface of crystal using lint-free wipes soaked in Acetone

- Performing multiple iteration of rinsing the crystal with DI-water, Acetone, IPA and then DI water again, and cleaning the surface with soft, post polish cleaning brush, while keeping the crystal under water to prevent scratching. The brush used has the brand name SoftPore, manufactured by Hydrofera Micron Technology LLC, and is a gas pore-formed polyvinyl alcohol (PVA),

concentric-nubbed cleaning brush treated with 1.0% hydrogen peroxide solution antimicrobial agent

It is reported that post polish cleaning of germanium surface can be obtained by etching it [326]. This indicates that the post polish cleaning process may not yet be optimized. For the procedure used at TAMU, this option was not pursued to ensure that the surface finish is not destroyed by the etching step.

K.3 Wet Cleaning

] Wet cleaning refers to chemical treatment of the crystal/wafer (or, substrate) to remove presence of organic and metallic impurities from its surface. The presence of these impurities affect the success of subsequent processing steps. To briefly explain, if a dust/contaminant residue of $\sim \mu m$ size is sitting on the detector surface, then it will cause a physical break/damage in any thin film (of nm thickness) deposited over it. Also, the presence of impurities affect the local properties of thin film sensors fabricated over them (example: presence of magnetic impurities change the T_c of tungsten TES, described in Section 5.1.3).

Since radon (decays from ambient radon in atmosphere implant ^{210}Pb less than a micron into the surface, which is a major background to WIMP analysis) and particle contamination is a major concern, this step is done in a radon-free class-100 clean room, and also observing necessary "clean-room" protocols (to prevent the user from carrying dust particles inside the room). The terms "class-100" means that there are 100 or less count of particles of size $\geq 0.5\mu m$ per cubic foot of air, maintained using. It is maintained using HEPA filters employing laminar air flow, from ceiling to floor. Ordinary room air is class-1,000,000.

K.3.1 Germanium Crystal/Wafer Cleaning

In the detector fabrication facility at TAMU, this step is done immediately after the previous step (post-polish cleaning). However, before the development of fabrication facility at TAMU, detector fabrication was done at Stanford and the polishing was done by external service providers. The cleaning step was done separately after the crystals were polished and handed back to the fabrication facility at Stanford, and so, this step is described separately, in conformation with the historical perspective.

.

Steps undertaken to clean germanium substrate is mentioned below. The chemicals involved are: De-Ionized water (DI water), Xylenes, Acetone, Iso-Propyl Alcohol (IPA), PRS-1000, 49%HydroFluoric acid (HF)

Cleaning steps used at Stanford (as inferred from [323]):

1. Ultrasonicate the germanium substrate in DI water for a $\sim$5 minutes.
2. Dunk in Xylenes, at room temperature, for 15 minutes
3. Spray with acetone, then dunk in acetone, at room temperature, for 5 minutes. This is necessary because Xylenes are miscible with Acetone, but not with IPA
4. Spray with IPA, then dunk in IPA, at room temperature, for 5 minutes
5. Dump rise (dunk entire content in DI water), and spin dry (spin drier are standard semiconductor fabrication equipments which dries the substrate by spinning it rapidly)
6. Dunk in the solvent, PRS-1000, at room temperature, for 10 minutes
7. Dump rinse, and spin dry. This step marks the end of process to clean germanium substrate. The subsequent steps are carried out immediately before

sending the substrate for further processing (the next step in detector processing is thin film deposition, described in the next section, Appendix K.4).

8. Dunk in mixture of 5:1 $DI\ water\ :\ HF$, kept at room temperature, for 8 minutes

9. Dump rinse, and spin dry. The dried substrate is required to be sent through the next processing step (thin film deposition) within 2 hours after this step

Cleaning steps used at TAMU:

1. Ultrasonicate the germanium substrate in DI water for a $\sim$5 minutes.

2. Rinse the beakers (to be subsequently used), thermometers, teflon tweezers, cassette (the slotted apparatus in which the substrate is loaded, as they are dipped in corresponding reagents) and storage container (where cleaned substrate will be stored). Rinsing is done using DI water, Acetone, Methanol, IPA, and DI water again. It is blow dried using dry nitrogen. The storage container is dried in oven, kept at 70°C for 5 minutes.

3. Spray with acetone, then dunk in acetone, at room temperature, for 5 minutes

4. Spray with IPA, then dunk in IPA, at room temperature, for 5 minutes (It is typical to use heated IPA. This is avoided to prevent any fire accidents.)

5. Rinse with DI water

6. Dunk in mixture of 3:1, kept at room temperature, for 5 minutes. Then, dunk in DI water for 5 minutes. Repeat 3 times.

    - Another effective alternative for removing metallic contaminants off germanium is to use HydroChloric acid (HCl) [324, 325]. HF is chosen to

conform to already established cleaning recipes, from Stanford. It is still unknown how the hydrogen passivation (by HF), or chlorine passivation (by HCl) affects the CDMS detector performance.

- Higher HF concentration is used to be make the reactant be more aggressive towards removing metallic impurities. However, it is not an optimal ratio. A Higher HF concentration also leaves the germanium surface rougher [324]. However the rms roughness $\sim 0.6 \pm 0.1nm$ is still much less than the smallest thickness of metallic film laid on the surface.
- Multiple iterations of HF dunking, followed by rinse in DI water is done for the following reason. Germanium can react with water to form oxide layer. Thus, multiple iterations of dunk in DI water and then in HF causes formation and subsequent dissolving out of oxide layer, allowing for a greater probability of surface contaminant removal. Currently, this process is not optimized, or even quantified.

7. Rinse in DI water, and spin dry. Keep in oven, heated at 70°C for ∼5 minutes to dry (thoroughly dehydrate). Transfer the substrate to the storage container and place it in dry box, or use immediately, as needed.

K.3.2 Silicon Crystal/Wafer Cleaning

Steps undertaken to clean silicon substrate is mentioned below. The chemicals involved are: De-Ionized water (DI water), Acetone, Methanol, Iso-Propyl alcohol (IPA), 98%Sulphuric Acid (H_2SO_4), 30%Hydrogen Peroxide (H_2O_2), 49%HydroFluoric acid (HF) and 30% HydroChloric acid (HCl). The steps used at Stanford and at TAMU are described separately.

Cleaning steps used at Stanford (as inferred from [323]):

1. Dunk in mixture of 9:1 $H_2SO_4 : H_2O_2$, heated to 120°, for 20 minutes

2. Dump rinse, and dry. This initial treatment removes surface contamination and the substrate can be stored, if not needed immediately. However, further cleaning is needed before they can are used for other fabrication steps.

3. Dump rise

4. Dunk in mixture of 4:1 $H_2SO_4 : H_2O_2$, kept at 90°C, for 10 minutes

5. Dump rise, but do not dry

6. Dunk in mixture of 50:1 $DI\ water : HF$, kept at room temperature, for 15-30 seconds

7. Dump rise in DI water

8. Dunk in mixture of 5:1:1 $H_2O : H_2O_2 : HCl$, heated to 70°C, for 10 minutes. This step creates a layer of native oxide on silicon surface and is usually, this step is done before the step requiring dunk in "50:1 $DI\ water : HF$ mixture", so that the substrate is oxide free before further processing. However, CDMS performs the combination in reverse, i.e. dunk in "50:1 $DI\ water : HF$" before a dunk in "5:1:1 $H_2O : H_2O_2 : HCl$", because the layer of native oxide formed preserves the substrate before further processing, is easily removed in through RF etching performed first in the immediately next step of processing.

9. Dump rise, and spin dry

Cleaning steps used at TAMU:

1. Rinse the beakers (to be subsequently used), thermometers, teflon tweezers, cassette (the slotted apparatus in which the substrate is loaded when it is

dipped in corresponding reagents) and storage container (where cleaned wafer will be stored). Rinsing is done using DI water, Acetone, Methanol, IPA, and DI water again. It is blow dried using dry nitrogen. The storage container is dried in oven, kept at 70°C for 5 minutes.

2. Load the substrate into the cassette and rinse it using DI water, Acetone, Methanol, IPA and DI water again.

3. Ultrasonicate them in DI water, kept at room temperature, for 5 minutes.

4. Dunk in mixture of 6:1 $H_2SO_4 : H_2O_2$, kept at 100°C, for 20 minutes

5. Dunk in DI water, kept at 70°C, for 10 minutes (this step is introduced with aim to prevent thermal shock)

6. Dunk in 50:1 $DI\ water : HF$, kept at room temperature, for 45-60 seconds. Ideal end point is when the water does not stick to surface as the substrate is removed.

7. Dunk in DI water, kept at room temperature

8. Dunk in mixture of 5:1:1 $H_2O : H_2O_2 : HCl$, heated to 70°C, for 15 minutes

9. Rinse with DI water, and spin dry. Dry the tweezer separately.

10. Transfer the clean, dry substrate into the clean, dry container. The container is sealed with a plastic bag inside the class-100 clean room, and then another bag before the wafers are carried out. Since the cleaning and thin film deposition facility is in separate room (and separate floors of the building), this procedure is necessary.

K.4 Thin Film Deposition - I

After the wet cleaning, the obtained substrate is flat, smooth and free of metallic and organic impurities. This provides a nice base upon which further detector fabrication efforts can be carried out. The first of these efforts involve deposition of thin films of amorphous silicon, aluminum and tungsten using RF/DC sputtering inside suitably prepared deposition chamber. The aluminum thin film will eventually form rectangular structures which collect phonons (by creating quasiparticles) and funnels them inside the TES. Since it is imperative that the detector surface is dust free and also to prevent radon gas from interacting with detector, the deposition is done in a radon-free class-100 clean room. Physics behind the sputtering process is discussed in Appendix J.1.3.

Due to the difference in thin film deposition machine used at Stanford and at TAMU, the exact sequence in which the film deposition steps are carried out, and the parameters used to deposit the film are slightly different. However, the end result in both cases is same. The description provided below is for the sequence of steps and corresponding deposition parameters used at TAMU.

1. Immediately before it is needed to deposit thin film, the chamber is prepared by coating it with aluminum, via DC sputtering, using argon gas to create the plasma (a discussion is provided in Section 5.2.3). It is done using 2kW DC-bias power, 18mtorr pressure (of argon gas), for 12:30minutes. In the subsequent steps, it is implicit that the gas pressure is of argon gas.

2. The substrate is then mounted inside the processing chamber, and prepared for further processing (a detailed description of this step is provided in Section 5.2.3).

3. To begin with, the substrate is subjected to RF etching (described in Appendix J.2.2) to remove the oxide layer on top of it. It is done using 350W RF-bias power, 10mtorr pressure, for 10:00minutes. However, it should be noted that it is currently not clear whether the role of RF etching (using applied processing parameters) is limited to removal of oxide layer, or if it also affects the roughness, damage and temperature of the substrate surface, thereby, affecting the properties of films deposited in subsequent steps.

4. A 40nm thick film of amorphous silicon is deposited, via RF sputtering. It is done using 500W RF-bias power, 8mtorr pressure, for 16:00minutes. This layer helps in reducing the occurrence of surface events by promoting an efficient charge collection for corresponding events [232, 327] (surface events are described in Section 3.3.3, and are undesirable because they form a major background to WIMP analysis). It also prevents the etching of underlying germanium surface in the etching steps, described in Appendix K.5 and Appendix K.7. The final verification of film thickness is done using SEM.

5. A 300nm thick film of aluminum is deposited, via DC sputtering. It is done using 2.5kW DC-bias power, 10mtorr pressure, for 7:18minutes. This forms the phonon collection fin, which interacts with the athermal phonons in the substrate, collects the energy via generation of quasiparticles and funnels it inside the TES, as discussed in Section 3.2.2. The choice of 300nm thickness of aluminum film is based on assumption that this allows for an efficient diffusion of quasiparticles with aluminum films (before they recombine back to form Cooper pairs) [235], also described in Section 5.1.2.

6. A 30nm thick film of tungsten is deposited, via DC sputtering. It is done using 2.5kW DC-bias power, 8mtorr pressure, for 0:36minutes, while simultaneously

applying a negative DC bias of -100V on the substrate. This layer is not the TES layer (it is important to apply the -100V substrate bias while depositing TES tungsten layer, discussed later, in Appendix K.6. The same is done for this layer also). The layer is deposited because it is its absence which hurts the detector design. If the surface is not coated with layer, and exposed to atmosphere, then a thin layer of aluminum oxide forms, which prevents a good contact (and a good diffusion of quasiparticles from aluminum fins to tungsten TES). With the tungsten layer being present, the oxygen reacts with it to form tungsten oxide, which is easily removed by RF etching the film before depositing the second layer of tungsten film (TES are made on the second tungsten layer, as described in Appendix K.6). Thus, quasiparticles can easily diffuse from the aluminum film to the TES, via the first tungsten layer. It might be argued that a RF etch can remove any oxide layer formed on aluminum film (and that the presence of first tungsten layer is unnecessary). But, in doing so, the aluminum may backsputter in the regions where TES would get fabricated, and cause an increases the T_c of TES fabricated in the corresponding regions. Thus, the average TES transition temperature and the variation of T_c across the substrate [330].

7. Finally, it should be noted that the "deposition recipe" is still not optimal. After the deposition of every film, the deposition machine also allows for the samples to be cooled by keeping it in vacuum. This parameter can be played around to verify if it has any affect on the quality of deposited film

K.5 PhotoLithography and Etching - I

This step creates separate rectangular structures out of aluminum film which collect phonons (by creating quasiparticles) and funnels them inside the TES. A

detailed description of "Photolithography and Etching" can be found in any general textbook on semiconductor manufacturing [331]. Since radon and contamination control is still a main focus, this step is done in a radon-free class-100 clean room. To describe briefly, it involves the following process (An accurate description of the processing parameters is not provided, since primary involvement in this activity was by another group member. The process is expected to be covered in subsequent Ph.D. thesis/research papers from our group):

1. The substrate is covered with a UV sensitive material, called "Photoresist", on top of the deposited thin films (Photoresist is a mixture of photoactive material in a resin. When exposed to UV light, it undergoes a chemical transforming changing its capability to dissolve in suitable solvents. Since we want a controlled exposure of the photoresist to UV light, it is necessary to ensure that the clean room also has UV-free lighting). A uniform, $\sim 1-2\mu m$ thick coating over the entire substrate face is obtained by pouring photoresist over the its surface, and then spinning it at $\sim 3000rpm$. An optimal thickness o

2. The crystal is then allowed to "soft bake", i.e. sufficiently heated/dessicated, so that the photoresist film becomes firm (and is not fluid), but it does not become unresponsive to further processing. An underbaked photoresist cracks, or become frothy when exposed to UV radiation (Traditionally, the metallic film on one side of the substrate is protected (covered) with a thick layer of photoresist which is heated and hardened, before the photolithographic procedures are carried out on the other side. However, the detector fabrication lab at TAMU has the capability to simultaneously perform the lithographic process on both sides of the substrate. After coating one side with photoresist, and softbaking it, the same is also done on the other side. Both sides are then

sequentially carried through each of the photolithographic operations described below).

3. An "OAI Model 200 Table Top Mask Aligner and UV Exposure System" is used to hold the photoresist coated substrate, while a mask (with electrical features imprinted on it) is put on top, and the resist is exposed to UV radiation (of desired intensity). The radiation passes through the transparent regions of the mask (and blocked elsewhere), before interacting with the resist. The regions of the photoresist which interacts with UV radiations becomes hardened, and hard to dissolve in developing solution (described later). The mask used in this step helps to create structures which eventually form the Quasiparticle traps for the TES.

4. Immediately after UV exposure and before developing the photoresist, it is "hardbaked", or heated/dessicated for a longer period to ensure that the photoresist sufficiently hardens that it does not get dissolved in the developer (in the regions where it was exposed to UV radiation).

5. The substrate, with photoresist on top, is dunked in a "developing liquid" which removes the region of photoresist which was not exposed to the UV radiation. Thus, following the above set of procedures, the circuit features designed on the mask gets imprinted on the photoresist.

6. Since the final aim is to imprint these circuit features in the deposited thin film lying below the photoresist, the substrate is subsequently carried through the chemical etching step. The chemicals react with the metallic film wherever the photoresist has been developed off, leaving the remaining portion of the thin film untouched (optimization of the etch timings is one of the ma-

jor achievements obtained at the fabrication facility at TAMU, as discussed in Section 5.2.3). The chemicals used for etching purposes are:

- To etch the topmost layer of tungsten: 30% Hydrogen peroxide (H_2O_2). The etch proceeds via formation of surface oxide which is dissolved by H_2O_2 [332].
- To etch subsequent aluminum layer: "Al-etch". Typical Al-etch contain mixtures of 1-5% Nitric acid (HNO_3) to oxidize aluminum into aluminum oxide, 65-75% Phosphoric acid (H_3PO_4) to dissolve out the aluminum oxide, exposing fresh aluminum to reaction with nitric acid, 5-10% Acetic acid (CH_3COOH) for wetting and buffering purposes, and Water (H_2O) to dilute and define the etch rate at given temperature. During aluminum etch, hydrogen gas bubbles may form on the thin film preventing chemicals from reacting with certain portions of the aluminum film, which leads to uneven etching of the film. Also, the etching process is exothermic and causes the substrate surface and nearby chemicals to heat up, which in turn changes the etch rate for aluminum film. For this reason, it is necessary to intermittently pause the etching process by dunking the substrate in de-ionized (DI) water [332].
- Due to the isotropic etching profile as obtained in wet etching process, an "aluminum undercut", or "tungsten overhang" develops after the previous step, as discussed in Section 5.2.2. This "tungsten overhang" needs to be removed, else it prevents a conformal deposition of subsequent thin film. Therefore, a second tungsten etch (using 30% H_2O_2) is performed after the above step.
- Lastly, it should be noted that the above mentioned etching process may

change in future. There are efforts underway in TAMU detector fabrication labs to allow thin film etch using reactive gases (dry etching), as against currently used wet chemical etching. In comparison to wet etching, the dry etching is more controllable and there is less variation in etched features [306].

7. After the etching step, the remaining photoresist is removed by dunking the substrate in the chemicals PRX-127, followed by dunk in PRS-1000. The substrate, with etched thin film pattern, is then cleaned using DI water, and dried.

K.6 Thin Film Deposition - II

The next step of processing involves depositing another thin film of tungsten on which TES sensors will be patterned (in a radon-free class-100 clean room). The following steps are carried out:

1. Immediately before it is needed to deposit thin film, the chamber is prepared by coating it with aluminum, via DC sputtering, using argon gas to create the plasma (a discussion is provided in Section 5.2.3). It is done using 2kW DC-bias power, 18mtorr pressure, for 12:30minutes.

2. The substrate is then mounted inside the processing chamber, and prepared for further processing (a detailed description of this step is provided in Section 5.2.3).

3. To begin with, the substrate is subjected to RF etching (described in Appendix J.2.2) to remove the oxide layer on top of it. After the previous photolithographic and etching step, the substrate surface is covered the mutually disconnected, aluminum quasiparticle traps, capped with a thin layer of tungsten. The etched area exposes the amorphous silicon layer which was deposited

before the other the aluminum and tungsten films. THE RF-etch step removes oxide layer from both tungsten and amorphous silicon. The oxide layer removal from tungsten surface helps the subsequently deposited tungsten thin film (on which TES element will be etched) to bond firmly with the quasiparticle traps (the aluminum fins), allowing for an easier transfer of the quasiparticle from the traps into the TES. Since the presence of oxygen catalyzes the formation of beta-pases of tungsten which has a high superconducting transition temperature (discussed in Section 5.1.3), it is necessary to ensure the removal of oxide layer from the exposed amorphous silicon layer before fabricating TES on it. RF-etch is done using 350W RF-bias power, 10mtorr pressure, for 10:00minutes.

4. A 40nm thick film of tungsten is deposited, via DC sputtering. It is done using 2.5kW DC-bias power, 8mtorr pressure, for 0:51minutes, while simultaneously applying a negative DC bias of -100V on the substrate. A larger, negative bias on the substrate promotes impingement by positively charged Ar^+ ions inside the plasma, acting to sputter etch any oxide layers which may be present on the substrate surface [351] (it is known that presence of oxygen promotes formation of β tungsten which has high T_c [311]).

K.7 PhotoLithography and Etching - II

A second photolithography and etching step is carried out (in a UV-free, radon-free class-100 clean room) to pattern TES in the newly deposited tungsten thin film. This also electrically connects the various, disjointed aluminum quasiparticle traps to the TES. Additionally, this step etches out most of the tungsten thin film which was previously existing on top of the aluminum quasiparticle trap (except for a very small contact between the TES and the trap). The design aspects (of TES, and its

connection with the quasiparticle trap) is discussed in details in [235].

K.8 PhotoLithography and Etching - III

A final photolithography step is needed on the side of substrate which is to contain the charge electrodes. Performed in a UV-free, radon-free class-100 clean room, this step creates a circular "trench", to form concentric inner and outer charge electrodes (Described in Appendix G.4). In developing the trench, the metallic thin films (tungsten and aluminum) and the amorphous-silicon film is etched off (amorphous silicon is dry-etched using plasma of reactive methane, CH_4, and fluorine, F_2, gas). Apart from it, there aren't any major features on the side of crystal containing charge electrodes, as shown in Fig. 3.1

K.9 Inspection and Wirebonding

A last step in detector fabrication is the visual inspection of each phonon sensor (in a radon-free class-100 clean room), to ensure that there is no short, i.e., there are no aluminum film/feature which did not get removed in the etching process and are now connecting the phonon bias lines. At $\sim 80mK$ temperature of operation, aluminum is superconducting and would create a zero resistance pathway, or, a short-circuit between the bias lines, rendering the phonon channel useless. If shorts are present, then it is "scratched" off (a fine needle tip is used to disconnect the shorted region).

Another feature which is inspected is the presence of opens, i.e, the bias lines do not connect to some/most of the TES. This is fixed by performing a "wirebonding", i.e., by connecting a fine, micron scale aluminum wire across the regions where he film is broken.